Ash formation and deposition in coal and biomass fired combustion systems: Progress and challenges in the field of ash particle sticking and rebound behavior

Kleinhans, Ulrich; Wieland, Christoph; Frandsen, Flemming J.; Spliethoff, Hartmut

Published in:
Progress in Energy and Combustion Science

Link to article, DOI:
10.1016/j.pecs.2018.02.001

Publication date:
2018

Document Version
Publisher's PDF, also known as Version of record

Progress in Energy and Combustion Science 68 (2018) 65–168

Contents lists available at ScienceDirect

Progress in Energy and Combustion Science

journal homepage: www.elsevier.com/locate/pecs

Ash formation and deposition in coal and biomass fired combustion systems: Progress and challenges in the field of ash particle sticking and rebound behavior

Ulrich Kleinhans[a,*], Christoph Wieland[a], Flemming J. Frandsen[c], Hartmut Spliethoff[a,b]

[a] Institute for Energy Systems, Technische Universität München, Boltzmannstr. 15, Garching 85748, Germany
[b] ZAE Bayern, Walther-Meissner-Str. 6, Garching 85748, Germany
[c] CHEC Research Centre, Department of Chemical Engineering, Technical University of Denmark, Lyngby DK-2800, Denmark

ARTICLE INFO

Article History:
Received 17 May 2017
Accepted 4 February 2018
Available online xxx

Keywords:
Solid fuel combustion
Slagging and fouling
Ash formation
Ash deposition
Ash particle properties
Particle-wall-interaction
Droplet impaction
Critical viscosity
Melt fraction
Particle stickiness
Particle rebound

ABSTRACT

The purpose of this paper is to review the present knowledge on ash formation, ash particle transport and deposition during solid fuel combustion, with emphasis on particle sticking and rebound behavior. A substantial part of the fuel can be inorganic, forming inorganic vapors and ash particles. The impaction of solid, molten or partially molten particles on surfaces is dependent on the particle and surface characteristics. For instance, a particulate deposit might capture incoming particles or be removed due to erosion, while a molten layer will collect all impacting particles, no matter if they are sticky or not. The main properties affecting the particle stickiness are the viscosity and surface tension for silicate-rich ashes. On the contrary, the stickiness of salt-rich ashes – typical for herbaceous biomass and wood- or waste-based fuels – is often described using the liquid melt fraction. Furthermore, the particle kinetic energy and the angle of impaction, are crucial parameters. If all kinetic energy is dissipated during the impact, the particle will remain on the surface. This review presents an overview of major ash forming elements found in biomass and coal, and discusses the heterogeneity of particles' inorganic composition. Ash transport and deposition mechanisms as well as their mathematical description are given and discussed, together with composition- and temperature-depended models for the estimation of ash particle and deposit properties. These properties are essential in order to describe the particle sticking and rebound behavior.

Ash particle sticking and rebound criteria can be divided into three main groups, based on either: (1) the particle melt fraction, (2) the particle viscosity, or (3) the energy dissipation of a particle, upon impaction. Sticking criteria are presented, their required parameters are discussed and typical particle and surface properties found in combustion systems, are summarized. Eight different sticking criteria are implemented in a computational fluid dynamics code and computations are compared against measurements from an entrained flow reactor. Uniform sized soda-lime glass particles are applied instead of inhomogeneous fly ash particles, since soda-lime glass is known to behave similar to coal fly ash. Best agreement for the deposition rates on a clean tube is achieved using a criterion based on the work of Srinivasachar et al. [1]. In this model, the sticking and rebound threshold, is a function of the particle kinetic energy, the angle of impaction, and, the particle viscosity. Particularly, the particle viscosity is confirmed as a key parameter for silicate-rich ashes. It should be calculated using temperature- and composition-dependent correlations, being aware that there is a significant scattering in the results from such models and that the models are often only valid in narrow compositional ranges, and cannot be used outside these. A mechanistic model is used to explain results from glass particle experiments and their dependence on the particle kinetic energy. Therefore, the impaction process is subdivided in four steps, and the energy dissipation of each step is calculated. These theoretical considerations show that the contact angle of a molten droplet with the substrate is of minor importance, and that the majority of depositing particles are dominated by the work of deformation against viscosity, rather than surface tension effects.

This review underlines the importance of the particle viscosity, and its accurate prediction for silicate-rich ashes. The proposed criterion is able to predict the sticking of small, solid particles below 10 μm diameter, as it is often observed in literature. Also, it is crucial to consider the surface structure and stickiness, in order to predict deposition rates in solid fuel-fired systems. Biomass ashes and their stickiness are more difficult, due to a different ash particle chemistry, compared to coal ashes. Salt-rich particles and their stickiness are

* Corresponding author.
E-mail address: ulrich.kleinhans@tum.de (U. Kleinhans).

http://dx.doi.org/10.1016/j.pecs.2018.02.001

controlled by the amount of liquid phase. Here, a link between the viscosity and amount of liquid phase is a promising approach, and should be addressed in future work. Furthermore, the viscosity of different ash particles – silicate-, salt- or Ca-rich – should preferentially be modeled from the chemical and physical structure instead of an empirical fitting procedure between fuel chemistry and viscosity measurements.

Contents

Nomenclature

Abbreviations:

ADLVIC	Ash deposit Local Viscosity, Index of refraction and Composition
PAS	Aerodynamic Particle Sizer
AT	Arrhenius Type
BFB	Bubbling Fluidized Bed
BLPI	Berner type Low Pressure Impactor
BSE	Back-Scattered Electron
C	Criterion
CCSEM	Computer-Controlled Scanning Electron Microscopy
CFB	Circulating Fluidized Bed
CFD	Computational Fluid Dynamics
CO	COndensation
COR	Coefficient Of Restitution
DEM	Discrete Element Method
DI	DIffusion
DMA	Differential Mobility Analyzer
DO	Discrete Ordinates
DSC	Differential Scanning Calorimetry
DTM	Discrete Transfer Method
EDX	Energy Dispersive X-Ray
EF	Eularian Formulation
EFR	Entrained Flow Reactor
EI	Eddy Impaction
ELPI	Electrostatic Low Pressure Impactor
ESP	ElectroStatic Percipitator
FB	Fluidized Bed
FG-DVC	Functional Groups - Depolymerization Vaporization and Cross-linking model
FLOREAN	FLOw and REActioN - CFD code
IN	INertial impaction
JKR	Johnson-Kendall-Roberts
KD	Kinetics/Diffusion limited char combustion model
KW 21	KraftWerke des 21. Jahrhunderts
LEADER	Low-temperature Engineering Algorithm of DEposition Risk
LHV	Lower Heating Value
LT	Lagrangian Tracking
MIT	Massachusetts Institute of Technology
MSW	Municipial Solid Waste
NBO	Non-Bridging Oxygen
PCGC	Pulverized Coal Gasification and Combustion
PF	Pulverized Fuel
PM	Particulate Matter
PSD	Particle Size Distribution
QEMSCAN	Quantitative Evaluation of Minerals by SCANning electron microscopy
RH	ReHeater
RMSE	Root Mean Square Error
RNG	Re-Normalization Group for turbulence modeling
SE	Semi-Empirical
SEM	Scanning Electron Microscope
SH	SuperHeater
SMPS	Scanning Mobility Particle Sizer
SR	Single Rate devolatilization model
SRF	Solid Recovered Fuel
SST	Shear Stress Transport
STA	Simultaneous Thermal Analysis
TEC	Thermodynamic Equlibrium Calculation
TGA	Thermo-Gravimetric Analyzer
TP	ThermoPhoresis
TR	Two competing Rates devolatilization model
UC	Unit Cell
UDF	User-Defined Function
WT	Weymann Type
XRD	X-Ray Diffraction

Latin symbols:

a, b [-]	fitting parameter
A [m^2]	area
A [$(m^3/kmol^{n-1})/s$]	pre-exponential factor
A_H [J]	Hamaker constant
A_O, A_W, H_O, H_W [-]	coefficients for the thermophoretic coefficient
A, B, C, D [-]	fitting parameter
Bi [-]	Biot number
B/A [-]	ratio of base to acid fuel ash components
c_i [mol/m^3]	concentration of species i
c_p [J/(kg K)]	heat capacity
C_e, C_m, C_{int} [-]	temperature jump, velocity slip, and interp. constant
C_m [-]	proportionally factor
Ca [-]	Capillary number
d [m]	diameter
D [m]	diameter of a tube/cylinder
$D_{A,B}$ [m^2/s]	diffusion coefficient of species A in species B
D_{Kn} [m^2/s]	Knudsen diffusion coefficient
D_p [m^2/s]	particle Brownian diffusion coefficient
DT [°C]	deformation temperature (ash fusion test for biomass)
e [A s]	elementary charge
e [-]	coefficient of restitution
e_n, e_t [-]	normal (n) and tangential (t) restitution coefficient
E [J]	energy
E [V/m]	electric field strength
E [MPa]	Young's modulus
E_A [kJ/mol]	activation energy
E_{ERE} [-]	excess rebound energy
f [-]	coefficient of friction
f_p [-]	melt fraction
f_{11}, f_{21}, f_{41} [-]	functions for the thermophoretic coefficient
F [N]	Force
FT [°C]	fluid temperature (ash fusion test)
g [m/s^2]	gravitational acceleration
G [MPa]	shear modulus
h [$W/(m^2 K)$]	heat transfer coefficient (often introduced as α)
h [kJ/kg]	specific enthalpy
h [m]	height
H [-]	function for the sticking probability
H_f [kJ/kg]	heat/enthalpy of fusion
HT [°C]	hemispherical temperature (ash fusion test)

IDT [°C]	initial deformation temperature (ash fusion test)
J_W [kg/(m^{2}s)]	mass flux of particles to the wall per unit area
$J_{p,\infty}$ [kg/(m^{2}s)]	mass flux of particles in the bulk per unit area
k [W/(m K)]	thermal conductivity
k^{-1} [m]	capillary length
k_{ero}, k_{shed} [-]	erosion and shedding frequency parameter
k_p, k_w [-]	parameter for the elasticity of the particle and wall
k_s^+ [-]	dimensionless surface roughness height
Kn [-]	Knudsen number
K_{tc} [-]	thermal creep coefficient
l [m]	length
m [kg]	mass
$\dot{m}$ [kg/s]	mass flow rate
M_i [kg/kmol]	molar mass of species i or symbol denoting species i
n, m [-]	exponents for Sherwood and Nusselt correlations
n, m, k [-]	index of refraction, complex refr. & absorptive index
p [Pa]	pressure
p_i [Pa]	partial pressure of species i
p [-]	porosity
p_{stick} [-]	sticking probability
P [N s]	impulse (momentum)
Pe [-]	Peclet number
Pr [-]	Prandtl number
q [A s]	electric charge of a particle
q [W/(m^{2}K)]	surface heat flux
$\dot{Q}$ [W]	heat flux
Q [-]	parameter for the chemical composition
r_o, r_i [m]	outer (o) or inner (i) radius
R [J/(mol K)]	ideal gas constant
R [K/W]	thermal resistance for A = 1 m^2
R [-]	function for the sticking probability
Re [-]	Reynolds number
s [m]	thickness (of layer or wall)
s^* [-]	dimensionless droplet thickness
s_L, s_L [m]	longitudinal and traversal pitch
S_i [-]	supersaturation ratio of species i
Sc [-]	Schmidt number
Sh [-]	Sherwood number
SST [°C]	shrinkage starting temp. (ash fusion test for biomass)
St [-]	Stokes number
Ste [-]	Stefan number
ST [°C]	softening temperature
t [s]	time
T [K], [°C]	temperature
u, v, w [m/s]	velocity component in direction x, y and z
u_* [-]	dimensionless friction velocity
$\overline{v}_M$ [m/s]	mean molecule velocity
V [m^3]	volume
$\overline{V}$ [m^3/kmol]	partial molar volume
V_{dep+} [-]	dimensionless deposition velocity
w_i [wt.%]	mass fraction of species i
W [J]	work
We [-]	Weber number
x [-]	fitting parameter for sintering law
x, y, z [m]	coordinates in all three spatial directions
x_i [mol.%]	mole fraction of species i
x_1, x_0, x_b [m]	elasticity length scale, distance, surface roughness
Y [MPa]	yield strength

Greek Symbols:

α_e, α_m [-]	energy and momentum accommodation coefficients for TP
α_{shed} [-]	order of shedding
β [-]	contact area ratio
χ [-]	radiative exchange factor
γ [kg/s^2]	surface tension (sometimes defined as σ)
ε [-]	emissivity
ε [-]	strain
ε [m^2/s^3]	dissipation rate
ζ [-]	electrical charge parameter
η_{front}, η_{back} [-]	impaction efficiency cylinder front and rear face
λ [m]	free mean path length of molecules
λ [-]	mean number of mineral inclusion per particle
λ [-]	parameter for the maximum contact pressure
μ [kg/(s m)]	dynamic viscosity (sometimes defined as η)
ν [-]	Poisson number
ν [m^2/s]	kinematic viscosity
ξ [-]	spread diameter
ρ [kg/m^3]	density
σ [W/(m^2 K^4)]	Stefan Boltzmann constant
σ [MPa]	mechanical stress
τ_g [s]	characteristic flow time for flow around cylinder
τ_p [s]	particle relaxation time
τ_{p+} [-]	dimensionless particle relaxation time
τ_w [kg/(s^2 m)]	wall shear stress
ϕ [kg/(s^3 m)]	viscous dissipation function
φ [rad]	angle of impaction between particle and surface
ψ [-]	correction factor for effective Stokes number
ω [s^{-1}]	specific dissipation rate
Δ [m]	distance between particle surface and substrate
Θ [rad]	angle indicating the position around cylinder
Θ_c [rad]	contact angle between substrate and droplet
Λ [-]	thermal conductivity ratio
Φ [-]	thermophoretic coefficient or phase function of thermal radiation

Subscripts:

0	initial
1, 2	collision partner 1 and 2
10, 50, 90	percentage under this value
ad	adhesion

a, ash	ash
BL	boundary layer
BP	boiling point
c, e	contact or equilibrium angle
cv	critical value
crit	critical
c, char	char
cond	conduction
conv	convection
cyl	cylinder
dep	deposit, deposition
def	deformation
DE	deformation energy
eff	effective
el	elastic, electrical
ext	external
EFR	entrained flow reactor
f, fuel	fuel (as received)
fri	friction
g	gas
g-s	gas-solid mixture
i, r	impact, rebound
imp	impaction
int	internal
kin	kinetic
KE	kinetic energy
liq	liquid, moisture in the fuel
LV	liquid-vapor interface
M	molecule
max	maximum
m, mineral	mineral matter
min	minimum
mix	mixture
n, t	normal, tangential
o, i	outer, inner
op	operational, operating
p	particle
pl	plastic
rad	radiation
ref	reference
rot	rotational, rotation
s	solid, surface, separation, stagnation, steam
surf	surface
SE	surface energy
SL	solid-liquid interface
SV	solid-vapor interface
th	thermal, thermophoretic
tot	total
tr	translational
v, vol	volatiles
w	water
w, W	wall
y	yield (limiting contact pressure)
∞	free-stream, bulk conditions

1. Introduction

Ash deposition on heat exchanging surfaces during solid fuel combustion, leads to a number of operational problems, and may cause frequent power plant shutdowns, reduced heat transfer rates or increased soot-blowing and cleaning activities [14–16]. The main route between a burning fuel particle in a furnace, and a troublesome deposit on a heat transfer surface, can be divided into a number of consecutive steps:

- Release of critical ash-forming elements (mainly K, Na, S, Cl, Zn, and Pb), during devolatilization, and subsequent char burnout,
- Formation of aerosol particles by nucleation and coagulation of flame-volatilized ash-forming elements,
- Formation and entrainment of coarse fly ash particles through mineral transformation (chemically and physically) during devolatilization and char burnout,
- Transport of ash species, i.e. gases, liquids (droplets) and solids (particles), from bulk gas to heat transfer surfaces,
- Sticking, adhesion or rebound of these ash species on heat transfer surfaces, and
- Build-up, sintering and consolidation, erosion and shedding of deposits.

Through several years, high-quality research has been conducted to characterize fuels [2–6], investigate fuel conversion and ash formation [7–11], as well as ashes and deposit formation in utility boilers fired with coal, biomass and waste fractions [12–20]. Huge amounts of experimental data have been gained, but the fact is that there are still in 2017, a number of big gaps in our current understanding of ash and deposit formation in utility boilers, and that we need to focus strongly on these points, in order to be able to describe, understand and quantify the process of deposit formation completely. Many high-quality data are available on the release of critical ash-forming elements, although most of the lab-scale measurements are performed under experimental conditions different from what happens in full-scale. The main difference being the particle size distribution of the fuels investigated, and the time-temperature history, mainly the heat-up rate and final temperature, experienced by the fuel particles. Further important differences between small-scale setups and furnace environments are particle concentrations affecting particle dynamics and particle formation by condensation, as well as the fact that drop tube studies are often conducted with high excess air and low gas velocities. Both, particle concentration and excess air, are crucial explaining partial vaporization, e.g. of alkali metals. Fly ash formation has been intensively studied for coal combustion, where the fly ash size distribution has a multi-modal size distribution [21–23]. Larger particles originate from mineral grains in coal and their size distribution depends upon the coal characteristics, pre-treatment (sizing) of the coal, and, the actual combustion conditions. Sub-micron particles on the contrary, originate mainly from homogeneous nucleation, and subsequent coagulation of flame-volatilized inorganic species. Other important processes going on include fragmentation of chars and mineral inclusions as well as coalescence of ash droplets on receding char surfaces. A number of basic mechanisms of ash species transport has been outlined and quantified in the literature during the last 20 years, but a very crucial aspect of ash deposition, the process when an ash particle impacts on a heat exchanging surface, is often not addressed or discussed in detail. There is a lack of a comprehensive review in the field of ash particle sticking and rebound behavior and a comparison of different sticking criteria in terms of accuracy and performance. In this field, many publications use inappropriate models underlining the necessity of a review. Therefore, this paper summarizes ash formation and deposition mechanisms, discusses the differences between biomass and coal, and presents a critical literature review on ash particle sticking and rebound criteria.

This paper is organized in the following manner. Section 2 provides the fundamentals of solid fuel combustion systems, inorganic constituents in solid fuels, ash formation, fly ash particles and their classification, deposit formation mechanisms as well as an overview on the effect of deposits on heat transfer. It is a summary of major

literature references, however, due to the enormous amount of studies in this wide field, it is not possible to include all findings. Section 3 gives mathematical models for the estimation of particle and deposit properties. These properties are required in order to describe the ash particle stickiness. The following two sections review experimental and theoretical studies on ash particle sticking and rebound behavior. Different sticking criteria found in literature are summarized and discussed critically for their applicability. Section 6 evaluates and compares different sticking criteria and explains main findings. Section 7 presents a comprehensive model describing all relevant processes during ash deposition in solid fuel-fired systems. Finally, an outlook and recommendations for future work is given and conclusions are drawn.

2. Fireside deposit formation

Solid fuel combustion has been subject to research for more than 100 years. But still today there are many unresolved problems and phenomena, which are not understood in detail. Many existing mathematical models describing solid fuel conversion are empirical in nature and fitted towards measurements. One of the main reasons is the heterogeneity and complex chemical structure of solid fuels and their changes during thermal conversion. Fuel conversion in combustion systems involves homogeneous and heterogeneous chemical reactions, changing particle structures entrained in a turbulent flow combined with radiative heat transfer. The complex interaction of these phenomena, is the main difficulty in understanding and modeling such systems.

2.1. Solid fuel combustion systems

Typical solid fuel combustion systems are illustrated and compared in Fig. 1. They comprise of three main types: grate combustion, fluidized bed (FB) combustion and pulverized fuel (PF) combustion systems. Characteristics of each boiler type are summarized underneath each schematic. The main difference among boiler types are boiler size, fuel quality, fuel processing before combustion, fuel-oxidizer ratio, gas flow conditions as well as temperatures.

Pulverized fuel boilers are the most commonly built systems for power generation from coal. Pulverized fuel, with a typical particle size smaller than 200 μm, is transported with preheated air or recirculated flue gas to the burner and into the furnace. Particles heat up, release combustible gases and react with oxygen, forming flue gas. The flue gas is transported with the remaining ash particles through the combustion chamber. Boiler walls and tubes inside the combustion system act as heat exchanging surfaces, where heat is transferred from the flue gas to the water-steam cycle. PF systems are designed in a way that combustion is completed before the flue gas reaches the first convective heat exchanger in the form of tube banks. This ensures lower temperatures of remaining fly ash particles, compared to burning particles, and thus a reduced threat of molten, sticky ash particles adhering to heat exchanging surfaces. There are studies indicating that char particles burn at temperatures up to 300 K higher than the surrounding flue gas [24]. A critical parameter, when designing the furnace and its height, is the ash softening and ash melting temperature. The furnace exit gas temperature should stay below the ash softening temperature. However, this criterion can also fail. There are studies reporting up to 50% of melt in the ash system at the ash softening temperature [25,26]. In this case, there can be excessive deposit formation, even though the furnace exit gas temperature is below the ash softening temperature. The main difficulty in boiler design is to achieve a high level of burnout, while staying below the ash softening temperature. This is challenging, since nowadays, fuel and load flexibility become more and more important. Within combustion systems, ash deposition is often defined as either slagging or fouling. Slagging occurs in the furnace area, where heat exchanging surfaces are exposed directly to flame radiation. A further definition states that particles or deposits are molten, and thus in the liquid state. Fouling is referred to deposits, which are not directly exposed to flame radiation. Deposits in this area are typically caused by solidified particles. Fouling layers are loosely bound or partly sintered, and therefore usually more easy to clean [15]. Fig. 1 shows areas threatened by slagging (filled with gray color) and fouling (no color). In modern tower boiler configurations, this area ends after the first superheater, when radiation of the flame is shaded by earlier tube banks. In the conventional two path boiler design, this area is in the cross-over path between the first and the second duct. The transition between slagging and fouling is smooth and the extent to which a certain fuel leads to slagging or fouling is highly dependent on the form and chemical composition of the inorganic material within the fuel as well as the process conditions inside the boiler.

Fluidized bed combustion systems can be characterized as either bubbling fluidized bed (BFB) or circulating fluidized bed (CFB) combustion systems. The basic idea is to burn the fuel in a hot bed of small particles, e.g. quartz sand, which are fluidized using combustion air from below. The bed material is typically kept at relatively low temperatures (800–900 °C) in order to reduce pollutant formation, particle agglomeration (e.g. caused by low melting ash particles), ash deposition and corrosion. Furthermore, chemically inert material is used to inhibit reactions between fuel ash and bed materials. An exception are sulfur-rich fuels (e.g. pet-coke), where limestone is added to the bed material, in order to reduce SO_2 emissions. The combustion air is injected using jets from below and depending on gas velocity, particle size and density of the bed material, bed material is entrained in the flow (CFB) or it remains in a bubbling bed (BFB - stationary fluidized bed). CFB systems circulate the bed material and require a separation unit, typically a cyclone. These systems enable a higher energy density and improved heat transfer rates, however design and operation are more complex. Furthermore, bed material such as quartz is known to be erosive, leading to erosion on heat exchanging surfaces and/or to the removal of deposits. Fluidized bed combustion systems are characterized by good mixing characteristics between fuel, combustion air and the bed material and thus a high momentum and heat transfer leading to a uniform temperature distribution.

Fluidized bed systems are typically built in medium size, from 30 to 350 MW_{el}, for troublesome fuel ashes or fuels with a low volatile content and thus low combustibility (e.g. pet-coke or sewage sludge with a high moisture content). Typical fuels are waste wood, pet-coke, solid recovered fuels (SRF) in the form of pellets or sewage sludge [27–29]. The fuels' high ash content and low ash melting temperature can be handled through a moderate and uniform temperature enabled by the good mixing behavior inside the bed material. The biggest concerns for operators are bed reactions and agglomeration. Bed agglomeration can lead to a decrease in heat transfer and fluidization. In extreme events it may lead to the total defluidization of the bed, resulting in unscheduled plant shut down [30]. Bed agglomeration is often caused by chemical reactions of inorganic vapors or molten phases of salts and/or silicates. These mechanisms and ash species can lead to coating, adhesion and sintering between sand particles [30,31]. Slagging is rarely reported for FB combustion, due to low temperatures and erosion by bed material, compared to grate firing or PF systems.

Grate combustion is typically used for low-grade fuels with troubling ash behavior. Commonly used fuels are municipal solid wastes (MSW), straw or wood including waste wood, forest residues or demolition wood. The fuel is burned without pretreatment on a moving grate, where combustion air is supplied from beneath. Modern systems use a staged air supply, where the combustion zone on the grate uses low stoichiometries in order to suppress nitric oxides.

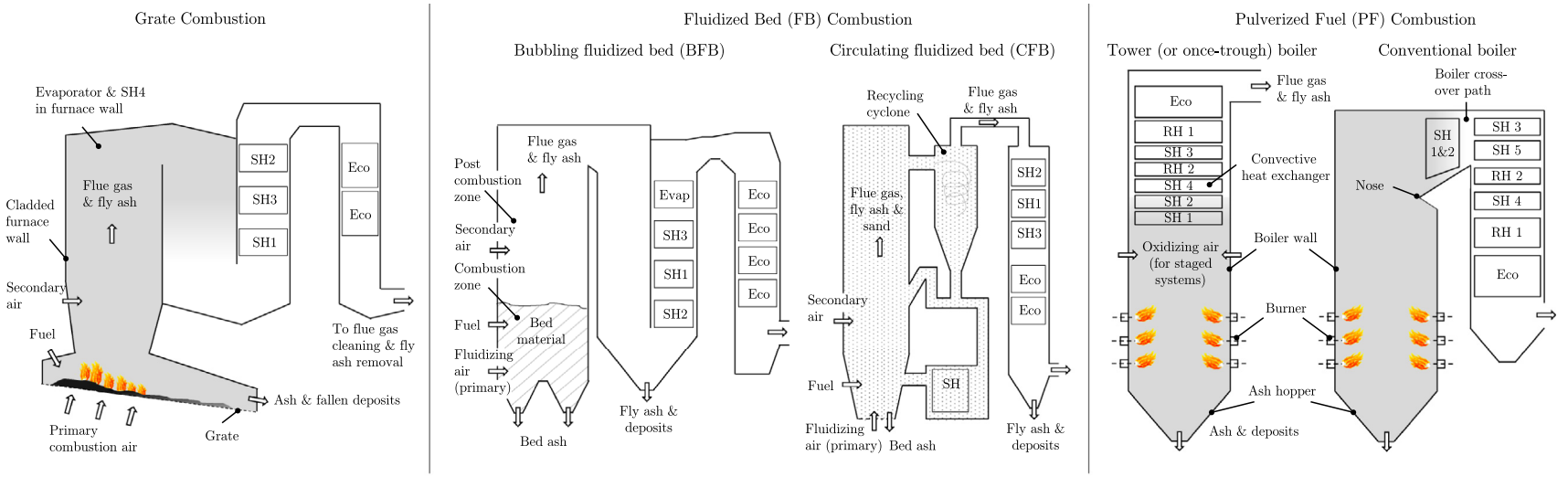

Fig. 1. Combustion systems for solid fuels showing locations threatened by slagging and fouling. Typical process conditions, fuels, steam temperatures and efficiency values are given.

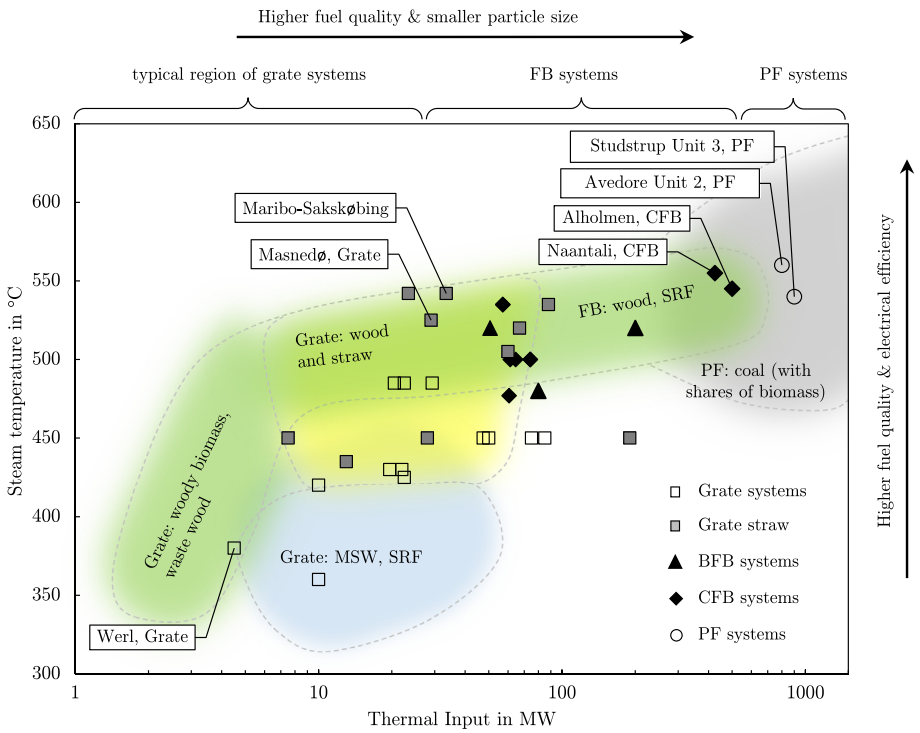

Fig. 2. Final steam temperatures of biomass-fired power stations as a function of plant size: Comparison of different firing systems currently using up to 100% biomass. BFB: bubbling fluidized bed, CFB: circulating fluidized bed, PF: pulverized fuel, MSW: municipal solid waste, SRF: solid recovered fuels (Figure modified and extended from [33]).

A substantial part of the inorganic material is transported out of the systems as solid ash particles and agglomerates via the grate. However, small ash particles and inorganic vapors can be entrained by combustion gases. They are liberated from the grate and transported through the flue gas duct of the boiler. The first duct is typically cladded in order to prevent the boiler wall from deposition of molten ash particles and excessive corrosion. Steam temperatures are often limited to values below 500 °C, due to high chlorine contents in the raw fuel, and, thus, the threat of high temperature chlorine-induced corrosion. Studies on straw grate firing have shown that fly ash is enriched in salt species consisting mainly of K, S and Cl, compared to bottom ash, which is silicate like and rich in K, Ca and Si [32]. This fly ash can lead to severe operational problems such as slagging in the furnace or fouling at lower temperatures further downstream, e.g. on secondary or tertiary superheaters.

When comparing combustion systems, the power plant size, final steam temperature and the net electrical efficiency increase typically in the order: grate firing, FB and PF as illustrated in Fig. 1. The choice of combustion system is mainly depending on the fuel, its availability and inorganic constituents. Fig. 2 shows steam temperatures for different firing systems as a function of thermal input. The steam temperature is directly connected to the plant electrical efficiency. The highest steam temperatures are currently obtained for supercritical coal-fired power plants, where the latest built generation reaches values slightly above 600 °C and 285 bar. In addition, Fig. 2 shows current steam temperatures of biomass-fired combustion systems. It can be seen that medium to large-scale systems with a thermal input of 10–200 MW_{th} have relatively low steam temperatures – up to 540 °C – compared to the latest design values of ultra supercritical coal-fired power stations, which exceed 700 °C at 330 bar. Currently, the highest steam temperatures in biomass combustion are found in a tangentially-fired PF system operated by DONG Energy. In 2000, DONG commissioned unit 2 at Avedore Denmark, a 563 MW_{el}, supercritical coal-fired boiler with 600 °C steam temperature and an electrical efficiency of 46%. The unit was converted to high-quality wood pellets in 2004. The operator had to reduce the steam temperature to 540 °C in order to reduce the risk of ash deposition and corrosion. In 2006, they introduced coal fly ash injection to avoid the corrosive environment and to increase steam temperatures to 560 °C, which led to an electrical efficiency of 43.8%. The process was successful, however, mechanisms are still not understood. Coal fly ash is assumed to absorb potassium, which otherwise forms corrosive KCl-rich inner deposits on superheater tubes. This conversion shows the main problem of today's power generation from solid biomass: deposition and corrosion caused by inorganic species. Even with high-quality wood pellets, steam temperatures are limited. This is even more troubling when using straw and other chlorine-rich biomasses. They are typically burned in systems with much lower steam temperatures, as shown in Fig. 2. Lower temperatures are mainly caused by the threat of severe ash deposit formation and high-temperature chlorine-induced corrosion [33]. An interesting approach was presented for grate-firing systems in Masnedø and Maribo Sakskøbing, where the superheater design was changed to so-called collecting superheaters. The new design enabled an increase in final steam temperatures from 450 to 540 °C by allowing the collection of ash deposits. Successful tests revealed a protective oxide layer formation as a shield against chlorine-induced corrosion [34].

Combustion systems also differ in process conditions, such as particle size, flue gas temperatures, or flue gas velocities, as listed beneath Fig. 1. With higher flue gas temperatures, ash particles are softer/contain a higher fraction of melt and thus their tendency to stick upon impaction on a surface increases. A higher flue gas velocity increases the particle kinetic energy, and thus the probability to impact on walls, such as the boiler wall or tubes. A detailed discussion on process conditions will be given in Section 4. Solid fuel combustion in a furnace involves a number of complex steps releasing chemically-bound energy as heat. Typically, there are four steps describing the process of solid fuel combustion [35,36]: (1) drying and release of moisture, (2) devolatilization, i.e. thermal decomposition and release of volatile matter, (3) ignition and combustion of volatile matter, (4) and char combustion. Char combustion is known as the slowest step and the parameter determining the furnace height in PF combustion systems. Char combustion has to be

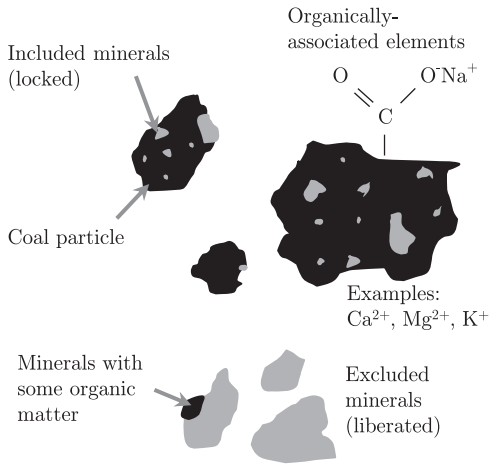

Fig. 3. Inorganic constituents in coal and their occurrence (see also Benson and others 1993 [14]).

completed before particles can enter the superheating region. Otherwise, particle temperatures are too high due to the exothermic oxidation and ash is molten, thereby increasing the sticking propensity and the risk of corrosion. During the process of combustion, inorganic constituents transform physically and chemically and form the remaining ash, which is dominated by solid ash particles. However, inorganics can also be found as gaseous species, as liquid droplets or as solids, depending on the fuel and flue gas temperature. The following sections focus on observations made in experiments and their implication for numerical models. They include an overview on fuel inorganics, as well as fundamentals of ash and deposit formation.

2.2. Fuel inorganic constituents

A substantial part of solid fuels can be inorganic in nature and is difficult to remove from the organic substance. This ash forming matter varies strongly among different fuel types, and for coal it can range from as low as 2 wt.% in a clean feedstock up to 40 wt.% for low-grade lignite. Unfortunately, there is large confusion and misunderstanding of definitions for inorganic constituents in the literature. A commonly used classification for inorganic material in solid fuels is presented by Ward [37]; where similar definitions go back to the pioneering work of Benson and Holm [38] applied for a low-grade coal. Work in the field of biomass can be found in the publication of Zevenhoven et al. [6], Werkelin et al. [4,135], Marschner [39] or Vassilev et al. [5]. It has to be mentioned that definitions differ in literature, but mainly four groups of inorganic constituents are used for coals and biomass:

- **Dissolved salts** and other inorganic substances in the fuel moisture. In coals they can originate from contact with sea water, and are contained in the pore water. In biomass, such as wood or straw, dissolved salts originate from the liquid phases inside the plants. Elements are typically found as cations of K^+, Na^+, Ca^{2+} and anions Cl^-, HPO_4^{2-}, $H_2PO_4^-$, SO_4^{2-} or $Si(OH)_3O^-$.
- **Organically-bound ash-forming compounds**: Inorganic elements that are incorporated in organic compounds (e.g. in the macerals of coals). Typically these are cations including K^+, Na^+, Ca^{2+}, Mg^{2+}, Fe^{3+}, Al^{3+}. A further group consists of covalently bonded non-metals such as organic S, P or Cl.
- **Included minerals** found as discrete inorganic particles within the fuel matrix, either crystalline or non-crystalline, representing mineral components. Within coals, these included mineral grains are often finely dispersed and intimately mixed with the organic substance and therefore difficult to remove. Within woody biomass, typical minerals are composed of Ca, Si, Mg; where Ca is frequently found in the form of calcium oxalate CaC_2O_4, which forms crystals during the drying of wood-based fuels. In the case of herbaceous fuels such as straw, soluble Si in the form of silicic acid $Si(OH)_4$ is transported within the cell walls and enriches in insoluble SiO_2 leading to the strengthening of the plant tissue.
- **Excluded minerals**, are liberated from the organic structure. For coals this can occur during the coalification process or during milling in the power station. Typical excluded mineral grains are quartz, pyrite or clay minerals. In the case of biomass, impurities originate from the soil or contaminants attached to the plant. Typical representatives are clay minerals in the form of aluminosilicats (rich in K, Na, Ca and Fe), feldspars or quartz.

Fig. 3 shows the most common forms: organically-bound inorganics, included and excluded mineral grains (not illustrated are dissolved salts). Ward [37] describes the first two groups (dissolved salts and organically-bound inorganics) as non-mineral inorganics. The amount of these inorganic constituents strongly depends on the fuel rank. An estimate on the amount of these elements can be found in Fig. 4 based on various literature references. The lowest quantity is typically observed for bituminous coals. Typical elements are alkali metals (Na, K), alkaline earth metals (Ca and Mg), P, S and Cl. High-rank coal inorganics have around 5–10 wt.% of these non-mineral inorganics, low-rank coals such as lignites or brown coals typically 10–40 wt.% of the total amount of inorganics [15,38]. In the case of biomass, this strongly depends on the plant type, where herbaceous biomass such as straw has around 15–58 wt.% (estimated

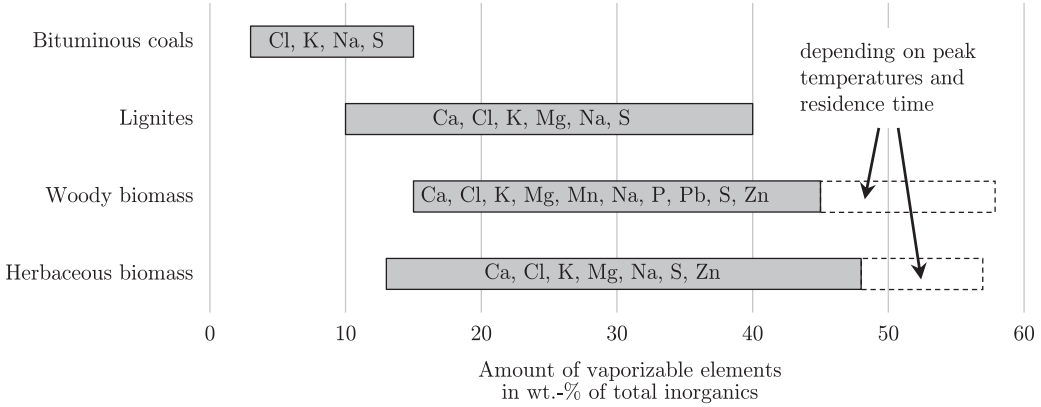

Fig. 4. Expected amount and elements that can be vaporized during solid fuel combustion as a function of fuel type (ranges estimated from various references for coal [15,38,57], woody biomass [43–45,52], and herbaceous biomass (mainly straw) [40–42]).

Table 1
Inorganic elements found within common solid fuels. Data taken from various references [175,188,536–538].

Biomass	Species	Ref.	Al	Ca	Fe	K	Mg	Mn	Na	Si	P	S	Cl	$m_{inorg.}$
			molar fraction, mol-%											g/kg_{dry}
Wood	Spruce	[536]	0.2	51.8	0.2	15.8	11.2	5.1	0.7	6.0	0.4	4.5	4.1	1.31
	Pine	[536]	0.3	33.6	0.3	21.9	16.3	3.1	1.4	9.2	2.8	6.2	5.0	1.69
	Birch	[536]	0.2	41.8	0.3	21.2	10.0	4.9	0.5	7.2	4.2	6.7	3.0	1.41
	Aspen	[536]	0.3	28.7	0.1	40.3	13.5	1.0	0.8	2.6	7.1	4.5	1.1	3.14
Bark	Spruce	[536]	1.0	58.9	0.2	14.7	10.1	3.7	0.3	1.7	4.1	3.2	2.1	13.4
	Pine	[536]	9.0	42.3	0.2	21.7	9.6	1.7	0.3	0.6	10.9	2.6	1.1	13.5
	Birch	[536]	0.2	66.0	0.1	14.7	4.5	3.3	0.2	1.4	4.7	3.5	1.4	11.5
	Aspen	[536]	0.1	56.4	0.1	23.4	10.9	0.9	0.1	0.6	4.1	3.1	0.2	19.4
Twigs	Spruce	[536]	2.3	29.6	0.8	25.0	10.3	2.5	1.2	9.6	9.6	6.7	2.5	12.9
	Pine	[536]	3.8	41.1	0.4	24.2	9.1	1.4	0.5	3.5	8.5	5.7	1.8	11.7
	Birch	[536]	0.3	43.5	0.3	28.5	6.8	2.4	0.7	0.9	9.8	5.7	1.2	10.2
	Aspen	[536]	0.3	53.0	0.1	30.7	5.4	0.7	0.2	1.4	4.7	3.1	0.5	18.7
Needles	Spruce	[536]	0.4	28.4	0.1	15.5	6.1	3.6	0.3	33.5	7.0	3.1	2.0	24.3
	Pine	[536]	3.6	26.6	0.2	31.5	8.5	3.9	0.3	5.0	10.6	6.8	3.0	14.1
Shoots	Spruce	[536]	0.2	6.3	0.1	56.1	5.6	0.7	0.1	1.6	18.6	6.2	4.6	24.1
	Pine	[536]	2.4	11.6	0.4	44.1	8.2	0.7	0.3	5.2	16.4	7.6	3.0	18.0
Leaves	Birch	[536]	0.2	30.1	0.2	31.9	11.0	3.9	0.2	1.5	13.4	7.0	0.7	27.7
	Aspen	[536]	0.1	19.4	0.1	48.8	9.6	1.0	0.0	0.4	13.2	6.3	1.1	45.8
Various biomass	Barley straw	[175]	0.2	14.8	0.2	24.6	3.9	4.0[a]	0.2	50.9	1.0	0.0	0.2	57.9
	Corn cobs	[537]	1.5	19.6	0.8	36.5	3.6	0.1	1.8	25.1	6.1	2.6	2.2	20.0
	Rice husks	[537]	0.1	1.6	0.1	2.6	0.4	0.0	0.2	93.9	0.5	0.4	0.1	180.0
	Switchgrass	[537]	1.3	15.1	0.7	9.9	8.2	0.1	0.8	59.8	3.4	0.3	0.2	51.0
	Sunflower shells	[537]	5.1	22.0	2.1	28.3	12.3	0.0	1.1	20.7	6.0	1.4	0.9	31.0
	Walnut shells	[537]	1.3	21.9	0.7	29.9	20.7	0.0	1.2	18.6	4.8	0.7	0.1	28.0
	Beech wood chips	[537]	0.1	72.3	0.4	1.9	14.3	0.4	0.9	8.0	1.4	0.2	0.1	8.00
	Marine macroalgae	[537]	0.4	15.3	0.8	13.1	18.1	0.0	23.0	1.2	7.1	7.6	13.4	23.6
	Plum pits	[537]	0.1	19.4	0.3	41.0	18.0	0.1	0.6	2.9	15.6	0.8	1.3	14.0
Bituminous coal	El Cerrejon	[188]	19.9	10.3	3.2	1.7	3.5	1.3[a]	0.9	56.8	1.5	1.0	n.d.	12.0
	Pittsburgh #8	[188]	16.5	1.8	2.6	3.3	1.5	0.2[a]	0.8	71.9	0.4	1.2	n.d.	125.6
	Calenturitas	[188]	10.8	3.8	9.7	1.8	2.3	0.1[a]	3.0	67.1	0.8	0.6	n.d.	66.1
	Peabody	[188]	15.2	4.0	7.0	2.1	2.2	0.2[a]	0.6	66.6	1.2	0.9	n.d.	169.8
	Sebuku	[188]	22.1	7.5	4.2	1.4	4.6	0.9[a]	1.9	55.2	0.6	1.7	n.d.	125.9
	Columbian bit.	[538]	14.6	6.4	5.1	2.2	4.9	0.2[a]	6.0	59.5	0.4	0.7	n.d.	112.0
Lignite	Lausitz	[188]	0.0	45.7	16.9	0.0	19.8	0.0[a]	0.0	5.2	12.4	0.0	n.d.	58.0
	Reinish	[538]	0.8	26.4	3.7	0.5	9.4	0.0[a]	1.6	54.7	2.8	0.2	n.d.	55.0

[a] Ti instead of Mn.
n.d. not determined

from data of e.g. [40–42]), and wood-based feedstocks range from 12 up to 56 wt.% (estimated from data of e.g. [43–45,52]). An interesting biomass that produces low quantities of inorganic vapors is rice husk. Rice husks are extremely rich in silicon, as shown in Table 1. Inorganics in rice husks are non-leachable as shown by chemical fractionation studies [53]. Based on these results it is estimated that the amount of vaporizable elements is very low, probably below 5 wt.%. However, it has to be mentioned that the amount is difficult to determine and strongly dependent on the fuel, the temperature during conversion, the heating rate, the residence time at a certain temperature, and the measurement device. These inorganic components (Al, Ca, Cl, Fe, K, Mg, Na, Si, S, Ti and trace elements) can be covalently and ionically bound to the organic matter. The elements are present in ion-exchangeable forms and as salts of carboxylic acids within the organic matter [56]. Dissolved salts in coals can for instance originate from contact with sea water. In addition, plants have soluble salts in their liquid phases [6]. Both groups, dissolved salts and organically-bound elements are known to vaporize during the combustion, leading to inorganic vapors in the gas phase. These vapors can re-condense to small particles, referred to as aerosols or sub-micron ash particles. A method that might be suitable in order to estimate the amount of vaporizable inorganics is chemical fractionation, often referred to as leaching. During this method, the fuel samples are dissolved in various solvents and the remaining residue and eluate are analyzed [38]. There are several methods and procedures described in literature [61]. Typical solvents are deionized water, ammonium acetate and hydrochloric acid. Elements that are leachable in the first two, are assumed to be vaporizable. Chemical fractionation of coals was for instance done in projects Sodium [54] and Calcium [55] at the Energy & Environmental Research Center (EERC) in early 1990s; see also Benson and Holm [38]. Chemical fractionation results of commonly used biomass can be found in the work of Zevenhoven et al. [6].

Discrete inorganic particles are often referred to as mineral matter in the fuel [56]. They are present as mineral grains within the organic matter or separated from it. Most minerals are in crystalline

Table 2
Typical ranges for ash content, ash fusion temperature and major ash forming elements for different fuel types. Data from various references [5,35,39,61–65].

Fuel type	LHV MJ/kg d.b.	Ash content wt.% d.b.	Ash fluid temp. °C	Major ash forming elements - and minerals sorted by typ. abundance
Bituminous coals	25–30	3–25	1200–1500	Si, Al, Fe - quartz, kaolinite, illite, pyrite
Lignites	18–27	5–40	1100–1450	Si, Al, Ca, Mg, Fe, S - quartz, carbonates, gypsum
Herbaceous biomass	14–17	4–12	950–1300	Si, K, Ca and rel. high Cl content - silicic acids[b]
Woody biomass	15–19	0.5–7	1150–1500	Ca, K, Si, Mg - oxalates[c]
Manures and sludges	9–14	15–50	1000–1300	Ca, P, Si, Na, S (can vary strongly)
MSW/SRF[a]	12–16	5–45	900–1300	various compositions often rich in Cl and heavy metals

[a] municipal solid waste (MSW) - solid recovered fuels (SRF) also called residue-derived fuels (RDF).
[b] silicic acids in the cell walls, which enriches in SiO_2 after harvesting.
[c] often found as calcium oxalate (CaC_2O_4), which forms crystals upon drying.

form, however some can exist as amorphous phases. Both transform during the combustion and the remaining residue is referred to as ash. Strictly, ash is the remaining solid residue after complete conversion [15]. However, literature is not consistent and an incorrect use of the terms ash, inorganic constituents and mineral matter is common. The amount, chemical composition and size distribution of ash is highly-dependent on the fuel and the form of inorganic constituents as well as the combustion system (temperatures, atmospheres) and fuel preparation (e.g. grinding, washing). Laboratory ash has a considerably different temperature- and time-history compared to ash samples collected in power plants. Furthermore, the atmosphere (i.e. oxidizing or reducing) will influence ash characteristics. Unfortunately, there is inaccuracy in the literature, and preparation or sampling techniques are often not stated clearly. Particular care must be taken for obtaining representative samples. This is less important in laboratory-scale, but can be of great importance in a PF boiler, as the amount analyzed is extremely small compared to mass flow rates in a full-scale furnace [15]. Furthermore, information on the feedstock and its origin (e.g. coal mine and storage) is missing in most studies. By knowing the amount of remaining ash, empirical correlations can be used to estimate the mineral matter content in the raw fuel. There are empirical equations in literature, which relate the mass fraction of mineral matter w_m to the proximate ash yield w_a and the total sulfur content $w_{S,total}$, such as the one suggested by Parr [58] given by:

$$w_m = 1.08 \cdot w_a + 0.55 \cdot w_{S,total} \quad \text{in} \quad \text{wt.\%}. \tag{1}$$

Equations relating ash yield to mineral matter content exhibit high uncertainties. These equations are often derived for high-temperature ashing and therefore, a significant amount of inorganic matter is already released to the gas phase. Generally speaking, inorganic matter transforms, decomposes and releases gaseous components during conversion. Typical components are H_2O, CO_2, Cl_2, HCl, SO_2 or H_2S depending on conditions and stoichiometry [59,60]. Therefore, in most correlations, the mineral matter content in the raw fuel is around 10% higher than the final ash content. The sulfur content, $w_{S,total}$, contributes to some extent to the ash yield depending on its occurrence. Sulfur can be either present in the form of organic sulfur bound to the coal structure, as sulphides originating from e.g. pyrite, sulphates, e.g. $CaSO_4$, or as elemental sulfur [35]. Detailed information and discussion of mineral transformations and decompositions are provided in the following sections. Vassilev and Tascón [56] come to another order. They argue that coal ash is the inorganic residue resulting from incineration of coal and that it is composed of original and new-formed inorganic phases generated from both inorganic and organic matter [56]. They state that the magnitude should be in the order of ash > inorganic matter > mineral matter; where the mineral matter is a part of the inorganic matter and organically-bound inorganic compounds are not included in the inorganic matter according to their definition [56]. However, lower values of ash than mineral matter are commonly observed when ash is produced at high temperatures and inorganic constituents volatilize [56] and minerals decompose. Furthermore, it has to be mentioned that measuring the amount of inorganic matter and mineral matter is highly difficult and an accurate and reliable method is currently not available. Different forms of inorganic compounds, various mineral types and the heterogeneity of solid fuels are the main reasons for the inconsistency and confusion in literature.

A compilation of different fuel types and their ash characteristics is presented in Table 2. Six major groups - comprising of bituminous coal, lignite, herbaceous biomass such as straw or grasses, woody biomass, manures and sludges as well as waste-based fuels - are summarized in terms of typical heating value, ash content, ash fusion (fluid) temperature and major ash forming elements. By far the highest ash content is observed for waste-based fuels and manures such as sewage sludge with values up to 50 wt.% on a dry basis (d.b.). There are some reports of lignites with very high ash contents, however typical coals have lower values between 10 and 20 wt.% (d.b.). Bituminous coals are dominated by Si, Al and Fe, which mainly originate from mineral grains composed of aluminosilicates, quartz or pyrite depending on the coal seam. The bulk ash fusion temperatures are fairly high, usually at around 1200 up to 1500 °C. However, there can be single particles with low melting eutectics with considerably lower melting temperatures in particular for iron bearing mineral grains. Lignites can vary widely and are often dominated by Ca, Mg, Fe, S and Si. Frequently found minerals are carbonates, gypsum, quartz and many others. Melting temperatures are typically slightly lower, compared with bituminous coals. Very low melting temperatures down to 950 °C are observed for straw and grasses, mainly due to the high potassium content. Si, Al, K species - found within the plant - can form low melting ash particles. This together with high chlorine contents leave straw to be a troublesome fuel. On the contrary, wood-based fuels are often reported to be less problematic. The have relativity high melting temperatures, mainly due to the abundance of calcium. The majority of ash forming elements is found within the bark - with ash contents of 5-8 wt.% (d.b.). Very difficult and heterogeneous fuels are manures and waste-based fuels, such as MSW or SRF, demolition wood and other residues. Manures are often rich in phosphorus and heavy metals, leading to problems concerning the ash utilization. A further summary of major ash forming species and their quantity within different solid fuels is presented in Table 1. Different groups comprise of bituminous coals, lignites and different biomass including Nordic wood, herbaceous biomass and agricultural residues. Woody biomass is differentiated into bulk wood, bark, twigs, needles and leaves. The table reveals that woody biomass is dominated by Ca and K making up for around 65 mol.%, followed by Mg and S. Twigs, needles and leaves have an increased content of K and P compared with bark and stem wood. Furthermore, it is shown that bark, twigs, shoots, needles and leaves have a strongly increased content of inorganic matter, up to ten times higher, compared with stem wood. The amount of inorganics found in annual biomass is similar to bark in the range of 3–10 wt.% of the fuel. Inorganic species in

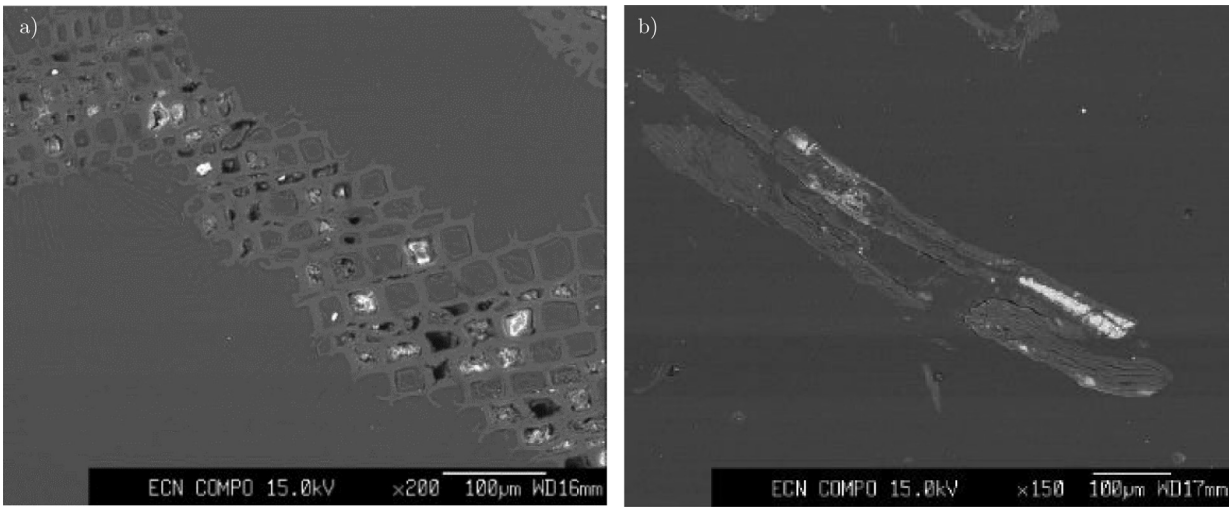

Fig. 5. BSE image of raw fuel particles: a) for wood and b) for straw (images recorded by the Energy Research Center of the Netherlands [66]).

annual biomass, such as straw or grasses, are dominated by Si, K and a fairly high Cl content.

Fig. 5 shows a back-scattered electron (BSE) microscope image of unprocessed wood (a) and straw (b). In BSE images, the intensity of the signal and thus the intensity of gray in the image is strongly related to the mean atomic number of elements in the sample. Therefore, minerals with high atomic numbers appear brighter, compared to the organic structure or the embedding material with lower atomic numbers. Wood, shown in Fig. 5(a), is in general a very clean feedstock with a low amount of excluded mineral grains or contaminants such as soil, sand or clay minerals. Most of the inorganic species are found embedded within the organic, regular wood matrix. They are typically 1-10 μm large grains composed of crystalline calciumoxalate or carbonates. Particles can contain Ca, Mg or Na as either silicates, or sulfates up to 40 μm [66]. The ash content of straw is increased compared to wood. A typical straw stem is shown in Fig. 5(b). The Energy research Centre of the Netherlands (ECN) estimated that around 75% of the Si is found in quartz particles, which are either embedded in the organic straw matrix up to 25 μm or form thin continuous linings at the outside of the straw stem [66]. In addition, some clay minerals containing Mg and/or Ca were found during the scanning electron microscopy (SEM) and SEM/EDX (energy dispersive X-ray spectroscopy) analyses.

A very powerful characterization method for inorganic constituents and their variation within one sample is the so-called "computer-controlled scanning electron microscopy" (CCSEM) analysis. This method allows to analyze the raw fuel sample directly without any thermal pretreatment such as ashing in a muffle furnace. The fuel is mount in epoxy, cut and the cross-section is polished. Conventional SEM or CCSEM are often applied for the identification (type, form and size) and quantification of minerals in coals. Fig. 6 shows a BSE microscope image of bituminous coal particles. It can be seen that a substantial fraction of the mineral matter is excluded from the fuel matrix. Additionally, the amount and number of mineral inclusions vary widely among different coal particles. Therefore, scanning electron microscopy is a key method for developing a detailed fuel model for numerical codes.

The CCSEM technique was developed during the late 1970's and early 80's when computer supported electron microscopy became available. The first studies using computer-controlled SEM techniques focused on classifying the mineral size distribution and composition within pulverized coals [67]. Steadman et al. [269] and Zygarlicke et al. [68] were among the first to differentiate between included and excluded minerals. During CCSEM, coal particles are mounted in an embedding material which is polished, carbon coated and placed in an electron microscope. In order to distinguish between included and excluded minerals, a distinct contrast between the embedding material and coal matrix is needed. Two possible methods can be found in the literature. The best contrast on the BSE pictures is derived using carnauba wax. Another method is to increase the average atomic number by dissolving ten percent iodoform in epoxy resin [69]. This resin is then mixed with coal particles and hardener. Once the sample is polished and carbon-coated, the cross-section can be investigated using SEM. CCSEM can be applied for coal, char and ash particle characterization. Typical results provide information on the mineral composition, its size and type (excluded or included). Eleven elements are detected most commonly including Al, Ca, Cl, Fe, K, Mg, Na, P, Si, S and Ti. The sample is scanned automatically by computer and X-ray detectors are used to quantify elements of individual mineral grains. The composition of a mineral grain is then compared with a database of mineral compositions and subsequently classified. It has to be mentioned that a classification leads to a loss in information. For instance, a mineral grain with a composition close to quartz is classified as pure quartz (SiO_2). Typical minerals in the system include quartz,

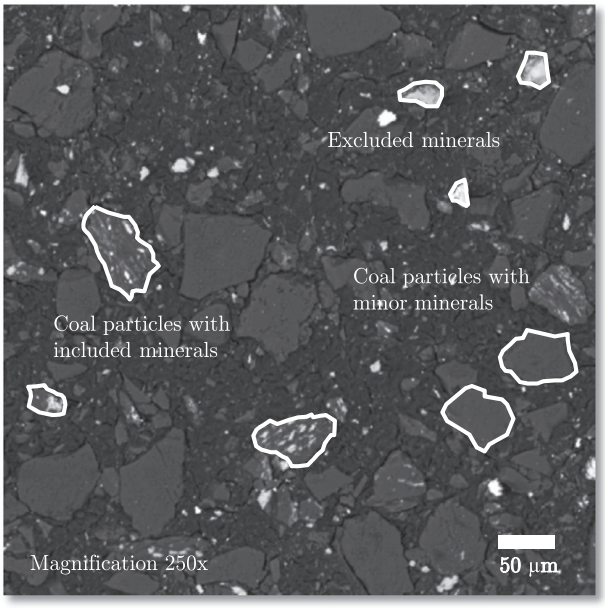

Fig. 6. BSE image of embedded bituminous coal particles and their classification.

kaolinite, pyrite, rutile, montmorillonite, apatite, gypsum, various silicates, and many others [3].

CCSEM analysis can provide very useful details and insight in the heterogeneity of a solid fuel, as shown in Fig. 7. Monroe [23] detected around 6000 mineral grains for a Kentucky No. 9 coal. It is shown that mineral grain composition varies widely within one fuel sample and therefore, each mineral grain has its own transformation and melting point. Where classic ash oxide analysis yields just one average point, CCSEM illustrates a number of points with varying composition. CCSEM is able to provide information on the variation in chemical composition, form and size of minerals. However, this method has to be applied with care. There are some limitations and disadvantages when using CCSEM techniques. Ignoring these limitations can lead to different results and wrong conclusions. For instance, particles in the sub-micrometer range cannot be detected without using very high magnifications, which is impracticable. A sufficiently high number of particles have to be analyzed in order to obtain statistically meaningful and quantitative results. Typical results are in the range of 2000-4000 particles. This is of special interest when a broad particle size distribution (PSD) has to be characterized. Furthermore, using different magnifications can lead to different results and more importantly, Sarofim and Helble [70] discuss that particle sizes in a cross-section are artificially shifted towards smaller diameters (due to the effect that the probability to intersect a sphere at its pole is low). Another problem is associated with the electron beam size. The size of the beam restricts the lower limit of mineral inclusions to about 1 μm, depending on the magnification. Often, small clusters of two or more different mineral grains close to each other and with different chemistry cannot be distinguished, and results show a misleading composition. Furthermore, they are classified as one instead of multiple grains. The penetration depth of the beam is also a parameter affecting the lower detection limit. Furthermore, atomically-dispersed elements, i.e. organically-bound inorganics, cannot be identified or quantified.

Although information on mineral-mineral (two different mineral grains in a cluster close to each other) or mineral-maceral association can be determined, commercially available CCSEM analyses do not provide such data. It is often difficult to differentiate between coal particles and resin; hence an automatic procedure is not applicable. There are only a few studies on the mineral-organic association using CCSEM [72–75]. An interesting approach is the QEMSCAN system, developed at CSIRO [76,77]. QEMSCAN describes a method that directly enables the measurement of mineral matter - organic matter association on a particle-by-particle basis. The difference compared to CCSEM analysis is that coal particles are included in the analysis and the whole cross-section is analyzed pixel by pixel. Mounting medium and coal particles are distinguished by the brightness of the BSE picture, and the X-ray spectrum. Around 4 000 particles are required for statistically significant results [78]. Studies on the distribution of inorganic constituents in solid fuels are rare in literature. Typically, CCSEM analyses are carried out providing information on the amount and type of included and excluded mineral grains. However, CCSEM analyses are not covering organically-bound inorganics and do not give information on the association of the coal matrix with mineral grains. A study of Liu et al. [78] uses the QEMSCAN technique to determine the mineral-maceral association for 14 different Australian coals. The most abundant particle type found by Liu et al. [78] were particles without mineral grains. Only, about 10% of the particles' cross-sections contained mineral inclusions. They defined three particle classes, based on these findings. Class 1: coal particles with 95% or more area covered with organic substance, class 2: particles with included minerals containing 40–90% organic substance, and class 3: excluded mineral grains, containing less than 40% organic substance. According to this classification, the majority of the studied coal samples had an included mineral matter content in the area of 50–80%. There was just one sample with more excluded than included minerals [78]. In a later study, Liu and co-workers [79] investigated the mineral-

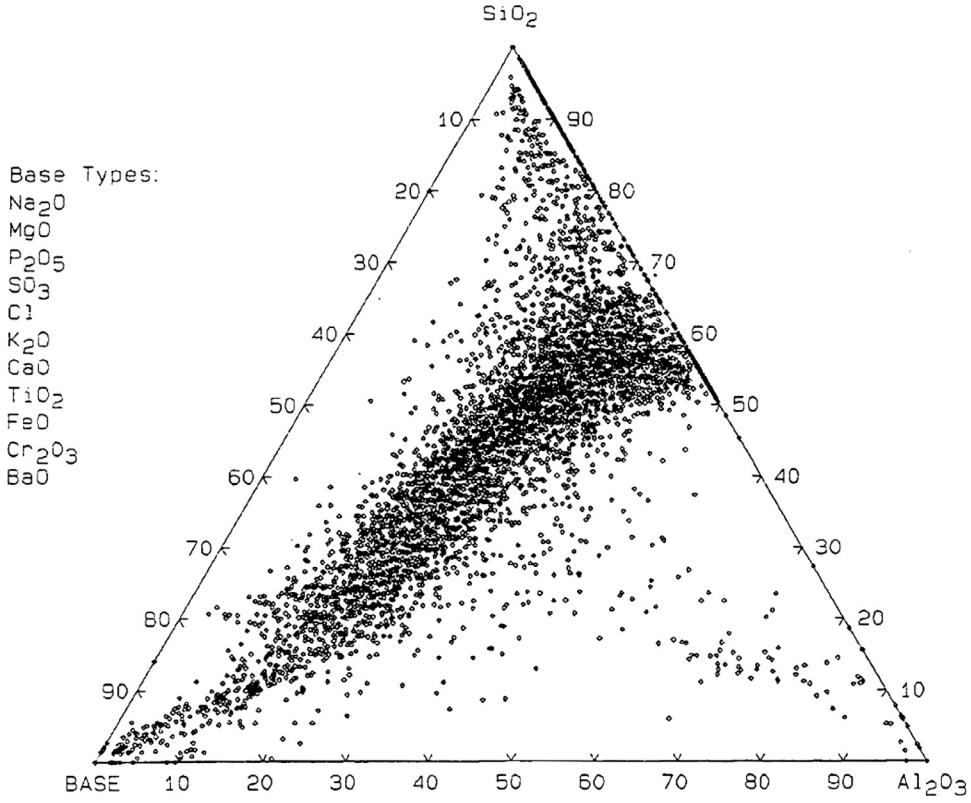

Fig. 7. Mineral particle composition distribution for 38-45 μm fraction of a raw Kentucky #9 coal. Each symbol represents the composition of one individual mineral grain measured using CCSEM (figure taken from Monroe [23]).

mineral association of excluded mineral grains. They studied three different coals and the corresponding ashes after combustion in a drop-tube furnace at 1400 °C, and came to the conclusion that illite, ankerite and siderite change their shape to spherical particles, while quartz, kaolinite and calcite do not show significant changes. They found mineral associations of quartz and kaolinite in excluded mineral grains, whereas combined particles of carbonates with silicates were rare [79].

Mineral matter is often reported to be enriched in smaller particle sizes. This trend has been observed in several studies [12,80–84] and can be explained by the fuel grinding process. Unsworth et al. [82] state that particles with high mineral matter content and thus high particle densities tend to be ground to a finer size and may liberate mineral grains. This is based on the effect of a classifier mill, which recycles heavier particles. Only if the particle inertia is low enough, the gas flow can entrain the particle. In particular higher-rank coals tend to demonstrate this behavior [15].

Data on the number of mineral grains per particle and their distribution among coal particle sizes are rare. Barta et al [72,86] developed the so-called "urn" model using CCSEM data. They used a Poisson law in order to distribute mineral grains among individual coal particles. SEM investigations of a size-graded Texas lignite (63–75 μm) revealed a mean value of 15 mineral inclusions per coal particle. Particles were embedded in epoxy resin, cut and polished for measurements using a back-scattered electron detector. An inverse Abelian transformation is applied, in order to obtain volume-based size distributions. The Poisson distribution law is used to describe the number of mineral inclusions per coal particle. For n mineral inclusions in m coal particles the probability P_j of finding j mineral particles in a coal particle is calculated by the following equation [72]:

$$P_j = \lambda^j \cdot \frac{e^{-\lambda}}{j!}, \tag{2}$$

where $\lambda = n/m$, the mean number of mineral grains per coal particle and j is the number of mineral grains per coal particle, which can take an integer value of 0 to n [70,72]. Eq. (2) is less accurate for coals with a high content of included mineral matter. The number of mineral inclusions n per coal particle of a given size $d_{p,c}$ can be estimated by [86]:

$$n = \frac{d_{p,c}^3 \cdot \rho_c}{M_{3,m} \cdot \rho_m} \cdot w_m, \tag{3}$$

where ρ_c and ρ_m are the density of the coal substance and of the mineral inclusion, $M_{3,m}$ is the third moment of the mineral size distribution, and w_m is the mass fraction of the mineral inclusion. Experimental work on the number of mineral inclusions per coal particle is rarely found in literature. A similar approach was followed by Monroe [23], who used SEM to measure the mineral size of Kentucky #9 coal, with a varying degree of cleaning. Monroe used a Monte Carlo method to distribute mineral matter among individual coal particles. Although there are some studies evaluating mineral size and distribution, general rules are not identified, and each fuel needs to be investigated separately. This is of particular concern for biomass with low mineral matter content. Often, power plant operators use more simplified and cheaper methods in order to determine the slagging and fouling potential of fuels. One of the first tests for new purchased fuels is the popular ash fusion test.

This laboratory test is applied to study the ash melting behavior under controlled conditions. Ash samples, typically produced in a muffle furnace, are pressed to a specimen, heated up under a controlled atmosphere and observed with an optical system. The silhouette recorded from the sample is judged to identify critical temperatures. There are several standards available in literature for ash sample preparation and ash fusion tests. According to Couch [15], the available standards differ quite significantly in terms of specimen preparation and characteristic temperatures. Specimen and silhouettes of characteristic temperatures are illustrated for the American standard in Fig. 8. These characteristic temperatures are referred to, as initial deformation temperature (IDT), softening (ST), hemispherical (HT) and fluid temperature (FT), respectively. Ash fusion temperatures are often used by boiler designers for selecting the maximum furnace exit temperature and for the estimation of slagging propensities using indices and the bulk ash chemistry. The ash fusion test for biomass uses different characteristic temperatures. Ash samples derived from biomass show a shrinking specimen and therefore the IDT is replaced by the so-called shrinkage starting temperature (SST). The second characteristic temperature is called deformation temperature (DT), whereas the rest is identical. Generally speaking, the applicability of the ash fusion test is questionable. Couch [15] states that laboratory ash is considerably different due to the slow formation process compared to conditions in a boiler. Laboratory ash absorbs SO_3 from sulphates and oxygen from ferric oxides which does not occur in a boiler. Furthermore, heterogeneity strongly influences ash melting temperatures. For example, quartz grains distributed within the specimen lead to a strong compound structure and ash fusion temperatures are often quite high, even though most of the other ash particles are already molten. Van Dyk et al. [88] reported that low viscosity ashes can have a high molten fraction without changing the geometry of the specimen. Another important parameter is the atmosphere under which the test is carried out. The atmosphere can be selected either as oxidizing or reducing. It is reported in literature that reducing conditions lead to lower ash fusion temperatures, typically around 50 K. A dominant role exhibit iron minerals and their transformation under reducing conditions [15]. Bryers [89] correlates the ash softening temperature under reducing conditions for eight eastern US coals to the sum of basic compounds in the ash. A parabolic curve can be found with the minimum temperature at approximately 50 wt.% of basic compounds. Therefore, the amount of basic compounds in the fuel can help to estimate the threat of slagging and fouling. However, detailed information on individual particles, which might melt at much lower temperatures (50–250 K), can only be obtained by SEM methods. Furthermore, detailed predictions on ash formation, in terms of ash particle size distribution and chemistry, can only be conducted if SEM data is available.

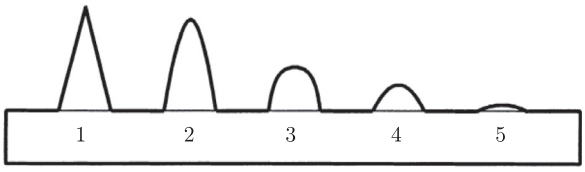

1		Cone before heating
2	IDT	Initial Deformation Temperature
3	ST	Softening Temperature (h=w)
4	HT	Hemispherical Temperature (h=1/2w)
5	FT	Fluid Temperature

Fig. 8. Specimen and silhouettes of the American standard ash fusion test (adopted from Hansen et al. [87], h: height and w: width of the silhouette).

2.3. Ash formation

Ash formation in solid fuel combustion systems involves several mechanisms and processes, producing gases, liquids - in the form of melts - and solids. There are three main aspects: the first, and probably most important one, being the distribution of inorganic constituents in the fuel matrix, which has been discussed in the previous section. Secondly, inorganic constituents undergo physical transformation including melting, fusion, vaporization, fragmentation, etc. And thirdly, inorganic constituents decompose and transform to ash,

which is dependent on process parameters such as flue gas temperature and composition. This process is often referred to as chemical or mineral transformation. The following sections address each of the two latter aspects, and summarize the current state of the art.

2.3.1. Physical transformations of inorganic constituents

Inorganic constituents in solid fuels undergo physical transformation processes, which are strongly dependent on the conditions inside the boiler, and on the fuel itself [14]. Possible physical transformations of inorganic constituents are:

- coalescence of mineral inclusions within the particle or on the particle surface [9,12,70,86,91,96,104],
- shedding of mineral or ash particles from char surfaces [91–93,165],
- coal/char particle fragmentation and incomplete coalescence of minerals [93–96,104,114,115,118,122],
- fragmentation of excluded minerals due to mineral transformations [12,79,183,540],
- formation of inorganic ceno- or plerospheres [57,97],
- vaporization of mineral species, their re-condensation and agglomeration [12,73,91–93], and
- vaporization of salts and release of organically-bound inorganics [43–45], their chemical reaction with ash particles [48–51,261,262], and their condensation [98–103, 212].

Fig. 9 illustrates the process of ash formation. It occurs along with devolatilization, char conversion and subsequent flue gas cooling. Depending on the fuel, a considerable amount of inorganic constituents may vaporize. Mainly, organically-associated inorganic compounds are released as inorganic vapors, during devolatilization and char conversion. These inorganic vapors are illustrated by open arrows, whereas solid particles are shown with filled arrows, in Fig. 9. Remaining inorganic constituents, mainly mineral matter, decompose, transform to ash, melt and coalesce (fuse together) depending on the mineral type and temperatures. The behavior of included minerals is complex. Most ash particles have a sufficiently high surface tension to form liquid droplets and thus, do no wet the char particle surface [57]. Included mineral grains are often reported to coalesce during char conversion. During coalescence, mineral inclusions come into contact with each other and fuse to one remaining ash particle. Coalescence of mineral inclusions has been investigated by several authors. Sarofim and Helble [70] suggest the **full coalescence** model as a good starting point for estimating the ash particle size distribution. In this model, every coal particle yields exactly one ash particle. The full coalescence model yields the largest possible particle size distribution (assuming no particle-particle collisions in the bulk flow). The opposite behavior and lower boundary for the ash PSD, is the so-called **no coalescence** model, where every mineral grain yields one ash particle. Eq. (4) can be used to estimate the ash particle diameter $d_{p,a}$ for a given coal particle diameter $d_{p,c}$ [70]:

$$d_{p,a} = d_{p,c} \cdot \sqrt[3]{\frac{w_a \cdot \rho_{p,c}}{n \cdot \rho_{p,a}}}, \tag{4}$$

where w_a is the ash mass fraction of the coal particle, n is the number of resulting ash particles from the coal particle with size $d_{p,c}$, and $\rho_{p,c}/\rho_{p,a}$ is the ratio of the densities of the coal and the ash particle. In this equation, the mineral matter content equals the ash content. Sarofim and Helbe [70] refer to a publication of Wall et al. [71], noting that Eq. (4) is less accurate for coals with high shares of included mineral matter content (e.g. $w_a > 20$ wt.%). For such coals, the volume occupied by the ash has to be considered. Wilemski and Srinivasachar [104] successfully used a Monte Carlo method for the mineral distribution in combination with the full coalescence model for the prediction of ash size distribution. However, the same model failed for a highly cleaned coal, which showed excessive fragmentation behavior. Barta et al. [86] developed the **random coalescence model** in combination with a char combustion model, providing limits for the coalescence of mineral inclusion. The model is based on input from CCSEM analyses. This model uses a simple char burnout formulation with two subsequent steps. In the beginning, char conversion is assumed to occur in the diffusion-limited regime with a shrinking particle diameter. Mineral inclusions are released step by step and assumed to adhere to the surface as molten particles. If ash particles get in contact due to a shrinking char structure, they start to coalesce. In the next step, the combustion is assumed to be in the kinetically-limited regime. Particles now burn from the inside and the diameter is unchanged. By this approach, coalescence is interrupted, and char particles break up once they reach a critical porosity. A further development was presented by Yan et al. [9] for high-rank coals using CCSEM data. Included and excluded minerals were treated differently. Included minerals were distributed randomly among coal particles using Poisson distribution. The authors found that small particles do not fuse together. Best agreement is reported when using a partial coalescence model as shown in Fig. 10. An interesting ash formation model for CFD codes is presented in a

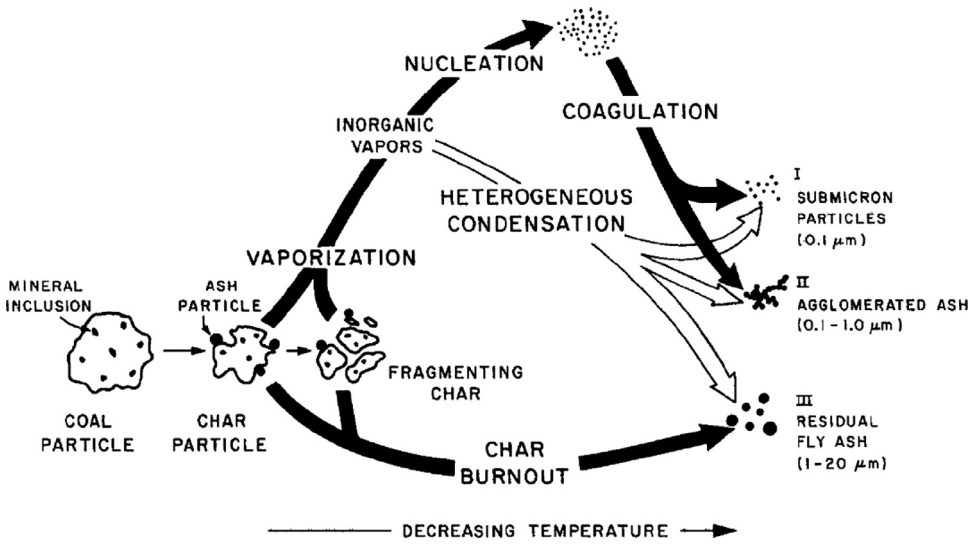

Fig. 9. Ash formation during PF combustion (taken from Helble and Sarofim [22]: open arrows show inorganic vapors, and filled ones represent solid particles).

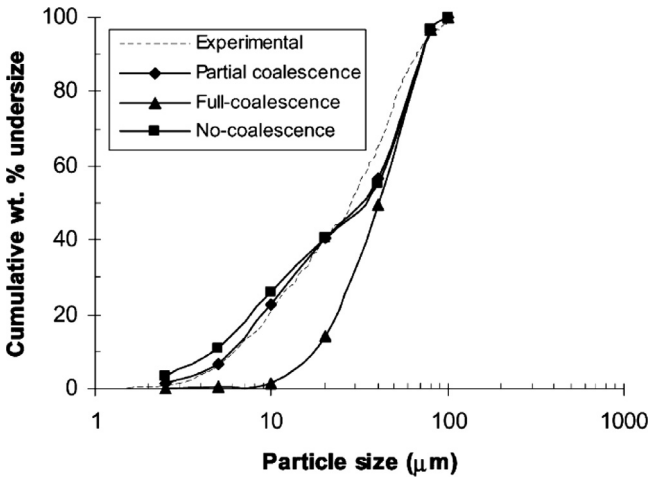

Fig. 10. Cumulative ash size distribution: Comparison of experiment and model results using different levels of coalescence. Taken from Yan et al. [9].

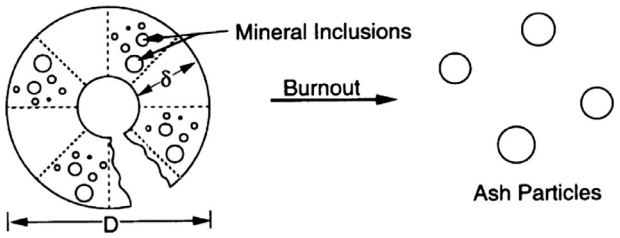

Fig. 11. Char fragmentation and ash formation model from Wilemski and Srinivasachar [104].

study of Zhou et al. [454]. The model accounts for ash layer collapse during char burnout and assumes coalescence. Such a model should be extended for char fragmentation and should be validated with measurements. In this case **char fragmentation** becomes important. Char fragmentation was first mentioned 80 years ago by Davis and Hottel [107] and is often given as an explanation for differences in predictions and observations of particle size distributions or fly ash formation. Fragmentation can occur during devolatilization, during char combustion, or for excluded mineral grains, in particular minerals, which undergo thermal decomposition. The majority of literature references reporting fragmentation observed char fragmentation. It is reported for different fuel ranks, however, mostly for swelling coals. Char fragmentation influences ash formation, as shown in Figs. 11 and 12, and therefore also the remaining particle size distribution as well as char conversion rates. The onset and extent of char fragmentation can be predicted using percolation models [109,116,477,478]. When the particle reaches a critical porosity, typically around 0.8, but values scatter in-between 0.2 up to 0.96 [113,125], it is assumed to fragment, where the number of fragments is dependent on the particle size, char structure and many other parameters [96]. Furthermore, the initial char structure is known to affect the ash formation. Wilemski and Srinivasachar proposed a fragmentation model for cenospherical particles, where particles break up into a certain number of fragments as shown by Fig. 11. Mineral grains in these fragments fuse together and form the remaining ash. A similar model considering different char particle shapes was presented by Wu and co-authors [105]. Fig. 12 shows the ash formation mechanism postulated for different char types and included minerals. Typically, three different char types are reported in literature [163,164]: type I chars are spherical to sub-spherical particles with thin walls ($< 5\,\mu m$) and high porosity values, so-called cenospheres. Type II particles show a sub-spherical shape with medium porosity, almost no swelling and variable wall thicknesses. And type III chars, which are relatively dense, have an angular shape and a swelling coefficient smaller than unity. Wu et al. [105] used a size-graded and density-fractionated Australian bituminous coal and studied their conversion in a drop-tube furnace at 1300 °C, atmospheric pressure and air. The coal sample was in a narrow size range of 63–90 μm and excluded minerals were removed by sink/float separation with an upper specific gravity of 2.0 g/cm^3 [105]. Combustion took place in the diffusion-limited regime. Depending on the char type, a different degree of coalescence is assumed. Char type III forms one remaining ash particle, whereas for char type I every mineral inclusion forms an individual ash particle. Thus, information on char structure is necessary according to the authors. They further argued that different char types have different observed reactivities. Char type I is assumed to fragment and burn four times faster than the dense and less porous char type III. This might also be due to different specific surface areas of varying char types. Char fragmentation of type I seems to determine ash formation during early stages of combustion, while the formation of coarse fly ash particles occurs by coalescence of included mineral matter during late stages of combustion [105]. Syred et al. [121] give an overview on mechanisms leading to particle fragmentation. Reasons can be:

- thermal stresses [126–130],
- pressure-induced fracture during devolatilization [94,133],

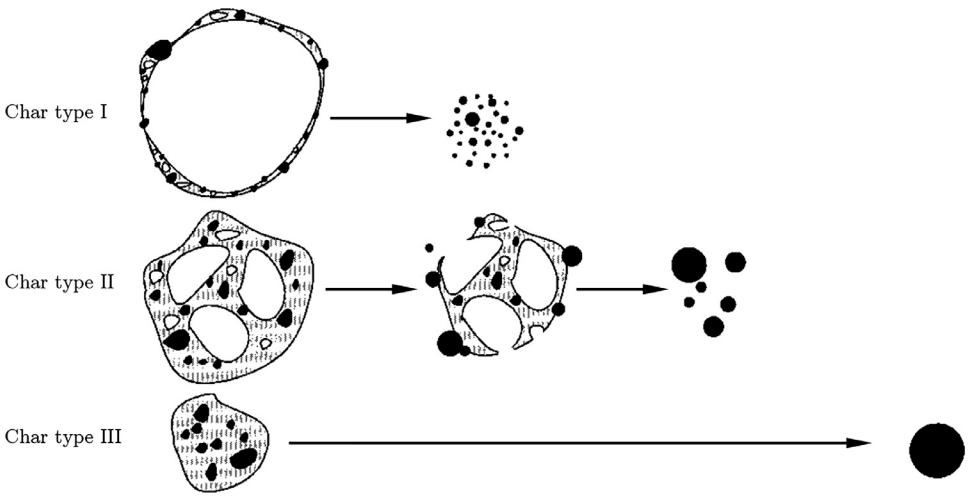

Fig. 12. Influence of char structure on ash formation by Wu et al. [105].

Table 3
Overview of reported particle fragmentation of solid fuels in chronological order and separated for coal and biomass (with acronyms for fragmentation mechanism: TS - thermal stress, PI - pressure induced fragmentation, AR - attrition and PM - percolative mechanism).

References	Fuel rank	Particle size	Mechanisms	Number of fragments
Sarofim et al. 1977 [95]	bit. & lignite	75–90 μm	–	3–5
Kerstein & Niksa 1985 [108]	synth. carbon	thin disks	PM	–
Helble & Sarofim 1989 [168]	sub-bit. coal	75–90 μm	PM	↑ when d_p↓ p_{O_2} ↑
	lignite	75–90 μm	PM	↑ when d_p↓ p_{O_2} ↑
	spherocarb	125–150 μm	PM	↑ when d_p↓ p_{O_2} ↑
Baxter 1992 [110]	bit. coal	1–100 μm	PM	1–100 for large d_p
	lignite	1–100 μm	–	1–2
Dacombe et al. 1994 [112]	anthr.	1–5 mm	TS	50–100
Mitchell & Akanetuk 1996 [94]	synth. char	90–106 μm	PM	> 100
Zhang et al. 1996 [111]	spherocarb	205 μm	PM	2
Dacombe et al. 1999 [128]	bit. coal	1–4 mm	TS	$10–10^4$
Liu et al. 2000 [169]	bit. coal	63–90 μm	PM	large for type I char
Feng & Bhatia 2000 [113]	diff. chars	varying size bins	PM	> 20
Senneca et al. 2011/2013 [114,133]	bit. coal & anthr.	1–2000 μm	TS, PI	50–600
Scala et al. 2006 [125],[a]	wood chips	3.35–9 mm	AR, PM	2.5-4.5[d]
	pine shells	5–20 mm	AR, PM	1.6[d]
	olive husk	3.35–5 mm	AR, PM	1.04[d]
Sreekanth et al. 2008 [134],[a]	tropical hard wood	10–30 mm	pri. frag.	–
Sudhakar et al. 2008 [124],[a]	tropical hard wood	10–25 mm	pri. frag.	up to 12
Costa and Costa 2015 [122,123][b]	olive stones	300 μm[c]	–	no fragmentation
	pine shells	500 μm[c]	–	fragmentation
	straw	–	–	fragmentation
Lin et al. 2015 [120],[a]	wood pellets	–	AR, PM	–

[a] fluidized bed combustion conditions.
[b] in a drop tube furnace.
[c] $d_{p,50}$.
[d] primary fragmentation multiplication factor.

- collision-induced attrition of small particles from the surface [131,132], and
- percolative mechanism in which oxidation (i.e. conversion) progressively erodes the solid network [108–111,131,168,169]

Fragmentation is often divided into primary and secondary fragmentation. Primary fragmentation refers to fragmentation induced by mechanical stresses (thermal or pressure), mostly during devolatilization, whereas secondary fragmentation is related to char conversion induced by coalescence of large pores at late stages of burnout (percolation) [112]. Experiments on fragmentation cover a broad range of fuels and carbons with different process parameters such as temperature, oxygen partial pressure and particle size. Table 3 summarizes experimental investigations on fragmentation, listing the fuel, particle size and the observed mechanism of fragmentation. Evaluation of this data indicates the predominant role of a percolative nature of char fragmentation.

Char fragmentation during coal combustion strongly depends on the particle size. Large particles are often reported to fragment due to thermal stresses as shown in Table 3 and the work Senneca et al. [114,133] or Dacombe et al. [112,128]. Small particles, typical for PF combustion, on the other hand fragment due to percolative mechanisms. The oxidation proceeds and erodes organic substance by releasing ash particles sitting on the char surface. A similar mechanism is expected to occur for biomass char. However, experimental data on biomass fragmentation is rare and only recently studies appeared. Fig. 13 shows spruce wood particles after pyrolysis. Cotton-like agglomerations of small ash particles and Ca-rich crystals are sitting on the char surface. It is assumed that these particles are liberated during burnout. However, direct experimental evidence is missing. Most of the studies on biomass presented in Table 3 were under fluidized bed combustion conditions with relatively large wood pellets or wood chips. In these cases, interaction between bed material and fuel particles occurs. The majority of these studies reported primary fragmentation during devolatilization together with attrition of ash particles from surfaces, probably caused by interactions between bed material and fuel. Percolative fragmentation during char conversion is also reported for biomass [120,125], probably due to the fact that biomass chars have higher porosity values compared with coal [119].

Fragmentation and its extent is difficult to determine in experiments, in particular for small particle sizes. Thermal stresses during heating or the oxidation of thin particle structures will lead to fragmentation. One can imagine that particle sampling and collision with tubes and boiler walls might also lead to fragmentation events, which is not discussed in literature. There are many uncertainties and sources of errors leading to a highly discussed field of research. The conclusions drawn from Table 3 are:

- char fragmentation is mainly percolative in nature and more pronounced for large particles,
- char fragmentation depends on the char type, and thus the maceral composition in the case of coal,
- the number of fragments increases with particle size, but varies widely among literature,
- cenospherical particles (type I chars) are the main source of fragments,
- char fragmentation most likely increases burning rates and the amount of fine fly ash,
- macro-porosity determines the extent of fragmentation with critical porosity values reported mostly in between 0.7 and 0.95,
- fragmentation can occur during devolatilization, mainly for biomass and large particles, and is induced by thermal stresses and internal pressure due to volatile release.

Shedding is illustrated in Fig. 14. During shedding, ash particles sitting on the char particle surface experience forces, mainly shear forces. These forces can detach the ash particle from the char structure and liberate it to the flow. Forces can be caused by particle rotation or slip flow between the particle and gas. Particle rotation is reported during devolatilization, where volatile jets evolve from

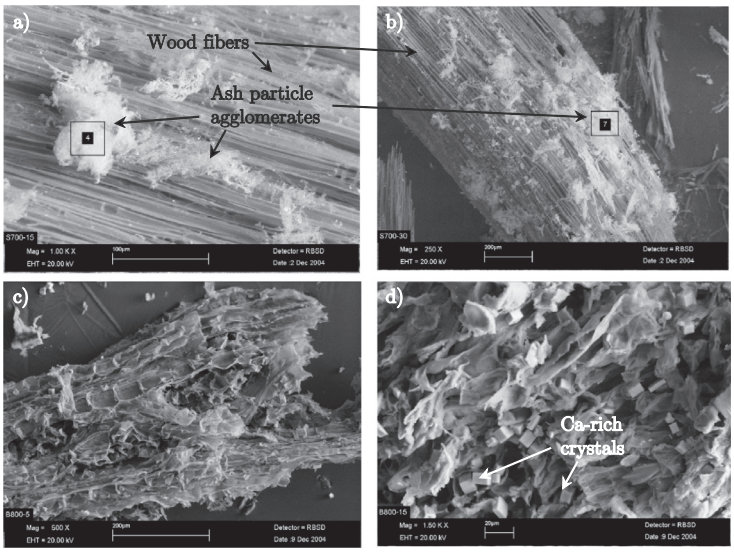

Fig. 13. Biomass char with ash particles sitting on its surface: (a) and (b) show spruce char particles produced at 700°C with cotton-like particles on its surface (area 4: 51% Ca, 11% K, 11% Mg, 8% P and 5% Mn; area 7: 47% Ca, 15% K, 12% Mg, 8% P and 5% Mn; values in mol-% and O,C-free). Fig. (c) and (d) show spruce bark pyrolyzed at 800°C. Ca-rich crystals can be seen on its surface. SEM images and data from [90].

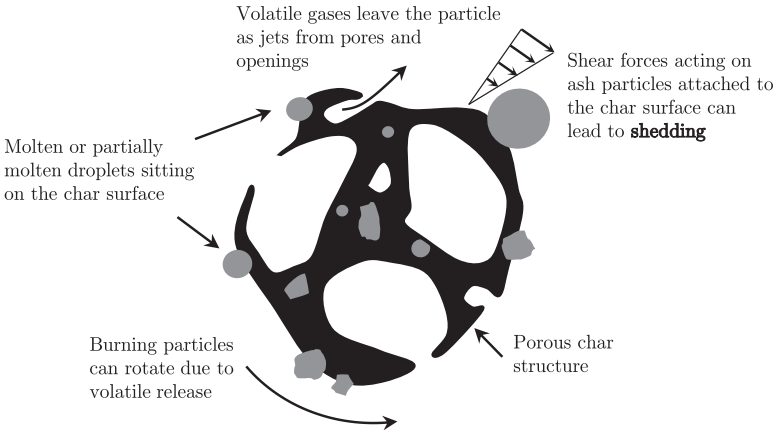

Fig. 14. Shedding of ash particles from char particle surface due to shear forces.

pores and openings. Studies on shedding are rare. Often shedding is referred to as a fragmentation event, leading to small particles in the range of 0.5–5 μm [165–167]. Helble [165] studied shedding using two color pyrometry and found values as high as 1000 revolutions per second for a 100 μm particle at the onset of char combustion. Theoretical considerations including rotational and surface tension forces showed that this effect is of minor importance for small, molten mineral grains sitting on the char surface. Nevertheless shedding might be a source of small particles in large-scale boilers with highly turbulent flow fields, when mineral grains are not properly attached to the char surface; e.g. if they are solidified. This effect should be studied in large-scale test rigs with considerably higher gas velocities (3–15 m/s compared to 0.2–2 m/s in lab-scale test rigs). Often it is difficult to differentiate between shedding and fragmentation due to the erosion of organic substance, called percolative fragmentation [168,169].

The behavior of **excluded minerals** depends on the mineral type. Quartz can be transported through the combustion system without any changes and maintain its sharp, angular structure [57]. Other excluded minerals such as clays can fragment during dehydration, melt and form cenospheres or plerospheres, i.e. cenospheres filled with small particles. The same can occur for carbonates. Pyrite is reported to fragment more easily due to its framboidal structure [57]. Both, coalescence and fragmentation have a significant effect on the ash size distribution. The remaining ash particles formed by coalescence and/or fragmentation are referred to as fly ash or coarse fly ash and are in the range of 1–50 μm for conventional PF combustion systems. During ash formation, particles are transported through the boiler with decreasing gas temperatures. Due to this temperature decrease, inorganic vapors start to condense. The **condensation** can be divided into homogeneous and heterogeneous condensation. The type of condensation is dependent on the supersaturation ratio S_i of the condensing species i. The supersaturation is calculated by the ratio of the partial pressure of species i, p_i, and its saturation pressure $p_{sat,i}$ at a certain location and temperature ($S_i = p_i/p_{sat,i}$ - see Section 2.5.3). Homogeneous condensation and the nucleation of sub-micron particles takes place at supersaturation ratios of approximately $S_i > 5$ (numbers in literature range from 1 to 10 [170–174]), whereas heterogeneous condensation is possible at values above unity. Heterogeneous condensation can occur on other particles (char or ash) or on heat exchanging surfaces. This layer can be liquid and sticky or porous depending on the temperature. Both homogeneous and heterogeneous condensation lead to the formation of sub-micron particles, and sub-micron modes depending on where nucleation of vaporized metals occurs. At high concentrations of these fine particulates, coagulation effects due to particle-particle

interactions can become important leading to agglomeration. This is of great importance for biomass combustion with high shares of inorganic vapors; see the work of Friedlander [171], Jöller [176], Brunner [101] or Balan [175]. For a detailed experimental and theoretical investigation of fine particulate matter formation during pulverized coal combustion, it is also referred to the work of Wieland [174]. Typical ash particle size distributions for a high-volatile bituminous coal, El-Cerrejón, and barley straw are presented in Fig. 15. The volume distribution is illustrated as a function of particle diameter. The volume distribution equals the mass distribution, if every particle has the same density. However, the heterogeneity in fly ash samples has been observed in various studies, implying that volume and mass distribution are not identical. Thus, the measurement of a mass distribution requires the identification of individual particle chemistry and size, and is therefore highly complex. Alternatively, sieve analysis can be used for the coarse fly ash PSD. However, as shown by Beckmann et al. [397], results can be misleading when compared with other methods such as CCSEM or laser diffraction. Furthermore, sieve analysis is difficult to apply for fly ashes with small particle size, e.g. obtained in PF systems. Both ash samples shown in Fig. 15 are derived from pulverized fuel combustion tests in an entrained flow reactor (for details see the work of Balan [175]). The ash particle size distribution shows two significant modes (local maxima). The first mode is in the area of $0.1 < d_p < 1\,\mu m$; the so-called sub-micron ash. The second and dominant mode is typically found around 20 μm. The ash sample of straw was collected using an electrostatic low pressure impactor (ELPI) for particles smaller than 10 μm, and a cyclone for larger particles [175]. The coal ash sample was extracted with the cyclone only. Both cyclone ashes and their size distributions were determined using the laser diffraction method. Wieland [174] used the same coal and showed that the amount of sub-micron ash is below 15 wt.% compared to coarse fly ash. As expected, the straw ash has a considerably higher volume fraction in the first mode compared to the coal ash sample. This is mainly due to the high amount of vaporizable species, e.g. organically-associated cations in the straw, in particular potassium. However, uncertainties due to the sampling of the coal ash particles are present and may lead to an increase of the first mode. Sarofim and Helble [70] mention an additional smaller first mode in the range of $0.02 < d_p \leq 0.1\,\mu m$, which is barely observed in Fig. 15. According to their investigation, this very small, first peak is due to condensation effects. However, they do not have an explanation for the second mode in the range of 0.1–1 μm. This mode might be caused by percolative fragmentation of ash particles from the burning char particle. Another interesting aspect is the plateau at large particle sizes above 100 μm, which might be due to unburnt carbon. It seems that char conversion has a strong impact on fly ash formation and only a combined approach including the distribution of mineral matter in coal and a detailed char conversion model is able to predict the remaining ash particles and their properties. However, detailed information on the fuel and char structure are required for this approach. Furthermore, many studies found indications of char fragmentation for coal [94,95,108,110,112–114,117,168] and biomass [119,120,122–124].

2.3.2. Chemical transformations of inorganic constituents

Inorganic constituents in coal not only undergo physical changes, such as melting, fusion or fragmentation, but also chemical transformation and decomposition. During heat up, part of the inorganic constituents and mineral matter is released as a gaseous species. The mass loss from mineral matter is due to the release of water from clay minerals, carbon dioxide from carbonates, and sulfur from pyrite [57]. This, and the release of organically-bound inorganics are challenges in predicting the ash composition. Gas release is usually included in the proximate analysis leading to erroneous results, especially for coals with a high ash content [57]. Not only the temperature treatment influences the decomposition and chemical transformation. Gas atmosphere and its composition can have a strong impact, in particular reducing environments. These reducing zones lead to a changed chemical transformation of some minerals. Crucial parameters are the availability of oxygen and the particle temperature. Reducing zones are also found inside burning char particles. Within regime II or III there is a depletion of oxygen and thus reducing environments. Fig. 16 shows the transformations of the main minerals found in coals, as a function of temperature. Depending on the mineral type, a very different behavior can be observed. Clay minerals, e.g. kaolinite or illite, are often dominating in the mineral systems. The transformation of **kaolinite** is well understood. Kaolinite loses water at around 425–525 °C, forming metakaolinite, which then changes to mullite and amorphous quartz, at around 900 °C [15]. The typical melting point of this amorphous phase is around 1700 °C [178]. **Illite** is a mineral containing most of the iron, magnesium, potassium and/or

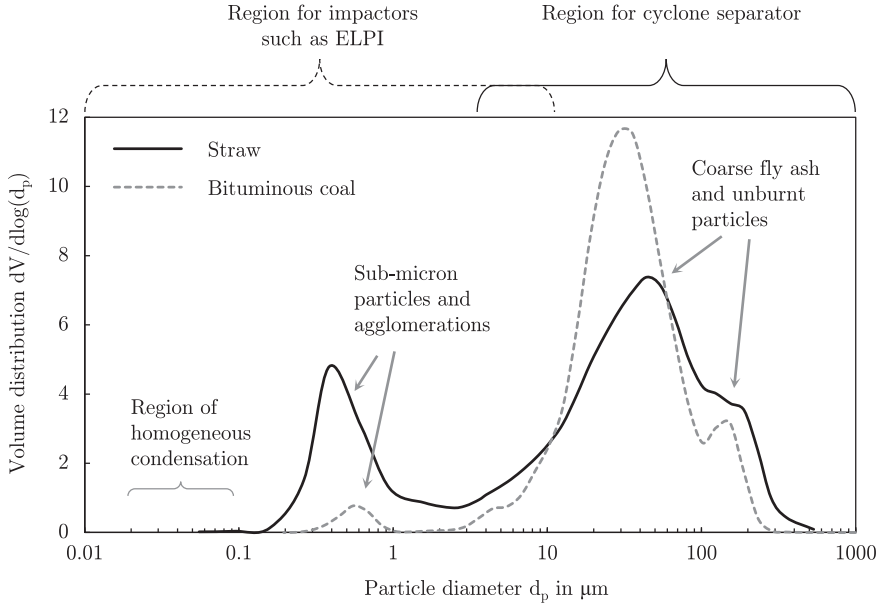

Fig. 15. Typical ash particle size distribution from PF combustion of straw and bituminous coal. Taken from tests in an entrained flow reactor [175,188].

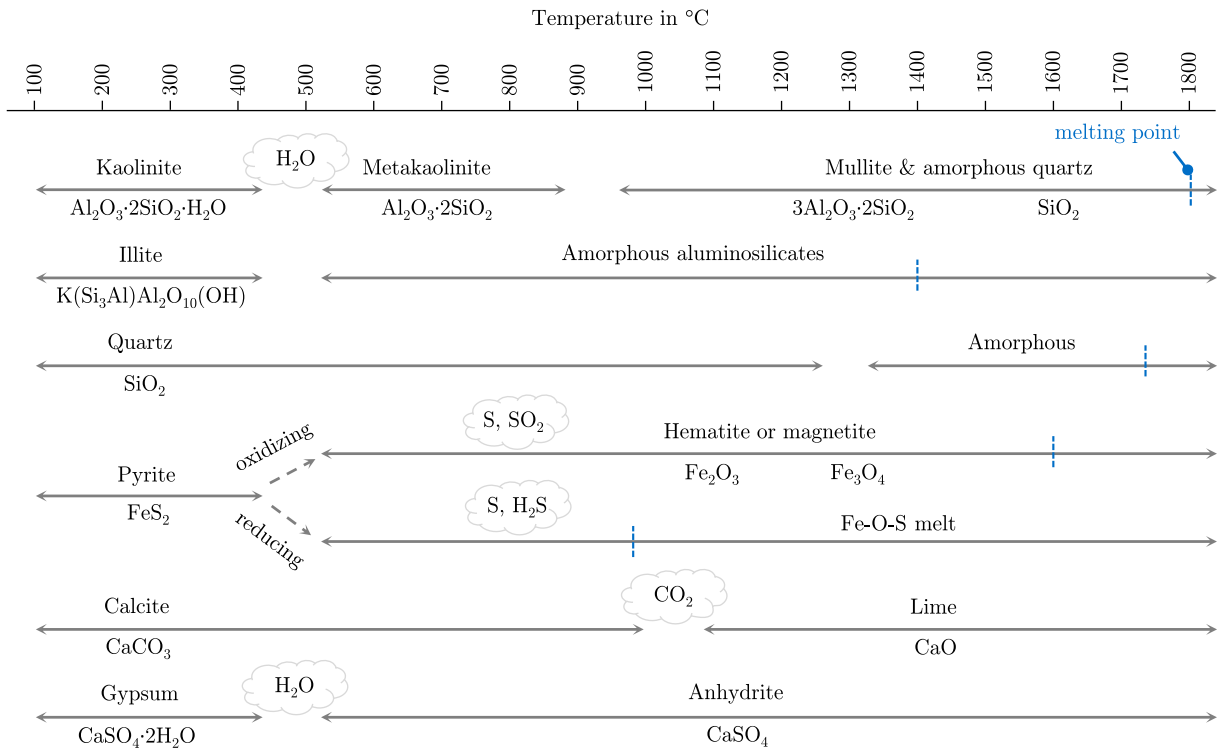

Fig. 16. Mineral transformation of coal minerals as a function of temperature (modified from Mitchell and Gluskoter [177], Unsworth and others [82], and Bryers [16]).

sodium of all clays [15]. It is often present in large quantities and with associations to other minerals, such as pyrite [178]. It also starts to decompose at around 400 °C, forming an amorphous aluminosilicate. The melting point strongly depends on the composition. Typical values are around 1400 °C, however, the melting point can be as low as 980 °C for certain eutectics in the K_2O - Al_2O_3 - SiO_2 system [16,179]. Included illite is often reported to coalesce and form low-temperature melts. Excluded illite does not show fragmentation or swelling behavior. **Quartz** has a very high melting point and is often reported to be inert. Quartz can be liberated during milling and be present as an excluded particle. It can be embedded in clay minerals or exist as a pure mineral [178]. Excluded quartz particles do not melt at temperatures below 1600 °C leading to sharp, erosive ash particles. Quartz is reported to start to volatilize at temperatures around 1650 °C, or above. The behavior of **pyrite** is rather difficult. Iron is often reported to be a key element in deposit formation [15] and many research has focused on its transformation [8,180,181]. Pure pyrite (Fe_2S) starts to decompose around 300 °C, releasing sulfur and forming pyrrhotite ($Fe_{1-x}S$), which subsequently oxidizes in the presence of oxygen, to form hematite or magnetite. Hematite and magnetite are again high melting minerals. There are two mechanisms reported in literature, one involving the thermal decomposition and subsequent oxidation, and, the second being a direct oxidation. Both are known to be slow and therefore, kinetic investigations were carried out [182]. Couch [15] mentions a low melting point for partially transformed pyrite. Similar behavior was observed in reducing conditions, where eutectics with melting points around 1220 °C, are reported [8]. Excluded pyrite was studied in a drop tube furnace by Yan et al. [183] observing fragmentation, where each pyrite grain (50 μm) yielded around four child particles. The authors successfully used the Poisson law, similar to Eq. (2), in order to predict fragmentation behavior not only for pyrite, but also for calcite. Included pyrite can form eutectics with even lower melting temperatures in the presence of aluminosilicates. McLennan and others [8] report iron bearing glass melts at temperatures as low as 1080 °C. Ten Brink et al. [181] studied pyrite transformation in a real 2.5 MW_{th} flame. They observed a decomposition to molten FeS, which then oxidized to solid iron oxide (Fe_2O_3 and Fe_3O_4). The kinetics of the decomposition were estimated to proceed as fast as devolatilization, and the subsequent oxidation as fast as char conversion [181]. Carbonates are known to decompose, and release carbon dioxide. **Calcite** ($CaCO_3$) for instance starts to loose CO_2 at around 800 °C. Other carbonates such as siderite ($FeCO_3$) or dolomite ($MgCO_3CaCO_3$), start at roughly 500 °C and 750 °C, respectively [15,16]. Sulfates, for example **gypsum**, decompose earlier, and form stable anhydrite by the release of water.

Chemical transformations and their complexity are discussed in various references [16,82,178,184]. Process conditions, such as temperature and oxygen content, can change the path of chemical transformations, and lead to a variety of possible routes. Details of the chemistry and mineral decomposition are poorly understood, in particular for particles containing a mixture of mineral inclusions. When considering the melting temperatures shown in Fig. 16, most values are above typical temperatures in combustion systems. However, ash deposition occurs already at much lower values, which is probably due to interactions of mineral inclusions. Associated minerals are referred to as combinations of different mineral types in one particle. These associated minerals and their compounds behave differently, leading to eutectics and lowered melting points. In addition, minerals are often contaminated with other elements. Therefore, modeling the fate of pure minerals is not able to capture real processes. An overview of mineral transformations can be found, for instance, in the work of Unsworth and others [82], Bryers [16], Božič [184] or Magda [178]. The bar chart illustrated in Fig. 17, gives the mineral composition of the Upper Freeport bituminous coal, before and after combustion [57]. It shows the transformation of major minerals, in particular the oxidation of pyrite to iron oxide, the formation of glass phases and of amorphous silicates. Benson et al. [57] discusses the vast variation of fly ash particles in size and chemical composition. They further claim the dominance of amorphous phases consisting mainly of silicate glass, summing up to 90 or more

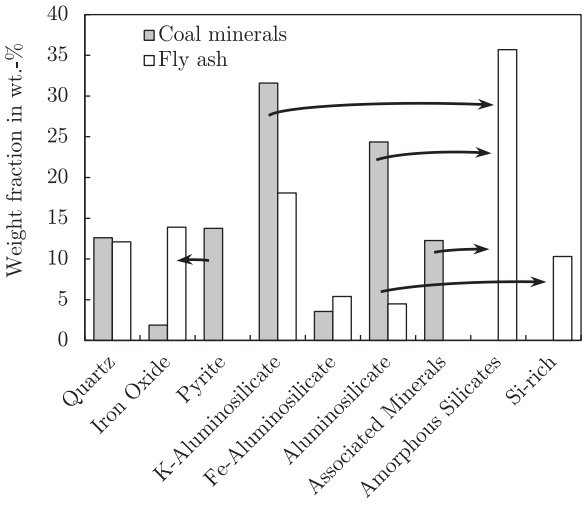

Fig. 17. Comparison of bituminous coal mineralogy and fly ash composition (in wt.%, data from Benson et al. [57]).

wt.%; where glass is defined as an inorganic product of fusion without crystallizing upon cooling from a melt [57]. Physical properties of ash particles, and their role during ash deposition, are discussed in the following sections.

Studies dealing with chemical transformation of inorganics from biomass are scarce. Arvelakis et al. [136,137] studied the effect of leeching on ash behavior of straw and olive residue, as well as, conducted simultaneous thermal analysis on high-alkali biomass ash. Observed reactions and transformation included the release of CO_2 from $CaCO_3$, evaporation of KCl and reactions of K_2CO_3 with SiO_2. Boström et al. [11] investigated minerals from woody biomass ashes using XRD analysis. The authors identified empirical biomass ash transformation phenomena in order to predict ash chemistry and underlined the complexity due to a high number of species. In the field of biomass ash formation, much attention was paid to inorganic vaporization and re-condensation, however, studies dealing with mineral inclusions and coarse fly ash formation are rare.

2.3.3. Flame-generated aerosols

Aerosols generated during solid fuel combustion and their characteristics received much attention during the 70's and 80's in the case of coal, and during the late 90's in the case of biomass, when the number of units firing lower-grade fuels, such as straw or wastewood, increased. Aerosols can be distinguished into organic and inorganic particles. Organic particles such as soot, polycyclic aromatic hydrocarbons etc., can be caused by incomplete combustion, typically for small-scale biomass boilers. Inorganic aerosols originate from inorganic vapors and their condensation. A typical number and mass distribution for wood combustion in a stove can be seen in Fig. 18(a) and (b), respectively. Different operation conditions show that aerosol concentration can be affected by process conditions such as temperatures, oxygen concentration and distribution. However, for large units such as PF boilers the variation and potential is considerably smaller. Carroll et al. [47] showed for small-scale applications that air staging can reduce particulate matter (PM_1) emissions by 16 up to 26% in the case of wood combustion. A much higher potential was reported when co-firing peat with straw [46]. Up to 70% of aerosols were reduced caused by reactions of gaseous alkali vapors with aluminosilicates found in peat - see also Section 2.5.4. Damle et al. [139] collected data on aerosols formed during coal combustion. Fig. 19 compares measured particle concentrations within coal-fired boilers. The first mode typically occurs around $d_p = 100$ nm with particle concentrations in the range of 10^6–10^8 per cm^3. It is difficult to compare different studies, since aerosol measurement devices differ, devices are highly complex, and locations inside a boiler, boiler type as well as process conditions highly affect results. Nevertheless, a qualitative estimate on typical particle sizes and their distribution can be drawn from such a comparison. Fig. 20 shows a similar collection of data on the particle number distribution in biomass fired systems. Particle numbers are slightly higher compared with coal measurements and shifted towards larger particle sizes with modes around $d_p = 100$–300 nm. This could be caused by an increased share of vaporizable inorganics as shown in Fig 4. An increased amount of inorganic vapor leads to a higher particle number, where a high particle concentration enhances particle coagulation and agglomeration. During this process, particles stick together, the particle number decreases, whereas the mass remains constant. The quantity, form and concentration of aerosols depends on the fuel, fuel preparation, firing system, but also on process conditions, such as stoichiometry and temperature [199]. Stoichiometry most likely affects organic aerosols produced during incomplete or under-stoichiometric combustion. This is often confirmed in small-scale wood fired grates [144]. Gas temperature strongly affects the vaporization of inorganic elements in the fuel, the supersaturation of inorganic vapors in the gas phase and thus, the condensation and formation of aerosols. These phenomena will be discussed within Section 2.5.3.

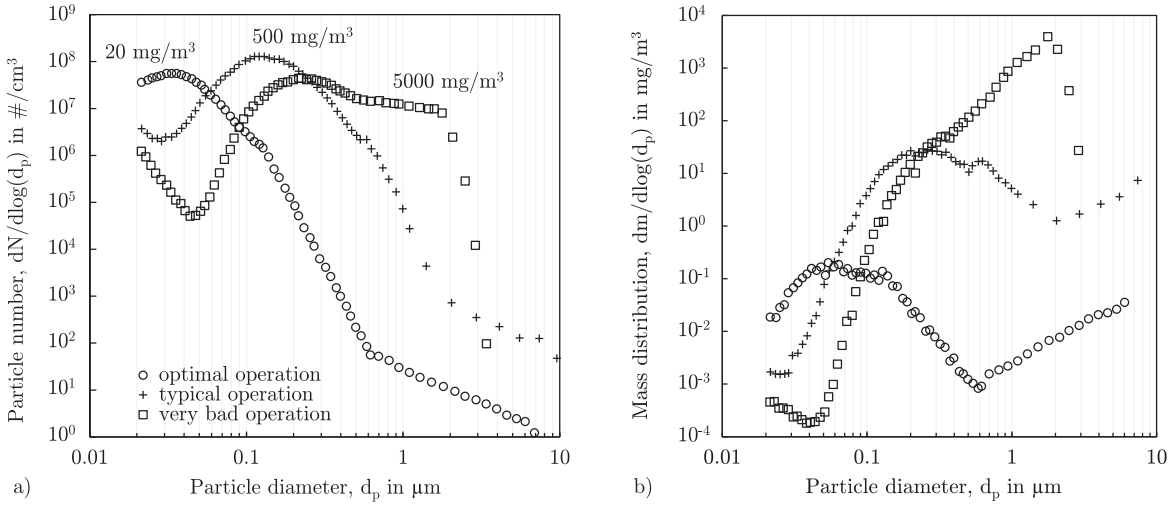

Fig. 18. Aerosol emissions from wood stoves under different operation conditions: a) number distribution, and b) mass distribution calculated from original data with the assumption of a constant particle density of 2.5 g/cm³ (data taken from Nussbaumer et al. [194], originally from Klippel and Nussbaumer [195]).

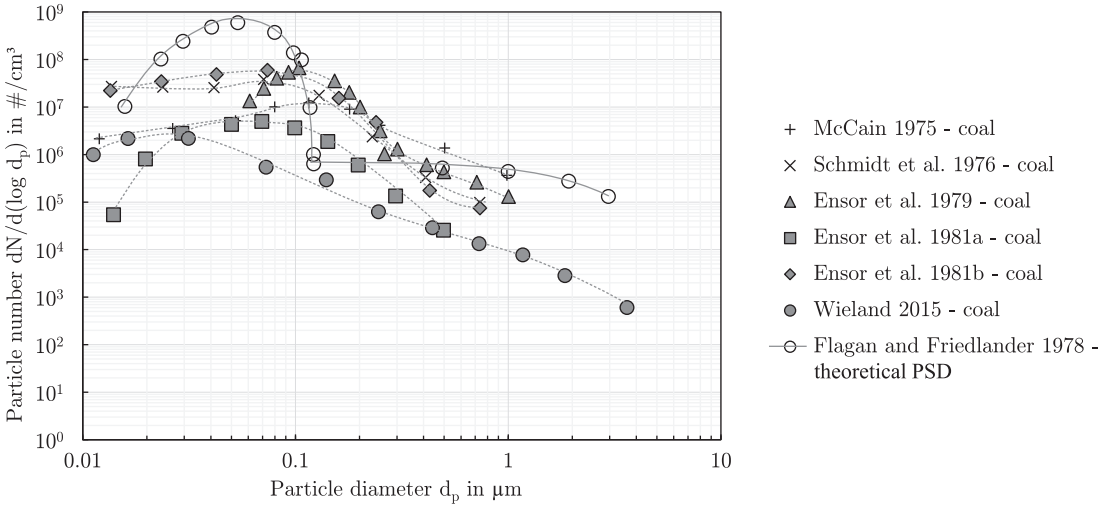

Fig. 19. Aerosol size distribution in the sub-micron range from coal combustion (adopted and extended from Damle et al. [139], further references [138,140–143,174]).

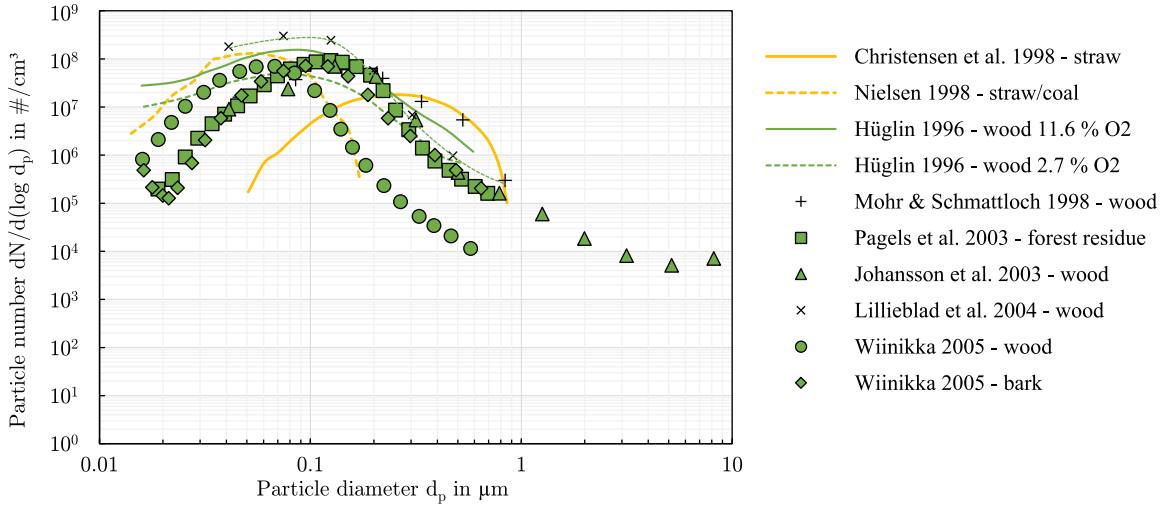

Fig. 20. Aerosol size distribution in the sub-micron range from biomass combustion (compiled from different references [145,148–154]).

Table 4 compares different publications dealing with aerosol measurements in all three firing systems. Typical devices that are applied are impactor cascades such as the Berner type low pressure impactor (BLPI), similar compared to an ELPI, the differential mobility analyzer (DMA), the scanning mobility particle sizer (SMPS) or the aerodynamic particle sizer (APS), where the latter two are typically applied in automotive industry. A detailed description and comparison of these devices can be found in literature, e.g. [101,151,158,175,194]. An interesting high-temperature impactor was presented by Brunner et al. [160], which enables studying aerosol formation at higher temperatures. All these devices are highly complex and influenced by various parameters, such as dilution gas in order to prevent agglomeration in the device, the ability of particles to carry electrical charge, particle shape and density, gas temperature and thus gas viscosity and gas density, as well as many more. Therefore, it is not surprising that measurement results scatter significantly. A comparison of different studies should be only qualitatively. When evaluating Table 4, one can see that most studies apply impactors in order to sample aerosols. The highest concentrations of aerosols are found for waste-wood and straw. This can be explained by the relatively high ash content and the fact, that these fuels are rich in alkali metals shown in Table 1. Aerosol concentrations for particles smaller than $d_p = 1\,\mu m$, also referred to as PM_1, show values up to 1500 mg/m^3_n as measured by Christensen et al. [149] in a straw-fired grate. Mikkanen [161] showed that around 66% of fly ash can be found in aerosols with $d_p < 3\,\mu m$. For coals, typically smaller numbers are reported, however, many different values can be found in literature. The chemistry of aerosols strongly depends on the parent fuel. Straw leads to aerosols rich in salts mainly composed of KCl and K_2SO_4. Aerosols from wood combustion are typically rich in K, Ca, Cl and Mg. On the contrary, bituminous coals lead to S-, Ca- and Si-rich aerosols. As discussed previously, the mode is typically around 100–200 nm, and is dominated by agglomerates. The combustion system can influence aerosol formation, however, there is no clear picture derived from Table 4.

Future studies should deal with the prediction of aerosol formation such as the work of Jokiniemi et al. [162]. There is a need for guidelines on how to present, calculate and evaluate aerosol measurements and emissions. Many studies do not provide all information that is needed in order to evaluate and interpret their measurement results. Further fundamental work has to be conducted and should be coupled with comprehensive CFD models enabling the prediction of ash deposition and hence, improve soot-blowing or plant design. It is believed that aerosol behavior is of great importance for slagging and fouling, in particular for biomass-fired boilers.

Table 4
Selected studies dealing with aerosol measurements in different combustion systems. Major findings summarized in terms of aerosol concentration, particle size and chemistry.

References	System and size	Fuel	Measurement technique	Concentration in mg/m_N^3	Mode in nm[a]	Chemistry[b]	Findings
McCain et al. 1975 [140]	different PF boiler	coal	impactor, optical	n.a.	100-200	n.a.	with and without ESP
Kauppinen & Pakkanen 1990 [155]	420 MW_{th} PF boiler	bit. coal	LPI	1460[g]	50 and 2 μm	Ca, S, Si	measurement up- and downstream of ESP
Hasler & Nussbaumer 1997 [144,159]	grate	wood	impactor	70–580[g]	< 260	n.a.	80% of mass in PM_1
Hüglin et al. 1997 [146]	60 kW_{th} wood chip burner	wood chips	DMA, SMPS, APS	n.a.	60–250	organic/inorganic	different operation modes studied
Valmari et al. 1998 [189]	3–12 MW_{th} CFB boiler	80% willow 20% wood pellets	BLPI	52–87[h]	200–400	K, Ca, Mg	measurement downstream convective section
Christensen et al. 1998 [149]	5 MW_{el} grate Haslev	straw (wheat/barley)	BLPI, SMPS	400–1500[f]	200–450[f]	K, Cl, S, P	measurement upstream of baghouse filter on diff. days
	7 MW_{el} grate Slagelse	straw (wheat/barley)	BLPI, SMPS	75–2094[f]	270–610[f]	K, Cl, S, P	
Nielsen 1998 [150]	380 MW_{el} wall-fired PF boiler	coal	BLPI, SMPS	47[l]	67[l]	Si, S, Ca, Al	primary particle size determined
		coal and straw	BLPI, SMPS	35–106[l]	50–87[l]	K, S, Ca, Si	vary. load 20% straw (energy basis)
Mikkanen 2000 [161]	275[i] MW_{th} UPM Kymmene Wisaforest mills recovery boiler	black liquor	BLPI	11000[j]	200–300	Na, S, K, Cl	measurements at different locations and temperatures
Lind et al. 2000 [156]	35 MW_{th} CFB co-generation plant	willow	DMA, ELPI	53	90[k]	K, S, Cl	bottom ash, fly ash and aerosol characterized
		forest residue	DMA, ELPI	17	100[k]	K, Cl, S	
Pagels et al. 2003 [151]	6 MW_{th} moving-grate furnace	moist forest residue	ELPI	79-145[e]	120-140	K, S, Cl	comparison of measurement devices and plant load
			SMPS	31-74[e]	n.d.	n.d.	
			APS	200-5400[e]	n.d.	n.d.	
Wiinikka and Gebart 2005 [147]	10 kW_{th} updraft pellet reactor	wood pellets	impactor, SMPS	10[m]	60–70	K, Cl, C, S	two temp. studied
		bark pellets	impactor, SMPS	48[m]	100-110	K, Cl, S	675°C taken
Jöller et al. 2007 [157]	404 MW_{th} PF boiler	sawdust and coal	BLPI	40[c]	110	Si, Ca, S	model is developed and validated
	40 MW_{th} grate (CHP plant)	waste wood	BLPI	170[c]	125	Cl, K, Pb	
	440 kW_{th} pilot-scale flame tube boiler	wood chips	BLPI	18[c]	90	Cl, K, Ca	
Brunner et al. 2013 [160]	20 MW_{th} grate	MSW	own LPI	384–1754[g]	250-700	Cl, Na, K, Zn (high Si at early stages)	high temperature LPI
Balan 2014 [175]	15 kW_{th} PF entrained flow reactor	straw (barley)	ELPI	5 wt.%[d]	130	K, Cl, S	additives are tested and evaluated
		wood dust (spruce)	ELPI	1 wt.%[d]	100	K, Ca, Cl, Mg, Si	
Wieland 2015 [174]	15 kW_{th} PF entrained flow reactor	bit. coal	ELPI	280–1270[g]	430	d_p > 500nm: Si, Al, Ca d_p < 500nm: K, P	aerosol model development and validation

BLPI: Berner-type low pressure impactor, ELPI: electrostatic low pressure impactor, DMA: differential mobility analyzer, SMPS: scanning mobility particle sizer, APS: aerodynamic particle sizer only sub-micron modes are considered.

[a] Given values based on number distribution.
[b] sorted by decreasing quantity.
[c] concentration at mode diameter and at 13% O_2 in the dry gas.
[d] mass in size class of the mode according to $dm/d\log(d_p)$.
[e] ELPI: PM_1 in mg/m_N^3, SMPS: $PV_{0.55}$ in mm^3/m_N^3, APS: Number > 1 μm in $1/cm_N^3$
[f] range from different days, diameter range given as geometric mean value.
[g] concentration in PM_1 before filter/ESP (electrostatic precipitator)
[h] d_p < 1 μm, measured at 160°C downstream convective section
[i] estimated from given data
[j] d_p < 3 μm, measured at the furnace exit at 3 vol.% O_2
[k] based on measured number distribution
[l] d_p < 1 μm and primary particle diameter in the size of 20 nm
[m] mg/MJ_{fuel}

2.4. Classification of fly ash particles

Ash particles and their behavior in combustion systems are particularly challenging, since they can occur as liquid droplets with Newtonian fluid flow behavior, as solid elastic particles, or somewhere in between with a partially molten particle containing crystals. Ash particles can be classified based on their physical properties such as size, shape and geometry, as well as based on their chemical composition and chemical structure.

Ash particle structures reported in combustion systems are [97,186–188]:

- molten, perfectly spherical particles (typically from fusion of low melting ash/mineral particles),
- cenospherical particles with variable wall thickness (hollow spheres),
- plerospherical particles (hollow spheres filled with small often sub-micron ash particles),

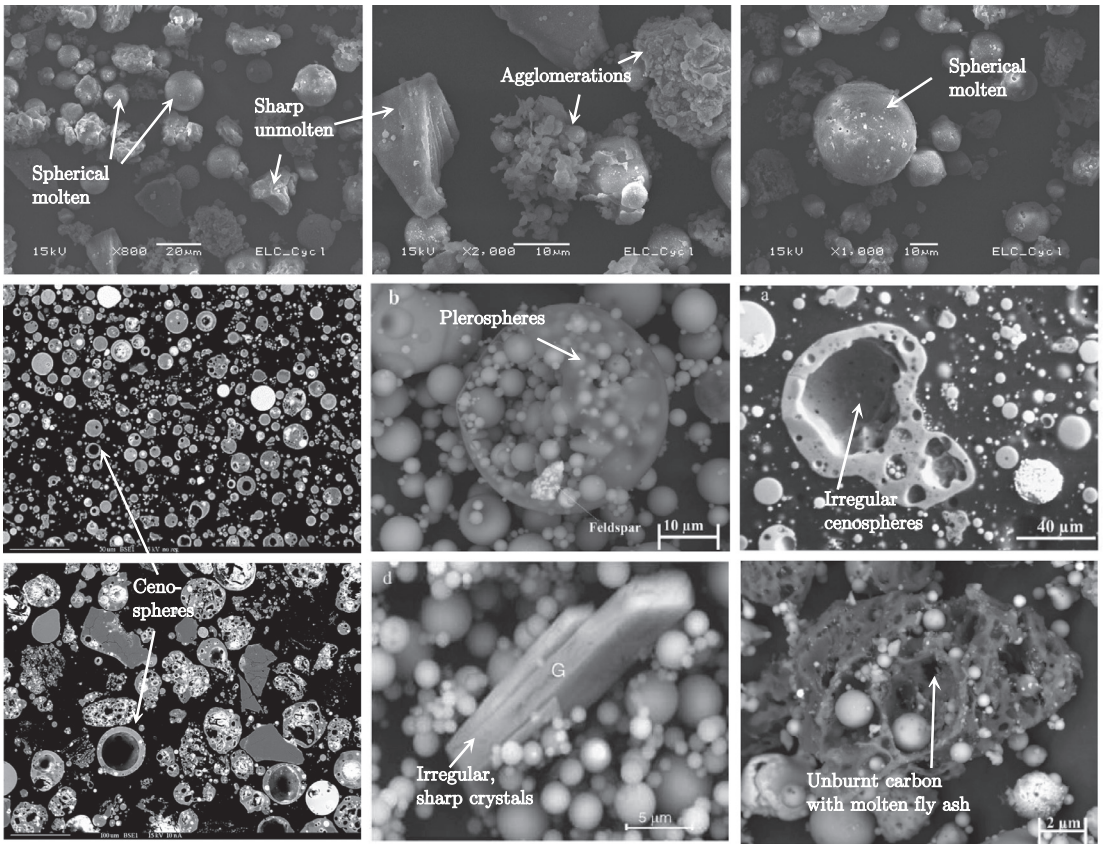

Fig. 21. Typical bituminous coal fly ash particles and their morphology (compiled from different references [97,185–187]).

- angular sharp particles (often reported for unmolten quartz),
- loose, irregular shaped and highly porous solids (mainly reported for biomass, or unburnt char), and
- agglomerations of small particles (often produced from included mineral grains partially undergoing coalescence or by condensation and coagulation).

A graphical illustration of typical ash particles produced from coal combustion is shown in Fig. 21. Spherical particles, as illustrated in the top right corner, indicate that they have been molten in the flame region. Raask [200] first explained the formation of cenospheres (see middle right image). Coal particles with a high number of included mineral grains form an ash layer around a reactive char core. Fusion of this silicate envelope leaves burning carbon residue inside, continuously releasing gases. If the remaining carbon contains mineral grains, plerospheres, as shown in the center of Fig. 21, are assumed to form. Agglomerates may form similarly, however melting/fusion temperatures of ash or partially-transformed mineral grains, does not occur. Sharp, unmolten particles are often found to be composed of quartz or feldspars [15,97].

Typical ash particles produced by biomass combustion are summarized in Fig. 22. At a first glimpse, one can see much more irregular particles. Perfect spheres are rarely observed. Instead agglomerates (lower right corner) and irregular-shaped ash particles or crystals are reported. Wood combustion leads to calcium-rich particles with high fusion temperatures, as shown in the top left corner [101]. Straw (lower three images) forms similar particles, however, fusion is more often observed. Typically, small aerosol collide with large ash particles, which can change the stickiness and thus the deposition process. Characteristic salt-rich aerosol are shown in the top-middle image. They can be angular, and have relatively low melting temperatures.

Ash particle structures mainly depend on the raw fuel - size, form and distribution of inorganics - and on the combustion system - plant size, fuel size, grinding, temperatures, stoichiometry and combustion intensity. The first point is often addressed in scientific studies. However, the impact of combustion system on fly ash particle structures has never been studied systematically. It is known that ashes from lab-scale flow reactors and full-scale boilers can differ significantly. Different heating rates and flow velocities can change particle structural development, char fragmentation, and thus, ash formation [105]. However, there are studies, such as the work of Xu et al. [192], reporting relatively good agreement between PSD of ashes from lab- and full-scale. As expected, their data reveals that full-scale systems have much higher particle concentrations [192]. In general, higher temperatures increase the probability of fusion/coalescence of included mineral grains and enhance burnout. A coal having high numbers of included mineral grains will form coarser fly ash particles with spherical shape when burnt in a PF boiler, compared with low-temperature laboratory ashes, where every mineral grain will form one remaining ash particle, as long as char burnout is identical and sintering does not occur. Char particles within ashes are typically large (50 µm and larger) compared with fly ash particles [193,196]. A comparison of ashes from different combustion systems such as grate, FB and PF using the same parent fuel is challenging. As shown in Fig. 1, grinding, and thus particle size differs significantly, which then affects mineral liberation and residual ash PSD. Furthermore, residence time and temperature profiles differ significantly affecting the whole fly ash formation process. Ashes from grate combustion are typically differentiated into fly ash and bottom ash. In general, bottom ash are known to be significantly larger. For instance, bottom ash particles in MSW combustion systems are in the size range of 0.5–4 mm [197]. Fly ashes collected in grate systems on the other hand are often reported to be rich in submicron ash particles with peaks at around 0.2 up to 0.5 µm,

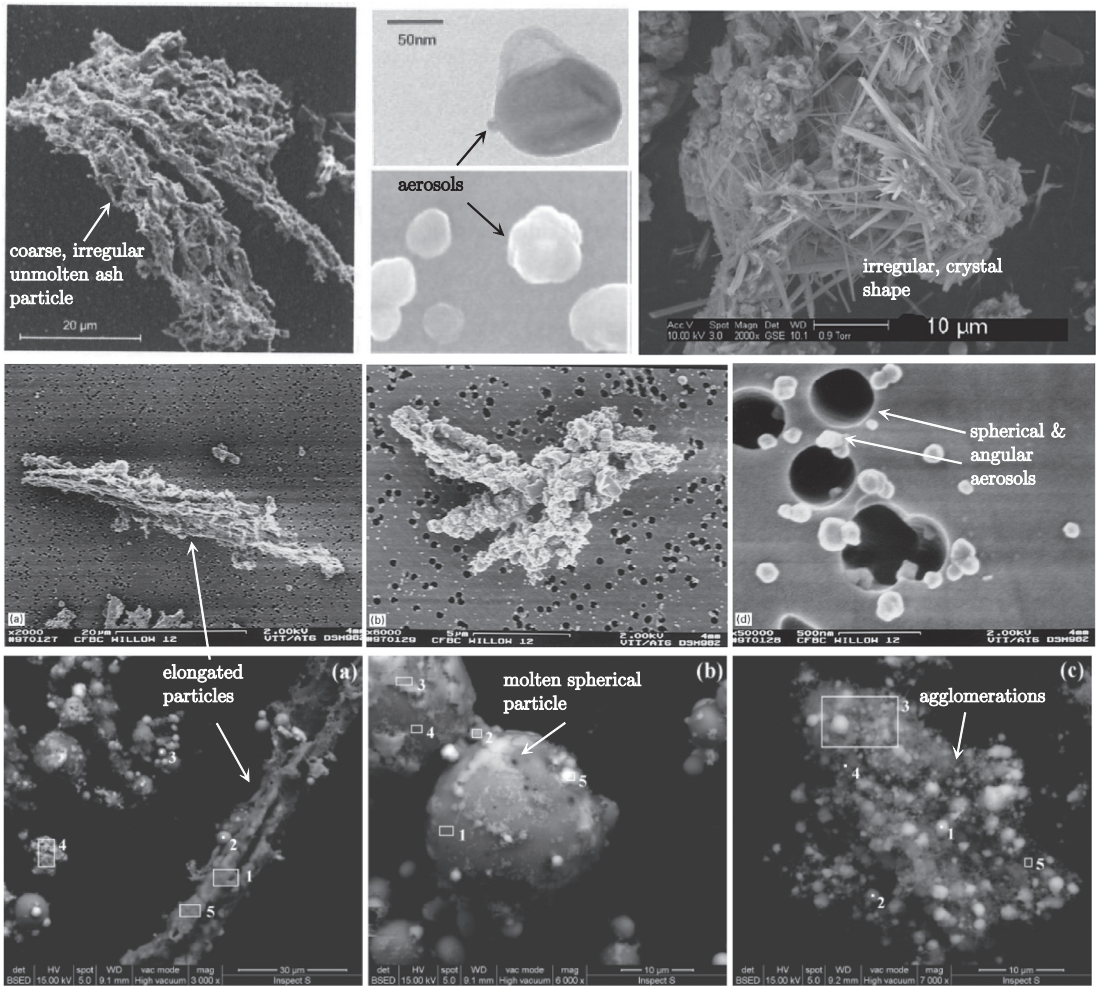

Fig. 22. Typical biomass fly ash particles and their morphology (compiled from different references; first two rows show ash particles from wood combustion in a grate [101], CFB system [189] and PF system [190]; third row shows typical straw fly ash particles [191]).

depending on the fuel and vaporization of inorganics [149,198]. Valmari et al. [189] studied fly ashes from willow combustion in a CFB boiler and found a bi-modal size distribution with peaks at 0.2–0.5 and 5–10 µm, respectively. Some large, irregular and unmolten particles with 100 µm were found indicating incomplete coalescence due to low temperatures [189]. In general, different combustion systems lead to changed fly ashes mainly caused by varying temperature profiles, residence times and parent fuels.

A classification based on chemistry is challenging. Within the same fuel sample, a wide range of chemical compositions and structural variations among fly ash particles, are observed. Coal ashes can produce glassy ash particles, particles containing crystals and intermediates. Therefore, a classification based on chemistry is not recommended. Instead CCSEM data can be a powerful tool, for determining the chemical composition and its variation. Care should be taken, when categorizing ash particles to mineral or ash classes. Instead a list of the raw elemental composition for each ash/mineral particle, might be more useful.

In general, ash particles differ significantly in size, shape, structure and chemistry. This is even more pronounced in case of waste-based fuels or biomass. Both, the shape and chemistry are known to affect the sticking probability. Therefore, it is recommended to use synthetic materials mimicking ash particles, in order to study sticking and rebound behavior under well-defined and controlled conditions. For instance, coal ashes can be simulated using soda-lime glass particles [1,201], or biomass ashes with synthetic salt particles [202,203].

2.5. Ash deposition mechanisms

Ash deposition strongly depends on the presence of ash particles or inorganic vapors at heat exchanging surfaces. Deposition of particles involves particle transport to the wall, particle impaction, and particle retention, often called particle sticking. Commonly it is differentiated between particle impaction, sticking, and capture efficiency, which are defined as [204,205]:

$$\text{Impaction } \% = \frac{\text{Mass of particulate impacting surface}}{\text{Total mass of particulate injected}}$$

$$\text{Sticking } \% = \frac{\text{Mass of particulate sticking surface}}{\text{Mass of particulate impacting surface}}$$

$$\text{Capture } \% = \frac{\text{Mass of particulate sticking to surface}}{\text{Total mass of particulate injected}} = \text{Impaction } \% \cdot \text{Sticking } \%$$

In this definition, the total mass of particulate injected should be calculated for the projected area in front of the obstacle, which is typically a cylinder with diameter D [206]. The difference between particle impaction and deposition rate are particles rebounding from heat exchangers. The capture efficiency can be calculated as the product of impaction and sticking efficiency. Physical phenomena affecting the transport of particles and vapors in the flue gas are summarized by Couch [15], who refers to an early study by Samms and Watt [207]. These phenomena are particle drag due to the flow,

molecular and Brownian diffusion, thermal and eddy diffusion, as well as gravity and electrostatic effects. Basically, each gradient in a flow field can lead to particle movement, where small particles are typically more prone to these gradients. This can be a gradient of shear forces, the so-called Saffman lift force [208], a gradient in species (referred to as diffusiophoresis) [209] or in turbulence (called turbophoresis), where particles are transported in the direction of lower turbulent kinetic energy [210]. The main transport mechanisms leading to ash deposition on a surface are [211,212]:

- **inertial impaction** including eddy impaction,
- **thermophoresis** and diffusional aerosol transport due to gradients in the flow,
- **diffusion** of inorganic vapors followed by heterogeneous condensation and/or heterogeneous chemical reactions with deposits.

The first two bullet points are related to particle deposition, where inertial impaction is often reported as the dominant mechanism of deposit formation, in terms of weight gain, and if a sticky initial layer is already existing. Heterogeneous condensation on the wall and chemical reactions of inorganic vapors with the deposit keep the surface concentrations of these gaseous species to zero. The behavior of inorganic vapors is difficult to study. They can form submicron particles during cooling within the boundary layer, which are then transported by thermophoresis and other diffusional effects to the surface. A graphical illustration of particle deposition mechanisms on a tube is shown in Fig. 23 [213]. Inertial impaction, and eddy impaction in a porous layer are dominating on the upstream cylinder face. Eddy impaction together with thermophoresis are dominating for small particles on both, the cylinder front and rear. They are often reported to be the dominant mechanisms on the cylinder rear. Thermophoresis, condensation and chemical reactions are often mentioned, however, their role is unclear. Experiments on particle deposition are mainly carried out in a vertical turbulent duct flow. Fig. 24 shows the rate of particle deposition on the wall of a circular duct, as a function of non-dimensional variables. The dimensionless deposition velocity V_{dep+} is plotted as a function of the dimensionless particle relaxation time τ_{p+}. The dimensionless deposition velocity is commonly defined as [214]:

$$V_{dep+} = \frac{J_W}{\rho_{p,g} \cdot u_*}, \tag{5}$$

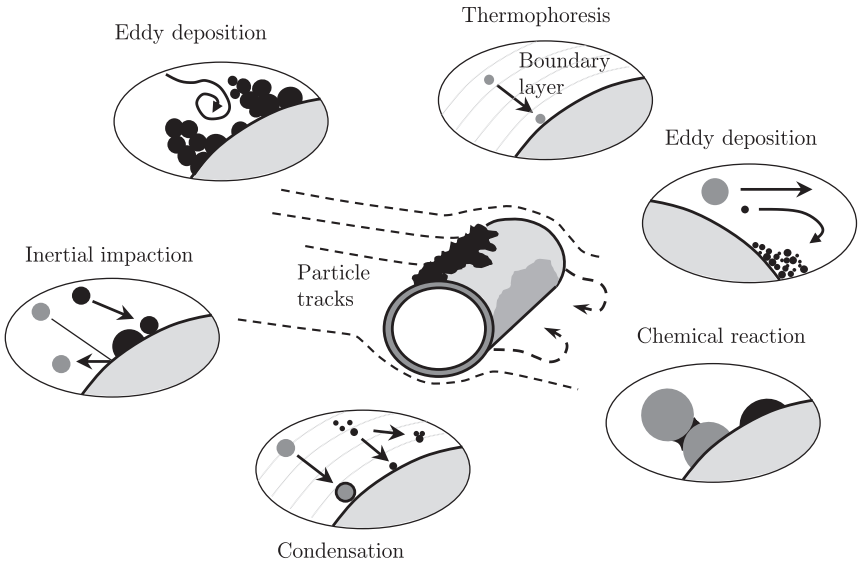

Fig. 23. Ash deposition mechanisms on a superheater tube (adapted with permission from Laursen et al. [213]. Copyright 1998 American Chemical Society.).

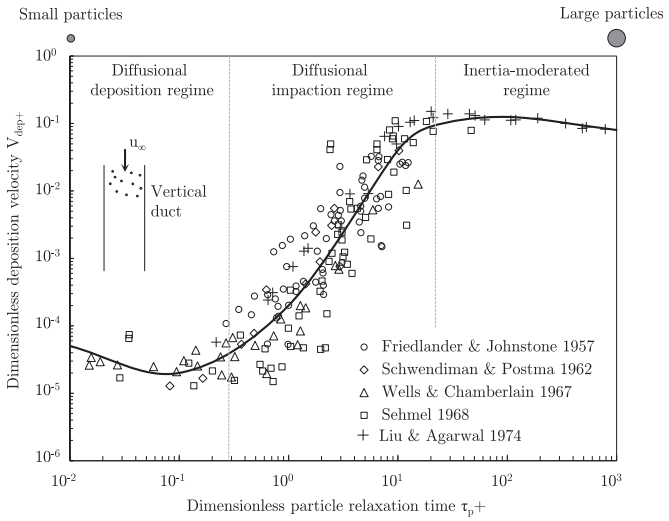

Fig. 24. Particle deposition from fully developed vertical turbulent duct flow (modified from Young and Leeming [214] and Guha [216]).

where J_W is the mass flux of particles to the wall per unit area (in kg/(m^{2}s)), $\rho_{p,g}$ is the mean particle concentration or density (in mass of particles per unit volume kg/m^3), and u_* is the friction velocity at the wall. The friction velocity can be calculated by $u_*^2 = \tau_w/\rho_g$, where τ_w is the wall shear stress and ρ_g the gas density. The wall shear stress $\tau_w = \mu_g \cdot (\partial u/\partial y)_{y=0}$ is expressed by the gradient of the velocity parallel to the wall ∂u, the distance to the wall ∂y, and the dynamic gas viscosity μ_g. The horizontal axis shows the dimensionless particle relaxation time, which can be viewed as the time scale of the particle's reaction to changes in the gas phase velocity. The relaxation time is the time that a particle, initially traveling with free-stream velocity, needs in order to reach equilibrium velocity due to drag (friction) [215]. The particle relaxation time τ_p is calculated by:

$$\tau_p = \frac{\rho_p \cdot d_p^2}{18 \cdot \mu_g}, \tag{6}$$

where μ_g is again the dynamic viscosity. This definition of the particle relaxation time is only valid in the region of Stokes drag law (see next Section 2.5.1). In the dimensionless form, the particle relaxation time is expressed by Eq. (7):

$$\tau_{p+} = \frac{\tau_p \cdot u_*^2}{\nu_g}, \tag{7}$$

where u_* is again the friction velocity, and ν_g is the kinematic viscosity of the gas ($\nu_g = \mu_g/\rho_g$). Measurements in Fig. 24 are taken from the review of Young and Leeming [214], with the original references being Friedlander and Johnstone [217], Schwendiman and Postma [218], Wells and Chamberlain [219], Sehmel [220], and the frequently cited publication of Liu and Agarwal [221]. The deposition curve is divided into three different deposition regimes. In the "diffusional deposition regime" (typical for small particles), the deposition velocity V_{dep+} is decreasing with increasing τ_{p+}. This regime is dependent on the particle Schmidt number, $Sc = \nu_g/D_p$, where D_p is the Brownian particle diffusion coefficient. It is dependent on turbulent diffusion of particles from the core of the duct and Brownian diffusion in a very thin layer adjacent to the wall [214,216]. Brownian particle diffusion is the random movement of particles due to collisions with molecules, which becomes important for very small particles, typically in the sub-micron region. Furthermore, it can dominate in laminar flows and within laminar boundary layers. Particles diffuse from regions with high particle concentrations to regions with lower values. This can be interpreted analogously to gas molecular diffusion. The Brownian particle diffusion coefficient D_p can be estimated using the Einstein equation (see the work of Young and Leeming [214]). Thermophoresis is caused by Brownian motion of particles. The difference between Brownian motion and thermophoresis is that in the latter case, a temperature gradient in the surrounding of the particle is present. This temperature gradient can exhibit a directed force as introduced in the upcoming Section 2.5.2. The intermediate regime is called "diffusional regime", where a strong increase of deposition velocity is observed. Early publications inferred that this region is dominated by the interaction between particles having significant inertia, and the fluid turbulent eddies [214]. The particle's inertia in the near wall region is large enough in order to cross the viscous sub-layer and deposit on the wall. The third "inertia-moderated" regime is not influenced by particle diffusion effects. Large particles having enough momentum from large eddies in the turbulent core reach the wall directly. A slight decrease in deposition rate with increasing particle size is observed. This is explained by the fact that larger particles show less response to turbulence [214]. Much effort has been devoted to the first two regimes in order to derive equations, predicting the particle behavior. However, only recently, advances are reported [216]. Particle deposition in a power plant is dependent on the wall type, e.g. tube or boiler wall, and shows some differences compared to turbulent duct flow experiments. In the following subsections each of the listed mechanisms is described, recent advances are discussed, and differences to vertical duct flow experiments are discussed.

2.5.1. Inertial impaction

Inertial impaction is often referred to as the dominant mechanism, leading to accelerated deposit build-up, and producing the biggest weight gain in a deposit. It describes the effect that larger fly ash particles ($d_p > 10\,\mu m$) cannot follow the streamlines around an obstacle, and thereby impact due to their inertia. This behavior is commonly expressed by the Stokes number, which is defined as the ratio of the particle relaxation time τ_p, given by Eq. (6), to a characteristic flow time scale τ_g:

$$St = \frac{\tau_p}{\tau_g} = \frac{\rho_p \cdot d_p^2 \cdot u_\infty}{9 \cdot \mu_g \cdot D}, \tag{8}$$

where the characteristic flow time scale is calculated for a tube by $\tau_g = D/2 \cdot u_\infty$, with D being the outer tube diameter, and u_∞ being the free-stream velocity. The flow time scale is the time that the free-stream flow needs to pass the cylinder radius. Fig. 25 illustrates the process of inertial impaction. The flow around a cylinder, with its recirculation zone in the wake of the tube, is shown by blue streamlines. Particles (black) approaching the cylinder cannot follow the curvature of the streamlines due to their large mass, which forces them to keep the current direction of the trajectory. Thus, inertial forces exceed aerodynamic forces. Larger particles with high inertia, and Stokes numbers of $St > 1$, barely respond to changes in the fluid flow, as illustrated by the top particle trajectory in Fig. 25. The particle impaction rate is highest for the front stagnation point of the cylinder at $\Theta = 0$ and decreases along the circumference. The maximum impaction angle Θ_{max} depends on the flow characteristics around the cylinder, and the separation point of the flow. Particle impaction on the cylinder rear side is also reported in literature, and is caused by the recirculation zone, which again is a function of the free-stream velocity u_∞. Often, the so-called impaction efficiency η is used to describe the impaction probability of a particle approaching a cylinder in the cross-flow. The impaction efficiency for the

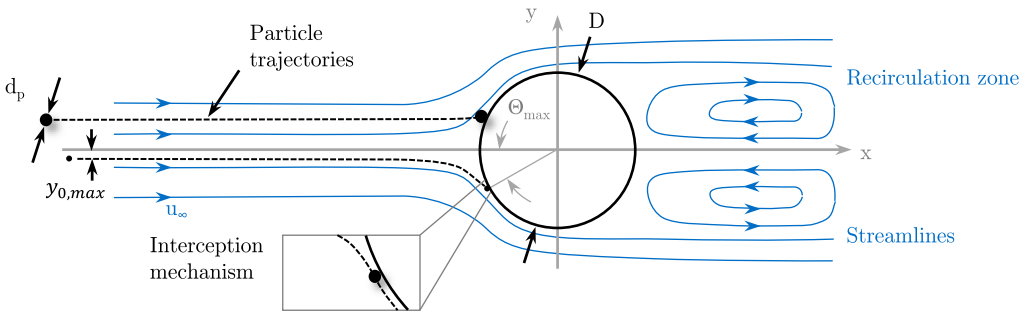

Fig. 25. Schematic illustration of inertial particle impaction on a circular cylinder in cross-flow. The detailed view shows the interception mechanism for small particles.

Table 5
Parameters for Eqs. 13(a) and (b).

References	Equation	Valid for	β_1	β_2	β_3
Wessel and Righi [224]	13a	$0.125 < St_{eff} < 0.5$	0.01978749	0.5136545	−0.0482858
Wessel and Righi [224]	13b	$0.5 < St_{eff} < \infty$	1.54424	−0.538013	0.2020116
Israel and Rosner [215]	13b	$0.14 < St_{eff} < \infty$	1.25	−0.014	0.000508

front face of the cylinder can be calculated by:

$$\eta_{front} = \frac{n_{p,imp}}{n_{p,\infty}} = \frac{2 \cdot y_{0,max}}{D}, \tag{9}$$

where $n_{p,imp}$ is the number of particles impacting on the cylinder front face and $n_{p,\infty}$ is the number of particles in the projected area of the cylinder further upstream [206]. Another method of determining the impaction efficiency is by finding the outermost particle trajectory still impacting on the cylinder, as given by the second part of Eq. (9). Here, $y_{0,max}$ is the maximum vertical distance from the centerline, at which a particle will impact the cylinder surface; see the lower particle track in Fig. 25. The impaction efficiency can be calculated by the vertical distance from the centerline to the starting point of the particle $y_{0,max}$ divided by the cylinder radius ($D/2$) [222]. Eq. (9) requires measurements or numerical simulations. A further way of estimating the impaction efficiency is by using correlations derived from potential flow calculations. These correlations are a function of the particle's Stokes number ($\eta = f(St)$). Equations suggested by Brun et al. [223] were extended to regions where the Stokes' law does not apply. The Stokes' law describes the frictional force (also called drag force) for a sphere within a low Reynolds number flow. For small flow velocities the drag force is a linear function of the Reynolds number. At higher Reynolds numbers it deviates from this linear function. Therefore, Israel and Rosner [215] introduced a correction factor ψ, in order to calculate the so-called effective Stokes number St_{eff}, accounting for this deviation:

$$St_{eff} = St \cdot \psi(Re_p), \tag{10}$$

where the correction factor is a function of the particle Reynolds number Re_p. The correction factor can be calculated by Eq. (11). The correction factor decreases from unity with an increasing particle Reynolds number. The particle Reynolds number for typical ash particles is $Re_p < 1$, which leads to a negligible influence of the correction factor ψ.

$$\psi(Re_p) = \frac{3 \cdot \left(Re_p^{\frac{1}{2}} \cdot \sqrt{0.158} - tan^{-1}\left(Re_p^{\frac{1}{2}} \cdot \sqrt{0.158} \right) \right)}{Re_p \cdot 0.158^{\frac{3}{2}}} \tag{11}$$

Wessel and Righi [224] use the free-stream particle Reynolds number in order to calculate the effective Stokes number, using the following definition:

$$Re_p = \frac{\rho_g \cdot d_p \cdot u_\infty}{\mu_g}, \tag{12}$$

Finally, the impaction efficiency can be estimated, using the following correlations:

$$\eta = \beta_1 \cdot ln(8 \cdot St_{eff}) + \beta_2 \cdot (St_{eff} - 1/8) + \beta_3 \cdot (St_{eff} - 1/8)^2 \tag{13a}$$

$$\eta = \left[1 + \beta_1 \cdot (St_{eff} - 1/8)^{-1} + \beta_2 \cdot (St_{eff} - 1/8)^{-2} + \beta_3 \cdot (St_{eff} - 1/8)^{-3} \right]^{-1} \tag{13b}$$

The valid range of Eqs. 13(a) and Eqs. 13(b), as well as the coefficients β_1, β_2 and β_3 are given in Table 5. The impaction efficiency as a function of the effective Stokes number is illustrated in Fig. 26(a). Values shown are calculated using Eqs. (10) to 13(b). The flue gas velocity is fixed to a value of $u_\infty = 10$ m/s, and the gas density as well as the dynamic viscosity, are computed for a gas temperature of $T_g = 1000\,°C$, with data from the VDI heat atlas [225]. The correlations given by Isreal and Rosner [215] and Wessel and Righi [224] show similar behavior. Small particles with effective Stokes numbers below $St_{eff} < 0.125$ do not impact according to the correlations. With increasing size, particles start to hit the surface and the impaction efficiency is monotonically increasing, with an increasing Stokes number. Particle impaction probability increases from around 8% for a 12.5 µm particle to around 35%, when doubling the diameter. A parametric study is conducted in Fig. 26(b). The impaction probability increases with increasing particle size and density. Two examples are shown for an aluminosilicate particle, with a density around $\rho_p \approx 2.5$ g/cm³, and an iron-rich particle, e.g. hematite, with a density around $\rho_p \approx 5.5$ g/cm³. It can be seen that particle density is along with the particle diameter a critical parameter. Thus, both parameters are crucial and an ash formation model needs to be able to predict both, in particular the particle size, since the Stokes number is a quadratic function of the particle diameter. The correlations given

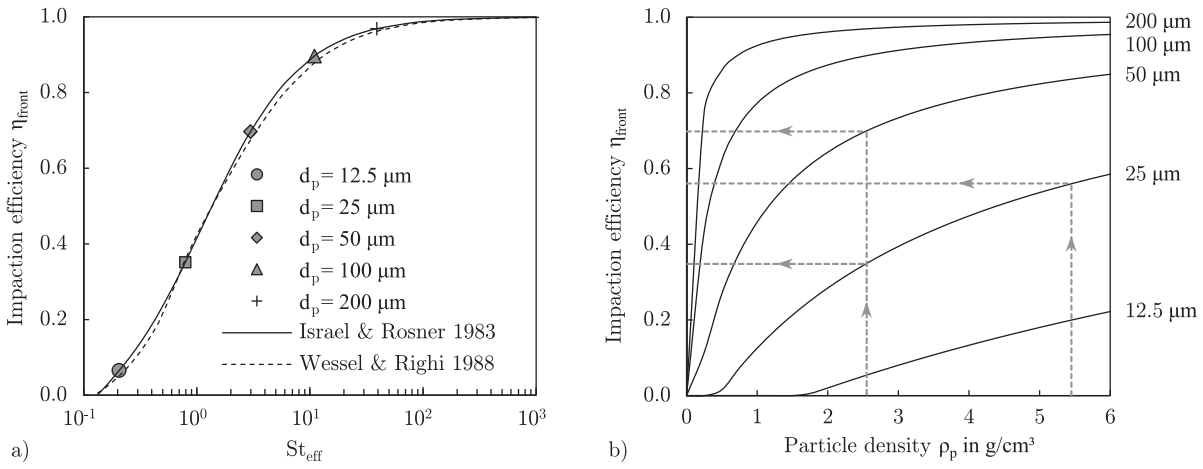

Fig. 26. Impaction efficiency calculated with Eqs. 13(a) and 13(b): (a) as a function of the effective Stokes number and (b) as a function of particle diameter d_p and density ρ_p. Calculated for a flue gas velocity of $u_\infty = 10$ m/s and a gas temperature of $T_g = 1000$°C.

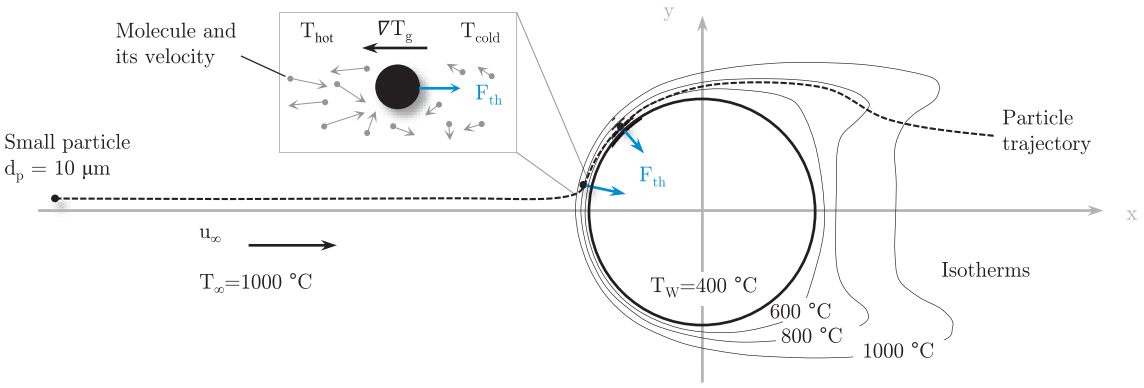

Fig. 27. Thermophoretic force on particles in a thermal boundary layer of a superheater tube. The detailed view illustrates, how molecules have a higher kinetic energy on the hot side of a particle and lead to a temperature-driven force.

are derived for in-viscous (potential) flow calculations and boundary layer effects are disregarded. It has been shown by Haugen and Kragset [226] that the cylinder Reynolds number Re_{cyl} influences the capture efficiency curve, since it changes the boundary layer thickness for a viscous flow. An increased cylinder Reynolds number (calculated by $Re_{cyl} = \rho_g \cdot D \cdot u_\infty / \mu_g$) shifts the impaction curve of Fig. 26(a) slightly to the left.

Particle impaction rates for small Stokes numbers cannot be predicted by potential flow calculations since boundary layer effects dominate this impaction process. Particles with $St < 0.1$, follow the streamlines around the cylinder almost perfectly. The impaction of these particles is solely due to their dimension. The particle center does not reach the surface, only the finite size of the particles leads to a contact between the cylinder surface and the particle surface. The small window in Fig. 25 illustrates this mechanisms. This effect is referred to as "interception" or "boundary layer interception". Typically, this effect can be calculated by viscous flow calculations using CFD (see e.g. Haugen and Kragset [226]). The role of this effect on slagging and fouling, however, might be small, due to the small mass of these particles, and low impaction probabilities.

Compared with the vertical duct flow experiment, a cylinder exhibits an external flow with laminar boundary layers, and a transition flow with turbulent structures approaching the cylinder. To sum up, inertial impaction is often referred to as the dominant mechanism leading to extensive deposition, when particles adhere to the surface. It is most pronounced for larger particles, as shown in Figs. 26(a) and (b).

2.5.2. Thermophoresis

Thermophoresis describes a force on particles in a flow with a non-uniform temperature field. This force is acting in the opposite direction of the temperature gradient, i.e. from the hot gas towards the cold gas. The force becomes relevant for smaller particles, however, it is still not completely understood [227]. Thermophoresis is often mentioned to be important, but rarely addressed in a scientific way for slagging and fouling in a PF system. Another difficulty is the potential of particle nucleation within the boundary layer, which makes it very difficult to actually quantify thermophoresis. The main reason is due to the complexity of this effect. It is difficult to isolate the thermophoretic force in a deposition experiment, and it is even more complex to measure small thermophoretic forces, which are in the range of 10^{-9}–10^{-15} N. The effect was first described by Tyndall [228] in the late 19th century, who observed the formation of a dust-free zone near a heated surface (see also the review of Young [227]). Small dust particles immersed in the flow could not reach the surface due to the thermophoretic force acting from the hot to the cold gas. There are several studies, such as Cawood [229], Walker et al. [230] or Cameron and Georg-Wood [231], indicating the dominant role of thermophoresis for the deposition of particles in the diameter range of $0.1 < d_p < 10\,\mu m$. GökoĞlu and Rosner [232] showed that the impaction rate increases by a factor of 1000 for a 1 µm particle, when the wall temperature is set to a value of 20% below the free-stream temperature. Fig. 27 illustrates the force on particles in the boundary layer of a superheater tube. Thermophoresis (TP) can be explained by varying bombardment of gas molecules on a particle surface. Gas molecules are carrying a higher kinetic energy on the hot side of a particle compared to the cold side. The higher kinetic energy of collisions between molecules and the hot particle surface leads to a net force on the particle in the direction of the cold flow. The mean gas molecule velocity $\bar{v}_M$, can be derived from the Maxwell–Boltzmann equation:

$$\bar{v}_M = \sqrt{\frac{8 \cdot k_B \cdot T_g}{\pi \cdot m_M}} = \sqrt{\frac{8 \cdot R \cdot T_g}{\pi \cdot M}}, \tag{14}$$

where k_B is the Boltzmann constant, T_g the gas temperature, and m_M the molecule mass. It can also be calculated using the molar gas constant R and the molar mass M of the gas. A dimensionless expression of the thermophoretic force F_{th} is given in a study by Healy and Young [233]:

$$\frac{F_{th} \cdot \rho_g}{\mu_g^2} = \Phi \cdot \frac{d_p \cdot \nabla T_g}{2 \cdot T_g}, \tag{15}$$

where ∇T_g is the temperature gradient in the gas phase at the position of the particle, if there is no particle present, and $\Phi = f(Kn, \Lambda)$ is the thermophoretic coefficient. This coefficient is a function of the Knudsen number Kn, and the ratio of the particle and gas thermal conductivity $\Lambda = k_p / k_g$ (note that definitions differ in literature). The gas thermal conductivity is the translatoric part of the thermal conductivity expressed by $k_g = 15/4 \cdot \mu_g \cdot R_s$, where R_s is the specific gas constant. The gas properties in Eq. (15) are also calculated for the center of the particle, if there would be no particle. The Knudsen number Kn, is defined as the ratio of the mean free path length λ of the fluid to the particle radius, according to the following equation:

$$Kn = \frac{2 \cdot \lambda}{d_p}. \tag{16}$$

The Knudsen number is used to judge, whether the flow characteristics can be described by continuum mechanics (for $Kn < 1$), or, by methods of statistical mechanics (for $Kn > 1$). For small particles ($d_p < 5\,\mu m$) in a PF boiler, the Knudsen number can exceed values of $Kn > 1$ depending on the gas temperature. In this case, the classical Stokes drag has to be corrected (see e.g. [226]). The mean path length λ, can be calculated by:

$$\lambda = \sqrt{\frac{\pi \cdot T_g \cdot R_s}{2}} \cdot \frac{\mu_g}{p}, \tag{17}$$

where p is the pressure in Pa, and the gas viscosity μ_g being a function of the gas temperature T_g. With an increasing gas temperature, the mean free path length increases leading to an increased Knudsen number. At ambient temperature, air has a mean free path length of $\lambda = 65$ nm. This value increases for a furnace temperature of $T_g = 1200\,°C$ to $\lambda = 450$ nm. At that temperature a particle with $d_p \approx 0.9\,\mu m$ reaches the critical Knudsen number of $Kn = 1$, requiring extra laws for particle drag. Many studies have focused on the formulation of a generally valid expression for Φ, given in Eq. (15) [227]. Most studies use experimental values to derive correlations. However, different results are reported in the transition region between slip-flow ($Kn \approx 0.1$) and free-molecule regime ($Kn \gg 1$). In this region, the thermal conductivity ratio has a strong impact on the thermophoretic force F_{th}. Epstein [234] recognized the dependence of the thermophoretic force on the thermal conductivity ratio in the slip-flow region, and proposed the following equation for low Knudsen numbers $Kn \ll 1$:

$$\Phi = \frac{-12 \cdot \pi \cdot K_{tc}}{2 + \Lambda}, \tag{18}$$

where K_{tc} is the thermal creep coefficient. Maxwell, who first postulated the theory of gaseous thermal creep, derived $K_{tc} = 0.75$ from simple kinetic theory calculations [227,235]. Recent work suggests values in the range of $1.02 < K_{tc} < 1.18$ [227]. The negative sign in Eq. (18) indicates the direction of TP, which accelerates particles in the opposite direction of the temperature gradient. Waldmann [236] suggested a correlation for the region of free molecular flow at $Kn \gg 1$:

$$\Phi = \frac{-2 \cdot \pi}{Kn}. \tag{19}$$

Φ is solely a function of the Knudsen number, and is not influenced by particle properties. A widely used theory is based on the work of Talbot et al. [237], who modified correlations originally proposed by Brock [238]:

$$\Phi = \frac{-12 \cdot \pi \cdot K_{tc} \cdot (1 + C_e \cdot \Lambda \cdot Kn)}{(1 + 3 \cdot C_m \cdot Kn) \cdot (2 + \Lambda + 2 \cdot C_e \cdot \Lambda \cdot Kn)}, \tag{20}$$

with

$$C_m = \left(\frac{2 - \alpha_m}{\alpha_m}\right) \cdot A_m, \quad \text{and} \quad C_e = \left(\frac{2 - \alpha_e}{\alpha_e}\right) \cdot A_e. \tag{21}$$

The velocity slip and temperature jump coefficients C_m and C_e, depend on the momentum and energy accommodation coefficients α_m and α_e as shown in Eq. (21), where A_m and A_e are constants [233]. Brock [238] suggested values of $A_m = 1.0$ and $A_e = 15/8 = 1.875$. Talbot et al. [237] used values of $A_m = 1.14$, $A_e = 2.18$, and $K_{tc} = 1.17$, which are similar to the ones proposed by Beresnev and Chernyak [239]: $A_m = 1.137$ and $A_e = 2.178$. The accommodation coefficients α_m and α_e describe the interaction of incident gas molecules with the particle surface, and are often set to $\alpha_m = \alpha_e = 1$ [233,239]. Another mathematical description of Φ was introduced by Beresnev and Chernyak [239], and is given by:

$$\Phi = \frac{-2 \cdot \pi}{Kn} \cdot \left[\frac{f_{11} + \Lambda \cdot f_{21}}{f_{31} + (1 + 2.5 \cdot \Lambda \cdot Kn) \cdot f_{41}}\right], \tag{22}$$

where the functions f_{kj} are only dependent on Kn and defined in look-up tables (see [239]). A further correlation was proposed by Yamamoto and Ishihara [240]:

$$\Phi = \frac{-6 \cdot \pi^{3/2}}{Kn} \cdot \left[\frac{A_W \cdot H_O - A_O \cdot (H_W + 2.5 \cdot \Lambda \cdot Kn)}{H_W + 2.5 \cdot \Lambda \cdot Kn}\right]. \tag{23}$$

Eq. (23) again uses look-up tables for the coefficients A_W, A_O, H_W, and H_O [240]. Since look-up tables are impracticable and their application is elaborate, simpler correlations, such as the one proposed by Talbot et al. [237], are often preferred for modeling purposes. A recent correlation of Φ has been proposed by Young [227], reassessing available measurements, without the need of look-up tables:

$$\Phi = \frac{-12 \cdot \pi \cdot \left[K_{tc} \cdot (1 + \Lambda \cdot C_e \cdot Kn) + 3 \cdot C_m \cdot Kn \cdot (1 - \Lambda + \Lambda \cdot C_e \cdot Kn)\right]}{\left[1 + 3 \cdot Kn \cdot e^{-C_{int}/Kn}\right] \cdot (1 + 3 \cdot C_m \cdot Kn) \cdot (2 + \Lambda + 2 \cdot \Lambda \cdot C_e \cdot Kn)}, \tag{24}$$

Young suggests a value of $C_{int} = 0.5$, for the interpolation constant. The correlation provides similar results as the one suggested by Beresnev and Chernyak [239], and is considered to be more accurate. Strictly it is only valid for $Kn < 0.2$, however, Young [227] suggests an application for the whole Kn-range. A comparison of different correlations for Φ is shown in Fig. 28. At $Kn \to 0$ all model curves are consistent with Eq. (18), suggested by Epstein [234]. The same behavior can be observed for large Knudsen numbers ($Kn \to \infty$), where they approach Eq. (19), suggested by Waldmann [236]. In the region $0.001 < Kn < 1$, models show large differences. In particular, the frequently cited equation proposed by Talbot et al. [237] differs considerably to equations suggested by Beresnev and Chernyak [239], and the model by Young [227]. The latter two show considerably lower values at the same Λ, indicating a decrease in thermophoretic force. At very high thermal conductivity ratios ($\Lambda = 1000$) the so-called "reversed thermophoresis" is predicted. This force from cold to hot was first postulated by Dwyer [241], who did theoretical calculations on the Boltzmann equations [227]. It is often also referred to as "thermal stress slip flow" or "second mechanism of thermophoresis". However, experimental evidence is still due [227]. This phenomenon can be seen in Fig. 28 when $-\Phi/2\pi$ yields negative values. At a low value of $\Lambda = 1$, the thermophoretic coefficient shows its highest values. The values decrease with decreasing particles size, but relative to the particle mass, thermophoresis becomes more important at lower values of d_p. Typical thermal conductivity ratios for a PF boiler are in the range of $3 < \Lambda < 100$, where both, the gas k_g, and the particle thermal conductivity k_p, are dependent on temperature and chemical composition. Rezaei et al. [246] gives values for the thermal conductivity of coal ashes in the range of $k_p = 0.3 - 4\ Wm^{-1}K^{-1}$. They further assume higher values for iron-rich ashes. The gas thermal conductivity is typically in the range of $k_g = 0.04 - 0.1\ Wm^{-1}K^{-1}$, where values are taken from the VDI heat atlas, and calculated for typical flue gas compositions [225].

The measurement of thermophoresis is a challenging task due to the small magnitude of this force. Early observations, such as the one reported by Tyndall [228], are strongly influenced by convection of the surrounding fluid. Later experiments focused on single particle studies, in a so-called Millikan cell. This enables the exact measurement of the particle diameter. Charged liquid droplets are held in an electric field between two electrodes, with the field strength E; see also [247–249]. By differential heating of the electrodes, one can establish the following equilibrium $e \cdot E = m_p \cdot g + F_{th}$, in which e is the elementary charge, m_p is the mass of the particle, and g is the acceleration due to gravity. This equation can be used to calculate the thermophoretic force by knowing the particle mass, which requires an exact determination of the particle size. This enables a direct measurement of the thermophoretic force on droplets or particles in a controlled environment. By changing the carrier gas and its pressure or the particle composition, the value Λ can be studied at different Kn numbers.

Studies on the role of thermophoresis in combustion systems are rare. An interesting experimental and modeling study with direct relevance and link to slagging and fouling, was presented by Zhan et al. [242]. They used a vertical surface in a 100 kW down-flow laboratory coal combustor in order to study the inner deposit layer formation and the role of thermophoresis within laminar flow. The authors introduced a thermophoresis number Tp being the ratio of the time a particle travels along a cold surface with thermophoresis

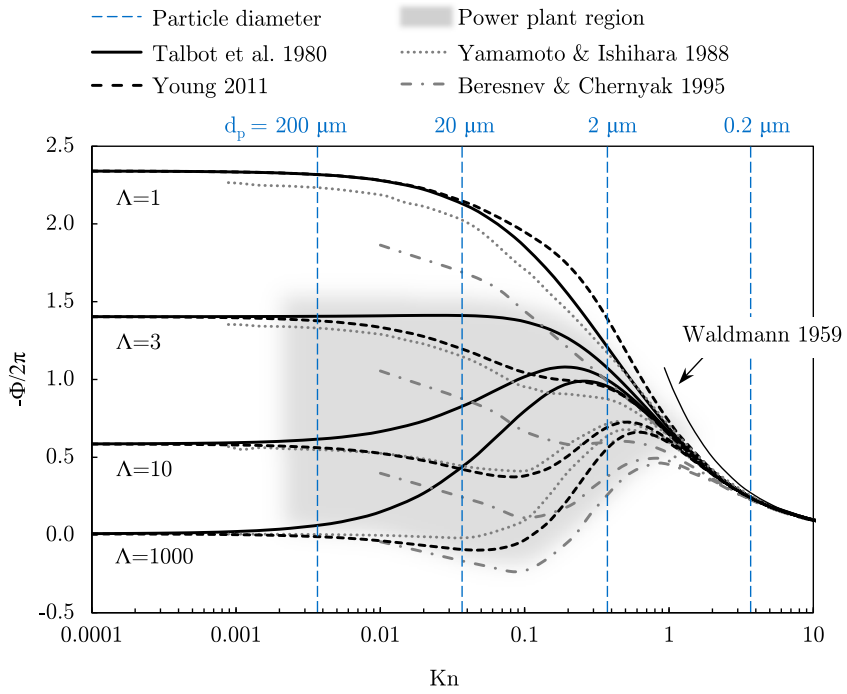

Fig. 28. Expression $-\Phi/2\pi$ as a function of *Kn* and Λ using different correlations (Eqs. (19)–(24)). Typical particle diameters and *Kn* numbers present in a solid fuel fired boiler at T_{FG} = 1000 °C are shown (based on a regime map of Healy and Young [233,243]).

and the time a particle would require without thermophoresis by considering only drag. If $Tp < 1$ particles are captured on the surface. By using this relationship, the authors could show reasonable agreement with measurements. Ash deposition rates increased linearly as the temperature difference between gas and surface increased. Future work will include thermophoresis in CFD codes and validate experiments.

A study [243] predicting the capture efficiency on a cylinder in the cross-flow with and without thermophoresis showed that the capture efficiency for particles with small Stoke numbers increased by three to four orders of magnitude depending on the thermophoresis model and the particle size. Two different models, i.e. Talbot et al. [237] and Young [227], were compared, where the latter one showed a decreased impaction efficiency. Furthermore, it was explained why small aluminosilicates particles experience a higher thermophoretic force compared with iron-rich particles. This is due to an increased thermal conductivity ratio Λ for iron-rich particles [243]. Lutro [245] conducted a similar study at lower cylinder Reynolds numbers and found similar results for a non-isothermal case.

Beckmann et al. [397] evaluated the influence of thermophoresis on the overall deposition rate using an isothermal plug flow reactor and a comprehensive and detailed CFD model. The CFD model included the effect of thermophoresis by using the model of Talbot et al. [237]. Predicted ash arrival rate on a cooled probe increased depending on the port in the test rig between 7 and 50%. The authors underline the important effect of temperature and the need for an accurate sticking criterion. A similar study was presented recently by Yang et al. [304], who used 2D CFD simulations in order to predict the deposit growth including thermophoresis using again the Talbot model. During early stages, thermophoresis increased the impaction efficiency from 0.02 to around 0.03. This effect diminished with increasing probe surface temperature and time. The authors found that ash deposition is dictated by inertial impaction and the stickiness of particles [304].

A different conclusion concerning thermophoresis was presented by Sinquefield [244]. He studied the role of different deposition mechanisms using the Multifuel Combustor at Sandia National Laboratories. Conditions from black liquor recovery boilers were mimicked using sub-micron and micrometer-sized particles together with a dynamic monitoring system for deposit growth rates. Results showed a linear deposit growth accompanied by a highly non-linear temperature increase, ruling out thermophoresis since temperature difference became smaller once the layer thickness increased. Sinquefield [244] showed that the rate remained constant even though the temperature difference dropped significantly, concluding that thermophoresis is not the rate-controlling mechanism. However, as the initial probe temperature was varied, deposition rate changed, indicating some sort of thermal effect. The author instead postulates an inertially-dependent mechanisms based on deposit morphology. Morphology of sub-micron deposits are dendritic with over 90% voidage. Particles are found to have a high sticking efficiency and do not roll or settle subsequent to impaction in the porous structure [244].

Thermophoresis is a temperature-driven effect, whose relevance during slagging and fouling is not clear yet. At early stages of deposit build-up, it may play an important role, however, detailed validation studies using CFD in order to explain experimental observations are rare in literature. Additionally, the effect of deposit structure is often neglected, mainly due to its complexity. Furthermore, uncertainty due to different correlations is high.

2.5.3. Condensation

The condensation of inorganic vapors occurs during cooling, when the flue gas is supersaturated and gas temperature falls beneath the vapor dew point. A fluid is saturated when the vapor pressure of the condensing species equals the saturation pressure of the same species. Condensation on a surface (fly ash particle or heat exchanger) is referred to as heterogeneous condensation. A direct particle formation in the gas-phase is called homogeneous nucleation; see also the work of Wieland [174]. In the case of a clean tube, condensation leads to the formation of a thin, sticky film, which might change the pick-up of other solids [15]. Further condensation effects can occur on fly ash particles or on existing deposits. The amount and chemical composition of inorganic vapors strongly depends on flue gas temperatures, and the fuel itself. In the superheater region with gas temperature around 800–1200 °C, these inorganic vapors are primarily compounds of alkali metals [15,102,212]:

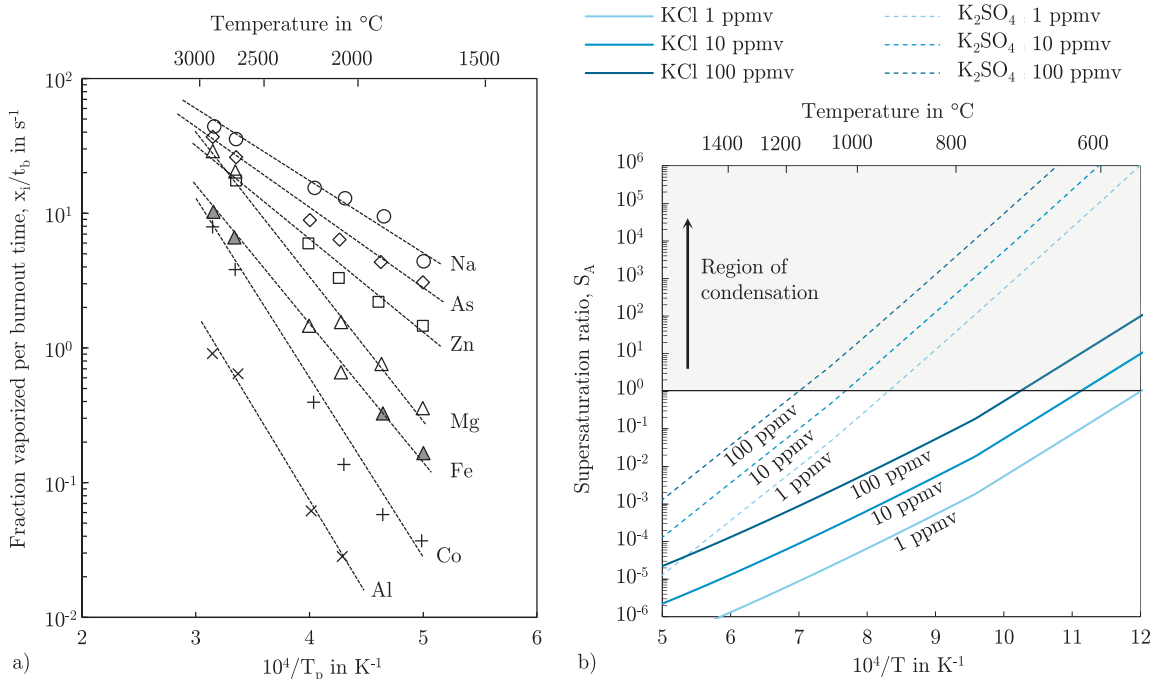

Fig. 29. (a) Inorganic element vaporization fraction x_i per unit burnout time t_b for a Montana lignite (original data from Mims et al. [250], data extracted from Sarofim and Helble [70]) and (b) supersaturation ratio as a function of temperature, for different alkali vapors (reprinted with permission from Kleinhans et al. [212]. Copyright 2016 American Chemical Society.).

- alkali chlorides (KCl, NaCl),
- alkali sulfates (K_2SO_4, Na_2SO_4),
- alkali carbonates (K_2CO_3, Na_2CO_3),
- alkali hydroxides (KOH, NaOH), and
- heavy metals and their compounds (Zn, Pb, $ZnCl_2$, etc.).

The vapors listed above are predominantly formed by chemical reactions in the gas phase [212], and depend on the vaporization and release of inorganics in the fuel as discussed by Fig. 4, which gives estimates on elements, which can be vaporized and their quantity. Fig. 29(a) shows the inorganic element vaporization fraction per unit burnout time for a Montana lignite. This study was conducted by Mims et al. [250] and shows that only a small amount of inorganic vapors forms at combustion temperatures of 1300–1500 °C. The fraction vaporized x_i divided by the burnout time t_b is shown as a function of temperature [70]. At $T = 2000$ K, the value x_i/t_b yields 5 for Na, implying that around 10% of the sodium in the lignite will vaporize during a burnout time of $t_b = 2$ s. The amount might be even lower for higher-rank coals [57]. On the other hand, condensation is important for fuels with high alkali metal contents, such as biomass. Dayton et al. [251] used a high-temperature reactor coupled with a mass spectrometer, in order to study the release of alkali and chlorine species during switchgrass combustion. Their findings suggest that potassium release mainly occurs during char conversion, with a slight overlap with devolatilization. Chlorine is released as HCl during devolatilization. Adding steam reduced the amount of KCl, and increased the release of KOH [251]. Heterogeneous condensation requires the presence of inorganic vapors at the heat exchanging surface. For typical clean superheater tubes, the flow around the cylinder is in the range of Reynolds number of 500–5000. At these numbers, the boundary layer is laminar, and vapor transport is driven by Ficks' first law of diffusion:

$$j_A = -D_{AB} \nabla c_A, \tag{25}$$

where j_A is the diffusive flux in mol/(m^2 s), D_{AB} is the molecular diffusion coefficient of species "A" in species "B", and ∇c_A is the concentration gradient in all spatial directions (e.g. $\partial c_A/\partial x$). A correlation for the diffusion coefficient of gaseous salts in nitrogen can be found in the work of Wilke and Lee [252] or [212]. Tomeczek and Wacławiak [253] use mass transfer laws, and give the following equation in order to calculate the mass flux of species "A" to the wall:

$$\dot{m}_A = \rho_g \cdot \beta_A \cdot \frac{p_A - p_{sat,A}}{p}, \tag{26}$$

where β_A is the mass transfer coefficient, p_A the partial pressure, $p_{sat,A}$ is the saturation pressure (or vapor pressure) of species "A", and p the total pressure. The mass transfer coefficient β, often also defined as k, can be calculated by the following expression:

$$\beta_A = Sh \cdot \frac{D_{AB}}{D}, \tag{27}$$

where Sh is the Sherwood number being a function of the Reynolds number (Re) and Schmidt number (Sc). The parameter D, is the diameter of a heat exchanger tube. An empirical correlation for the Sherwood number of a tube in a cross-flow, is given by:

$$Sh = c \cdot Re^m \cdot Sc^n \cdot (Sc/Sc_W)^{0.2}, \tag{28}$$

where the coefficients c, m and n are dependent on the flow characteristics, and thus on the Reynolds number. Analogous equation for a spherical ash particle can be found in the literature (see Baehr and Stephan [254]). The last term in Eq. (28) is a correction for differences in the Schmidt number of the free-stream Sc and of the wall Sc_W, where the Schmidt number is defined as the ratio of momentum- to mass-transport: $Sc = \nu_g/D_{AB} = \mu_g/(\rho_g \cdot D_{AB})$ [212]. An important quantity is the saturation pressure $p_{sat,A}$, e.g. needed in Eq. (26). It is a function of gas temperature and concentration of species "A". Typically, it is calculated using the Antoine equation:

$$log_{10}\, p_{sat,A} = A - \frac{B}{C + T}, \tag{29}$$

where A, B, and C are fitting coefficients, and T is the temperature in °C (e.g. given in [212,255]). Another option for the calculation of the saturation pressure is by using thermodynamic equilibrium calculations. A useful number for the estimation of condensation is the supersaturation ratio S_A of the gas phase with species "A". It

can be predicted by the following expression:

$$S_A = \frac{p_A}{p_{sat,A}(T)}. \quad (30)$$

At high supersaturation ratios $S_A \gg 1$, homogenous condensation is likely to occur, whereas at $S_A = 1$ the system is in equilibrium, as it is shown in Fig. 29(b). Homogeneous condensation (particle nucleation) starts at a gas temperature of $T_g = 1000\,°C$ and $S_A > 5$ for alkali species [171,172,174]. Thus, ash deposition due to heterogeneous condensation is expected to play a key role in the range of $1 < S_A < 5$ [212]. Fig. 29(b) shows, that depending on the vapor concentration, K_2SO_4 starts to condensate at relatively high temperatures of 950–1200 °C. Thus, it will most likely occur on fly ash particles in the superheater region or within boundary layers of heat exchangers. Alkali chlorides (KCl) supersaturate at lower temperatures and hence, they are likely to condense directly on the tube. Experimental studies on inorganic vapor deposition on surfaces are reviewed in the work of Haselsteiner [256]. There are only few studies present dealing with heterogeneous condensation such as the one by Nielsen et al. [257], Akbar et al. [258], Lindberg et al. [203] or Yang et al. [304]. An important characteristic is the metal vapor dew point. Below this point, condensation effects, e.g. of inorganic vapors in the boundary layer of a tube, lead to sub-micron particles enhancing deposit built-up. Is an inorganic vapor above its dew point, chemical reactions can take place, either with other gases or with solids, e.g. ash particles or deposits. These reactions can then change the melting temperature or lead to a sticky surface, enhancing again ash deposition rates.

2.5.4. Chemical reactions

Heterogeneous chemical reactions can occur between gas phase species and deposited mass or ash particles. Often alkali metal vapors are dominating inorganic reactions, e.g. on particles or boiler walls. Couch [15] states that chemical reactions can determine whether a particles sticks and deposit starts to grow. The most important chemical reactions reported in literature are [15,259]:

- formation of low temperature eutectics from the interaction of Fe, Na, Ca, Al, and Si,
- sulfation,
- alkali absorption,
- carbonation, and
- oxidation or reduction.

Strictly, the first point is not a chemical reaction, however, it is strongly influenced by reaction and diffusion processes. Sulfation typically occurs for compounds of Na and K, Ca, Mg or Zn with reactions being:

$$2MCl + SO_3 + H_2O \rightleftharpoons M_2SO_4 + 2HCl \quad (31)$$

$$2MCl + SO_3 + 1/2O_2 \rightleftharpoons M_2SO_4 + Cl_2 \quad (32)$$

In Eqs. (31) and (32) "M" stands for instance for alkali metals Na or K. Both reactions can also proceed with SO_2, instead of SO_3. However, sulfation is reported to be orders of magnitude faster with SO_3 [260]. Both reactions can either occur as a gas phase reaction, or as gas-solid reaction [257]. Furthermore, Eqs. (31) and (32) release chlorine species, which can then attack the metal surface and lead to corrosion, dependent on the metal temperature [175]. The chemical absorption of alkali species in the deposit is mainly attributed to aluminosilicates (such as kaolinite), and their ability to absorb alkali sulphates, or, alkali chlorides [48,49,261,262]:

$$Al_2O_3 \cdot 2SiO_2 + M_2SO_4 + 2H_2O \rightarrow M_2O \cdot Al_2O_3 \cdot 2SiO_2 + SO_3 + 2H_2O \quad (33)$$

$$Al_2O_3 \cdot 2SiO_2 + 2MCl + 2H_2O \rightarrow M_2O \cdot Al_2O_3 \cdot 2SiO_2 + 2HCl + H_2O \quad (34)$$

This absorption process leads to a formation of low-melting silicates. The transformations can include sintering and strongly affect physical properties of the deposit, depending on the temperature [15]. The reaction rate is slow for the absorption process, compared with sulfation. However, the absorption of alkali metal vapors above their dew point and at high temperatures, where condensation cannot occur, is known to be faster, in particular when aluminosilicates are molten. Lindner and Wall [263] claimed that sodium silicate formation is significantly higher in the case when NaOH reacts instead of NaCl. The reaction path is accordingly:

$$2MCl + 2H_2O \rightarrow 2MOH + 2HCl \quad (35)$$

$$Al_2O_3 \cdot 2SiO_2 + 2MOH \rightarrow M_2O \cdot Al_2O_3 \cdot 2SiO_2 + H_2O \quad (36)$$

Hydroxides are mainly stable at high temperatures and in systems with low concentrations of sulfur, e.g. when firing biomass. At lower temperatures, chlorides become stable, and even further down the temperature axis carbonates may show up. It is easier to capture hydroxides since their chemistry fits better into the alumina-silicate 3D structure, compared with relatively large chloride molecules. Sulfur has the effect to rise the dew point by forming sulfates that condense [49]. It is concluded that sulfur lowers the time available for reaction between alkali vapors and aluminosilicates, and consequently, the amount of alkali metals scavenged [48]. Fagerström et al. [46] showed that the number of aerosols in the range of 0.05–1 μm is reduced by more than 70% when co-firing peat with straw. In particular the amount of alkali chlorides decreases leading to less corrosive deposits. High temperatures in the flame can have two effects. On the one hand, vaporization rates increase leading to a higher concentration of inorganic vapors. On the other hand, the absorption of alkali metals in aluminosilicates is much faster at higher temperatures, and thus, it can lead to a decrease in aerosol concentration. Another aspect of chemical reactions is the deposition of unburnt carbon. Typically, this value is below 2 wt.% in fouled deposits, and no unburnt carbon is found in slagging deposits [15]. Unburnt carbon can lead to further reactions and reducing conditions, accompanied with heat and gas release inside deposits. All chemical reactions are a function of temperature, which can vary strongly within deposits as shown later on in Fig. 32.

2.5.5. Further transport mechanisms

There are further transport mechanisms reported in the literature with mostly unknown relevance for slagging and fouling. These mechanisms lead to forces on fly ash particles, change the impaction efficiency, and can therefore influence the deposition process. An often mentioned but rarely addressed transport mechanism is the so-called "eddy impaction". Turbulent eddies in the vicinity of heat exchanging surfaces can accelerate small particles, which are then able to leave the eddy due to their inertia and penetrate the boundary layer. This effect might be important for the wake of a superheater tube (lee side of the cylinder), however, it is only relevant for smaller particles. A further force on particles is induced by "Brownian motion" of molecules affecting the movement of, again, only small particles. Saffman [208] proposed a force induced by shear stresses. It is often referred to as the Saffman lift force and should be included in regions with high shear stresses such as in the vicinity of walls. This force can enhance the deposition velocity of particles, and for deposition calculation a modified expression should be used including effects of the proximity of a wall [216]. The sign of the Saffman lift force depends on the direction of the slip velocity perpendicular to the wall.

Electrophoresis is a force on dispersed particles in an electric field. The force is given by $F_{El} = q \cdot E$, where q stands for the total charge of a particle. In addition, in the presence of a charged wall, particles can experience an electrostatic force [216]. Guha [216]

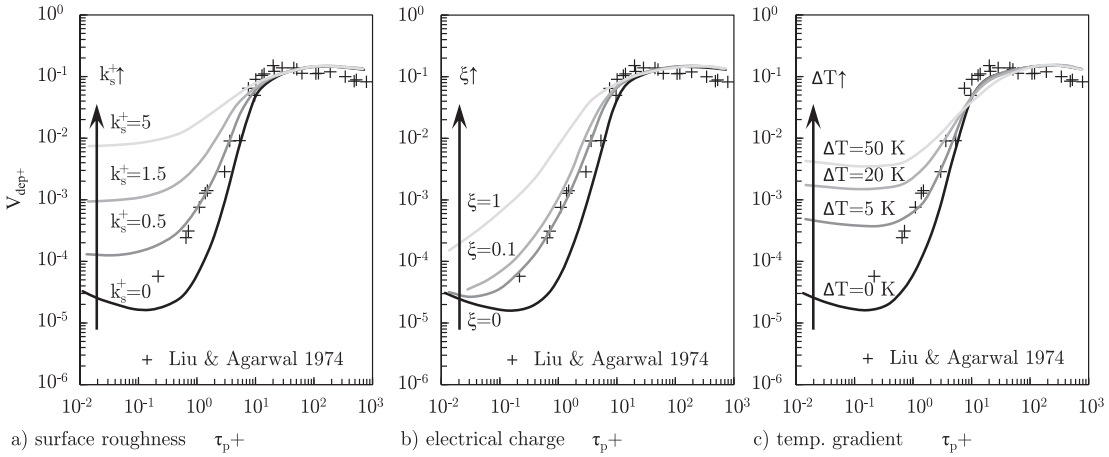

Fig. 30. Impact of surface roughness, particle electrical charge, and gas phase temperature gradient on dimensionless deposition velocity (data from Guha [216]).

uses the parameter ξ to relate the charge of a particle q_p to the maximum possible charge $q_{p,max}$ ($q_p = \xi \cdot q_{p,max}$). Since a furnace has no significant electric fields, this is only of importance for electrostatic precipitators.

Guha [216] further calculates the impact of different effects on the dimensionless deposition velocity, given in Eq. (5). The main influences affecting the particle impaction are:

- a temperature gradient in the boundary layer ∇T, referred to as thermophoresis,
- the surface roughness of the substrate k_s^+, and
- an electrical charge of particles ξ referred to as electrophoresis.

Guha [216], solves a particle continuity equation for a fully developed flow in a turbulent duct in order to study the impact of each mentioned effect. Fig. 30 shows the results of his studies. A detailed description of the approach can be found in his works [216,264]. It can be concluded that all three effects have a considerable influence for small particle relaxation times, and thus, small particles. Increasing the surface roughness height k_s^+, leads to a strong increase in the dimensionless deposition velocity (Fig. 30(a)). The value increases by up to three orders of magnitude leading to deposits of fine particles. This is a crucial parameter since a clean and smooth superheater tube only exists at the commissioning of a power plant. After a short period of operation, surfaces collect small particles due to thermophoresis or heterogeneous condensation, and, form dentritic structures. The impact of different electrical charges ξ of particles is shown in Fig. 30 (b). The deposition velocity is again increased, but not as pronounced as by the surface roughness. The maximum electrical charge $\xi = 1$ leads to an increase in dimensionless deposition velocity of one up to two orders of magnitude for small particles. The effect of temperature difference between the gas and the wall is shown in Fig. 30(c). A similar effect compared to the surface roughness can be observed. A slight temperature increase of $\Delta T = 5$ K leads to a 25 times higher deposition velocity due to thermophoresis (see Section 2.5.2).

2.5.6. Mechanisms removing deposits

Besides mechanisms leading to deposit formation, deposit removal is a phenomenon which is often observed. The main mechanisms leading to removal, according to a review of Zbogar et al. [265], are:

- shedding of deposits due to thermal shock, mechanical stresses or gravity,
- erosion caused by sharp, angular, unmolten particles, or
- melting and drip off.

Shedding of deposits can be caused by various mechanisms such as gravity, thermally- or mechanically-induced tensions. Thermal tension can be the result of combustion fluctuations, load changes or soot blowing. Mechanically-induced tensions are typically due to soot blowing or mechanical fluctuations, such as vibrations [265,266]. Soot blowers and water cannons use pressurized steam or water and spray it on heat exchanging surfaces in order to cause stresses in the deposit and clean the boiler wall. Fig. 31 shows the effect of soot blowing on steam generation. However, the efficiency of soot blowing strongly depends on the deposit structure, its chemistry, age and location in the boiler. A classification of deposits and the influence of removal mechanisms on deposit types is given in Table 6. Erosion is the process when sharp unmolten particles collide with non-sticky areas on a deposit surface [265]. Typically, in coal-fired boilers, these are quartz particles with relatively high melting points. Erosion, as a gradual removal of material, can be divided into deformation and cutting actions. Deformation is relevant for brittle materials and caused by the normal velocity component of incoming particles, whereas cutting actions are related to the tangential velocity component, and most relevant for ductile surfaces. Raask [12] differentiates between erosion of abrasive, hard, and angular quartz particles, which cause erosion by cutting, and glass particles leading to surface deformation and brittle failure. Main parameters influencing erosion are particle hardness, shape, diameter, impact velocity, and angle of impaction. Table 6 shows that erosion is dominant for the removal of dry, powdery deposits, whereas molten slags are not affected by erosion effects. Gravity shedding is caused by gravitational forces due to the deposit weight, which lead to a break down and/or fracture in the structure [265]. The gravitational force can exceed forces in the bonding of the deposit, or the interface of deposit and steel surface. Large deposits are reported to fall into the ash hopper, causing damage to the tubes. This effect is most relevant for powdery or lightly sintered deposits. Gravity is also causing the removal of molten slags. A thermal shock leads to fracture due to different thermal expansion coefficients of the deposit and the tube material. A sudden shrinkage caused by cooling (e.g. by soot blowing) leads to thermal stresses and failure inside the deposit [265]. This mechanism is more pronounced for sintered deposits, with higher thermal conductivities and lowered porosity values. Removal mechanisms are manifold and dependent on many characteristics, such as deposit strength and structure, cleaning devices inside the boiler, chemical composition and particle characteristics. It is therefore not surprising that modeling of deposit removal is challenging and rare in literature.

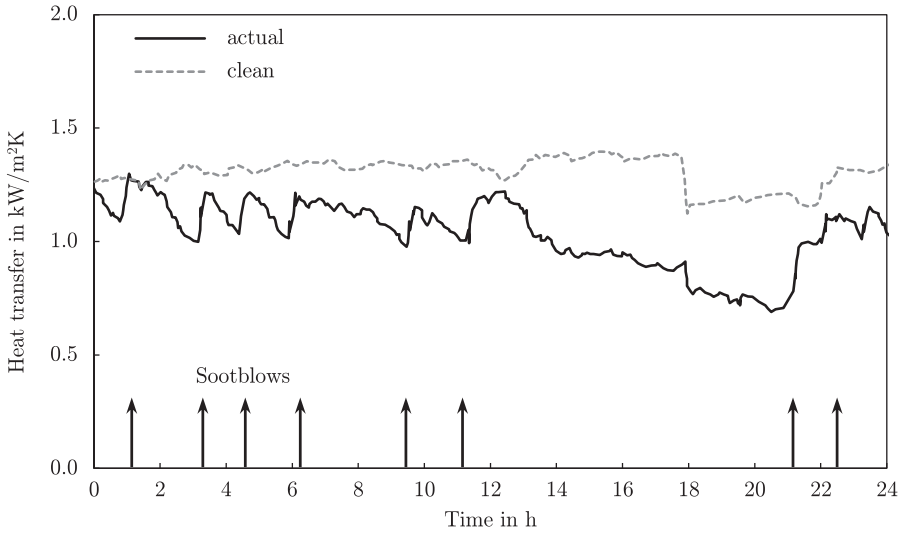

Fig. 31. Heat transfer characteristics over time for a radiant superheater (taken from Wynnyckyj et al. [272]).

2.6. Deposit growth and effects on heat transfer

Deposit formation is strongly dependent on process conditions inside the boiler and fly ash characteristics, i.e. chemical composition and size distribution, as discussed in the previous section. Main process parameters influencing the extent of slagging (superheater region with molten or partially molten ash particles) and fouling (low temperature region such as economizer with lower flue gas velocities and solid ash particles) are the flue gas temperature, velocity, and composition (reducing or oxidizing environment). Slagged or fouled heat exchanging surfaces lower the heat transfer rate to the water-steam cycle and thus reduce the boiler efficiency and significantly affect the operability. Van Beek et al. [267,268] reported a reduced heat transfer coefficient of 25%, due to the formation of a powdery deposit in the economizer region (fouling layer). In this region, ash particle are solidified due to lowered temperatures; flue gas temperatures are typically between 400 and 600 °C, and steel tube temperatures around 300 °C. During early stages of deposit formation (clean tube), only sub-micron particles can deposit, since their velocity is low enough. Large particles will rebound and possible erode loosely-bound particles [268]. This is confirmed by study of Steadman et al. [269], who observed a thin 10-100 μm thick layer, composed of sub-micron particles. At later stages, once the surface roughens and may sinter together, larger particles in the size range of 1-10 μm are reported to deposit and stick [268,270].

The main reason for deteriorated heat transfer is the low thermal conductivity of ash deposits. A deposit layer has a relatively low thermal conductivity ($0.2 < k_{deposit} < 3$ $Wm^{-1}K^{-1}$), compared to steel tubes ($15 < k_{steel} < 57$ $Wm^{-1}K^{-1}$), leading to a deteriorated heat transfer from the flue gas to the water-steam cycle. The thermal conductivity of steel depends on its composition. Austenitic steels (such as X8CrNiNb1613) show values around 15 $Wm^{-1}K^{-1}$, whereas ferritic steels (such as 10CrMo9) have higher values of 35 $Wm^{-1}K^{-1}$ at ambient temperature [271]. Wynnyckyj et al. [272] developed an integrated monitoring system in order to determine boiler performance and a cleaning strategy for heating surfaces by sootblowers. They applied a combination of thermocouples, heat flux meters and pyrometers. A furnace in Saskatchewan, Canada was used to install "dirty" and "clean" heat flux meters directly on the boiler wall. The clean heat flux meters were protected from slagging by purging air, whereas dirty ones were exposed to ash accumulation. Results for heat transfer over time are shown in Fig. 31. This figure clearly reveals a reduced heat transfer when an ash layer builds up. It shows that selective soot-blowing can increase heat transfer rates. This kind of monitoring system is often used to optimize soot-blowing in order to increase steam production, save steam from being used in soot-blowers, and hence, increase overall boiler efficiency.

The temperature profile of a fouled/slagged superheater tube is illustrated in Fig. 32. The curve shows a qualitative profile, and not computed or measured values. The steam temperature inside the superheater tube for typical PF systems is in the range of 400–650 °C depending on the boiler type and the materials used. The heat transfer coefficient at the inner tube wall (number "1" in Fig. 32) is relatively high in the range of $500 < h_{i,s} < 5\,000$ $Wm^{-2}K^{-1}$ for steam. Even higher values are typical for liquid water with $1\,000 < h_{i,w} < 10\,000$ $Wm^{-2}K^{-1}$ or a water-steam mixture with $15\,000 < h_{i,w/s} < 600\,000$ $Wm^{-2}K^{-1}$[35]. The outer heat transfer coefficient (number "4" in Fig. 32) depends on whether radiation is present or not, and is typically in the range of $30 < h_o < 100$ $Wm^{-2}K^{-1}$. Heat transfer in the radiant section is controlled by the heat flux and flame temperature, whereas the convective heat exchange is dominated by the temperature difference between the flue gas and the water-steam-cycle. In the case of radiative heat exchangers, this implies a lowered heat transfer coefficient through deposits. The temperature profile is shifted downstream and furnace exit temperature increases. A mathematical description of the heat flux $\dot{Q}$ from the flue gas to the water-steam cycle is given in Eq. (37):

$$\dot{Q} = \frac{T_\infty - T_{w/s}}{R_{tot}}, \tag{37}$$

Table 6
Deposit removal mechanisms and their influence on different deposit types (taken from Zbogar et al. [265], originally from Stitt et al. [266]).

Mechanism	Deposit type			
	Powdery	Lightly sintered	Heavily sintered	Liquid slag
Erosion	++	+	–	–
Gravity shedding	++	+	–	–
Mechanical shock	++	++	+	–
Thermal shock	–	+	++	–
Melting (i.e. flow of liquid slag)	–	–	–	++

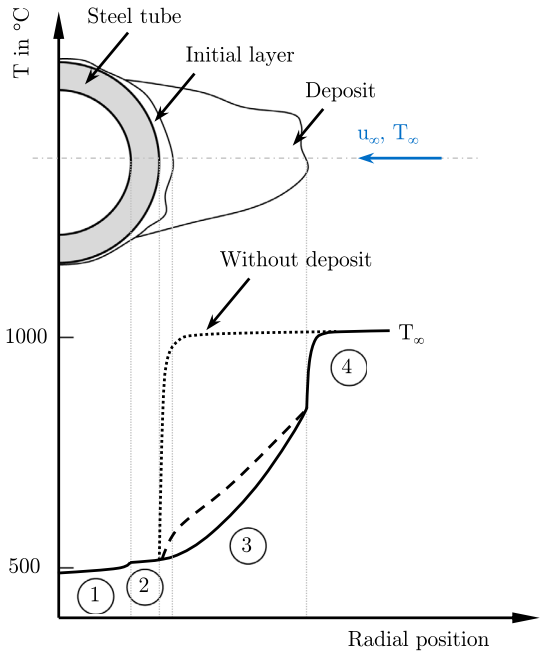

Fig. 32. Qualitative temperature profile from the water-steam-cycle to the flue gas.

where $T_\infty = T_{FG}$ and $T_{w/s}$ stand for the flue gas and water/steam temperature, and R_{tot} is the total thermal resistance. The calculation of the thermal resistance for a tube, is given by:

$$R_{tot} = \frac{1}{A_o}\left(\frac{r_o}{r_i \cdot h_{i,c}} + \sum \frac{r_{j,o}}{k_j} \cdot ln\left(\frac{r_{j,o}}{r_{j,i}}\right) + \frac{1}{h_{o,c} + h_{o,r}}\right), \tag{38}$$

where A is the surface area of the heat exchanger, $h_{i,c}$ is the heat transfer coefficient at the tube inner surface due to convection, r_i and r_o stand for the inner and outer tube radius, $r_{j,i}$ and $r_{j,o}$ for the inner and outer deposit layer thickness of the material j, k_j is the thermal conductivity of the material j, and $h_{o,c}$ and $h_{o,r}$ are the heat transfer coefficient at the outer surface due to convection (index "c") and radiation (index "r"). The sum of the thermal resistance due to conduction $\sum r_{j,o}/k_j \cdot \ln(r_{j,o}/r_{j,i})$ typically includes the heat transfer through the inner and outer steel oxide layer, the conduction through the steel itself and the deposit including an initial layer. The initial layer is often composed of condensed inorganic elements and/or fine particles. It can have a dry and powdery nature, and therefore, a high porosity. If it is composed of condensed inorganic vapors, it is often sticky. Couch [15] describes different mechanisms being responsible for the initial layer formation:

- surface attraction between fine ash and the tube,
- local eddies in finger-like/dendritic structures,
- inherent tube roughness due to oxide layer formation,
- liquid phases on the tube surface,
- thermophoresis, and
- diffusion and condensation of inorganic vapors.

The initial layer is followed by a porous layer formed by large fly ash particles. The conduction through this porous material exhibits the highest resistance and thus limits heat transfer. This can be observed by the slope in region "3" in Fig. 32. However, high uncertainties exist for the effective thermal heat conductivity in the inner layers [273]. Deposit porosity, chemistry and temperature strongly influence thermal conductivity (see Section 3.9). During deposit growth, larger particles are able to stick leading to irregular surfaces structures. As the layer grows and consolidates, the surface temperature increases towards that of local gases [15,274]. The temperature gradient inside a deposit at its outer surface can reach values in the region of 30–100 °C/mm, depending on its thermal conductivity and the local heat flux [275]. Furthermore, during operation, the temperature gradient can exceed 200 °C/min [276]. Hence, knowing the surface temperature when predicting the particle sticking behavior can be challenging. Wibberley [275] lists four requirements for deposit formation [15]:

- inorganic vapors and/or fly ash particles are able to penetrate the boundary layer of the tube or wall and get in contact,
- material adheres to the surface,
- sufficient cohesion which prevents material from detaching as a result of local turbulence, temperature changes, vibration or gravity, and
- thermal and chemical compatibility of the steel surface and the depositing material.

Fig. 33(a) illustrates the process of heat transfer from the hot flue gas to the boiler wall and the water-steam cycle. Heat is transferred by radiation and convection to the deposit surface and conducted through the deposit and the steel tube. The deposit radiation properties change during growth and thus heat transfer rates change [273]. Using a heat balance, one can obtain Eq. (39). Heat conduction is equal to the energy transferred to the deposit surface due to

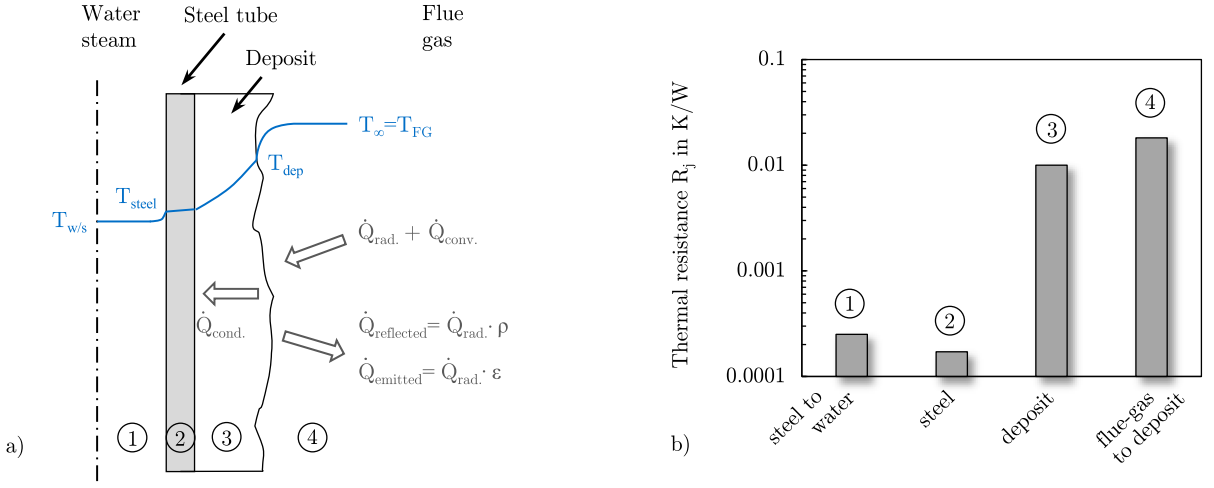

Fig. 33. Effect of deposit on heat transfer: (a) heat transfer to and through ash deposits (modified from Zbogar et al. [273]) and (b) calculated thermal resistances for a flat wall analogous to Eq. (38) with $A_o = 1\ m^2$.

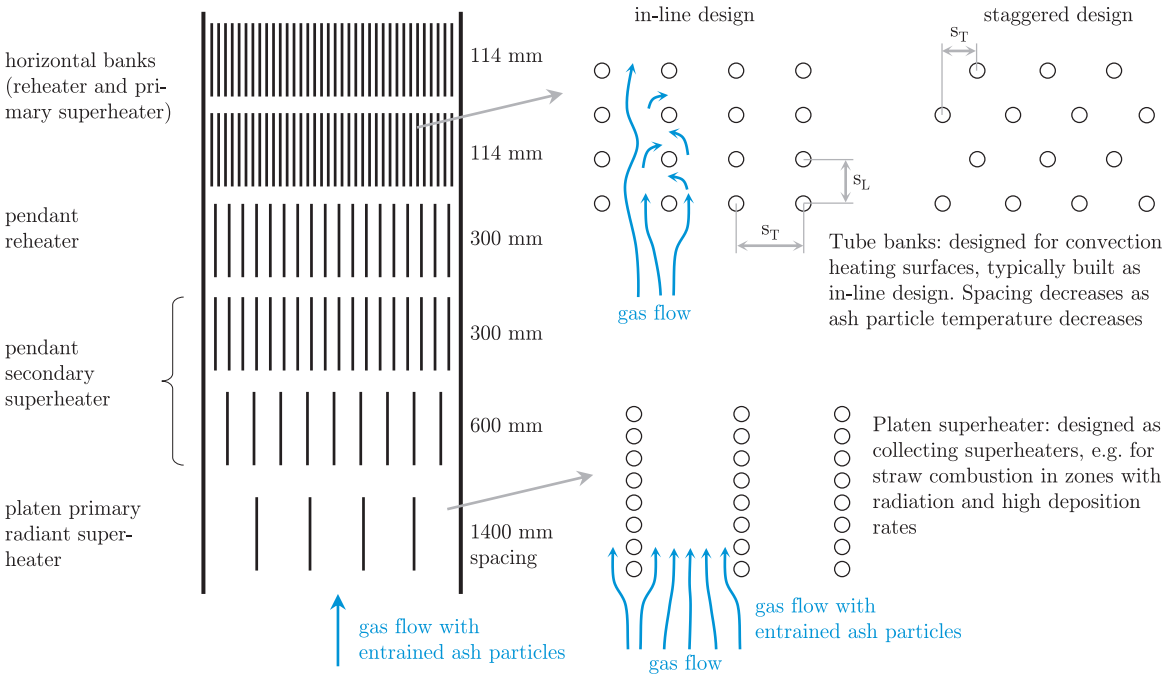

Fig. 34. Tube arrangement in solid fuel fired boilers (adopted and extended from Couch [15]).

convection and radiation by accounting for reflected and emitted heat.

$$\dot{Q}_{conduction} = \dot{Q}_{convection} + \dot{Q}_{radiation} - \dot{Q}_{reflected} - \dot{Q}_{emitted} \tag{39}$$

Zbogar et al. [273] rewrite Eq. (39) with a flame emissivity equal to unity (valid for a large boiler) and assuming that heat conduction through the tube wall and the steam film is negligible. The following expressing can be obtained for a cylindrical geometry:

$$\dot{Q}_{cond} = \frac{T_{dep,o} - T_{steel,i}}{\frac{r_{dep,o}}{\pi \cdot k_{dep}} \cdot ln\frac{r_{dep,o}}{r_{steel,i}}} = h_{conv} \cdot (T_\infty - T_{dep,o}) + \alpha_{dep} \cdot \sigma \cdot T_\infty^4 - \varepsilon_{dep} \cdot \sigma \cdot T_{dep,o}^4, \tag{40}$$

where $T_{dep,o}$ and $T_{steel,i}$ are the deposit outer surface and steel tube inner surface temperatures, k_{dep} is the deposit thermal conductivity, α_{dep} the absorption coefficient of the deposit layer, σ the Boltzmann constant, and ε_{dep} the deposit emissivity. Calculated thermal resistances for a plane boiler wall normalized to $A = 1m^2$ are illustrated in Fig. 33(b). The highest thermal resistance is due to heat transfer from the flue gas to the deposit (number 4) and through the ash layer (number 3). Heat conduction through the initial layer shows a relatively low value, due to the small layer thickness, and is comparable to the resistance caused by the steel tube. The thermal resistance due to convection on the water side strongly depends on the flow characteristics in the tubes and is low compared to the resistance of the deposit and the flue gas.

Deposit formation depends on the flow characteristics, ash particle chemistry, size and temperatures as well as the plant design. Typical tube arrangements that can be found in boilers are shown in Fig. 34. Commonly, the first superheater is designed as a platen array of tubes with wide traversal pitch s_T, ranging up to more than one meter (s_T/D = 5-35), and a small longitudinal pitch s_L (s_L/D = 1.2), where D stands again for the outer tube diameter [15,253]. This wide spacing in traversal direction is necessary in order to prevent blockage caused by ash deposition. As flue gas temperatures cool down, and thus, the threat of particle sticking decreases, the spacing can be reduced leading to an increase in heat transfer surface per unit volume. Typical values for the convective section are $s_T/D = 1.5$ for the traversal and $s_L/D = 2$ for the longitudinal pitch, respectively.

Predictions of deposit formation and growth over time are illustrated in Fig. 35(a) and (b). Wagoner and Yan [278] predicted changing deposit shape for different tube diameters, flue gas velocities, particle diameters and densities, by considering inertial impaction. The model predicts an increase in deposit layer thickness, when tube diameter decreases, and, flue gas velocity, particle diameter or density increases. The model reveals a high sensitivity towards particle diameter and velocity, and thus the particle kinetic energy. However, the deposit formation is highly over predicted. The layer formed within six hours at a tube temperature of 593 °C indicating a missing sticking criterion. Tomeczek and Wacławiak [253] conducted two-dimensional CFD simulations for different tube longitudinal pitches and particle sizes. The free-stream flue gas velocity is set to $u_\infty = 8.36$ m/s. Their study shows the influence of particle size in particular on the cylinder rear. In general, the deposit formation on the cylinder front is considerably higher compared with the cylinder rear, which agrees with observations from power stations.

The formation of ash deposits on superheater tubes and water walls is illustrated in Fig. 36. The surface temperature of a clean superheater tube, e.g. at the commissioning of a power plant, is around 0.5–10 K higher than the water-steam temperature and thus significantly lower than flue gas temperatures. Ash particles impacting on the cold surface solidify and rebound. The initial layer is formed by heterogeneous condensation [15] or the migration of small particles to the surface. Inorganic vapors cool down in the boundary layer, start to saturate, and condense either directly on the surface or to sub-micron particles which are then captured. The inner layer is rich in K/Na, S and Cl, while the outer layer is often more slag like, porous and rich in Ca, Si, Al, Fe and other elements depending strongly on what fuel is fired. The outer layer is often reported to be loosely bound and can be more easily removed by soot-blowing compared with the inner layer. This inner layer is typically white, composed of alkali- or earth alkali-compounds and tightly bound, as shown in Fig. 37(a) and (b). Fig. 37(b) shows a SEM image of a superheater deposit taken from a straw-fired grate, where the innermost layer was composed of a dense layer of K_2SO_4, followed by porous layer of KCl. The outer layer was similar to fly ash and sintered together. It is believed that the innermost layer is formed by deposition of KCl with subsequent sulphation [280].

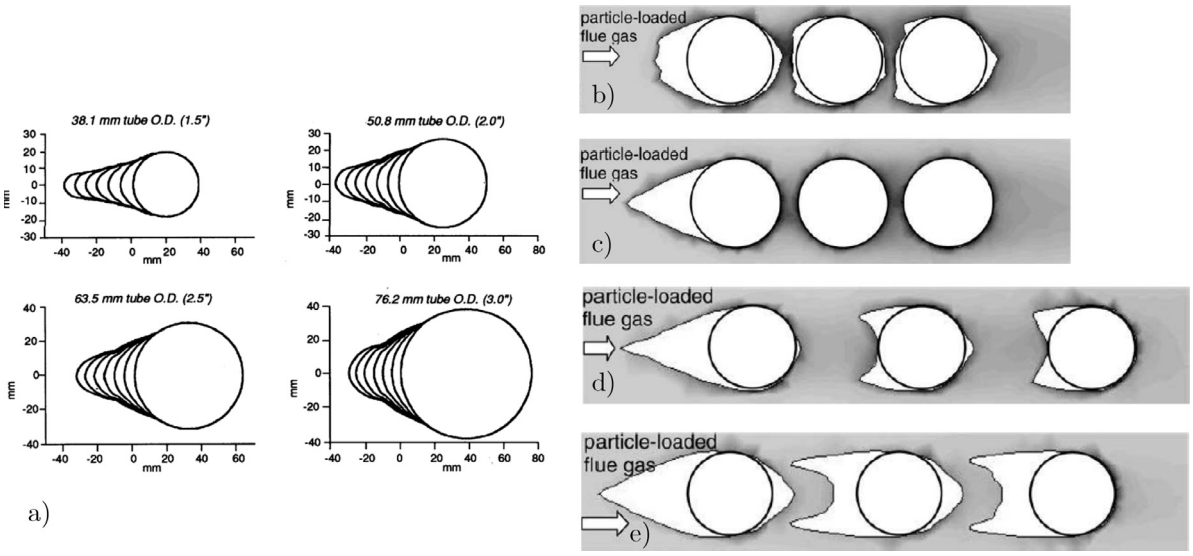

Fig. 35. Deposit built-up over time: (a) predictions from Wagoner and Yan [278] considering inertial impaction for a period of six hours and a gas velocity of 18.3 m/s, and (b) to e) CFD simulations of Tomeczek and Wacławiak [253] considering inertial impaction and condensation. Fig. (b) show predictions for a platen superheater after 9 month operation and $d_p = 1$ μm; Fig. (c) platen superheater after 5 month operation and $d_p = 33$ μm; Fig. (d) and (e) show platen superheater with wider longitudinal pitch after 9 month and $d_p = 33$ and 50 μm, respectively.

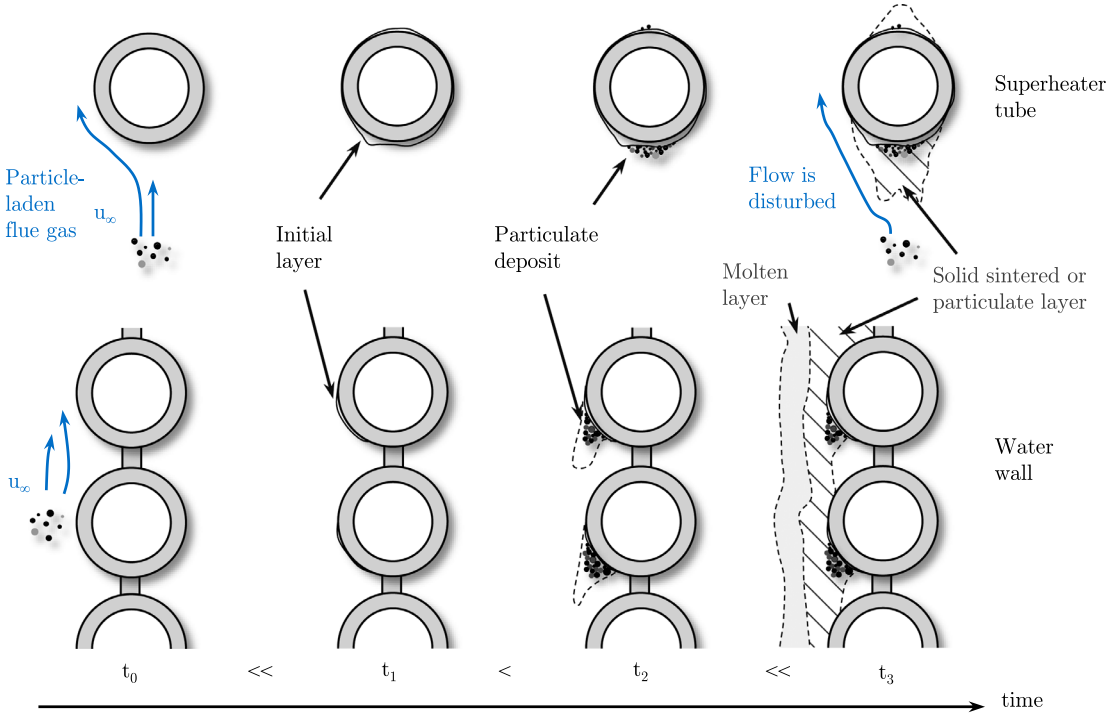

Fig. 36. Schematic of time-dependent deposit build-up for a superheater tube and the water wall (modified from Heap et al. [277], Couch [15], and Richter [222]).

However, if KCl deposits as a condensed aerosol or as a vapor is not completely understood. The exact role of aerosols during initial layer formation is unknown. Aerosols might act as glue and probably accelerate consolidation and chemical reactions. They fill up gaps and voids, and thus, increase contact area between particles. Jensen et al. [289] studied deposition rates in straw-fired grate boilers using a deposition probe simulating superheater coils. Results are shown in Fig. 38. An increase in aerosol concentration resulted in higher deposition rates. These findings were confirmed for two different boilers. Furthermore, their study revealed that the potassium content in the raw fuel correlates well with deposition rates. Again a linear increase in deposition rate with increasing K-content in the fuel was found. Sinquefield [244] collected deposits using sub-micron particles simulating ash deposition in black liquor boilers. He found a dendritic structure composed of long chains and strings of particles growing radially outwards. The author reported sintering of particles in these chains, however there was little contact between different chains [244]. Kaufmann et al. [281] also showed the importance of aerosols during deposit formation, when firing herbaceous biomass. The authors found sub-micron particles in the deposit and explained their deposition due to thermophoresis. An overview on typical deposition rates for different fuels and firing

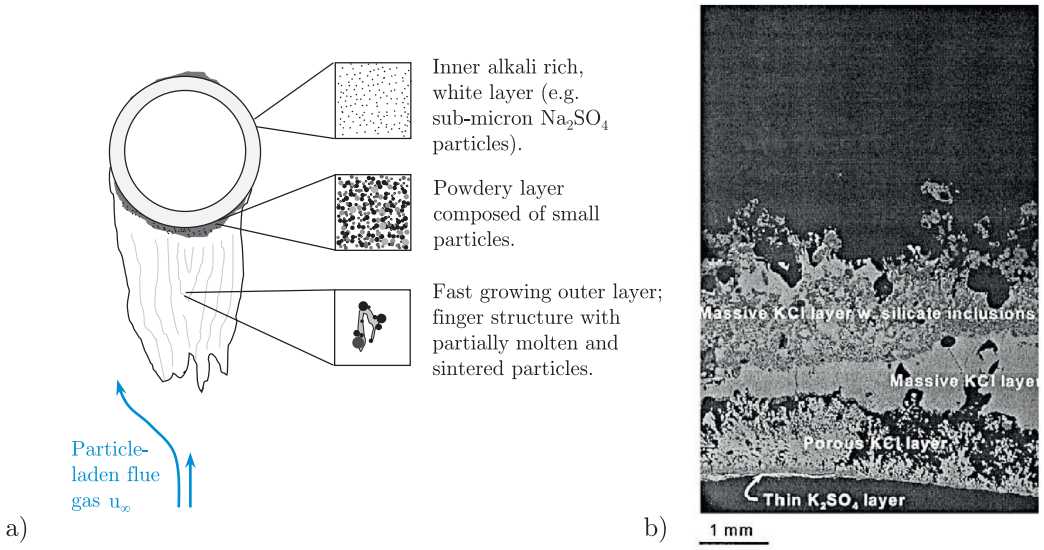

Fig. 37. Deposit structure and chemistry over time: (a) structure of a fouled deposit from low-rank coals (see also [263,279]), and (b) deposit collected in a straw fired boiler (image taken from Hansen et al. [280]).

systems can be found in Table 7. It can be seen that most experimental studies report values around 20–100 g/(m^2 · h). The deposition rate mainly depends on the flue gas temperature, as well as the fuel quality. Bashir et al. [284] showed that deposition rate was influenced by flue gas temperature and straw-share, while changes in probe surface temperature had no significant influence. This suggests that large particles are controlled by the gas temperature and are not affected by boundary layer effects. On the contrary, aerosol temperatures is not crucial assuming that these particles cool down in the boundary layer. Aerosol sticking seems to be independent of their temperature. However, confirmation for this behavior is needed. Weber et al. [287] reported a similar finding, where the deposition rate and thus the sticking efficiency strongly increased with increasing fly ash particle temperatures. Highest sticking efficiencies were found for a bituminous coal ash followed by sawdust and mixed wood, where lowest values are reported for low melting ashes from grain and fermentation residues. There was no relation between sticking efficiency and ash softening temperatures or calculated viscosity values found. A possible explanation could be an increased collection efficiency of a porous deposit - in the case of bituminous coal - compared with a molten layer - grain and

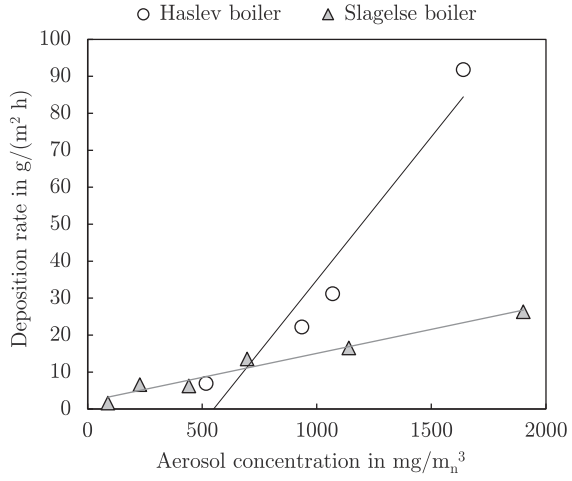

Fig. 38. Deposition rate on a probe mimicking a superheater tube as a function of aerosol concentration. Data from Jensen et al. [289] showing measurements conducted in two Danish straw-fired grates.

fermentation residues - as shown in Fig. 71(a) and discussed later on. Every incoming particle is captured in a porous layer, whereas when a molten layer exists, particles travel around this smooth surface. Kupka et al. [285] found increasing deposition rates with increasing co-firing shares of sewage sludge, when fired with a bituminous coal. This was caused by the low melting ashes of sewage sludge. A high deposition rate was reported when firing RDF [286]. A relatively high carbon content in the deposit might be caused by the condensation of tars. Much lower deposition rates are reported for the initial layer formation in a bituminous coal-fired boiler [188], probably due to low quantities of aerosols and alkali vapors. Furthermore, this table indicates that CFD studies are likely to over estimate deposition rates. The time required to form an initial layer is relatively long and can take several weeks. Condensation is particularly important for lignites and biomass with high shares of organically-bound inorganics. As the layer grows, the surface temperature increases and the formation of a liquid interface starts collecting ash particles. In the next step, larger ash particles start to adhere and form a powdery deposit. Again, the thicker the layer gets, the smaller is the temperature difference between the flue gas and the deposit surface. The deposit changes the flow around the tube and therefore the impaction process. Particle impaction on the water wall is shown in the lower part of Fig. 36. It is dependent on the configuration of the tubes, i.e. whether the tubing is vertical or in a meandering pattern. There are also publications reporting a deposit growth starting at the bridge in between tubes, due to increased surface temperatures at those locations [288]. Once the deposit layer grows, it can form a molten slag layer threatening boiler operation, as shown in the bottom right corner.

Fig. 39 shows a compilation of photographs taken from various power plants [288]. Typical areas affected by ash deposition are presented. Fig. 39 shows:

a) a partially slagged water-wall and the nose of a two-pass boiler. This section, introducing a change in the flow direction (boiler nose), is particularly in danger of ash deposition. Particles cannot follow the direction of the flow and impact on the surface.
b) a critical condition in a boiler. The cross-over path is partially blocked and only a small section is left for the flue gas to enter into the second pass. The flow accelerates, potentially leading to enhanced corrosion, erosion or deposition. Deposits in this

Table 7
Deposition rates reported in literature for different firing systems and fuels. Data collected from different studies comprising of CFD simulations and experiments. See also Bashir et al. [284] for a detailed report on straw-fired units.

Study	System –	Fuel –	Type –	Dep. rate g/(m^2 h)	T_{wall} °C	Location and findings –
Richter 2002 [222]	PF boiler	coal	sim.	up to 14000	n.a.	predictions for water wall
Pyykönnen and Jokiniemi 2003 [99]	recovery boiler	black liquor	sim.	300–540	480	dynamic built-up model
Kær et al. 2006 [360]	grate	straw	sim.	up to 150	520	different dep. mechanisms
Tomeczek and Wacławiak 2009 [253]	PF boiler	coal	sim.	7–72	527	convective superheater tube
	PF boiler	coal	sim.	18–180	527	radiative superheater tube
Schulze et al. 2010 [495]	pellet furnace	wood pellets	sim./exp.	up to 1	62	good agreement with measurem.
Kreutzkam 2014 [490]	PF boiler	bit. coal	sim.	100–430	450	predictions for water wall
Jensen et al. 1997 [289]	grate	straw	exp.	20–70	450	rate increases with K-content
Kaufmann et al. 2000 [281]	flow reactor	miscanthus	exp.	60[a]	400-450	dep. mechanisms studied
	flow reactor	herbage-grass	exp.	40[a]	400-450	
Lokare et al. 2006 [204]	flow reactor	sawdust	exp.	31%[b]	500	different biofuels tested
	flow reactor	straw	exp.	41%[b]	500	
Theis et al. 2006 [282]	EFR	peat	exp.	20	550	influence of co-firing rate examined
	EFR	bark	exp.	80	550	
	EFR	straw	exp.	160	550	
Tobiasen et al. 2007 [283]	PF boiler	straw	exp.	56	480	superheater region
	PF boiler	straw	exp.	41	500	superheater region
	PF boiler	straw & wood	exp.	33	500	superheater region
	PF boiler	wood	exp.	~1	500	after convective pass
Kupka et al. 2009 [285]	lab-scale comb.	coal	exp.	47	550–700	at port 3
	lab-scale comb.	coal-sew. sludge	exp.	77	550–700	co-firing with 95% coal
	lab-scale comb.	coal-sew. sludge	exp.	114	550–700	co-firing with 85% coal
Bashir et al. 2012 [284]	grate	straw	exp.	33–41	500	boiler measurements
Weber et al. 2015 [287],[c]	lab-scale comb.	mixed wood	exp.	193	1167	36.9-41%[d]; Ca, K, Si[e]
	lab-scale comb.	mixed wood	exp.	42	978	8.1-9.0%[d]; Ca, K, Si[e]
	lab-scale comb.	sawdust	exp.	54	1140	38.1-43.8%[d]; Ca, K, Mn[e]
	lab-scale comb.	ferm. residue	exp.	623	1115	26.8-30.9%[d]; K, P, Ca, Si[e]
	lab-scale comb.	ferm. residue	exp.	80	978	3.4-3.9%[d]; K, P, Ca, Si[e]
	lab-scale comb.	grain residue	exp.	464	1118	26.8-29.8%[d]; Si, K, P[e]
	lab-scale comb.	grain residue	exp.	124	975	7.1-7.9%[d]; Si, K, P[e]
	lab-scale comb.	bit. coal	exp.	118	1096	36.3-60.3%[d]; Si, Al, Ca, S[e]
	lab-scale comb.	bit. coal	exp.	192	1125	59.3-98.6%[d]; Si, Al, Ca, S[e]
Beckmann et al. 2016 [397]	lab-scale comb.	bit. coal	exp./sim.	60.3	600	steel probe
	lab-scale comb.	bit. coal	exp./sim.	37.4	1125	ceramic probe
Kleinhans 2017 [188]	EFR	bit. coal	exp./sim.	45-144	1200-1400	growth rate determined
Kleinhans 2017 [188]	PF boiler	bit. coal	exp.	~4[f]	700	initial layer deposition rate

EFR: entrained flow reactor, PF: pulverized fuel
[a] probe surface area estimated: $A = L \cdot A_{proj} = 0.012\text{m} \cdot 0.002\text{m} = 0.0024\text{m}^2$.
[b] sticking efficiency given in %. Note that authors using different terminology (sticking efficiency is capture efficiency).
[c] deposition rate calculated with projected probe area: $A = 0.0066\ \text{m}^2$.
[d] sticking efficiency.
[e] most abundant elements found in ash with decreasing quantity.
[f] estimated based on SEM images, layer thickness, composition and porosity.

region are not affected by the radiation of the flame, leading to porous, sintered structures.

c) a slagged superheater, with the danger of detachment and falling deposits. Deposits in the region of radiant superheater are fused and molten depending on layer thickness and temperatures. Normally, these are removed by sootblowers.

d) and e) show pictures through a boiler opening. Opposite walls are partly slagged. Removed deposits and large fly ash particles are collected in the ash hopper. The major issue at the furnace bottom is not the deposition itself, but associated with large fused deposits falling from higher up. There are reports of falling deposits damaging tube material at the furnace bottom leading to a power plant shut down. Furthermore, large deposits can block the ash hopper.

f) so-called burner eyebrows can form in the burner mouth. Recirculation zones from swirl burners can lead to particle accumulation around the burner mouth leading to changed aerodynamics.

3. Ash particle and deposit properties

Deposit and ash particle properties are crucial for estimating the sticking probability, predicting deposit formation or estimating the influence of deposits on boiler efficiency. Most important characteristics are the particle/deposit viscosity, chemical composition, porosity, surface tension, density or thermal conductivity. Therefore, the following subsections summarize deposit and ash particle characteristics and provide empirical correlations for their mathematical description and estimation.

3.1. Material strength

The material strength can be important for the rebound behavior of solid spheres on a heat exchanging surface [290]. Furthermore, it is known to be crucial for deposit shedding [265]. The material strength is usually governed by the yield stress Y, a quantity above which a material deforms irreversibly. Below this value, the material deforms elastically upon load, and once the load is removed, it retains its original shape. A typical material test yielding the stress-strain curve is the tensile test. The stress-strain curve for steel and a brittle material are illustrated in Fig. 40. The stress expressed as load per area (N/mm^2) is determined by measuring the force applied to a specimen. The strain is quantified by the change in length divided by the original specimen length. At a certain point, the strain-stress curve deviates form a proportional line, the so-called elastic limit. For ductile materials, e.g. structural steel, this point is determined

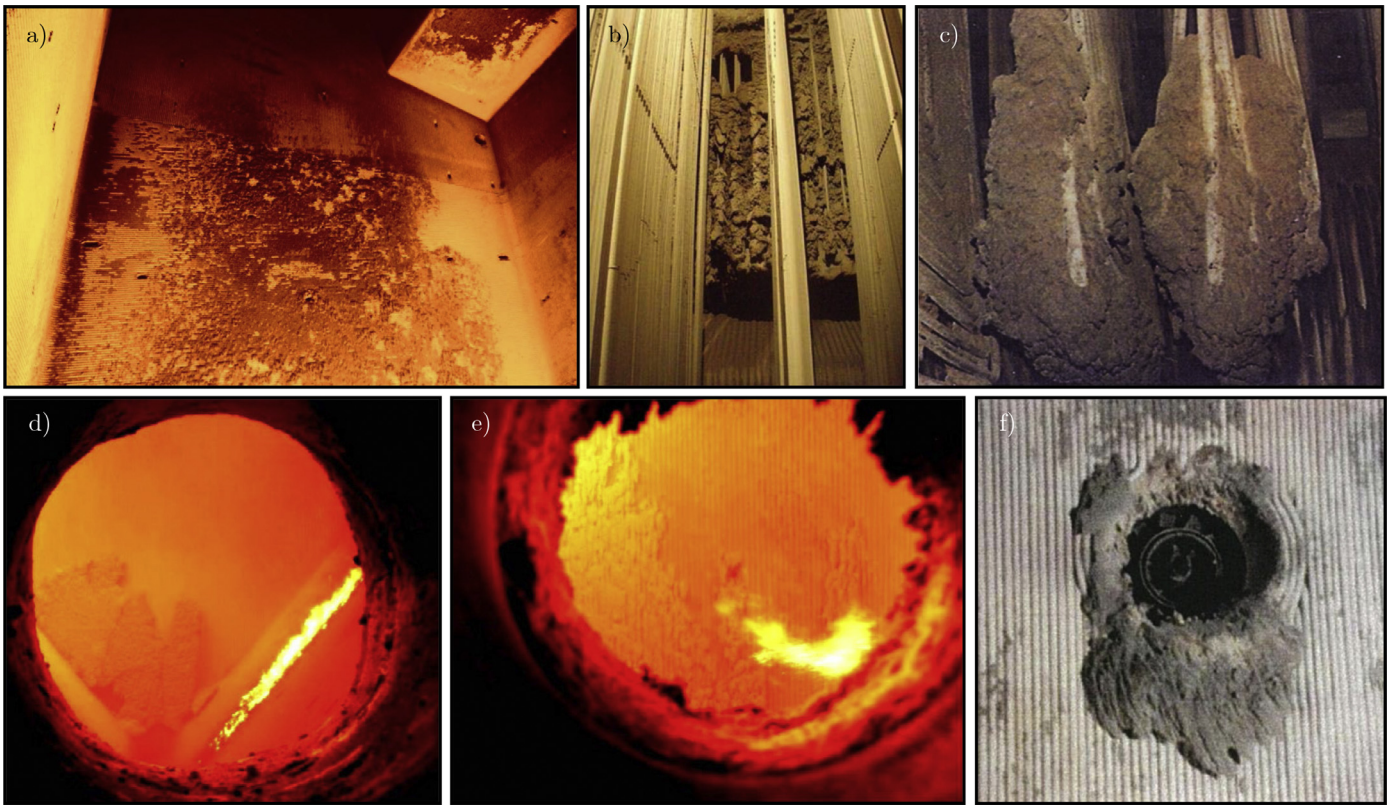

Fig. 39. Photographs of typical ash deposits within PF systems taken from Schumacher and Juniper [288] - (a) boiler wall and nose, (b) boiler cross-over path, (c) radiant superheater (d) ash hopper, (e) boiler wall, and (f) burner eyebrows.

easily by creeping. However, for brittle material this point is more difficult to find, typically a value of 0.1 or 0.2% strain is used. This value is often referred to as $R_{p,0.2}$ and used instead of Y. The material's elasticity (stiffness) is described by Hooke's law, relating stress to strain. Within the proportional region, the slope of the stress-strain curve reveals the materials elasticity, referred to as Young's modulus E and given by Eq. (41). Typically, brittle materials such as ceramics have a considerably higher Young's modulus compared with steel. Analogously, the shear modulus G of a solid, elastic material can be determined. The shear modulus describes the deformation, which takes place when a force is applied parallel to one face of an object while the opposite face is fixed by another equal force. A further important quantity describing the response of a material is the Poission's ratio ν. It relates lateral strain to longitudinal strain.

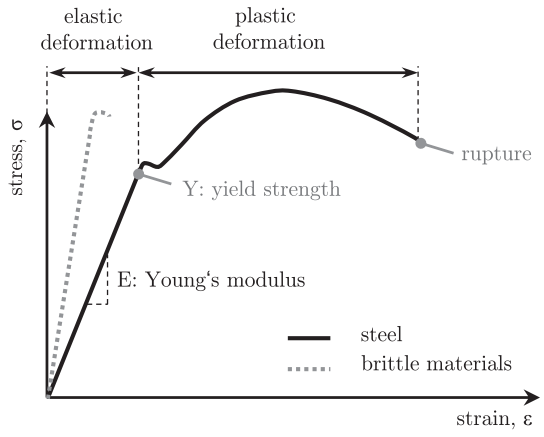

Fig. 40. Yield-stress diagram for steel and brittle material.

For most materials, Poisson's ratio will fall in the range 0–0.5 [265]. For a perfect isotropic material, Poisson's ratio is 0.25, with most glasses and ceramics being between 0.20 and 0.25 [265,291]. For linear-elastic, homogeneous and isotropic material the following relation is valid:

$$E = 2(1+\nu)\cdot G = \frac{\sigma}{\varepsilon} = \frac{\text{stress}}{\text{strain}} \tag{41}$$

The material properties Y, ν and E are well documented for steel and other materials at room temperature. A compilation of typical values is given in Table 8. Even though values have been quantified for ash particles [296], glass or minerals such as quartz or mullite, the variation among reported values can be high and temperature dependence is often unknown. Fig. 41 shows Young's modulus as a function of temperature for different materials. Most of the measurements are conducted for temperatures below 1000 °C and with increasing temperature, a decrease in Young's modulus is observed, except for vitreous SiO_2 [294]. However, it is mentioned that a decrease is expected at higher temperatures. The lower curve shows values for soda-lime glass measured by Marx and Sivertsen [292]. Data is extrapolated towards the melting temperature determined either with an ash melting microscope or predicted using thermodynamic equilibrium calculations. Uncertainty in this region is high. The Poisson's ratio is often reported to slightly increase with temperature, but again literature is not consistent and materials behave differently. Furthermore, particle structures vary significantly and material properties for structures such as agglomerates are difficult to determine. Therefore, it is doubtful that temperature-dependent data for various ash particle compositions and structures can be found. Ai and Kuhlmann [297] used the following temperature-dependent relation

$$E(T) = a\cdot exp(-b\cdot T), \tag{42}$$

Table 8
Selected material properties at room temperature.

Study	material	Y	E	ν
Unit	–	MPa	GPa	–
–	structural steel	310–690	210	0.27–0.30
–	stainless steel	400–800	190	0.28
–	glass	7–70	40–90	0.18–0.30
–	quartz	40–50	70–100	0.17
–	NaCl, KCl	–	40, 30	–
Vanorio et al. [299]	koalinite	–	6–12	–
Wain et al. [291]	different slags	220–2780	–	–
Matsunaga et al. [296]	fly ash	–	82–126[a]	–
Matsunaga et al. [296]	Al_2O_3	–	390	–
Matsunaga et al. [296]	mullite	–	230	–
Wachtman and Lam [293]	mullite	1103[b]	140	0.238[b]
Pérez et al. [301]	K_2SO_4	410	30	0.3
Wang et al. [455]	fly ash (MSW)	3800	192	0.13

[a] cenospheres showed considerably lower values of E = 13-16 GPa.
[b] data taken from [305].

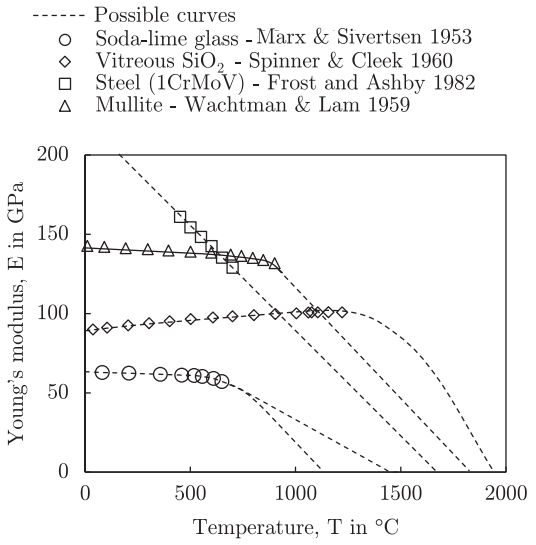

Fig. 41. Young's modulus as a function of temperature. Data collected from various references including [292–295].

where a and b are fitting parameters. They used deposition experiments for coal fly ash particles of different size, in order to fit coefficients a and b for the prediction of Young's modulus. However, it is questionable if results are applicable for other experiments, and the influence of chemistry is missing. Here more effort for temperature- and composition-dependent correlations is needed, similar to work of Roberts and Garboczi [298], who presented a model for elastic constants as a function of porosity.

3.2. Melt fraction

The melt fraction is often used to describe the stickiness of ash particles, or the flow behavior of slags, in entrained flow gasifiers. The melt fraction f_p of ash particles is the total mass of liquid phases or components within an ash particle or, more general, in a system, relative to the overall mass. It is usually defined by weight, and can take values from zero to unity, according to the following equation:

$$f_p = \frac{m_{p,liquid}}{m_{p,liquid} + m_{p,solid}}, \tag{43}$$

where $m_{p,liquid}$ and $m_{p,solid}$ are the liquid and solid particle mass, respectively. A method measuring the melt fraction is the differential scanning calorimetry (DSC) analysis. Fig. 42 shows the signal of a

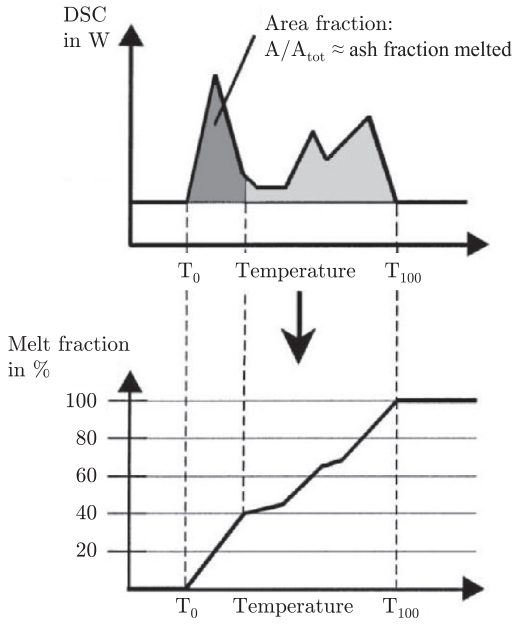

Fig. 42. Calculation of a melting curve from STA data (adopted from Hansen et al. [87]).

differential scanning calorimetry (DSC). This data is derived from simultaneous thermal analysis (STA), where the temperature and mass change of a sample to an inert reference sample is continuously recorded during constant heating. The signal is shown in a DSC-T-plot of an ash sample. The irregular shape or peaks of the signal identifies endothermic melting events, reactions or phase transitions, while sample mass remains constant. Changes in sample mass usually indicate thermal decomposition and release of gases or chemical reactions with the surrounding gas. By assuming, that the melt fraction is proportional to the area of the DSC signal over temperature, the following equation can be used to interpret the melt fraction:

$$f_p(T) = \frac{A(T)}{A_{tot}}, \tag{44}$$

where A is the area underneath the measured curve to a certain temperature (shown in Fig. 42) and A_{tot} the total area. The above equation leads to a continuous melting curve as shown in the melt fraction-temperature plot in the bottom illustration of Fig. 42. Limitations of this method are as follows: (1) simultaneous evaporation processes or reactions can only be distinguished from melting processes with additional methods; (2) individual fusion enthalpies can differ significantly and are not taken into account; (3) the method can only be applied to bulk ash and not to single particles. The latter is crucial, since the chemical composition of individual ash particles can vary significantly from the bulk ash. The melt fraction can also be determined by thermo-mechanical analysis (TMA), where the shrinkage of a sample is measured during heating (see e.g. [400–402,405]). This method was developed as an alternative to ash fusion tests at the University of Newcastle. It yields sensitive shrinkage measurements correlating with the formation of liquid phases. The method is applied for various purposes including characterization and extent of slagging [401], determination of slag viscosity [404], or deposit structure [403].

Besides the fact that the composition of individual mineral inclusions or ash particles can differ significantly from the bulk ash, the composition of a single particle can consist of multiple species and is influenced by a multitude of different reactions. In order to obtain a fundamental understanding of phase transitions and melting processes it is of crucial importance to investigate systems with only few components to isolate single effects and reduce cross sensitivity

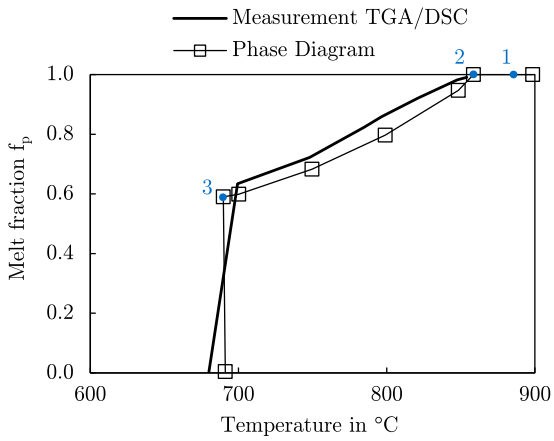

Fig. 43. Comparison of measured STA curve and data from phase diagrams (data from Hansen et al. [87] for 15 mol.% KCl and 85 mol.% K_2SO_4).

or influences from other reactions. To understand the single mechanisms thermodynamic equilibrium calculations (TEC) are often used to predict stable phases in dependence of different parameters, e.g. composition, temperature, or atmosphere. The thermodynamic equilibrium is based on the minimization of the Gibb's enthalpy, which is implemented in various commercial software codes, such as FactSage thermochemical software and databases [306] or ChemApp [307]. The results are plotted in so-called phase diagrams. An example is shown in Fig. 44, for the binary system KCl-K_2SO_4. The solid black lines denote phase transitions. The blue dashed line shows exemplarily a system of constant composition of KCl and K_2SO_4, which is heated from 500 to 900 °C. After exceeding the temperature at point 3, the first liquid phase occurs, but K_2SO_4 is still in the solid phase. Exceeding 850 °C at point 2, the solid phase K_2SO_4 gets liquefied. Both components (KCl and K_2SO_4) are entirely in the liquid phase at point 1. When evaluating results it is important to consider that the thermodynamic equilibrium represent an ideal stable state after infinite time. Reaction rates or catalytic effects cannot be included.

A comparison of STA measurements and results from the phase diagram is shown in Fig. 43. Results are presented for the vertical blue line in Fig. 44 using a system composed of 15 mol.% KCl and 85 mol.% K_2SO_4. Hansen et al. [87] conducted STA measurements for different binary salt mixtures, as well as for straw and coal ashes. Salt mixtures show a good repeatability; the melting onset is determined within 10 °C and the melt fractions at a given temperature within 10% when compared with phase diagrams. Ash samples

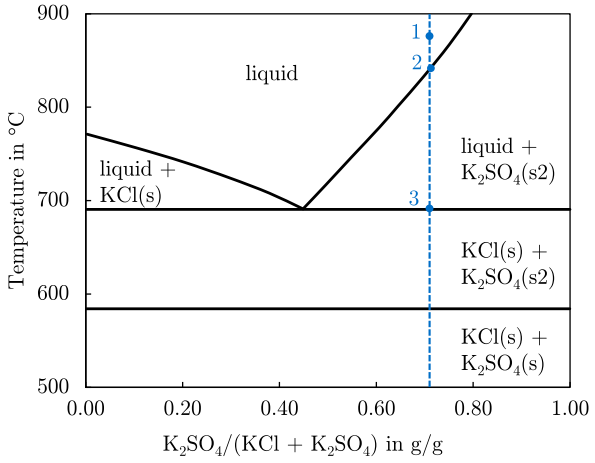

Fig. 44. Phase diagram for KCl-K_2SO_4 showing characteristic points: (1) molten salt, (2) liquidus and (3) solidus temperature (data from [203]).

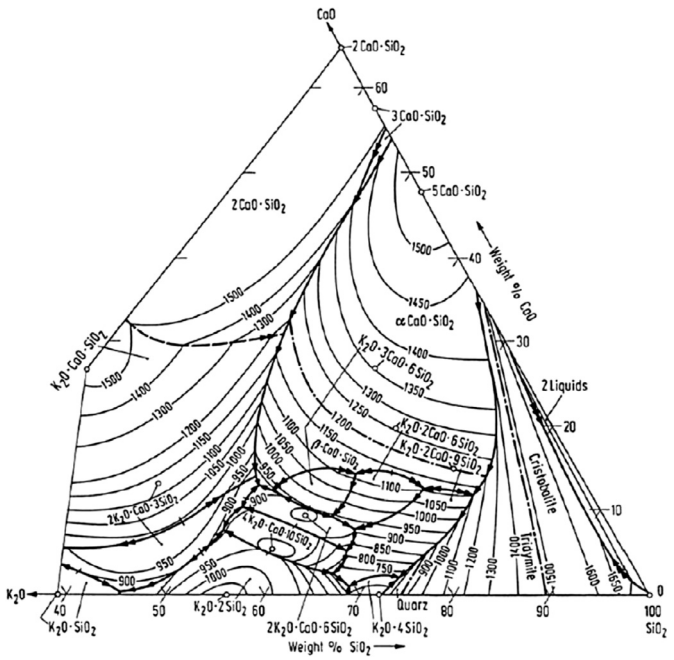

Fig. 45. Ternary phase diagram for the K_2O-CaO-SiO_2 system, relevant for straw and wood ash (taken from [308], originally from [309]).

showed lower melting temperatures, between 50 and 100 °C when compared with the ash fusion test results [87]. The authors suggest to use CCSEM results to identify individual melting events recorded in the STA curve. A more complex ternary phase diagram for K_2O-CaO-SiO_2, can be seen in Fig. 45. This figure can explain the troubling behavior of straw ash compared with wood ash. Straw ash particles are typically composed of K-silicates, having an eutectic melting temperature as low as 750 °C, at a mixture of 70 wt.% SiO_2 and 30 wt.% K_2O. On the contrary, Ca-rich particles have melting temperatures above 1500 °C (not shown for pure CaO) and thus a low stickiness and adhesiveness. In real combustion systems, particles are compounds of even more than three species and equilibrium is not reached due to small time scales complicating the application of phase diagrams. Nevertheless, they can be a useful indicator explaining certain ash behavior. Another application was presented by Jak [310]. The author used thermodynamic equilibrium calculations in order to predict the ash melting behavior. Results are calculated for Al-Ca-Fe-O-Si systems, and compared with ash fusion test results. Results show good agreement underlining the capability of theoretical predictions. Masiá et al. [311] studied biomass and waste ashes using leaching methods, STA and thermodynamic equilibrium calculations. STA measurements did not prove to be suitable for their ashes. In contrast, equilibrium calculations showed good results and are recommend by the authors for the determination of the melt fraction. Wieland et al. [312] found that the predictions from STA are shifted towards higher temperatures, compared to results from thermodynamic equilibrium calculations. Differences are explained by heat transfer limitations and reaction kinetics. Babat et al. [186] explained iron-rich deposits collected in a full-scale power station using thermodynamic equilibrium calculations. The authors could show that pyrite forms low melting eutectics in reducing conditions, where melting starts at temperatures as low as 950 °C. In general, TEC or STA methods provide useful information on the melting behavior of ashes, however they have to be applied with care. For predictions using TEC, databases have to be selected, which are not fully available for the vast set of ash chemistry systems, in particular for biomass or waste ashes. Furthermore, these predictions assume infinite time and kinetics of chemical transformations cannot be

considered. Kinetics are known to be important for instance for relatively slow pyrite transformation.

3.3. Viscosity

The dynamic viscosity μ (sometimes η is used instead) of ashes or slags is frequently applied in modeling studies. Sticking criteria are often based on particle viscosity, and flow behavior of slags in entrained flow gasifiers is mainly described by its viscosity. Typical slag flow is occurring when the dynamic viscosity is in the range of $\mu_{slag} = 15–25$ Pa · s, at temperatures of around 1400–1500 °C, depending on the fuel and ash composition [313]. At these temperatures, slag can be described as a Newtonian fluid, where viscous stresses are linearly proportional to strain rates. However, once the slag cools down, crystals can form in the melt, and the slag can no longer be treated in such a way. This transition point is often defined as the critical viscosity temperature T_{cv} [16], and is shown in Fig. 46. The temperature viscosity curve changes abruptly at T_{cv} [323]. This temperature is time dependent and strongly affected by the crystal formation rate and thus, there might be no single value. Instead, the temperature of critical viscosity can change over time. Nevertheless, attempts were made for an estimation. In order to find viscosity values, empirical relations were developed, relating slag composition and temperature to measured viscosity values [314]. Nicholls and Reid [315] were the first to observe that at a given viscosity the gradient of the viscosity-temperature curve is similar for all coal ash slags within the Newtonian region. This behavior is expressed by the following equation [314]:

$$\frac{d\mu}{dT} = f(\mu) \neq f(T) \tag{45}$$

Eq. (45) implies, that if viscosity curves can be moved horizontally in a $\mu - T$ plot, they will all overlap. This temperature shift is the principle of many empirical models. These models describe the viscosity in the form of an Arrhenius-type (AT) equation, by:

$$log\ \mu = A + \frac{B}{T - T_0}, \quad \text{or} \quad log\ \mu = A + \frac{B}{T} \tag{46}$$

where A and B are constants, and, T_0 is a temperature correction parameter. This relationship is often used to describe viscosity at high temperatures in the range of $10^2–10^3$ Pa · s [316]. Another commonly used type of equation for the prediction of slag viscosity is the Weymann-type (WT) equation [317] given by:

$$\mu = a \cdot T \cdot e^{1000 \cdot b/T}, \tag{47}$$

where a, and b are composition-dependent fitting parameters. Eqs. (46) and (47) are commonly used and fitted to a set of slag compositions and temperature-viscosity measurements. Browning et al. [314] give a brief overview on advances in describing slag viscosity by empirical equations. Another good review is provided by Vargas et al. [323]. Table 9 shows a selection of viscosity models, available in literature. There are more models available, in particular in the glass industry or vulcanology. Mathematical descriptions of the models can be found in the Appendix A. Early models, such as the one by Watt and Fereday [319] or the S^2-correlation, were developed for British coals with a limited range of application (only valid for a certain range of Si and Fe content, as shown in Table 9). A widely used model considering different elements and their role in the melt was proposed by Urbain [321]. They used the analogy of slag and glass melts. They fitted viscosity measurements of different SiO_2-Al_2O_3-CaO-MgO systems to the Weymann-type equation [314,321]. Kalmanovitch and Frank [322] re-evaluated the data of Urbain [321], and modified their equations for improved accuracy. They included all major ash forming elements into the proposed equations, calculating the coefficients a and b. But still, the range of applicability was limited to high temperatures, with viscosity values $\mu < 10^3$ Pa · s. Senior and Srinivasachar [316] examined many different glass compositions at lower temperatures, and found a change in the slope at approximately 10^4 Pa · s. Fig. 46 compares different slag viscosity measurements for two coal ashes with high silica content (Reid [324] - glassy coal ash slags with $SiO_2 \approx 57$ wt.%, and Oh et al. [325] - Sufco coal ash with $SiO_2 \approx 60$ wt.%), and three other coal ashes with medium SiO_2 content (Pittsb. #8, Shenfu, Boadian, with $SiO_2 < 50$ wt.%). The glassy slags do not show a change in slope at given temperatures. It is assumed that the change will occur at lower temperatures, as mentioned by Senior and Srinivasachar (when $\mu = 10^4$ Pa · s). The three other coals with low silica content show a steep increase in the $d\mu/dT$-slope at around 10–20 Pa · s, which is considerably lower than those of glassy slags. The slope parameter B in Eq. (46) increases from around $B = 1.1$ to $B = 6.4$. All coals show a similar slope in the low- and high-temperature regime, underlining the validity of Eq. (45). Often, the change in slope is referred to as the critical temperature T_{cv}. Different approaches have been used to predict the critical temperature. Sage and McIlroy

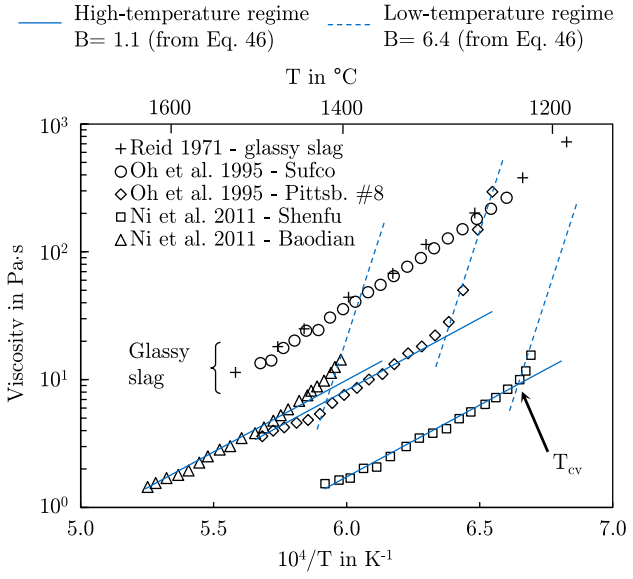

Fig. 46. Comparison of measured slag viscosities from various literature references [324,325,333]. Two types of coal slags are compared, Si-rich (glass type) and slags with medium Si-content. A change in the slope can be observed for the latter class at lower temperatures.

Table 9
Comparison of different viscosity models for molten silicates and their range of validity (data summarized from various references).

Model	Eq. type	Species considered	Notes, comments and range of validity
Reid and Cohen [318]	–	Si, Fe, Ca, Mg	alkali metals not considered
S^2 correlation [313]	AT	Si, Fe, Ca, Mg	Si < 55% and Fe < 5%[a]
Watt and Fereday [319]	AT	Si, Al, Fe, Ca	Si > 80% and Fe > 15%[a]
Bottinga and Weill [320]	–	a large number of compounds[c]	varying constants for different T and SiO_2-contents
Urbain [321]	WT	Si, Al, Ca	high temp. < 10^3 Pa · s
Kalmanovitch and Frank [322]	WT	all major oxides[d]	extension of Urbain et al. for more elements
Senior and Srinivasachar[b] [316]	WT	all major oxides [d]	ash particles at $10^4–10^8$ Pa · s
Browning et al. [314]	AT	all major elements[d], S, Mn	wide range of SiO_2, Al_2O_3, FeO

[a] greater accuracy in this range.
[b] has a low-temperature region for crystal formation.
[c] of Si, Al, Fe, Ca, Mg, Na, K, Ti, Mn, Sr, Ba, Li and Al-compounds.
[d] of Si, Al, Fe, Ca, Mg, Na, K, Ti.

[326] related the hemispherical temperature from the fusion test to the critical viscosity. Song et al. [327] showed that the critical temperature correlates well with the liquidus temperatures, predicted using FactSage, for a large number of synthetic slags. The concept of low- and high-temperature regions is used by Senior and Srinivasachar [316] in their empirical model. The model concept is based on the network structure of silicate melts. These melts can be described as polymers consisting of a basic building block, the SiO_4^{4-} anion. Silicon and oxygen have a strong covalent bonding forming a glassy silica network, which can accommodate different cations. Senior and Srinivasachar [316] define three different categories, interacting within the network:

- glass formers (Si^{4+}, Ti^{4+}, P^{5+}),
- modifiers (Ca^{2+}, Mg^{2+}, Fe^{2+}, K^+, Na^+), and
- amphoterics (Al^{3+}, Fe^{3+}, B^{3+}).

The elements Ti^{4+} and P^{5+} can also act as glass formers, similar to Si^{4+}. Modifier ions lead to a lowered viscosity by disrupting the glass structure. The last group can act as a glass former in combination with a modifier ion by balancing their charge and thus forming a stable metal oxygen anion group fitting into the silicate network [316]. However, when modifier ions are missing in the mixture, amphoteric cations can act as modifiers themselves. This behavior of the elements is often used in the glass industry or for example by Senior and Srinivasachar in order to develop a model for the viscosity of coal ash particles. Their goal is to provide a model being able to predict the ash particle viscosity, based on ash composition for a wide range of temperatures. This region includes the beginning of particle sticking at around $\mu = 10^4 - 10^8$ Pa · s [316]. Therefore, they used a high- and low-temperature regime in which the $d\mu/dT$-slope changes. In contrast, the majority of viscosity models only focuses on the region of high temperatures, in which the slag acts as a Newtonian fluid. However, at lower temperatures, crystals may form in the melt, leading to a sharp increase in viscosity as shown by Fig. 46 [106]. A compilation of ash particle viscosities for different fuel ashes and chemical compositions can be seen in Fig. 47(a). The measured viscosity ranges over a wide span from 10^{-3} for liquid salts to 10^5 Pa · s for coal slags and glasses. The lowest values are observed for salts even at temperatures as low as 800 °C. High viscosity values can be found at low temperatures, e.g. for glassy slags, but also at high temperatures as soon as crystals form in the melt. In general the viscosity of ash particles from straw combustion exhibit lowest values followed by woody ash and coals. However, variations in chemistry among different ash particles within one sample can lead to a different order.

Browning et al. [314] recently published an interesting approach, in which they investigated 1715 data points of 117 slag compositions, and developed an empirical equation similar to Eq. (45). The temperature shift is calculated composition-dependent and is given in Appendix A. The authors suggest that potassium acts as a network former, unlike Urbain [321], who counted K^+ to the network modifiers. The reason why potassium increases the viscosity is its effect on the amphoteric aluminum oxide in the slag. They further state that the model is not valid for alumina-free samples containing K_2O [314]. A comparison of models and measured viscosities is shown in Fig. 47. The best agreement for the high-temperature regime is achieved with the correlation suggested by Browning et al. [314]. Viscosity models not shown in Fig. 47 showed larger deviations. None of the models is able to predict the changing slope at lower temperatures. It is concluded that viscosity can be predicted relatively well in the region of high temperatures for typical coal slags. However, predicting ash particle viscosity at lower temperatures and with a highly variable composition is still challenging. The model of Senior and Srinivasachar [316] is validated for glassy slags containing modifiers. However, if particles have no modifiers or high Fe or Ca contents in the absence of Si, the correlation might yield unsatisfying results. Nevertheless, this model is the only available one in literature being capable of predicting the viscosity at lower temperatures of 800–1300 °C, which are typical for ash particle deposition in a boiler.

In general, there is a need for better viscosity models in particular for Ca-rich or salt-rich ashes - typical for biofuels. Vargas et al. [323] compared viscosity models and their predictive capabilities with a number of viscosity measurements mainly for silicates. Best performance was attributed to the model of Bottinga and Weill [320]. Another model showing good agreement with measurements, is the model of Browning et al. [314]. However, both are only valid for silicates in a certain range of composition and in the Newtonian region at high temperatures. Therefore, more fundamental work should be directed towards models for biomass ashes and for lower temperatures.

A method considering the formation of crystals in the melt, and their influence on the viscosity, was presented by a number of studies. Vargas et al. [323] present an overview on models relating the solid fraction of crystals in the melt to the viscosity of the mixture

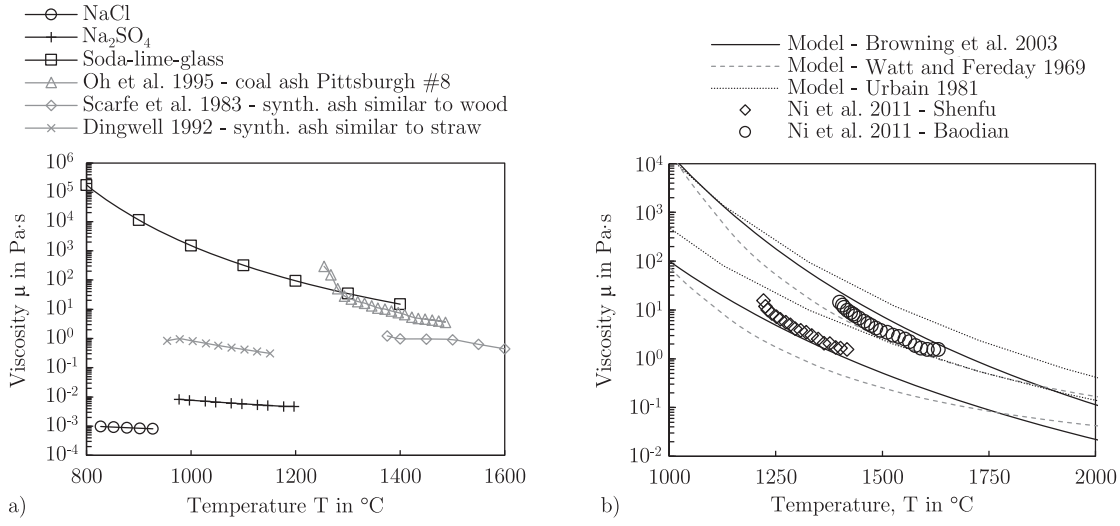

Fig. 47. Viscosity of ashes: (a) comparison of viscosity measurements of coal ash (Pittsburgh #8 [325]), molten salt (NaCl [328], Na_2SO_4 [329]), synthetic ash (similar to wood [330] and straw ash [331]), and soda-lime glass [332], and (b) comparison of predicted and measured molten slag viscosities (experimental data from Ni et al. [333]). Three lower continuous lines give model results for the Shenfu coal, and three upper lines for the Baodian coal.

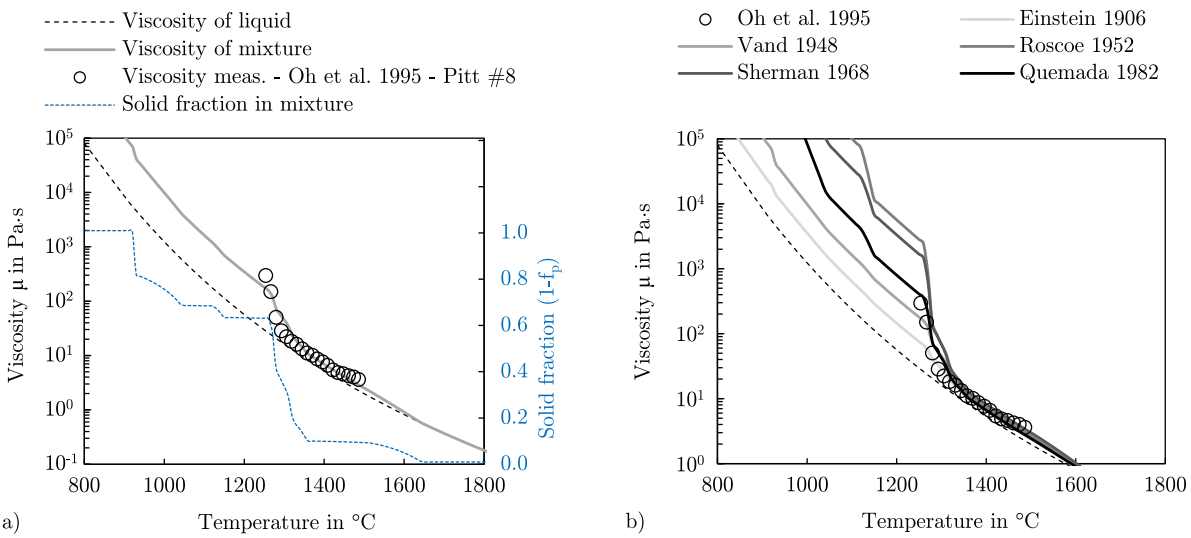

Fig. 48. Comparing measured viscosity for a bituminous coal ash (Pittsburgh #8) with model predictions: (a) with and without considering the solid fraction in the melt, and, (b) using different models for solid-liquid mixtures.

μ_{mix} and the liquid phase μ_{liq}, respectively. The models differ in their complexity - all models consider the amount of crystals and some can consider the crystal shape. Vargas et al. [323] describes two classes, models for dilute suspensions with mostly spherical crystals such as the work of Einstein [334], Vand [335], Sherman [336], Roscoe [337], and models for dense slurries, e.g. Quemada [338]. A validation of these models is beyond the scope of this work, however, data of Oh et al. [325] is used to compare model predictions. Therefore, the viscosity of the melt is predicted using the composition of the Pittsburgh #8 ash and a fit of the model of Browning et al. [314]. The measurements and predictions are shown in Fig. 48(a) as points and dashed line, respectively. Relatively good agreement is observed at high temperatures. With decreasing temperature, a sharp increase of the measured viscosity is observed at around 1270 °C due to crystal formation. The fraction of crystals (solids) in the melt is determined using thermodynamic equilibrium calculations (FactSage and the FToxide database [306]). The blue curve shows the fraction of solids as a function of temperature. First crystals are predicted at around 1650 °C. A significant increase in the solid fraction is observed at around 1350 °C. The third curve (continuous line) in Fig. 48(a) shows the predicted viscosity of the solid-liquid mixture μ_{mix} following a model suggested by Vand [335]:

$$\mu_{mix} = \mu_{liq} \cdot \left[1 + c \cdot (1 - f_p) + d \cdot (1 - f_p)^2\right], \tag{48}$$

where μ_{liq} is the viscosity of the liquid phase and f_p is the fraction of molten material within a particle or a slag sample. The solid fraction is accordingly obtained by $(1 - f_p)$. The coefficients c and d are assumed to equal $c = 2.5$ and $d = 9.15$ [325,339]. A further model yielding good results is presented by Roscoe [337]. Equations are based on the work of Einstein [334]:

$$\mu_{mix} = \mu_{liq}\left[1 - c \cdot (1 - f_p)\right]^{-5/2}, \tag{49}$$

where the coefficient c is set to $c = 1.35$. In general, all these models yield improved results as shown in Fig. 48 compared with viscosity model for liquid melts. However, these model require the fraction of crystals in the melt and therefore additional effort.

3.4. Rheology

The fluid flow behavior, often referred to as rheological behavior, of coal ashes and/or slags is complex and controversy. Fluids are classified as **time-independent fluids** or **time-dependent fluids**. Both are illustrated in Fig. 49. The most common time-independent fluid is a Newtonian fluid describing most gases and liquids. Viscosity is expressed as the ratio of shear stress to shear rate. Pseudoplastic fluid, often called shear-thinning material, shows a decrease in viscosity with increasing rate of deformation. The fluid is termed plastic, if this effect is very strong. Typical examples are polymeric

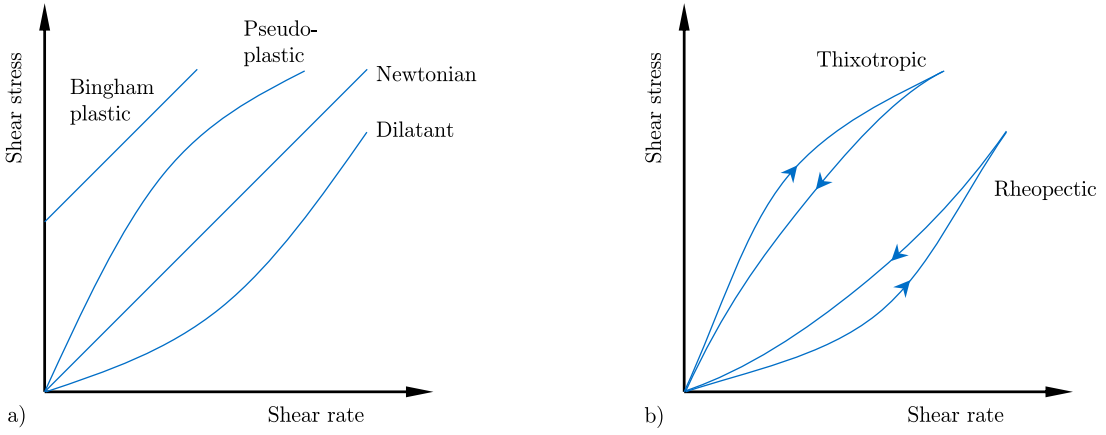

Fig. 49. Flow type classification (adopted from Vargas et al. [323]): (a) time-independent and (b) time-dependent fluids.

solutions or melts [323]. The opposite behavior is rarely observed. It is termed dilatant or shear-thickening. Bingham plastics are fluids which require a finite deformation to initiate flow, e.g. tooth paste. Time-dependent fluids exhibit a changing shear stress with duration of shear [323]. Thixotropic fluids have a decreasing viscosity with time of shear, thus a time-dependent shear-thinning. This decrease in viscosity is often caused by structural changes or breakdown in the fluid. The behavior is shown in Fig. 49(b), where the shear rate is steadily increased at a constant rate to a maximum value and then decreased to zero. During the decrease a lower shear stress is observed yielding a typical hysteresis curve. Paints, ink or mayonnaise behave this way. Again, the opposite behavior, so-called rheopectic fluid, is rarely observed. A special form of time-dependent fluids are viscoelastic materials. They behave as both, viscous fluids and elastic solids. The elasticity is typically a result of bond stretching along crystallographic planes, whereas the viscosity is due to diffusion of atoms or molecules inside an amorphous material [340]. Viscoelastic materials have a characteristic time constant called relaxation time. If deformation takes places during longer periods than this relaxation time, the material behaves as a viscous fluid. Within shorter periods, the material is deformed and recovers to its original shape after deformation [341]. Losurdo et al. [342] used viscoelatic models to describe ash behavior. This is an interesting approach, however experimental confirmation for this behavior is still due.

The actual behavior of ash particles or slags is rarely studied. Typically, viscosity curves are measured and described with empirical equations. Song et al. [343] investigated the flow behavior of coal ash slags, using a high-temperature rheometer. The effect of shear rate and temperature on viscosity are studied between 1200 and 1340 °C. The authors found that the sensitivity of slag viscosity to temperature variation decreased with increasing shear rate. They observed a thixotropic behavior, which could be related to the formation of crystalline phases during cooling. Vargas et al. [323] reviewed measurements on the viscosity of silicate melts with various compositions. Non-Newtonian fluid behavior was only present when crystals appeared in the melt or a separation of the melt in two or more immiscible liquid phases occurred.

Rheology is only important when crystals form inside the melt. However, data for the effect of time and deformation on viscosity are rare. Liquid melts behave as Newtonian fluids and are thus rather simple to describe. In general, viscosity should be described with composition- and temperature-dependent models. The effect of time and stress on viscosity can neglected due to its complex nature, and weak data set available in the literature.

3.5. Surface tension

The surface tension γ (in N/m) is typically used in particle deformation calculations, such as droplet impaction on a surface in internal combustion engines. In some publications it is defined as the variable σ. Generally, the higher the surface tension is, the stronger are the forces to reduce the surface area of a droplet. Surface tension can be estimated using the composition-dependent relation [273],

$$\gamma = \sum_{i=1}^{N} (x_i \cdot \gamma_i), \tag{50}$$

where γ_i and x_i are the surface tension and molar fraction of species "i". A linear temperature dependency is proposed in literature [344]:

$$\gamma_i = \gamma_{i,1300\ ^\circ C} + \left(\frac{0.004}{1000}\right) \cdot \Delta T, \tag{51}$$

where values for $\gamma_{i,1300\ ^\circ C}$ can be taken from Table 10. Mills and Rhine [345] give composition-dependent values for γ_i, presenting probably the best available data set for coal ash slags. Typical values for ashes range from around $\gamma_p \approx 0.05$ N/m for low viscosity ashes such as salt particles up to values around $\gamma_p \approx 0.6$ N/m for aluminosilicates (Al-Si).

Table 10
Partial molar volumes and surface tension values taken from various references.

Ash Oxide	V_i in m³/kmol	$\gamma_{i,1300\ ^\circ C}$ in N/m
Al_2O_3	$28.31 + 32 \cdot x_{Al_2O_3} - 31.45 \cdot x^2_{Al_2O_3}$ [345]	0.58 [357]
CaO	16.5 [353]	0.51 [357]
Fe_2O_3	38.4 [345]	–
K_2O	46.0 [353]	0.01 [357]
MgO	11.6 [353]	0.52 [357]
Na_2O	28.9 [353]	0.295 [357]
P_2O_5	65.7 [345]	–
SiO_2	$19.55 + 7.966 \cdot x_{SiO_2}$ [345]	0.29 [357]
SO_3	40.4 [539]	–
TiO_2	24.0 [345]	0.25 [357]

3.6. Contact angle with the substrate

The contact angle Θ_c of a liquid droplet with a substrate is illustrated in Fig. 50. The contact angle and the so-called wetting, i.e. the area that is covered with the liquid, strongly depend on the liquid and its surface tension, as well as the substrate's surface energy and morphology. Small contact angles $\Theta_c \ll 90°$ correspond to a high wettability, low surface tension of the droplet, a good adhesiveness and high solid surface free energy [346,347]. The contact angle can be described mathematically using Young's equation [348]:

$$\gamma_{SV} = \gamma_{SL} + \gamma_{LV} \cdot \cos(\Theta_c), \tag{52}$$

where γ_{SV}, γ_{SL} and γ_{LV} are the solid-vapor, solid-liquid and liquid-vapor surface tension. All three interfacial tensions act as forces on the droplet, and the contact angle forms under mechanical equilibrium for an ideal surface [347]. In reality, this equilibrium is often not observed, instead the contact line is always moving, leading to a dynamic contact angle [347]. Often the liquid–vapor and solid–vapor surface tension is approximated with the droplet's and substrate's surface tension and free energy, respectively. Another method relates the contact angle to the surface tension of a droplet γ_p and the work of adhesion following the Young–Dupré equation:

$$\gamma_p \cdot (1 + \cos(\Theta_c)) = W_{ad}/A, \tag{53}$$

where W_{ad} is the work of adhesion and A the contact area between the droplet and the substrate. Since surface tension and viscosity values of molten ash particles are fairly high compared with e.g. water droplets, the contact angle of ash droplets on steel tubes or ceramics show typically high values. The contact angle measurement is a challenging task, in particular for ash particles since they require high temperatures in order to become liquid. One technique is the so-called Moza-Austin sticking test [349]. A pellet of mineral or ash is formed, and held in the center of a ring burner flame, until it melts and falls onto a pretreated steel specimen (typically oxidized), maintained at a certain temperature relevant for heat exchangers. The contact angle of the solidified droplet was determined optically, and the adhesion force determined by shearing the droplet off the surface [349]. By using this method, realistic values for supercooled surfaces are obtained, which differ from equilibrium contact angles. Heat exchangers are typically much colder compared with ash melting temperatures. Therefore, heat transfer and cooling affect the contact angle of ash particles with the surface. Ni et al. [333] used a Boltzmann-type equation, and fitted measurements of Abbott and Austin [350], in the form of:

$$\Theta_c = A + (B - A)/(1 + exp[(T - C)/D]), \tag{54}$$

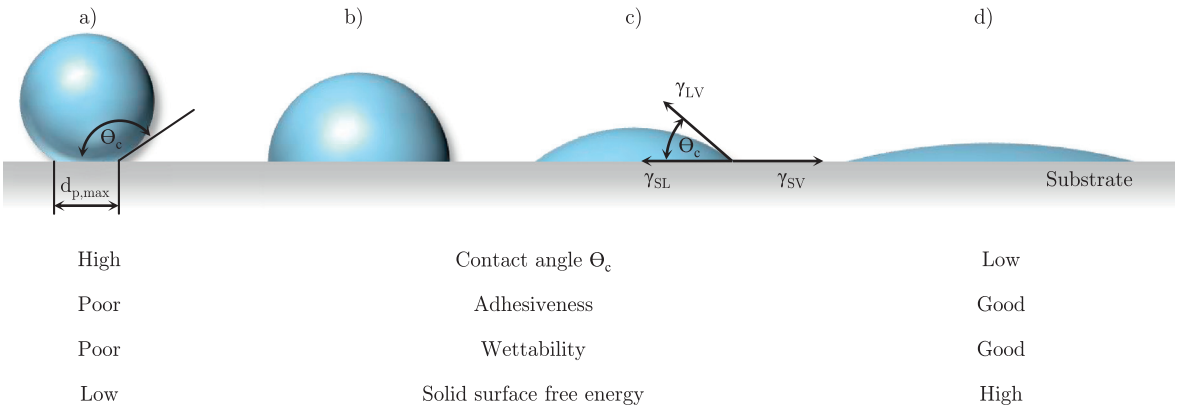

Fig. 50. Contact angle for droplets on solid substrates (adopted and modified from [346]).

where constants were determined to $A = 100$, $B = 150$, $C = 445$ and $D = 35$ to reproduce measurements from Abbott et al. [351] shown in Fig. 51 and T is the substrate temperature. Abbott et al. [351] measured the contact angle and adhesive force of synthetic ash mixtures, on a preoxidized carbon steel, maintained at temperatures up to 700 °C. It can be seen that the contact angle decreases with increasing substrate temperature. The droplet cools slower upon contact and thus plastic deformation is increased due to lower viscosity values. The adhesive force increases rapidly with increasing substrate temperature, showing a higher connectivity, which can explain accelerated deposit formation at higher steel temperatures. Similar tests were conducted using pyrite, pyrite-quartz, pyrite-kaolinite and pyrite-illite mixtures [350]. Considerably lower contact angles down to 50° with high adhesive forces were observed in the case of pyrite-illite mixtures. Probably caused by a low melting eutectic.

Another method for determining the contact angle is the capillary bridge method developed by Restagno et al. [352]. This method puts a spherical solid surface in contact with a liquid, as illustrated in Fig. 52. The contact angle can be approximated by the following relation:

$$A = 2 \cdot \pi \cdot d_p/2 \cdot (k^{-1} \cdot \sqrt{2(1 + \cos(\Theta_c))} - h), \tag{55}$$

where A represents the wetted area, h is the distance between the particle and the surface from the liquid bath, and k^{-1} is the capillary length, which is known for common liquids [347]. The area A strongly depends on the distance h. This method has some similarities compared with solid ash particles impacting a molten, slagged surface. The area A, which is a function of geometry and liquid properties can be used to estimate adhesive forces preventing the particle from rebound. However, further research in this area is needed.

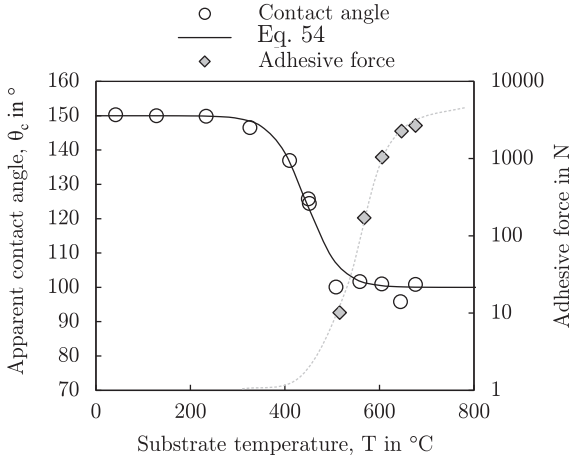

Fig. 51. Contact angle and adhesive force of synthetic ash droplets on a preoxidized medium carbon steel (SA515). Data taken form [351].

3.7. Density

The density of a deposit or a slag layer depends on porosity and chemical composition, where the following equation relates the true/solid density $\rho_{dep,true}$ to the apparent density $\rho_{dep,app}$:

$$\rho_{dep,app} = \rho_{dep,true} \cdot (1 - p_{dep}). \tag{56}$$

A simple estimation of the true density can be achieved by using the empirical correlation $\rho_{dep,true} = 2.54 + 0.00978 \cdot w_{Fe_2O_3}$ in g/cm^3, where $w_{Fe_2O_3}$ is the mass fraction of Fe_2O_3. A more sophisticated approach was developed for slags and uses the method of partial molar densities [345,353],

$$\rho_{dep,true} = \sum_{i=1}^{N} x_i \cdot M_i/V_i, \tag{57}$$

where V_i is the partial molar volume, x_i is the molar fraction and M_i is the molar mass of species "i". Values for the partial molar volumes can be taken from Table 10. Temperature-dependent density changes are small and often neglected.

3.8. Sintering and fusion

Measurements on the sintering behavior of ash deposits are rare. Models are mainly developed for metal powders such as the one presented by Mackenzie and Shuttleworth [354]. They developed a sintering model for viscous flow sintering, similar to the following

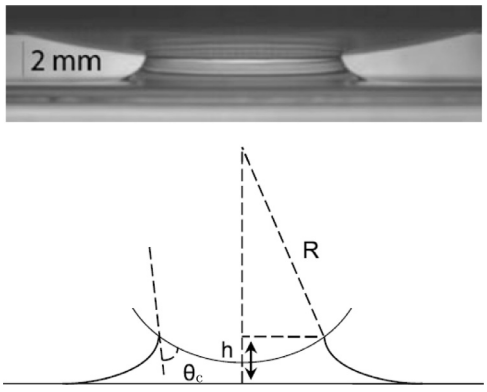

Fig. 52. Photograph and capillary bridge between a spherical particle and a liquid (taken from Yuan and Lee [347], originally from Restagno et al. [352]; reprinted with permission. Copyright 2009 American Chemical Society).

equation [355],

$$p_{dep}(t) = p_{dep,0} \cdot exp\left(-\frac{3 \cdot \gamma \cdot t}{d_p \cdot \mu \cdot x}\right), \quad (58)$$

where $p_{dep,0}$ is the initial deposit porosity, d_p is the average pore size (average particle size is used in this work), and x is an added fitting parameter. Fig. 53 shows the calculated sintering behavior of a Pittsburgh #8 ash. An initial porosity of $p_{dep,0} = 0.5$ and a fitting parameter of $x = 1000$ are assumed to calculate sintering for different temperatures. It can be seen that sintering starts at around 1100 °C. Without the fitting parameter, sintering to $p_{dep} = 0$ would occur within seconds for a temperature of 1100 °C. Meinel [356] used a similar value to fit his results. Generally, a slight increase in temperature leads to a strong decrease in porosity. Eq. (58) depends on deposit viscosity, which is a strong function of temperature. The calculations shown in Fig. 53 are carried out for viscosity measurements of the Pittsburgh #8 ash (see Fig. 46). The surface tension of ash particles is calculated based on Eqs. (50) and (51). Gupta et al. [357] reported the same temperature range in which sintering is observed (900–1200 °C). The presented equations can also be used to describe melting by adjusting the parameter x. Another type of sintering, besides sintering due to viscous forces, is caused by chemical reactions, as described in Section 2.5.4. Typical reactions leading to a decrease in porosity can be carbonation or sulfation [31].

3.9. Thermal conductivity and radiative properties

Thermal conductivity and radiative properties of deposits define the temperature profile in the deposit and thus, heat transfer to the water-steam cycle as illustrated in Fig. 32. Therefore, these parameters are of importance not only for modeling studies, but also for boiler operation. Heat transfer through the deposit is often expressed by an effective thermal heat conductivity, k_{eff} that combines heat conduction and radiation which might occur in parallel or in series [273]. Radiation increases the heat conductivity through a porous deposit by penetrating the inside structure and absorption of radiation. Heat conduction through a deposit can then be expressed as one-dimensional, transient heat transfer through a cylindrical shell by:

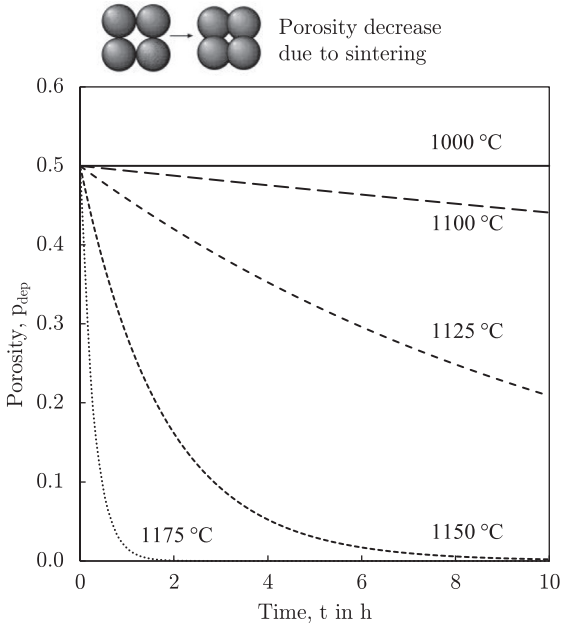

Fig. 53. Porosity decrease as a function of temperature over time due to sintering (calculated for a Pittsburgh #8 ash using Eq. (58)).

$$\rho_{dep} \cdot c_{p,dep} \cdot \frac{\partial T}{\partial t} = k_{eff} \cdot \left[\frac{1}{r}\frac{\partial}{\partial r}\left(r\frac{\partial T}{\partial r}\right) + \frac{1}{r^2}\frac{\partial^2 T}{\partial r^2}\right] \quad (59)$$

This equation considers the temperature change as a function of time t and radial direction r, where ρ_{dep} is the deposit density, and $c_{p,dep}$ is the deposit heat capacity. This equation can be solved analytically by ignoring the transient term to [32]:

$$T(r) = T_i - \frac{q \cdot r_i}{k_{eff}} \ln\left(\frac{r}{r_i}\right), \quad (60)$$

where q is the surface heat flux and the index "i" denotes the deposit inner surface. Using this equation, the steady-state temperature profile in a deposit layer can be calculated with the surface heat flux and effective thermal conductivity. The effective thermal conductivity is mainly dependent on deposit characteristics such as:

- porosity and degree of sintering,
- temperature of the deposit,
- particle size,
- chemical composition, and
- radiative properties.

The deposit **porosity** p_{dep} has the strongest impact on the thermal conductivity. A decrease in porosity leads to an increase in the effective thermal conductivity, and enhances heat transfer. Robinson et al. [358] found that the initial layer has a relatively low thermal conductivity due to its particulate structure and relatively high porosity. However, in the case of biomass, this layer can consist of condensates and therefore have a molten, dense structure and high conductivity. Outer layers show a sintered structure with strongly increased thermal conductivities. Fig. 54(a) shows measurements of deposit thermal conductivity with varying porosity values. Rezaei et al. [246] measured the thermal conductivity for a set of different coal ashes. The porosity strongly depends on the deposit type. It decreases in the order of: powdery > particulate > sintered > molten type of deposit. Typical values range from 0.1 for molten deposit with gas inclusions, up to 0.9 for a loosly-bound, powdery deposit layers [358–360]. The porosity is reduced with time due to sintering. This causes a densification of the deposit, and thus, an irreversible increase in effective thermal conductivity [273].

Fig. 54(b) shows the influence of **temperature** on measured thermal conductivities. As a general rule, a slight increase in thermal conductivity with increasing temperature, can be observed. Rezaei et al. [246] found that the change in thermal conductivity, is more pronounced at higher temperatures. They explain this behavior by sintering. Above temperatures of 600–800 °C sintering occurs, leading to an irreversible change in morphology and thereby a change in deposit thermal conductivity. Gupta et al. [357] found coal ash sintering between 900 and 1200 °C. This change in structure and particle connectivity leads to a higher thermal conductivity during the cooling of the sample, as shown in Fig. 54(b). A description of the measurement device can be found in the work of Rezaei et al. [246]. Anderson et al. [361] give another explanation for the strong increase at higher temperatures: Thermal radiation is causing an increase, at temperatures above 500 °C. Their measurements show a strong increase at around 1200 °C, which might also be due to fusion of the sample. The samples of Rezaei et al. [246] did not show a significant change in porosity after cooling. They explained the increased thermal conductivity during cooling by sintering, which caused a better connectivity between the individual particles, but only a slight change in porosity. Zbogar et al. [273] give a further explanation, based on changes in emissivity upon structural changes.

Not much literature is available on the influence of **particle size** on heat conductivity. Rezaei et al. [246] sieved two coal ash samples to particles smaller than $d_p < 45$ μm and between $45 \leq d_p < 106$ μm.

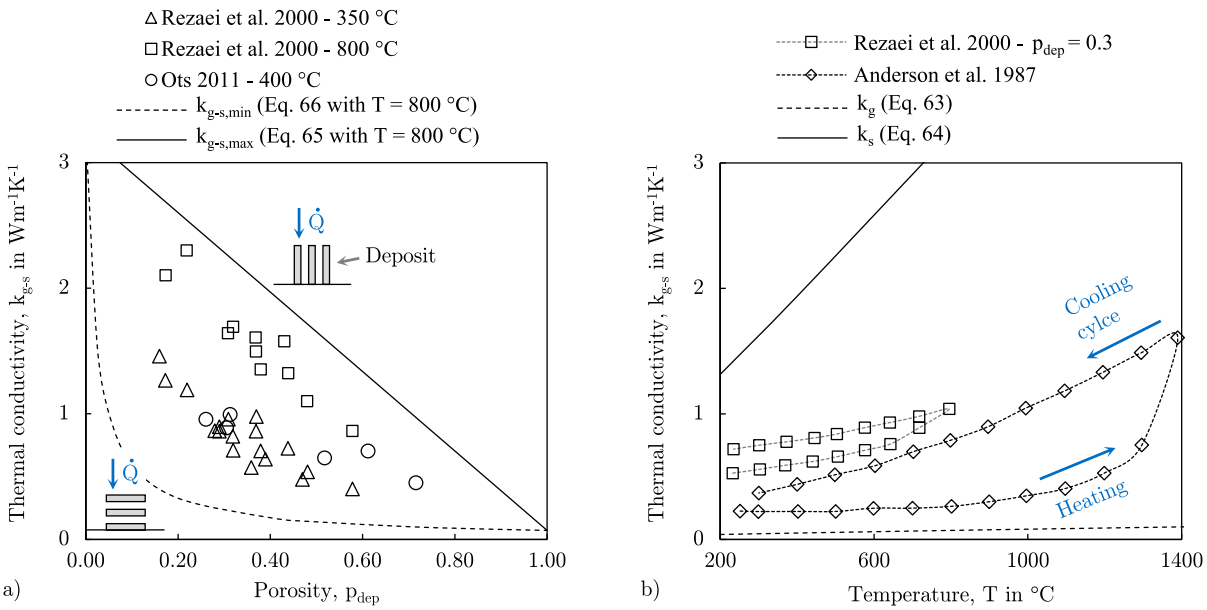

Fig. 54. Thermal conductivity and its theoretical boundaries: (a) as a function of porosity and (b) as a function of temperature (measurements taken from Rezaei et al. [246], original data also from Anderson et al. [361]).

Both unsintered ash samples show an increased thermal conductivity by 30% to 100%, when coarse particles are used. But the authors do not explain this behavior. The review of Zbogar et al. [273] found an increase with increasing particle size at higher temperatures, whereas at low temperatures no change is observed. A possible explanation are changed radiative properties for larger particles. Wall et al. [362], found a sharp decrease in deposit absorbance, α_{dep}, for an initial layer composed of small, sub-micron particles. They further state that small particles reflect most of the incident radiation, whereas large particles show a high absorbance.

The influence of the **chemical composition** dominates the sintering and melting behavior of ash deposits and therefore also its structure and thermal conductivity. Rezaei et al. [246] found only small changes at identical sample porosities. But they refer to the glass industry, where correlations were developed yielding an equation for a composition-dependent thermal conductivity [366]. Raask [12] found a lowered sintering temperature for iron-rich slags, and, thus, an increased thermal conductivity. This is confirmed by comparing thermal conductivities of different materials, as shown in Table 11. It can be seen that glasses (silica-rich) have a considerably lower thermal conductivity, compared to magnetite (Fe_2O_3). A volume-weighted correlation might be suitable to calculate the thermal conductivity of the mixture [273,362]. Wall et al. [367] also state that the chemical composition affects emissivity. The presence of coloring agents, such as iron, leads to an increased absorptivity, and, thus, a higher deposit temperature, which then influences sintering and deposit properties. An interesting approach is presented by Mills et al. [368] relating the thermal conductivity of a solid ash particle k_p at room temperature to its chemical composition. The authors use NBO/T ratio, defined as the ratio of non-bridging oxygens to tetrahedral/bridging oxygens in a melt (see [14] or the Appendix A, Eq. (176)), in order to relate chemistry with the experimental data:

$$k_p = \exp[-0.424 + 0.00002 \cdot \exp(Q/0.299)] \quad \text{with} \quad Q = 4 - NBO/T \tag{61}$$

where the Q value is related to the NBO/T ratio. Eq. (61) is valid in the range of $2 < Q < 3.3$ [368]. With this equation, increased thermal conductivities are predicted when the iron content increases. However, more experimental evidence is needed and the range is very limited.

Radiative properties are difficult to measure and influenced by a number of parameters. They depend on temperature, wavelength of radiation, structure of the deposit, average particle size and its chemical composition. Often, deposit emissivity is treated as a gray body (not a function of wavelength) and as opaque (transmissivity equals zero). Wall et al. [367] state that a deposit must have a thickness of 1 mm or more in order to be considered as opaque. Furthermore, an increased particle size in a deposit leads to a higher emissivity [370]. On the contrary, the emissivity of ash particles strongly depends on iron and residual carbon content. If both, Fe and C, are present, reported emissivity values are considerably higher. Burning char particles show values around $\varepsilon_p = 0.9$ depending on char conversion and mineral matter content. Literature values show large variations due to the heterogeneity of particles and deposits as well as the dependence on many process parameters. Typical values for deposit and particle emissivities are given in Table 12.

A mathematical description of thermal conductivity through porous media or a packed bed often applies so-called “unit cell” or

Table 11
Thermal conductivity k_s of different solid materials at a temperature of $T = 400°C$.

Material	k_s in $Wm^{-1}K^{-1}$	when $T\uparrow$	Reference
Quartz (fused) SiO_2	1.6–2.2	↗	Powell et al. [363]
Polycrystalline Al_2O_3	1.0–1.4	↗	Powell et al. [363]
Soda-lime glass	1.8	↗	Kingery [364]
Ferrous Oxide FeO	5.0	↘	Takeda et al. [365]
Magnetite Fe_2O_3	8.0	↘	Takeda et al. [365]

Table 12
Emissivity ε for different materials and their temperature dependence in combustion systems.

Material	ε	when $T\uparrow$	Reference
Char particle	0.85–0.95	↘	Rego-Barcena et al. [369]
Ash particle	0.6–0.95	↘	Boow and Goard [370]
Particulate deposit	0.5–0.8	↘	Mulcahy et al. [371]
Sintered deposit	0.6–0.8	↓	Mulcahy et al. [371]
Fused deposit	0.75	–	Mulcahy et al. [371]
Slag	0.85–0.90	–	Boow and Goard [370], Wall et al. [378]

Table 13
Thermal conductivity models and their characteristics (UC stands for "unit cell" and SE for "semi-empirical" models).

Model	Type	Characteristics
Nimick and Leight [379]	UC	developed for granular porous media
Hadley [380]	UC	suggested by Zbogar [273] for sintered deposits
Brailsford and Major [381]	UC	best results for particulate deposits (see Fig. 55)
Yagi and Kuni [382]	SE	suggested by Zbogar [273] for particulate deposits
Robinson et al. [358]	SE	two layer approach considering sintering

"pseudo-homogeneous" models; see also the review of Zbogar et al. [273]. The difference between both is the treatment of thermal radiation. "Unit cell" models treat radiation as a local effect taking place between adjacent particle surfaces and voids in the unit cell [273]. They either add the radiative conductivity by

$$k_{eff} = k_{g-s} + k_{rad}, \tag{62}$$

where $k_{g\text{-}s}$ is the effective thermal conductivity through the porous media, and k_{rad} is the increase in thermal conductivity by thermal radiation. Or they include the radiative conductivity as a resistance in the network. "Pseudo-homogeneous" models consider packed beds to be a continuum for radiation, where the bed is often assumed to be a pseudo-homogeneous medium, in which radiation can penetrate freely [273]. An estimation of theoretical boundaries for thermal conductivities can be achieved by comparing the gas k_g and solid k_s thermal conductivity. Rezaei et al. [246], suggest the following empirical, temperature-dependent correlation, for the flue gas thermal conductivity k_g:

$$k_g = 0.00038 \cdot T^{0.75}. \tag{63}$$

This equation is illustrated in Fig. 54(b) as the lower boundary (dashed line) and roughly yields temperature-dependent values for air. The solid thermal conductivity k_s (also shown in Fig. 54(b) by the continuous line) is the upper boundary when the deposit has no porosity. It can be estimated by [246]:

$$k_s = 0.0015 \cdot T^{1.1} \tag{64}$$

Both Eqs. (63) and (64) can then be applied to calculate theoretical boundaries for heat conduction of packed beds. The upper boundary is given by heat transfer in the direction of parallel layers of gas and solid material. Fig. 54(a) shows this curve as a continuous line. A mathematical expression is given by:

$$k_{g-s,max} = p_{dep} \cdot k_g + (1 - p_{dep}) \cdot k_s, \tag{65}$$

where, p_{dep} is the porosity of the deposit layer. The lower boundary is expressed by (dashed line in Fig. 54(a)):

$$k_{g-s,min} = \frac{k_g}{p_{dep} + \frac{1-p_{dep}}{k_s/k_g}}. \tag{66}$$

Different models were developed for calculating the thermal conductivity of packed beds. Most common ones, are summarized in Table 13. Mathematical descriptions are given in the review of Zbogar et al. [273]. A comparison of model predictions and measurements available in literature, is given in Figs. 55(a) and (b). It can be seen that best agreement is achieved by the model of Brailsford and Major [381]. At both, low and high temperatures, predictions follow measurements of Rezaei et al. [246] well. Brailsford and Major [381] developed a unit cell model and derived the following complex expression:

$$k_{g-s} = \frac{[3(1-p_{dep})-1]k_s + (3p_{dep}-1)k_g + \left\{[(3(1-p_{dep})-1)k_s + (3p_{dep}-1)k_g]^2 + 8k_s k_g\right\}^{0.5}}{4} \tag{67}$$

An estimation for the radiative conductivity is given by the following equation:

$$k_{rad} = 4 \cdot \sigma \cdot \chi \cdot d_p \cdot T^3 \tag{68}$$

where d_p is the mean particle diameter of the deposit and χ is the radiative exchange factor. It can be calculated using the equation suggested by Godbee and Ziegler [383]: $\chi = \varepsilon_{dep}/(1 - p_{dep})$, where ε_{dep} is the deposit emissivity. Many other radiation exchange factors have been proposed. They are summarized by Zbogar et al. [273]. Best results are obtained with Eq. (68). Figs. 56(a) and (b) compare the effective thermal conductivity considering both radiation and conduction through a porous media. Measurements of Mulcahy et al. [371] can be fitted with a deposit porosity of $p_{dep} = 0.55$, an emissivity value of $\varepsilon_{dep} = 0.8$ and a relatively large particle size of $d_p = 350\,\mu m$. The measurements of Anderson et al. [361] could not be reproduced adequately with the given equations. Deviations are probably due to changing structures during heating such as sintering and fusion. These are often reported to be more important than increased heat conduction through radiation [273].

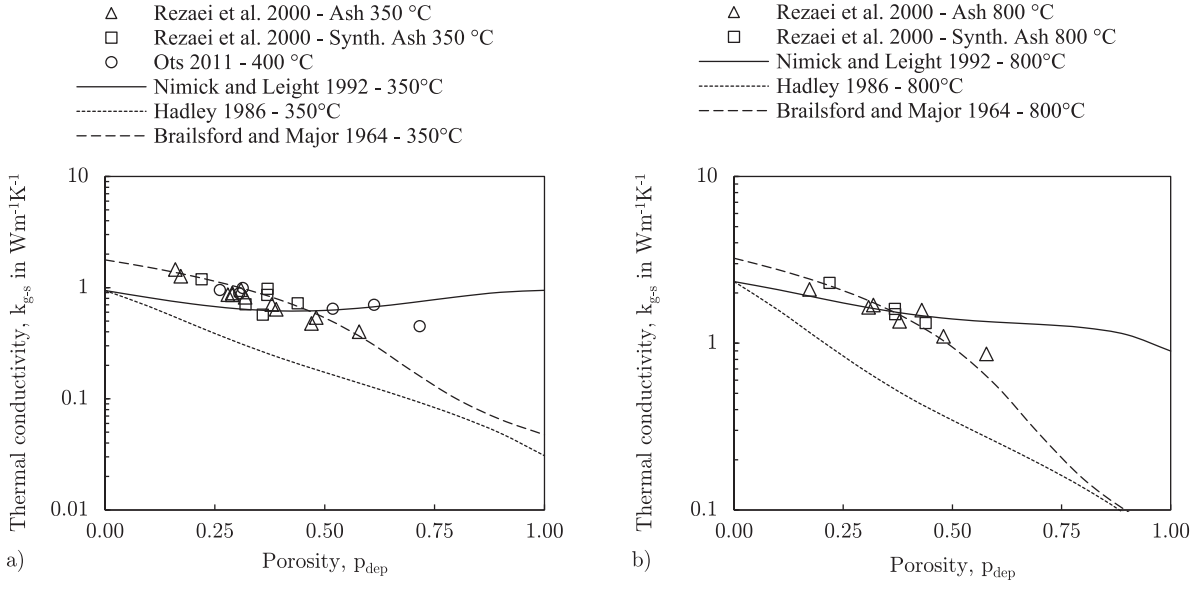

Fig. 55. Comparison of thermal conductivity models with measurements: (a) for low temperatures, and, (b) for higher temperatures.

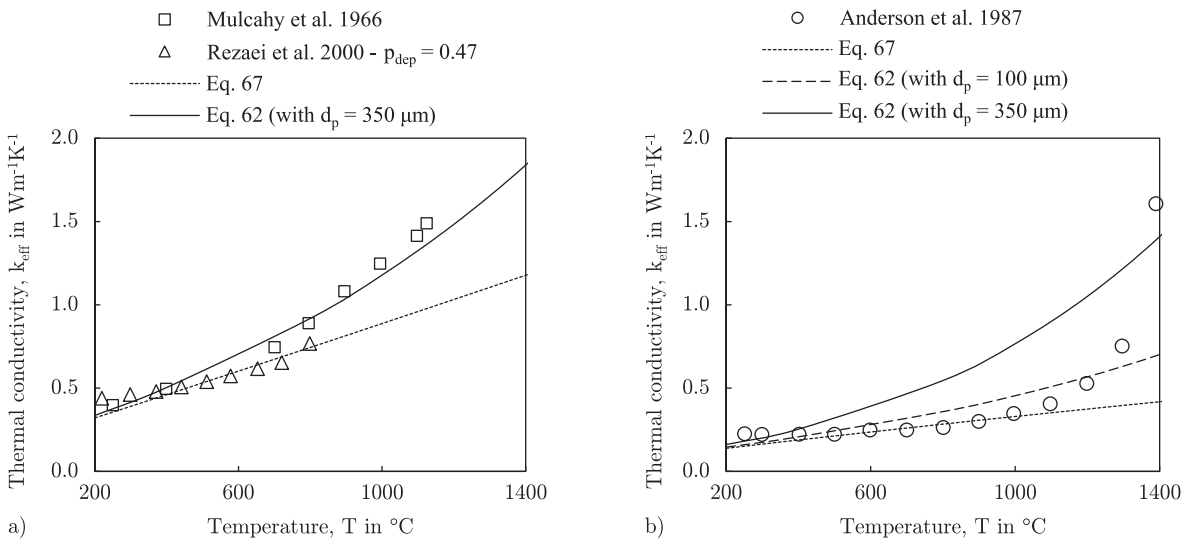

Fig. 56. Comparison of thermal conductivity models including radiation with measurements of: (a) Rezaei et al. [246] and Mulcahy et al [371], (b) from Anderson et al. [361]. Eqs. (62), (67) and (68) are calculated with $\varepsilon_{dep} = 0.8$.

3.10. Aerosol properties

Particles in the sub-micron size range exhibit some interesting phenomena. For instance, the melting temperatures of nanoparticles starts to decrease [376]. Fig. 57(a) shows the melting temperature of aluminum particles as a function of particle size. Different theoretical studies are in agreement with measurements of Eckert et al. [373]. The melting temperature of aluminum starts to decrease down to values of 200 °C for particles in the size range of 10 nm, compared to melting temperatures of 660 °C of bulk aluminum. Other studies reported a decrease in surface tension for nanoparticles. The surface tension of aerosol depends on the so-called Tolman-length δ_{Tol} [377]. Both effects are often studied theoretically since measurements in this size range are highly complex and require high efforts. The role of such effects is questionable. Section 2.3.3 on aerosols has shown that the majority of submicron particles is found in the size range of $d_p \approx$ 100–200 nm, probably as agglomerates of smaller particles. If these agglomerates have primary particles below 50 nm, effects can become relevant. However, uncertainty is high and more studies in this field are needed.

4. Ash particle sticking behavior

The probability of an ash particle adhering to a surface – also referred to as substrate – needs to be described by mathematical models. Particle impaction on a substrate is mainly dependent on properties of the particle and the surface. The following list summarizes main parameters influencing particle sticking behavior:

- particle properties such as melt fraction, viscosity, surface tension/energy,
- particle kinetic energy and its deformation upon impaction,
- particle shape and surface roughness,
- the angle of impaction,
- substrate roughness and geometry,
- substrate properties, such as melt fraction, viscosity, surface tension/energy, and
- forces between particles and the surface (e.g. adhesion or van der Waals forces).

Fig. 58 shows five possible scenarios of a particle (molten, partially molten or solid) impacting on a clean, solid substrate. The

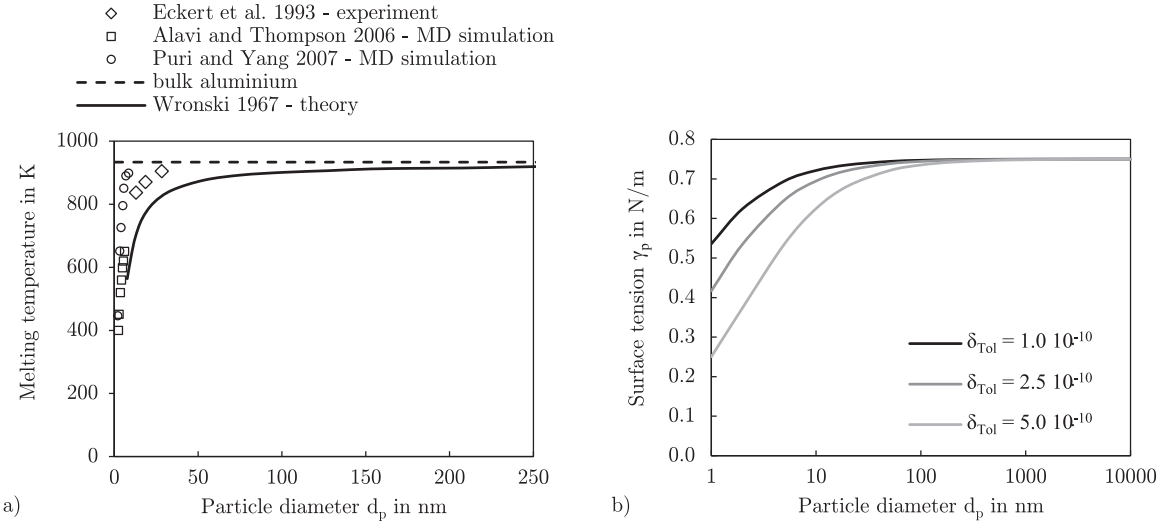

Fig. 57. Nanoparticle properties: (a) melting temperature of aluminum particles as a function of particle diameter (taken from Huang et al. [372], original data from [373–376]; MD: molecular dynamics simulation), and (b) surface tension as a function of particle diameter (adopted from Jöller [176]).

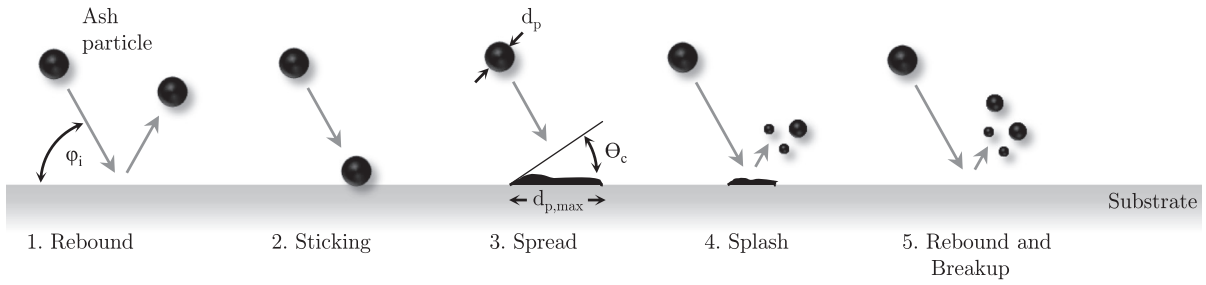

Fig. 58. Particle impaction on a solid substrate: possible phenomena.

particle impacts at an angle φ, with a well-defined kinetic energy. The particle kinetic energy $E_{p,kin} = 1/2 \cdot m_p \cdot v_p^2$, without rotational energy, depends on the particle mass m_p and its velocity v_p. A particle will remain on the surface (2), if its kinetic energy is dissipated during the collision. If the particle kinetic energy is higher than the energy dissipated during collision, it will rebound (1) [290,384,385]. The dissipation of energy can be due to deformation, friction between particle and surface, or adhesion [222]. Typically, it is distinguished between an elastic and an inelastic – sometimes referred to as plastic – collision. An elastic collision is defined as a collision of two bodies, where there is no loss in kinetic energy. The kinetic energy of two bodies after collision equals to their total kinetic energy before the encounter. This type only occurs in theory, when there is no conversion of kinetic energy into other forms such as heat. An inelastic collision, in contrast, is a collision in which kinetic energy is converted in other forms. There are energy losses due to e.g. internal friction, plastic deformation, vibrations and others. Ash particles occur as pure solids, liquids and mixtures [323], and are therefore assumed to collide inelastic, with and without plastic deformation. Examples of collisions with plastic deformation are particles with low viscosity values at high temperatures spreading during impact (3). Particles deform at the surface and retain their deformed shape, either due to cooling and solidification, or low surface tensions. The maximum spread diameter $d_{p,max}$ is frequently used to describe this phenomenon. This type of impaction can be identified by deformed ash particles found in the cross-section of a deposit. Splash (4) or rebound with breakup (5) are not reported for ash particles due to their relatively high viscosity and high surface tension.

The forces acting on a particle settled on a substrate are shown in Fig. 59. The particle is in contact with the surface, forming an interface, which depends on particle and surface properties. The contact diameter $d_{p,max}$ (also called spread diameter) mainly depends on the particle viscosity, surface tension/energy and roughness. The contact angle Θ_c is typically large for ash particles, which indicates poor adhesiveness, low wettability due to high surface tension, and low free surface energy. This behavior can also be observed for a liquid water droplet on a hydrophobic surface. The forces acting on the particle can be divided into forces acting parallel and perpendicular

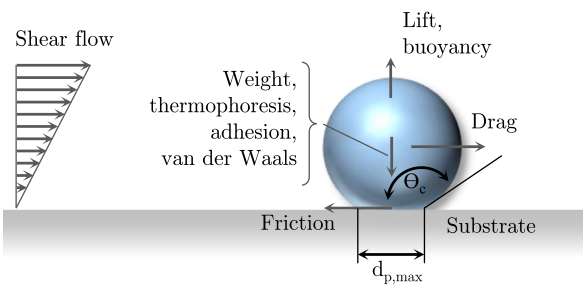

Fig. 59. Forces acting on a settled particle (modified and extended from Abd-Elhady and Malayeri [386], originally from Cabrejos and Klinzing [387]).

to the substrate. Parallel forces are drag, friction and shear forces induced by the flow in the boundary layer. Perpendicular forces are lift, buoyancy, gravity, thermophoresis, and surface forces, being caused by adhesion or van der Waals forces. Depending on the geometry, forces can act in different directions, in particular for a superheater tube. Another parameter affecting particle sticking can be due to shock cooling upon impaction on the surface. The temperature difference between flue gas and clean heat exchanger can be as high as $\Delta T = T_\infty - T_W = 500$ K, leading to a rapid cooling of ash particles within the boundary layer and/or during the impaction. Here, the Biot number plays an important role, whether there is a temperature gradient inside the particle ($Bi > 0.1$), or not ($Bi \leq 0.1$). The Biot number is defined as $Bi = h \cdot d_p / k_p$, where h is the total heat transfer coefficient between particle and flue gas. The effects taking place in the boundary layer are rarely addressed in literature. Despite this lack, many different particle sticking criteria have been developed. They can be classified in three main groups - sticking criteria based on the **melt fraction** of a solid particle, based on the particle **viscosity** or based on **energy conservation** during the collision.

4.1. Critical melt fraction

This criterion uses the melt fraction of a particle to judge its sticking probability. Is the melt fraction above a critical value, a particle is assumed to adhere. While pure substances melt at a defined temperature, multi-component systems can melt over a wider temperature range. Often, thermodynamic equilibrium calculations are carried out for multi-component system to calculate the melt fraction based on composition and temperature. See for example the work of Wieland et al. [312] who calculated the melting curves for two coal ashes (Pittsburgh #8 and El Cerrejon). Isaak et al. [388,389] were the first to propose the melt fraction as a sticking criteria for salt particles in black liquor combustion systems (black liquor is a Na-rich residue of the pulp and paper industry). Müller et al. [202] used thermodynamic equilibrium calculations for synthetic salt mixtures. Another method is to use simultaneous differential thermal analysis, where the melting curve is measured in a thermo-gravimetric analyzer (TGA). Wieland et al. [312] also conducted this method for coal ashes of the Pittsburgh #8 and El Cerrejon. Müller et al. [202] use a critical melt fraction of $f_{p,crit} = 15\%$, at which particles are assumed to adhere. They measured deposition rates on a cooled probe (550 °C) in an entrained flow reactor maintained at 1000 °C and a flow velocity of 2 m/s. Different salt particles are used and 50 g are fed over a time interval of 40 min. They further used numerical simulations to calculate deposition rates on the cooled probe. Müller et al. [202] found that the deposit layer will grow until the surface temperature reaches a value at which 70% are molten. At this point, they assume an equilibrium between incoming particles and deposit flowing off. The sticking probability p_{stick} is defined as:

$$p_{stick} = \begin{cases} 0 & \text{for } f_p = 0 - 0.15 \\ 1 & \text{for } f_p = 0.15 - 0.7 \\ 0 & \text{for } f_p = 0.7 - 1 \end{cases} \quad (69)$$

The numbers of $f_p = 0.15$ and $f_p = 0.7$ are not universal numbers, and different values can be used instead. A comparison between numerical simulations and experiments shows a good correlation for particles smaller than 75 μm. For larger particles, predictions overestimate the mass deposited. Müller et al. [202] infer that the critical melt fraction is not applicable for larger particles. They suggest an energy criterion based on the work of Mao et al. [390] (see Section 4.3), which yielded better results.

Zhou et al. [391] developed a mathematical model describing the deposit build-up over time. It goes back to work of Hansen et al. [392] and Kær [393]. They apply a critical melt fraction model for particles larger than $d_p > 10\,\mu m$, in which particles are treated as sticky once they reach $f_p \geq 10\%$. Zhou et al. define a sticking probability for particles between $10\% < f_p \leq 70\%$. In this region, the sticking probability increases linearly. Unlike Müller et al. [202], every particle above $f_p > 70\%$ is assumed to stick. Eq. (70) summarizes their model:

$$p_{stick} = \begin{cases} 0 & \text{for} \quad f_p = 0 - 0.1 \\ \dfrac{f_p}{0.6} - \dfrac{0.1}{0.6} & \text{for} \quad f_p = 0.1 - 0.7 \cdot \\ 1 & \text{for} \quad f_p = 0.7 - 1 \end{cases} \tag{70}$$

Particles between $10\% < f_p \leq 70\%$ are assumed to show splash behavior (Nr. 4 in Fig. 58). Only part of the ash particle adheres to the wall, while the remaining mass rebounds. A decrease in deposited mass is described by slag flow and drop-off as well as erosion. They use a dynamic mathematical model, which is based on a set of equations and estimations. It is not coupled to CFD, and needs many input parameters, such as particle concentration, velocity and size. Nevertheless, their results show good agreement with experimentally observed deposition rates from a grate-fired boiler using straw as a feedstock. There are further studies using particle sticking criteria based on a critical melt fraction. Akbar et al. [258] uses a similar criterion as Müller et al. [202], however, they do not provide a sticking probability above $f_p = 70\%$. They studied the deposition behavior of KCl particles from biomass combustion in an entrained flow reactor using a cooled deposition probe with a temperature of 650 °C. Their modeling results indicate the dominant role of condensation effects during early stages in biomass-fired systems. Brink et al. [394] used the melt fraction predicted by TEC in order to describe the particle stickiness. The maximum temperature a particle has experience in the flame is assumed to control the amount of amorphous slag phase. This history based approach is an interesting aspect, which should be included in modeling studies, ideally in a comprehensive ash formation model.

4.2. Critical viscosity

Another frequently applied particle sticking criterion is based on the viscosity of ash particles. Particles are softer and stickier at lower viscosity values. Different approaches have been proposed in the literature.

A viscosity-based sticking criterion for ash particles was first proposed by Walsh et al. [395]. They carried out ash deposition tests of two bituminous coals, at the MIT combustion tunnel, with a heat input of 1.5 MW_{th}. The gas temperature at the deposition probe was in the range of 1450–1480 °C, the probe was maintained at 540 °C, and the gas velocity had a value of $v_g = 15$ m/s [395]. The sticking probability is calculated by:

$$p_{stick} = \begin{cases} \dfrac{\mu_{p,ref}}{\mu_p} & \text{for } \mu_p > \mu_{p,ref} \\ 1 & \text{for } \mu_p \leq \mu_{p,ref}, \end{cases} \tag{71}$$

where the reference viscosity $\mu_{p,ref}$ is typically determined in experiments. Particles with a viscosity above the reference viscosity are again treated as a partially sticking particles, and the fraction remaining on the surface is calculated by $\mu_{p,ref}/\mu_p$. This approach was applied in several studies, however, inaccuracies in the use emerged. Often, a binary sticking criterion was used instead, where $\mu_{p,crit}$ is the critical viscosity, at which sticking of particles starts to occur. Above this critical value, particles are assumed to rebound. It is defined as:

$$p_{stick} = \begin{cases} 0 & \text{for } \mu_p > \mu_{p,crit} \\ 1 & \text{for } \mu_p \leq \mu_{p,crit}, \end{cases} \tag{72}$$

where $\mu_{p,crit} \neq \mu_{p,ref}$. Richter [222] estimates the following relation $\mu_{p,ref} = 0.01 \cdot \mu_{p,crit}$ between reference and critical viscosity. Table 14 summarizes reference and critical viscosity values, found in literature. A large variation between 2 and 10^9 Pa · s, can be seen. This variation can have several reasons. The chemistry and melting behavior can have an influence, where at a given viscosity one particle is sticky and another is not. Another reason could be different particle velocities. Studies with low critical/reference viscosity used relatively high particle velocities (Walsh et al. [395] with 15 m/s and experiments of Liebetruth et al. [396] are estimated around 8 m/s). This would indicate a dependence on particle kinetic energy. Another problem is the use of bulk ash chemistry and bulk ash viscosity values. Bulk ash can have significantly higher viscosities compared to individual ash particles forming low-melting eutectics for example. A large number of modeling studies use bulk ash chemistry and results can be misleading.

Table 14
Comparison of different reference and critical viscosity values reported in literature.

Reference	Reference viscosity $\mu_{p,ref}$ in Pa · s	Notes and comments
Walsh et al. 1990 [395]	8	for two US bituminous coals
Kær 2001 [393]	10^3	high silica particles
Liebetruth et al. 2002 [396]	2	for German lignite
Beckmann et al. 2016 [397]	17-25	for Middelburg coal (17 Pa · s was measured)
	Critical viscosity $\mu_{p,crit}$ in Pa · s	
Boow 1972 [399]	10^4–10^8	measured deposit viscosity at 700 - 1100°C
Wibberley and Wall 1982 [406]	10^5–10^7	for a Na-silicate film on fly ash particles at 870 K
Srinivasachar et al. 1990 [1]	10^5–10^8	soda-lime glass particles with varying size
Srinivasachar et al. 1992 [407]	10^5	for four western US coals
Richards et al. 1993 [408]	10^5	modeling study
Yilmaz and Cliffe 1997 [409]	$6.7 \cdot 10^9$	soda-lime glass experiments
Costen et al. 2000 [410]	10^5	for a bituminous coal
Rushdi et al. 2005 [411]	10^8	adopted from other studies
Laycock and Fletcher 2012 [412,413][a]	170 / 610	different values calculated based on ash chemistry

[a] small particle sizes: $d_p = 3$ and 13 μm and high gas velocities: $v_g = 200$ m/s.

Srinivasachar et al. [1] conducted experiments with soda-lime glass particles. The advantage of such a material is that there are no particle-to-particle variations in density, structure or chemical composition, and it has a well-known temperature-viscosity curve. Furthermore, it is reported to behave similar to coal ashes [1]. They used a heated laminar flow furnace, and placed the deposition probe in a conical section. The fluid velocity can be set by changing the position within this conical section. Narrow-sized soda-lime glass particles (28–53 and 53–74 μm) were used to fix particle kinetic energy. At a given kinetic energy, the temperature in the system is varied and the threshold, at which sticking begins is determined. This temperature corresponds to the critical viscosity value. Fig. 60 shows the particle kinetic energy $E_{p,kin}$ as a function of critical viscosity $\mu_{p,crit}$. With increasing particle kinetic energy, a lower particle viscosity and thus higher temperature is needed for a particle to stick. In other words, the smaller a particle the higher its sticking

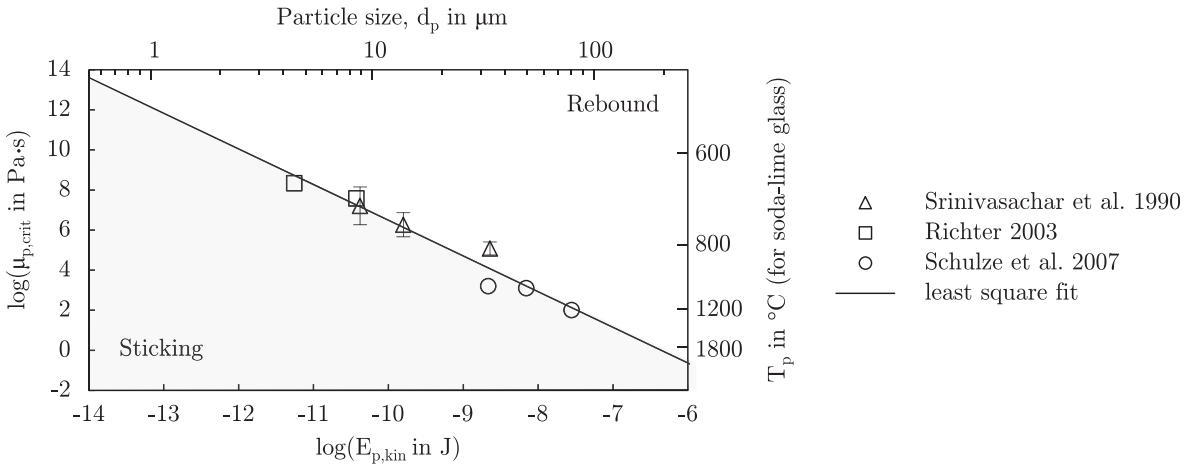

Fig. 60. Critical particle viscosity as a function of particle kinetic energy (points adopted from Srinivasachar et al. [1], Richter [222] and Schulze et al. [201]). Particle diameters are calculated with $v_p = 10$ m/s and $\rho_p = 2.4$ g/cm^3, and corresponding particle temperatures for viscosity values are given for soda-lime glass.

probability at a given temperature and chemical composition. Richter [222] did similar experiments in an entrained flow reactor with lower particle velocities and confirmed this relationship. A third study was conducted at the Energy Research Center of the Netherlands (ECN) with higher particle velocities and a cooled steel probe [201]. An overview of experimental conditions is given in Table 15. The following empirical correlation can be derived from the data points by a least square fit. The critical viscosity is a power-law function of the particle kinetic energy,

$$\mu_{p,crit} = A \cdot E_{p,kin}^{B} = 5 \cdot 10^{-12} \cdot E_{p,kin}^{-1.78}, \tag{73}$$

where coefficients A and B are determined from Fig. 60. The particle viscosity is then used in combination with Eqs. (72) and (73). Particles stick to the surface, if the calculated particle viscosity is below the critical viscosity, and rebound if $\mu_p > \mu_{p,crit}$. Fig. 60 also shows corresponding particle sizes for an exemplary velocity of 10 m/s (secondary horizontal axis), and the equivalent temperature to viscosity values of soda-lime glass particles (secondary vertical axis). Experiments for very small particles are missing. A further binary sticking criteria was proposed by Richards et al. [408]. They define a particle as sticky, when the particle viscosity is below the ash melting viscosity. However, the melting viscosity is difficult to determine and various definitions exist in literature. The criterion uses again the bulk ash and not the individual chemical composition of fly ash particles.

4.3. Energy conservation and critical velocity

A further method is based on energy conservation of a particle, during impact. This method was often applied for solid particles impacting a smooth, flat surface using contact mechanics, or in the field of liquid droplets impinging on a smooth wall. The main difference is the particle/droplet deformation. In the case of solid particles, the impaction process involves elastic deformation and depending on the particle kinetic energy and the material properties also plastic deformation. On the contrary, elastic deformation is negligible during liquid droplet impact. Droplets deform heavily and might break-up. Therefore, the focus is on the energy dissipation due to particle deformation, the particle break-up and phenomena occurring when substrate and particle temperature differ significantly.

4.3.1. Solid particle impacting a solid smooth surface

The energy balance is used to calculate critical parameters, such as the critical velocity. If the particle velocity is smaller than this critical value, particles stick, in all other cases particles rebound. The particle velocity can either be the absolute value v_p, or the normal component $v_{p,n}$ relative to the surface, which becomes important for oblique (non-normal) impacts, e.g. on a superheater tube. An energy balance, which might be suitable for ash particle impaction is given by the following equation:

$$E_{kin,i} + E_{surf,i} = E_{def} + E_{ad} + E_{surf,r} + \cancel{E_{kin,r}}^{0, \text{ if particle sticks}} \tag{74}$$

The parameters in Eq. (74) are the particle kinetic energies E_{kin}, the particle surface energies E_{surf}, the work of viscous dissipation (deformation) E_{def}, and the work of adhesion E_{ad}. The index "i" stands for initial conditions of impacting particles and "r" for rebounding particles. Particles stick, if the kinetic energy on the right equals zero. Further energies involved, such as potential energy, rotational energies of the particle, energy due to van der Waals forces between two solids or elastic wave propagation (during collision, when part of the energy is radiated into the substrate as elastic waves) are often neglected [390]. Eq. (74) can then be applied to calculate critical parameters, such as the critical velocity $v_{p,crit}$, and evaluate the

Table 15
Experimental conditions for particle sticking tests using soda-lime glass.

Study	d_p in µm	v_p in m/s	$log_{10}(\mu_{p,crit})$ $\mu_{p,crit}$ in Pa · s	T_p in °C	comment
Srinivasachar et al. [1]	40.5	1	7.2	683	uncooled probe
	40.5	2	6.3	733	uncooled probe
	63.5	4	5.1	810	uncooled probe
Richter [222]	43.5	0.33	8.3	609	uncooled probe
	81.5	0.33	7.6	632	uncooled probe
Schulze et al. [201]	71	3.1	3.2	1010	cooled probe
	105	3.1	3.1	1020	cooled probe
	105	6.2	2.0	1190	cooled probe

sticking probability in the following form (with $E_{kin,r} = 0$):

$$p_{stick} = \begin{cases} 0 & \text{for } v_p > v_{p,crit} \\ 1 & \text{for } v_p \le v_{p,crit} \end{cases} \quad (75)$$

Thornton and Ning [290], use a simplified energy conservation equation to describe the stick-bounce behavior of adhesive, elastic-plastic spheres. The energy conservation equation is defined as

$$\frac{1}{2} \cdot m^* v_i^2 = \frac{1}{2} \cdot m^* v_r^2 + E_{ad}, \quad (76)$$

where v_i and v_r are the velocities before and after the impact. The parameter E_{ad} describes the work of adhesion and m^* stands for the equivalent mass of both impact partners "1" and "2" and is calculated by

$$\frac{1}{m^*} = \frac{1}{m_1} + \frac{1}{m_2}. \quad (77)$$

If the particle collides with a tube with significantly higher mass, m^* equals the particle mass. Thornton and Ning [290] derived an equation for a sphere impacting on a flat substrate. They express the work of adhesion as a function of particle and substrate properties, and rewrite Eqs. (76) and (77) to

$$v_{p,crit} = 1.84 \cdot \left(\frac{\left(\frac{\Gamma^*}{r_p}\right)^5}{\rho_p^3 \cdot (E^*)^2} \right)^{\frac{1}{6}}, \quad (78)$$

where r_p stands for the particle radius and the equivalent Young's modulus E^*, is obtained by the following equation,

$$\frac{1}{E^*} = \frac{1 - \nu_1^2}{E_1} + \frac{1 - \nu_2^2}{E_2}, \quad (79)$$

with E_1, E_2 and ν_1, ν_2 being the Young's Modulus and Poisson's ratio of each collision partner. Thornton and Ning [290] do not give an expression for the interface energy Γ^*. Losurdo et al. [342] use the Young-Dupré equation, for liquid droplets on a solid substrate, in the form of:

$$\Gamma^* = \gamma_1 + \gamma_2 - \gamma_{12} \cdot cos\ \Theta_c, \quad (80)$$

where γ_1 and γ_2 are the surface energy (solids) or the surface tension (liquids) of the collision partners. The parameter γ_{12} is the interfacial tension between two partners, and Θ_c is the contact angle. The model of Thornton and Ning [290] is also able to describe the contact of incoming particles, with particles deposited on a substrate. This equation differs from Eq. (78) and can be found in their publication. Losurdo et al. [342] use Eq. (78) and derive a simple expression, where the critical velocity is estimated by $v_{p,crit} = 0.0001 \cdot v_p$. They then calculate the total rebound velocity $v_{tot,r}$ of a particle by:

$$v_{tot,r} = \sqrt{v_{n,r}^2 + v_{t,r}^2} = \sqrt{(e_n \cdot v_{n,i})^2 + (e_t \cdot v_{t,i})^2}, \quad (81)$$

where v_n, v_t and e_n, e_t are the normal and tangential velocity components and restitution coefficients. The calculation of the restitution coefficients is not given in their publication. If $v_{tot,r} \le v_{p,crit}$ the particle is assumed to stick. They applied this model to simulate glass particle deposition experiments, conducted at ECN, and also used in the study of Schulze et al. [201]. Glass particles in the size of 71–105 μm are injected in a lab-scale methane combustor. Particles are then collected on a steel tube maintained at 500 °C with a surrounding gas temperature of 1200 °C. The simulation shows adequate results and the authors recommend this model.

Wall et al. [414] compared literature data on the critical velocity below which the particle will adhere to the surface. The critical velocity strongly depends on the particle size, and increases with decreasing particle diameter. Different material combinations yield different slopes, ranging from −0.39 to −6.11 as shown in Fig. 61. Dong et al. [420] determined the critical velocity of fly ash particles on stainless steel, however, only at room temperatures. Their data show a strong dependence on the diameter with the highest slopes. A difficulty is the inhomogeneity in fly ash, where particles are not perfectly spherical and differ in chemistry. The authors report that the majority of fly ash particles is composed of quartz and mullite [420]. This data should be extended to higher temperatures, where the ash softens, and impact behavior changes. There is currently no theory incorporating all energies involved during impact and rebound, and thus being able to predict different rebound behavior shown in Fig. 61. Table 16 summarizes major experiment using solid particles impacting on a solid substrate. Typically, this data is used to set up and validate models including elastic and plastic deformation effects. Table 16 focuses on particle impaction studies with diameters and velocity values relevant for ash deposition. Again, studies using high temperatures are not available. Furthermore, the majority uses exotic materials, mostly polymers or metals, with limited application to ash deposition.

Brach and Dunn [428] derived a mathematical model for the impaction of micrometer-sized spheres, at moderate velocities and arbitrary angles of impaction on a flat substrate. According to the authors, the model can be applied for solids, for spheres in the transition regime between solid and liquid (i.e. viscoelastic, elastic-plastic), and other materials or combinations. Assumptions of this model, are that the processes of adhesion and material deformation, are independent of each other. They argue that energy loss due to adhesion only occurs during rebound [428]. The model is validated using experimental data from the impaction of ammonium fluorescein spheres against a molybdenum surface. The model is based on Newton's law, the conservation of momentum, and given by:

$$m_p \cdot (v_{n,r} - v_{n,i}) = P_n = P_{def} + P_{ext} - P_{ad}, \quad (82)$$

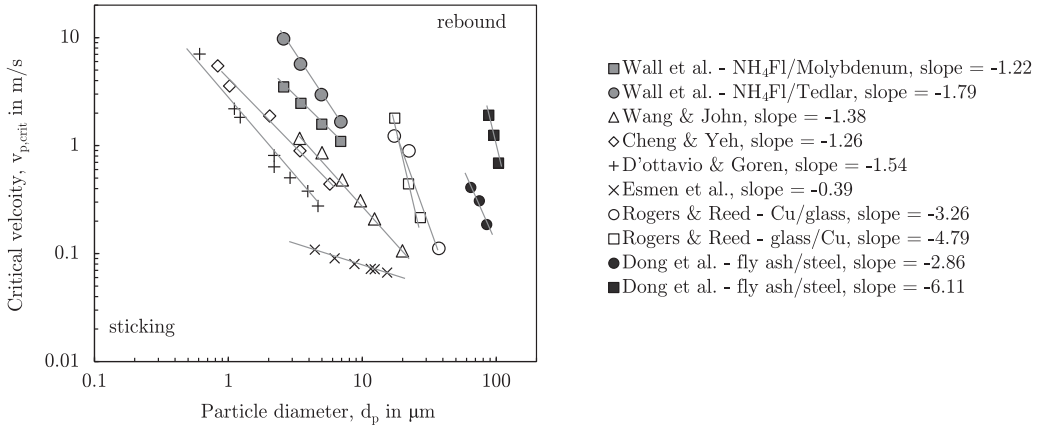

Fig. 61. Comparison of literature data showing the critical velocity as a function of particle size (figures reproduced and extended from Wall et al. [414], data from [414–421]).

Table 16
Overview on major particle impaction studies and their parameters (data taken and extended from Krijt et al. [422]).

Study Unit	d_p μm	v_p m/s	particle material	substrate material	Characteristics and Key Findings –
Dahneke 1975 [423]	1.27	2–15	polystyrene latex	quartz	bouncing behavior of normal
	2.02	5–35	polyvinyl-toluene	quartz	impact considering adhesion
Cheng and Yeh 1979 [416]	0.8–5.7	3.9–26	latex	stainless steel	impactor cascade
Rogers and Reed 1984 [418]	7.5–20	0–6	copper/glass	glass/copper	critical velocity determined for different material pairings
	15–32.5	0–6	copper/steel	steel/copper	
	5–10	0–6	steel/glass	glass/steel	
Wall et al. 1990 [414]	4.9	5–120	ammonium fluorescein	mica	broad spectrum of v_p including the plastic deformation regime;
	4.9	5–110	ammonium fluorescein	silicon	electrostatic forces are found to be negligible for adhesion
	4.9	3–16	ammonium fluorescein	tedlar	
	4.9	5–60	ammonium fluorescein	molybdenum	
Dunn et al. 1995 [424]	8.6	2–20	Ag-coated glass	aluminum	impact angle was studied ranging from 20 to 90°
	8.6	2–20	Ag-coated glass	copper	
	8.6	2–20	Ag-coated glass	steel	
	8.6	2–20	Ag-coated glass	coated steel	
Li et al. 1999 [425]	55	0.4–2	steel	silicon	same experimental setup as Dunn et al. 1995
	90	0.4–2	steel	silicon	
Kim and Dunn 2007 [426]	40	0.04–0.44	Ag-coated glass	silicate	model for CFD codes suggested
Sorace et al. 2009 [427]	3960	0.1–1	acrylic	acrylic	large sphere collision investigated
	3000	0.05–0.5	steel	steel	
	3000	0.05–0.5	ceramics	ceramics	
Dong et al. 2013 [420]	60–90	0.1–16	fly ash[a]	steel	coefficient of restitution & $v_{p,crit}$
Dong et al. 2013 [421]	88–104	0.1–16	fly ash[a]	steel	identical to previous study
Troiano et al. 2017 [456]	150–180	0.2–2.3	fly ash and char[b]	ref. material	hot and cold wall

[a] dominated by quartz and mullite.
[b] from wood chips and corn stover.

where P_n is the resultant normal impulse, P_{def} is the impulse due to particle deformation, P_{ad} is the impulse of the adhesion force and the impulse P_{ext} is caused by external forces such as van der Waals forces or electrostatic forces [428]. These external forces lead to a lower particle rebound velocity and therefore to a higher sticking probability. The proposed model does not include external forces, however, they can be incorporated. Another, external force might be caused by thermophoresis, which is not included in this study or any other study. By using expressions for the individual terms in Eq. (82), the authors describe the critical velocity by:

$$v_{p,crit} = \left[\frac{H \cdot \left(1 + \left(\frac{1}{tan\varphi}\right)^2\right)}{r_p \cdot R^2}\right]^{\frac{10}{7}}, \tag{83}$$

where φ is the angle of impaction in radians (see Fig. 58) and the parameter R relates the impulse of deformation before and after the contact. It can be approximated by $R = \sqrt{1 - E_{def}/E_{kin,i}}$. Brach and Dunn [428] fit R to measurements, where they found values of $0.952 < R \leq 0.983$ based on experiments with critical velocities in the range of $0.7 < v_{p,crit} \leq 3.14$ m/s. The variable H is a function of material properties, and is calculated by:

$$H = 0.51 \cdot \left[\frac{5 \cdot \pi^2 \cdot (k_p + k_w)}{4 \cdot \rho_p^{3/2}}\right]^{\frac{2}{5}}, \tag{84}$$

where k_p and k_w describe the elasticity of the particle and the wall. The particle elasticity can be expressed by $k_p = \left(1 - \nu_p^2\right)/(\pi \cdot E_p)$. The elasticity of the wall is derived analogously.

Konstandopoulos [429] examined literature data on experiments on non-normal impact and concluded the existence of a critical impact angle $\varphi_{p,crit}$. Below this angle, particles will rebound even if the criterion for the critical velocity: $v_{p,n} \leq v_{p,crit}$, given by Eq. (75), is fulfilled:

$$p_{stick} = \begin{cases} 0 & \text{for } \varphi_p < \varphi_{p,crit} \\ 1 & \text{for } \varphi_p \geq \varphi_{p,crit} \end{cases} \tag{85}$$

The critical angle $\varphi_{p,crit}$ shown in Fig. 62(a) is dependent on the material properties of the two collision partners. An expression is derived using an energy balance between the tangential kinetic energy of the particle and the minimum energy required to break its contact area with the surface according to:

$$tan\left(\frac{\pi}{2} - \varphi_{p,crit}\right) = \frac{v_{p,t}}{v_{p,n}} = \frac{f^*}{\left(32 \cdot \beta^3\right)^{1/2}} \sqrt{\frac{E^*}{G^*}} \approx 0.034021 \frac{f}{\beta^{3/2}} \cdot \sqrt{2\frac{2-\nu}{1-\nu}}, \tag{86}$$

where f^* is an effective friction coefficient either set to the friction coefficient itself f or $(1/3)^{3/2} f$ as suggested by Thornton [430], and E^*, G^* are the effective Young's modulus and effective shear modulus, respectively. Note, that the letter f is used for the friction coefficient instead of μ, since μ denotes viscosity in this study. The parameter

$$\beta = A_0/A \tag{87}$$

is defined as the ratio of the maximum possible contact area A_0 to the actual contact area A between two colliding objects (see therefore Fig. 77). The contact area A_0 can be calculated according to the Johnson-Kendall-Roberts (JKR) theory [431], explained and discussed later on in Section 5.1, with the following expression [429]:

$$A_0 = \left(\frac{9 \cdot \pi \cdot \gamma_p \cdot d_p^2}{4 \cdot E^*}\right)^{1/3}. \tag{88}$$

Konstandopoulos [429] furthermore investigated literature data on the maximum angle of deposition $\Theta_{max,dep}$ as depicted in Fig. 62. He showed that the critical angle along the cylinder circumference Θ_{crit} obtained when $v_{p,n} \leq v_{p,crit}$, is not the limiting angle until which particles will stick. The maximum angle observed in experiments is obtained by using particle trajectory calculations and Eq. (86). Experimental results are from the work of Aylor and Ferrandino [432], who studied the deposition of 15 - 30 μm pollen (ragweed and lycopodium) on glass rods of 3 - 10 mm diameter, and the work of Wang and John [419], who applied monodisperse ammonium fluorescin particles with a size range of 3.35 - 20 μm on stainless steel cylinders of 1.6 and 3.2 mm diameter. The data is illustrated in Fig. 62(b), showing the maximum deposition angle, as a function of the Stokes number. It can be seen that the angle to which particles

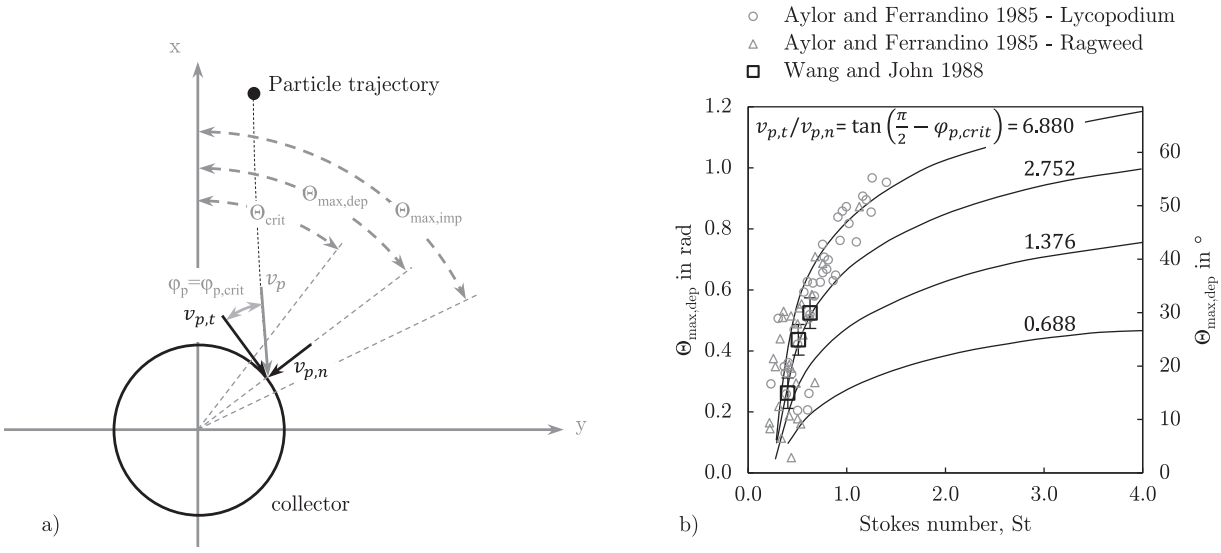

Fig. 62. Oblique impact and sticking criterion according to Konstandopoulos [429]: a) comparing normal and oblique impact angles (shown angle φ_p equals $\varphi_{p,cirt}$ since the particle impacts at the maximum angle, at which sticking can occur $\Theta_{max,dep}$), and b) dependence of $\Theta_{max,dep}$ on the Stokes number St for different values of $v_{p,t}/v_{p,n}$.

stick, depends on the Stokes number, and the ratio of $v_{p,t}/v_{p,n}$. This ratio is known to depend on the physical and material properties of the particle-surface combination [429] as given by Eq. (86). In order to calculate the critical angle $\varphi_{p,crit}$ using Eq. (86), the ratio (E^*/G^*), μ^* and β are needed. The ratio (E^*/G^*) is only a function of the Poission's ratio ν, and typical values are about 2.1–2.2 [429]. The data shown in Fig. 62(b) can be applied to estimate the parameter $\beta \approx 0.09 - 0.15$ with $f = 0.2 - 0.3$ for the material pair of Wang and John [419].

A similar approach was developed by Rosner and Tandon [433], in order to describe particle deposition rates for a cylindrical target in a dust-laden stream. A model is presented for dry, granular deposits, where the fraction sticking is described with [433,434]:

$$p_{stick} = \begin{cases} 1 & \text{for } v_p < v_{p,crit} \\ exp\left[-0.8 \cdot \chi(\Theta_i) \cdot (v_p/v_{p,crit} - 1)\right] & \text{for } v_p \geq v_{p,crit} \end{cases} \quad (89)$$

where Θ_i is the impact angle defined in Fig. 25, and the parameter χ is calculated by:

$$\chi(\Theta_i) = 1 + 0.2 \cdot \Theta_i \quad \text{with } \Theta_i \text{ in radians.} \quad (90)$$

This model uses equations with an exponential decay for particles above the critical velocity. It could be shown that only smaller particles are able to stick to the target/tube. However, an validation with experiments is missing. Further interesting models are presented by Hærvig et al. [474] and Chen et al [541].

4.3.2. Liquid droplet impacting a solid smooth surface

The impaction of liquid droplets on a solid surface has been investigated in a large number of studies, often in the field of internal combustion engines, aiming at the deposition of fuel droplets on walls [436–438], fundamental studies using water or alcohol droplets impacting on various solid surfaces [390,435,439–444], or, spray coating [445]. Most studies are used to develop mechanistic or semi-empirical models describing the impaction process for variable droplet sizes, viscosities, surface tensions at different impaction angles and speeds. Fig. 63 shows the stages of a low viscosity droplet such as water impacting on a flat solid surface. The schematic is based on the work of Chandra and Avedisian [435], who used a camera system in order to record different stages of droplet impaction and deformation. Particle or droplet impaction on a solid substrate can be divided into six consecutive stages. Fig. 63 illustrates different stages for a low viscosity liquid. The incoming particle of size d_p and impact velocity v_p starts to wet the substrate during stage "1". This process is strongly dependent on the contact angle Θ_c between the surface and the droplet, which depends on liquid properties and surface characteristics. Young's equation given by Eq. (52) can be used to relate the contact angle to the surface tension and surface energy. At stage "2", the maximum spread diameter $d_{p,max}$ is reached and the kinetic energy approaches zero. At this point, the droplet height finds its minimum $h_{p,min}$. During the next two stages, the droplet starts to deform back to a sphere and oscillate, forming the maximum height at stage "4". At stage "5" the droplet either rebounds or sticks, depending on energy dissipation during previous stages. For a low viscosity droplet the sticking probability is quite high due to large deformations. However, splashing is untypical for ash particles since viscosity is still high compared to liquids such as water or gasoline.

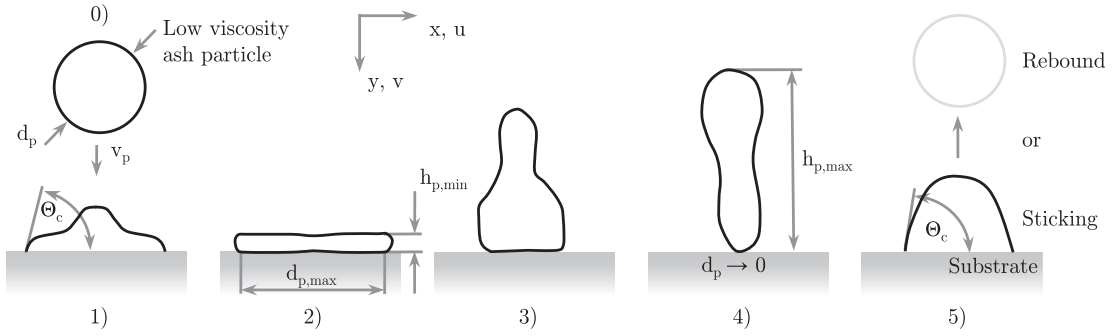

Fig. 63. Impaction stages for a low viscosity droplet, such as water (adopted from Chandra and Avedisian [435]).

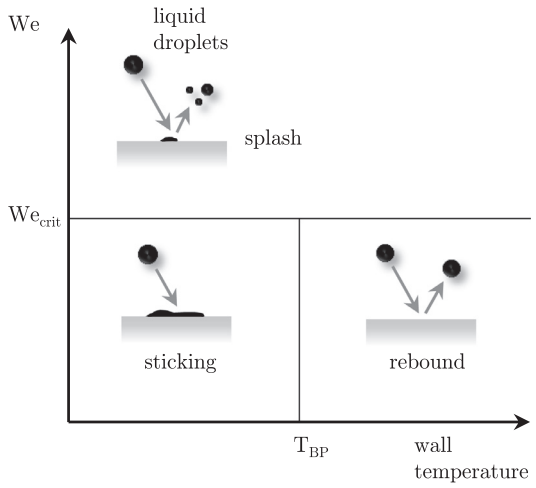

Fig. 64. Regime map for droplet-wall interaction (based and modified from Grover and Assanis [446], and, Bai and Gosman [447]; T_{BP} stands for the boiling temperature of the liquid droplet).

Rein [448] subdivided experimental investigations in the following main groups [440]: impaction on heated surfaces with temperatures above the evaporation temperature of the fluid, impaction on cold surfaces, and impaction on liquid films (see e.g. review of Yarin [449]). This differentiation is used to establish regime maps, as shown in Fig. 64. The droplet Weber number is used in combination with the substrate temperature in order to differentiate between a sticking, rebound and splash regime. The Weber number is defined as the ratio of droplet kinetic energy to surface energy using the following expression [441]:

$$We_p = \rho_p \cdot v_{p,i}^2 \cdot d_p / \gamma_p. \tag{91}$$

At low Weber numbers and temperatures below the boiling point T_{BP}, the droplet will stick due to its low kinetic energy, which is completely dissipated during collision. However, the behavior changes at high surface temperatures, where a vapor film between the droplet and the surface prevents the droplet from wetting and deformation. In this case, rebound is reported [446]. A study of Bai and Gosman [447] further differentiated into break-up, splash and rebound with break-up regimes depending on further characteristic temperatures. Splashing behavior is commonly reported at very high Weber numbers, independent of the substrate temperature. A regime map for ash particle deposition has to consider supercooled liquids instead. Molten particles can solidify in the boundary layer, depending on the particle velocity and boundary layer thickness. Typically, a 20 μm particle with 15 m/s (St ≈ 1 for a superheater tube with diameter 30 mm) is the threshold. Larger particles are unaffected and no deceleration and cooling occurs inside the boundary layer, as estimated by Walsh et al. [395] and predicted using CFD (around 30 μm particle with 6.8 m/s was the threshold [188]). This behavior inside the boundary layer can be significant for small particles. Therefore, the applicability of a regime map without considering cooling effects is doubtful. A summary on major experimental droplet impaction studies is given in Table 17. Most investigations use relatively large droplets, with low viscosity values, compared to ash particles. Nevertheless, the experiments are valuable for the development of sticking and rebound models. There are some studies, such as Chandra and Avedisian [435] or Šlančiauskas and Kalpokaitė [437] using high viscosity fluids with relevant properties.

Pasandideh-Fard et al. [441] studied the impaction of liquid droplets on solid surfaces using experimental and numerical methods. Impacting water droplets were photographed, and maximum spread diameters and contact angles, were obtained from these images. The droplet diameter was around $d_p \approx 2$ mm and the impact velocity was $v_{p,i} = 1$ m/s [441]. The authors derive correlations for the maximum droplet diameter after impaction $d_{p,max}$ (defined in Fig. 63 or 58). After impaction, the droplet deforms, and loses its circular shape, forming a thin film on the substrate, as shown in stage 2, within Fig. 63. This deformation process is described using energy conservation as given in Eq. (74). The authors show that the ratio of maximum spread diameter $d_{p,max}$ to initial droplet diameter d_p can be calculated by:

$$\xi = \frac{d_{p,max}}{d_p} = \sqrt{\frac{We_p + 12}{3 \cdot (1 - cos\ \Theta_c) + 4 \cdot (We_p / \sqrt{Re_p})}}. \tag{92}$$

The maximum spread ξ of the droplet is a function of droplet contact angle Θ_c at $d_{p,max}$, droplet Weber number We_p, and, droplet Reynolds number $Re_p = \rho_p \cdot v_p \cdot d_p / \mu_p$, which are both calculated for a spherical droplet before impaction. The Reynolds number is calculated using the droplet viscosity in contrast to Eq. (12), where the viscosity of the surrounding fluid is used instead. Since most droplet impaction studies are conducted at stagnant air flow, it is unclear if the

Table 17
Overview on major droplet impaction studies and their parameters (data taken and extended from Mahulkar et al. [450]).

Study Unit	d_p μm	v_p m/s	T_{Wall} °C	liquid –	Characteristics and Key Findings –
Wachters and Westerling 1966 [439]	2000	0–1.7	up to 400	water	rebound behavior
Chandra and Avedisian 1991 [435]	1500	0.93	24–250	n-heptane	normal impact recorded by camera system; spread and splash characteristics determined
Mundo et al. 1995 [440]	60–150	12–18	25	ethanol, water	non-normal impact with varying surface tension and viscosities; deposition-splash boundary identified
Pasandideh-Fard et al. 1996 [441]	2050	1	n.s.	water[c]	capillary effects negligible if $We_p > Re_p^{0.5}$, and spreading of droplets
Mao et al. 1997 [390]	1500–3500	0.5–6	25	water–surcose mixtures	model for droplet rebound
Aziz and Chandra 2000 [451]	2700	1–4	25–240	tin	solidification upon impact
Rioboo et al. 2002 [452]	1200–4900	0.78–4.1	n.s.	various[b]	effect of surface roughness on spreading
Bai et al. 2002 [442],[a]	1–300	up to 20	25	iso-octane	spray non-normal impact, stick-splash transition, regime map
Šikalo et al. 2005 [438]	1000–3000	1.54	25	water, glycerol, iso-propanol	spread and splash on inclined surfaces with and without liquid films
Vander Wal et al. 2006 [436]	2000	2.17–4.22	n.s.	alkanes	stick-splash criterion
Šlančiauskas and Kalpokaitė 2006 [437]	750	n.s.	400–700	heavy fuel oil	effect of surface roughness
Hsiao et al. 2009 [453]	273–287	3.6–3.9	183	liquid metal	wetting and bouncing behavior
Shen et al. 2010 [443]	1000–1300	1.18	23–185	water	spread and rebound behavior
Fujimoto et al. 2010 [457]	530–2500	1.7–4.1	170–500	water	photographs of spreading and splashing droplets
Negeed et al. 2013 [444]	300–700	1.0–4.0	800	water	max. spread and contact time with oxidized surfaces

n.s. - not specified.
[a] experimental data from Arcoumanis et al. [458] and their private communication.
[b] including acetone, isopropanol, ethanol, water, silicone oils and mixtures of glycerine and water.
[c] with different surfactant concentrations changing the surface tension and contact angle.

relative velocity between the droplet and the gas flow or the absolute velocity has to be used; however, the latter seems more appropriate. Mao et al. [390] conducted similar experiments, and studied the impaction of droplets composed of a water-surcose mixture on glass, steel or paraffin substrates. Studied droplets had diameters of $1.5 < d_p \leq 3.5$ mm and velocities in the range of $0.5 < v_p \leq 6$ m/s. The authors used a similar energy-based approach as Pasandideh-Fard et al. [441], but with a changed formulation for the surface energy at the contact. They derive the following implicit formulation of ξ:

$$\left(\frac{1}{4}\cdot(1-cos\ \Theta_c)+0.2\cdot\frac{We_p^{0.83}}{Re_d^{0.33}}\right)\cdot\xi^3-\left(\frac{We_p}{12}+1\right)\cdot\xi+\frac{2}{3}=0 \tag{93}$$

Mao et al. [390] compared the solution of Eq. (93) with measurements and found a maximum deviation of 10%. They observed the formation of a ring after maximum spread, which then contracts towards its center forming a conical droplet, and separates from the substrate. The droplet rebounds, if the energy dissipated due to viscous forces and the work of adhesion is higher than the surface energy after impaction. The authors use a parameter called excess rebound energy E_{ERE} in order to estimate the rebound behavior of droplets. The droplet will stick ($p_{stick} = 1$) if $E_{ERE} \leq 0$ and rebound otherwise ($p_{stick} = 0$) [390]:

$$p_{stick}=\begin{cases}0 & \text{for } E_{ERE}>0\\ 1 & \text{for } E_{ERE}\leq 0\end{cases} \tag{94}$$

where the excess rebound energy E_{ERE} is calculated by the following expression:

$$E_{ERE}=\frac{1}{4}\cdot\xi^2\cdot(1-cos\ \Theta_c)-0.12\cdot\xi^{2.3}\cdot(1-cos\ \Theta_c)^{0.63}+\frac{2}{3}\cdot\frac{1}{\xi}-1\leq 0 \tag{95}$$

Aziz and Chandra [451] studied the impact and solidification of molten tin droplets on a flat steel plate with varying temperature ($d_p \approx 2.7$ mm and $v_p = 1$–4 m/s). The rebound behavior can be affected if the substrate temperature is below the melting temperature of the droplet. Deformation and maximum spread $d_{p,max}$ are influenced by solidification and smaller compared to studies without a cooled substrate. Aziz and Chandra [451] used the following expression to estimate the maximum spread:

$$\xi=\frac{d_{p,max}}{d_p}=\sqrt{\frac{We_p+12}{3/8\cdot We_p\cdot s^*+3\cdot(1-cos\ \Theta_c)+4\cdot(We_p/\sqrt{Re_p})}}. \tag{96}$$

The parameter s^* is the dimensionless thickness of the solidified droplet. It is estimated by:

$$s^*=\frac{s}{d_p}=\frac{8}{3}\cdot Ste\cdot\sqrt{\frac{3\cdot k_w\cdot\rho_w\cdot c_{p,w}}{2\cdot\pi\cdot Pe\cdot k_p\cdot\rho_p\cdot c_{p,p}}}, \tag{97}$$

where s is the thickness of the solidified droplet, $k_{w/p}$ is the wall and particle thermal conductivity, Ste is the Stefan number, and Pe the Peclet number. The Stefan number is a measure for the duration of the solidification process, and is defined as $Ste = c_{p,p} \cdot (T_m - T_W)/H_f$, with the heat capacity of the particle $c_{p,p}$, the melting temperature of the droplet T_m, the wall temperature T_W, and the latent heat of fusion H_f. The Peclet number is a measure of advective to diffusive transport and defined as $Pe = v_p \cdot d_p \cdot \rho_p \cdot c_{p,p}/k_p$ [451]. Eq. (96) simplifies to Eq. (92) if there is no temperature difference between the droplet and the substrate (s^*=0). Ni et al. [333] used the findings of Aziz and Chandra [451] and applied the given equations for a sticking criterion in slag-flow gasification systems. However, there is no validation of the model. They carried out parameter studies for relatively large ash particles, and used the viscosity model of Browning et al. [314] as well as measurements of the apparent contact angle of Abbot and Austin [350]. Their parameter study showed versatile behavior. Generally, the sticking probability increases with increasing temperature. Sticking was also be found for small particles with low velocities ($d_p \ll 1$ mm and $v_p \ll 1$ m/s) and large particles with relatively high impact velocities ($d_p > 3$ mm and $v_p > 3$ m/s) [333].

4.4. Evaluation of sticking criteria

A simple comparison of presented sticking criteria is shown in Table 18. It can be seen that sticking criteria are in agreement on the effect of individual parameters, such as changing particle temperature, diameter, velocity or angle of impaction. Generally, the probability of an ash particle to stick to a heat exchanging surface is high for small particles with high temperatures, which impact with a low velocity and small impaction angle. However, the role of the impact angle is barely understood, mainly due to the scarcity of measurements and the fact of contradictory models and experimental results [428,429]. The models presented in Table 18 require a number of temperature- and composition-dependent properties. One can imagine that with a higher number of parameters, it is more difficult to use such a model. Therefore, simple correlations and equations are favorable over complex models, such as the one of Thornton and Ning [290]. The biggest challenge is to find temperature-dependent properties for different ash particle compositions and structures.

4.5. Role of existing deposit layers and limitations

Most of the sticking criteria described above are developed for a clean, often flat surface with well-defined properties. For such a surface, particle impaction and sticking rates can be predicted, such as the ones shown in Fig. 65(a). Walsh et al. [460] calculated the sticking probability for sodium sulfate-coated calcium aluminosilicate particles and found a narrow range of sizes around 10–15 μm, which is able to deposit. Particles smaller than 10 μm did not impact on the surface since diffusional effects and thermophoresis are not considered. On the other hand, large particles did not stick, which goes along with the sensitivity study shown in Table 18. The sticking probability decreases with increasing particle size. In comparison to a clean surface, there are a number of changes for heat exchanging surfaces in a power plant. Sticking criteria are typically missing effects such as surface roughness or stickiness of the substrate. Once there is a deposit layer (powdery, sintered or molten) the sticking

Table 18
Comparison of different sticking criteria and their variables (adopted from Scholz [459]).

Critical parameter	References	Properties needed	Sticking probability due to increase of			
			T_p	d_p	v_p	φ_i
Melt fraction	Zhou et al. [391]	f_p	↑			
Viscosity	Walsh et al. [395]	μ_p	↑			
	Srinivasachar et al. [1]	μ_p	↑			
	Srinivasachar et al. [1], Richter [222]	μ_p, ρ_p	↑	↓	↓	
Velocity	Thornton and Ning [290]	$\gamma_{p/w}$, $\nu_{p/w}$, $E_{p/w}$, ρ_p	↑	↓		
	Losurdo et al. [342]	same as [290], plus e_n, e_t	↑	↓		
	Brach and Dunn [428]	$\nu_{p/w}$, $E_{p/w}$, ρ_p	↑	↓		↓
Spread diameter	Pasandideh-Fard et al. [333,390,441]	μ_p, γ_p, ρ_p, Θ_c	↑	↓	↓	

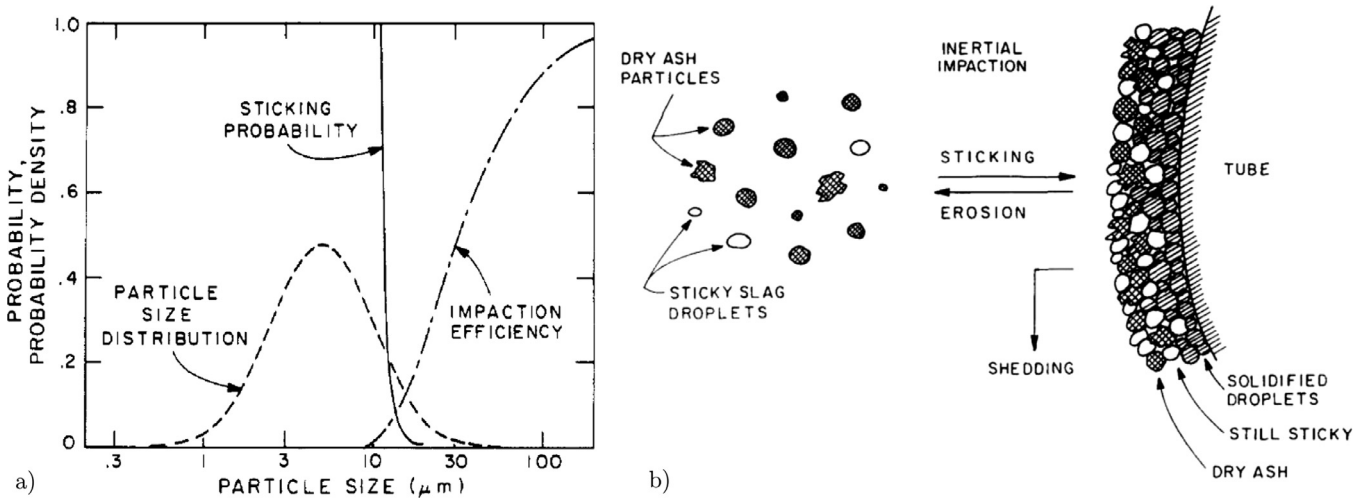

Fig. 65. Ash deposition in PF fuel combustion: (a) particle size distribution, calculated impaction efficiency, and sticking probability for a lignite [460], and (b) layer formation and growth for a bituminous coal [395]. Reprinted with permission from Walsh et al. [460]; copyright 1992 American Chemical Society.

tendency changes due to changed surface properties. This is particularly challenging when describing the deposit build-up. Fig. 65(b) illustrates the process of deposit formation. A clean tube collects only sticky particles, which then solidify as long as the layer is thin [395]. With an increasing deposit layer, the surface temperature increases becoming sticky itself, causing an increase in collection efficiency. Non-molten, dry ash particles can adhere to a sticky surface. The viscosity approach of Walsh et al. [395], is one of the few approaches considering the stickiness of the surface. They use the following equation to describe the net mass fraction sticking to the surface $p_{stick,tot}$:

$$p_{stick,tot} = p_{stick,p}(T_g) + [1 - p_{stick,p}(T_g)] \cdot p_{stick,W}(T_W) - k_e[1 - p_{stick,p}(T_g)] \cdot [1 - p_{stick,W}(T_W)], \quad (98)$$

where the particle and wall sticking probabilities are calculated, using Eq. (71). The viscosity in Eq. (71), can be calculated using the corresponding particle and wall temperature in combination with the chemical composition. The parameter k_e describes the erosivity of the dry ash particles towards the deposit. The overall deposit growth rate in mass per unit area and time, can be calculated according to [395]:

$$\frac{1}{A} \cdot \frac{dm_{dep}}{dt} = J_{imp} \cdot p_{stick,tot} - k_{shed} \cdot \left(\frac{m_{dep}}{A}\right)^{\alpha_{shed}}, \quad (99)$$

where A is the projected area of the tube in a plane perpendicular to the undisturbed flow direction, J_{imp} is the mass of ash particles impacting on the tube per unit time and unit projected area in kg/(m^{2}s), α_{shed} is the order of the shedding process, and k_{shed} is the shedding frequency in 1/s when $\alpha_{shed} = 1$ [265,395]. For long periods, the deposit mass per area approaches the following expression:

$$\frac{m_{dep}}{A}|_{t \to \infty} = \left(\frac{J_{imp} \cdot p_{stick,tot}}{k_{shed}}\right)^{1/\alpha_{shed}}. \quad (100)$$

This expression is however only valid if sintering or changes in deposit strength do not occur [395]. Further investigations of particles impacting a powdery or liquid layer are discussed in Section 5.3, dealing with the particle rebound. Another very critical factor is the heterogeneity of ash particles. Often sticking criteria use bulk ash chemistry to calculate deposition rates. An individual treatment on a particle-by-particle basis is essential. A low melting iron-sulfide particle might stick at temperatures as low as 1000 °C, whereas a quartz particle needs temperatures above 1600 °C. However, finding temperature-dependent properties for all possible chemical compositions of ash particles is rather impossible. Therefore, due to the large diversity of ash particles in terms of chemical composition, size, density and shape, it is straightforward to use simple sticking criteria, without the need of knowing all particle and wall properties, e.g. Young's modulus, Poisson's ratio, contact angle or viscosity.

4.6. Parameters affecting the stickiness and rebound behavior

Most ash particle sticking criteria are based on ideal conditions, when spherical particles or droplets impact on a flat solid surface. However, within solid fuel-fired boilers different and much more complex scenarios can occur. Fig. 66 summarizes a number of possible phenomena. Ash particles can be trapped by a molten sticky layer, as outlined in the previous section. Furthermore, a solid, powdery deposit can act as a filter element for particles. The flow might be able to penetrate the inside of the deposit, however, the particles are not. They are collected by the porous structure. Condensation and/or chemical reactions of alkali vapors with fly ash particles can change the stickiness as found by Wibberley and Wall [406]. A thin, low viscosity layer forms around silicate ash particles and allows particles to deposit on a cooled steel surface (600 °C) free from condensed material [406]. Another mechanisms is the cementation of solid fly ash particles. Particles impacting on the surface are followed by a molten droplet acting as a glue between the surface and the fly ash particle. This mechanism, however, is difficult to verify in experiments. A further interesting aspect is the deposition of unburnt char containing molten and/or solid ash grains. The remaining char will oxidize and ash remains on the heat exchanging surface. This mechanisms is mainly reported for entrained flow gasifier. Another phenomena could be the sintering and reaction of particles during the contact. However, experimental evidence is again missing.

Rarely discussed is the deposition of agglomerates or thermal effects at the interface as shown by the last two mechanisms. The ash particle shape is often ignored in literature. Fly ash particles are commonly irregular formed agglomerates with different impaction, and deformation behavior. An agglomerate is able to dissipate kinetic energy by rearrangement of its structure and therefore its sticking probability might be higher compared with spherical particles of the same size. Furthermore, its impact velocity is lower compared with a spherical particle at the same flow conditions due to its high surface to volume ratio and thus its high drag coefficient. An aspect that misses in Fig. 66 is the formation of a scale and/or oxide layer. The dynamics of oxide layer formation are illustrated in Fig. 67. The following steps are reported [66]:

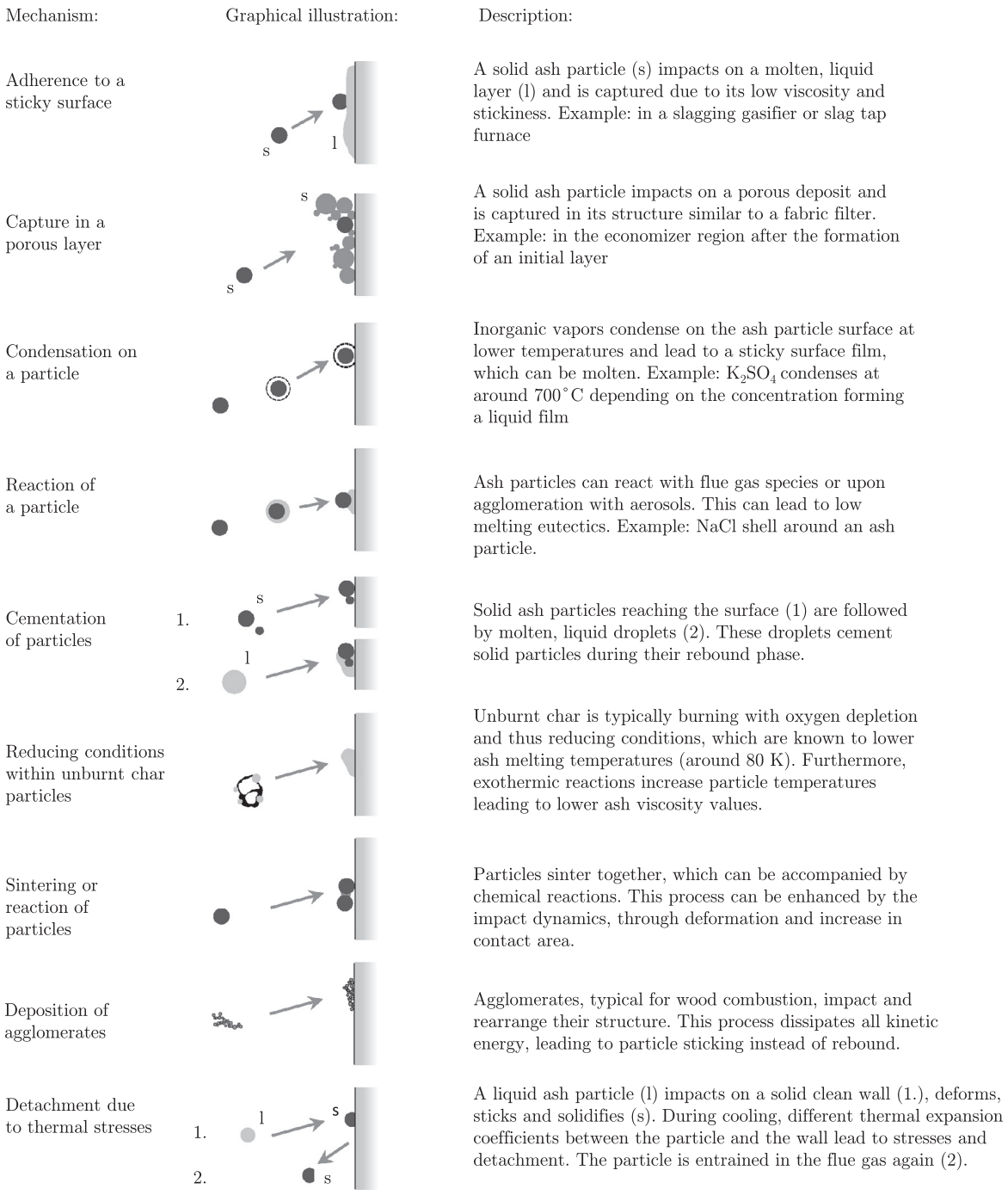

Fig. 66. Mechanisms affecting the sticking and rebound behavior of ash particles (s: solid, l: liquid - adopted, modified and extended from Couch [15], originally from Hsu et al. [461]).

Step 1: The formation of a thin, initial oxide layer due to oxidation. It is expected that ash particles do not play a significant role here. However, the presence of gaseous chlorine or SO_2/SO_3 significantly increases the rate of layer formation.

Step 2: In the following step, the oxide layers starts to grow due to the higher diffusion rate of iron compared with chromium and nickel. Alkali chloride or alkali sulfate vapors begin to condense on the oxide layer. Reactions between Cl/S and the oxide layer further increase the growth and porosity, where the porosity might be caused by the release of volatile metal chlorides. Furthermore, it was found that an increasing K-content in the ash leads to a strong increase in oxide layer thickness, as shown in the SEM images (c)–(e) in Fig. 67.

Step 3 and 4: Cracks and gaps form in the oxide layer, as shown in Fig. 67(b). Detachment can occur due to thermal stresses or growth stresses between different layers. An increase in surface temperature leads to an accelerated particle collection promoting ash deposition. The temperature increase is caused by the insulating oxide layer and/or by detachment and insulating gas between oxide layers. Higher ash accumulation rates increase the chlorine content in the deposit enhancing corrosion rate.

Depending on the chemical bonding between the interfaces, oxide layers might detach, and existing deposits and oxide layers are removed, leading to a repetition in the above-mentioned steps [66].

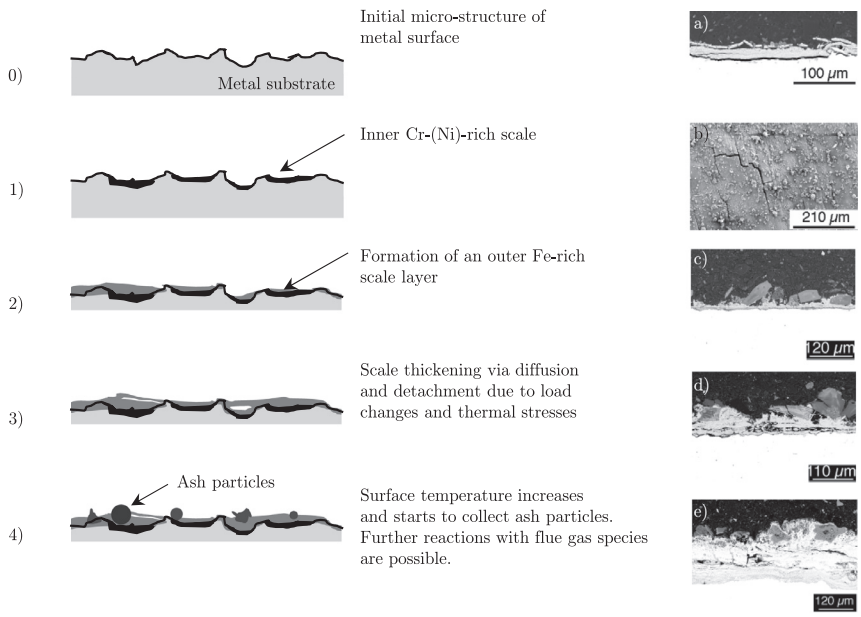

Fig. 67. Formation of scale and oxide layer leading to enhanced ash particle collection and corrosion (mechanism and SEM images from [66]). SEM images (a) and (b): cross-section and top view of a scale layer on a X20CrMoV12-1 steel after 5 hour exposure to a co-firing ash at 600 °C; SEM images (c), (d) and (e): scale and deposit morphologies after reactions with three synthetic ashes at 600 °C for 15 hours with 7, 15 and 20 wt.% K_2O, respectively (rest is composed of: SiO_2= 37, Fe_2O_3= 1, Al_2O_3= 3, CaO= 5 and Na_2O= 5 wt.%).

The oxide layer formation is often neglected, or not mentioned when studying ash deposition, however, it can play an important role. It is essential to estimate and know relevant mechanisms, when developing an ash particle sticking and rebound criterion. A comparison of parameters and their ranges, as well as energies involved during particle impact are presented in Table 19. Three different scenarios are compared:

- First, the deposition of a small, sub-micron, salt-rich ash particle formed by inorganic vapor condensation. This particle slows down drastically inside the boundary layer and migrates with a very small velocity magnitude to the surface. The particle temperature is identical to the superheater tube during impact.
- Second, the deposition of a large, massive Fe-rich particle. The particle originates from pyrite and forms a low melting eutectic

Table 19
Parameters and properties of fly ash particles upon contact with heat exchanging surface. Values are used for estimating energies involved during sticking and rebound. Lower boundary is estimated for a sub-micron salt particle at low temperatures, upper boundary for a large, Fe-rich and low melting particle, and a typical aluminosilicate particle with 20 µm.

Parameter	Symbol	Unit	small salt-rich	large Fe-rich	typical Al-Si
Particle temperature[a]	T_p	°C	500	1200	1100
Particle velocity	v_p	m/s	0.1	15	7
Particle diameter	d_p	µm	0.01	100	20
Particle density	ρ_p	g/cm^3	2.0	5.5	2.6
Particle viscosity	μ_p	Pa · s	10^{12}	10^{-2}	10^{2}
Particle surface tension	γ_p	N/m	0.6	0.2	0.4
Contact angle with substrate	Θ_c	°	160	40	120
Particle kinetic energy	$E_{kin,\,p}$	J	$5.8 \cdot 10^{-24}$	$3.2 \cdot 10^{-7}$	$3.3 \cdot 10^{-10}$
Particle potential energy[b]	$E_{pot,\,p}$	J	$1.1 \cdot 10^{-25}$	$2.8 \cdot 10^{-13}$	$1.3 \cdot 10^{-15}$
Particle adhesion energy	$E_{ad,\,p}$	J	$1.1 \cdot 10^{-18}$	$2.7 \cdot 10^{-9}$	$9.2 \cdot 10^{-12}$
Particle deformation energy	$E_{def,\,p}$	J	$7.0 \cdot 10^{-11}$[e]	$9.3 \cdot 10^{-8}$	$6.9 \cdot 10^{-10}$
Particle van der Waals energy[b,c]	$E_{vdW,\,p}$	J	$6.4 \cdot 10^{-16}$	$1.6 \cdot 10^{-10}$	$2.6 \cdot 10^{-12}$
Particle friction energy[d]	$E_{fri,\,p}$	J	$2.5 \cdot 10^{-30}$	$1.5 \cdot 10^{-12}$	$1.1 \cdot 10^{-16}$
Sticking probability (energy balance[f]: $\sum E_i$)	p_{stick}	–	1	0	1
Particle Stokes number[g]	St	–	$2.3 \cdot 10^{-9}$	$5.7 \cdot 10^{1}$	$6.0 \cdot 10^{-1}$
Particle Knudsen number[h]	Kn	–	$4.1 \cdot 10^{1}$	$8.6 \cdot 10^{-3}$	$3.7 \cdot 10^{-2}$
Particle Reynolds number	Re_p	–	$2.2 \cdot 10^{-18}$	$8.3 \cdot 10^{2}$	$3.9 \cdot 10^{-3}$
Particle Weber number	We_p	–	$3.7 \cdot 10^{-7}$	$6.2 \cdot 10^{2}$	$6.8 \cdot 10^{0}$
Particle spread factor Eq. (92)	ξ	–	0.11	2.7	0.21
Particle spread factor Eq. (93)	ξ	–	0.81	2.2	0.58

[a] small particles migrate to the surface and have the local gas temperature.
[b] calculated using a distance between the particle and the surface of $\Delta = 10$ nm [462,463].
[c] calculated using the Hamaker constant of $A_H = 7 \cdot 10^{-20}$ J [462,463].
[d] estimated with a friction coefficient of $f = 0.2$.
[e] estimated using different viscosity values.
[f] $E_{kin,\,p}$ and $E_{pot,\,p}$, minus the remaining energies.
[g] calculated with a tube diameter of $D = 30$ mm, and the viscosity of N_2 at a gas temperature equal to T_p.
[h] mean free path length calculated for a gas temperature equal to T_p with Eq. (17).

(Fe-O-S melt) caused by reducing furnace conditions. The particle is not affected by the boundary layer and its temperature is identical compared to the flue gas temperature of $T_\infty = 1200\,°C$. The particle velocity is also unchanged at high values of 15 m/s.
- And third, a typical aluminosilicate (Al–Si) particle with a size of 20 μm impacting with moderate velocity of 7 m/s. This particle is difficult to judge since it could be affected by the boundary layer depending on the position and angle of impact.

For all three particles, a normal impact, at the front face of a cylinder (superheater tube with diameter of 30 mm), is assumed. Particle properties are estimated using equations from Section 3, or taken from literature. The particle viscosity shows the largest deviation. The sub-micron particle is solid with a relatively high, estimated value of $\mu_p \approx 10^{12}$ Pa·s, compared to the very low value of $\mu_p \approx 10^{-2}$ Pa·s for the Fe-rich particle. The variation in surface tension is low as long as particles are liquid. In the case of solid particles, surface energy values have to be used. Using these values, energy ranges can be calculated. The particle kinetic energy for instance spans over 17 orders of magnitude. All calculated energy values are illustrated in Fig. 69. The calculation of a potential energy is questionable since particles do not drop from a certain height, instead, they are entrained in the flow. However, it is shown that potential energy is orders of magnitude smaller, compared to other energy values and thus negligible. The energy loss caused by frictional forces can be estimated using the following relation:

$$E_{fri,p} = -f \cdot F \cdot \xi \cdot d_p \tag{101}$$

where f is the friction coefficient, F is the net force acting on a settled particle, and $\xi \cdot d_p$ is the contact diameter between the ash particle and the substrate. The net force F can be a combination of forces acting at the interface, as illustrated in Fig. 59. Depending on this force, the friction coefficient can differ quite significantly, however, it is relatively small compared to the particle kinetic energy. The estimation of energy losses due to van der Waals forces is difficult. Van der Waal forces are known as the non-covalent interaction between atoms or molecules at interfaces. Fig. 68(a) shows how momentary dipols form at the interface due to random movement of electrons. The majority of particles carry a small net charge that will lead to an attractive force to an opposing charge found at surfaces. The dipoles and resulting forces contribute to particle adhesion alongside with surface tension effects and electrostatic forces [158,244]. Fig. 68(b) shows the impact of rough surfaces on a microscopic scale. There are only few contact points and contact surface area is reduced. The van der Waal energy can be viewed as the work/energy required to separate two bodies in contact, without other forces such as adhesion, gravity. The energy due to van der Waals forces between a sphere and a wall can be calculated according to the following equation [462,463]:

$$E_{vdW,p} = A_H \cdot \frac{d_p}{12 \cdot \Delta}, \tag{102}$$

where A_H is the Hamaker constant set to a value of $A_H = 7 \cdot 10^{-20}$ J and Δ is the distance between the particle surface and the wall as shown in Fig. 68(b). This distance is difficult to estimate. If two perfectly smooth bodies are in contact, their distance might be in the range of $\Delta \approx 0.2$ nm. However, most ash particles are not perfectly smooth, leading to much higher values of $\Delta \approx 10$ nm [463]. Eq. (102) predicts considerably higher energy values due to van der Waals forces, compared to friction and potential energy. Values are slightly lower, compared with adhesion energy. The adhesion energy of a particle in contact with a substrate is calculated using Eq. (141), introduced later on. The contact area and the contact angle between the deformed particle and the surface are crucial. By far the highest energy losses are due to particle deformation no matter if the particle is solid or liquid. In Table 19 it is assumed that the small salt-rich particle has an extrapolated, high viscosity. The work against viscosity required to deform the particle to the predicted spread factor ξ

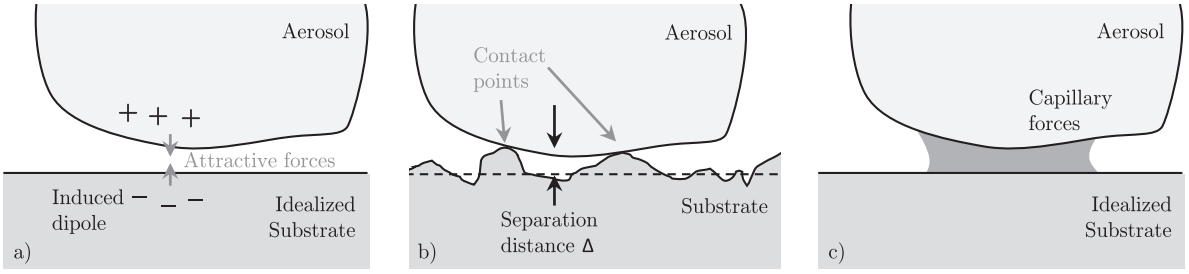

Fig. 68. Particle surface interactions: (a) induced dipole forces contributing to particle adhesion, (b) surface roughness and contact points prior to sintering, and (c) capillary forces (adopted from Hickey et al. [542]).

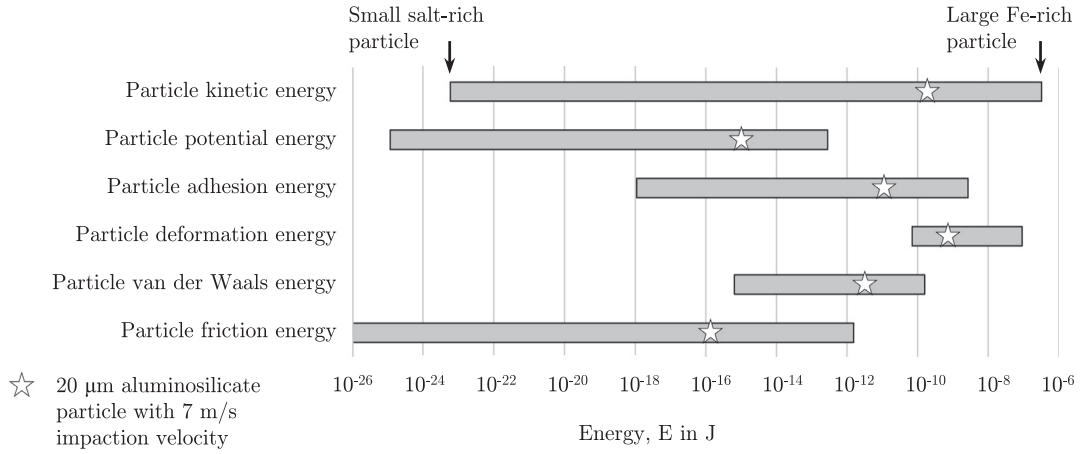

Fig. 69. Ranges of kinetic, potential, adhesion, deformation, friction and van der Waals energies for fly ash particles on a steel surface. Numbers are computed from Table 16.

can be as high as its kinetic energy. In this case, all energy is dissipated, and the particle will stick if the connectivity between the substrate and the particle surface is high enough to overcome shear forces, caused by the flow. The error in predicting the deformation energy for small, high viscosity particles is expected to be high, and future research should be directed towards this issue. A further mechanisms which might be of relevance is the thermal expansion coefficient, which can vary with temperature and material. Thermal stresses at the interface can occur leading to a detachment and re-entrainment of a fly ash particle. The sticking probability can be judged using Table 19. When the energy loss due to deformation, adhesion and van der Waals forces exceed the kinetic and potential energy, the particle will stick. Comparing all three cases, surprising results can be observed. The small, salt-rich particles and Al-Si particle stick, whereas the large, low viscosity, Fe-rich particle will rebound. The small particle sticks since it has an almost negligible kinetic energy, which is completely dissipated during impact. Each of the following components adhesion, deformation and van der Waals forces are large enough to cause deposition/sticking. In the case of the Al-Si, the deformation and thus, the work against viscosity, leads to the sticking behavior. On the contrary, the kinetic energy of the Fe-rich particle is too high and cannot be completely dissipated even though the deformation is high ($\xi > 2$).

Table 19, further gives dimensionless numbers. The Stokes number in a power plant can range from extremely low values of $St \approx 10^{-9}$ up to $St \approx 60$. Inertial impaction becomes dominant at around $St \approx 0.5$, which is in the region of a 20 μm particle (see Fig. 26). The Knudsen number ranges from low values for large particles to high values for the sub-micron particle. Thus, sub-micron particles do not follow the Stokes drag law and the thermal conductivity ratio does not influence thermophoretic force. The particle Reynolds number ($Re_p = \rho_p \cdot v_p \cdot d_p / \mu_p$) and Weber number also span over more than ten orders of magnitude. This huge spread is the main problem for finding generally valid correlations. It can be seen that the particle spread factor can differ significantly for small particles when using different correlations. The correlation of Mao et al. [390] predicts higher spread factors and thus higher dissipation rates compared with correlations suggested by Chandra and Avedisian [435].

4.7. Sticking behavior of aerosols

Experimental studies dealing with aerosol impaction and deposition are rare. The main difficulty is the small particle size. Particles are difficult to handle and not visible with standard optical devices such as camera systems. Most of the work is theoretical in nature and uses models to predict aerosol sticking. Often it is assumed that every aerosol that impacts on a wall will stick. The common believe is that they are kept along surfaces by relatively weak van der Waal and electrical forces. However, experimental evidence is still due. A lot of work on aerosol deposition was conducted in the filtration industry, e.g. the work of Wang and Kasper [467]. They compare the critical velocity with typical particle impact velocities and derive laws and models for the filtration efficiency. According to their study, the mean particle impact velocity for the diffusion-dominated particle impaction regime is characterized by its thermal velocity following the Maxwell-Boltzmann distribution analogously to Eq. (14):

$$v_{imp} = v_{thermal} = \sqrt{\frac{48 \cdot k_B \cdot T_g}{\pi^2 \cdot \rho_p \cdot d_p^3}} \tag{103}$$

The critical velocity is calculated in the work of Wang and Kasper [467], by equating the elastically stored kinetic energy of the particle and the adhesion energy E_{ad} according to:

$$v_{cr} = \sqrt{\frac{2 \cdot E_{ad}}{m_p \cdot e^2}} \tag{104}$$

The parameter e stands for the restitution coefficient, which will be introduced later on in Section 5. For nano-particles or molecules, the coefficient of restitution is commonly assumed to be unity, hence a perfectly elastic collision without energy losses [467]. When using Eq. (104), an expression for the adhesion energy is needed. One approach goes back to the work of Bradley [475] and Hamaker [462], referred to as the Bradley–Hamaker adhesion energy. It integrates all molecular attractions over the entire volume. Substituting their expression in Eq. (104), leads to the following expression:

$$v_{cr,B-H} = \sqrt{\frac{A_H}{\pi \cdot \rho_p \cdot d_p^2 \cdot \Delta}}, \tag{105}$$

where A_H is again the Hamaker constant and Δ the minimum separation between particle surface and wall. The main drawback of the B-H theory is that it assumes point contact between the particle and wall, where in reality a finite contact area forms [467]. Another commonly used model, which overcomes this shortcoming, goes back to the JKR model [431]. The JKR theory calculates the critical velocity by:

$$v_{cr,JKR} = \left[\frac{3^7 \cdot \pi^4 \cdot (k_w + k_p)^2 \cdot \sigma_{p,w}^5}{\rho_p^3 \cdot d_p^5}\right]^{1/6}, \tag{106}$$

where k_w, k_p are again the elasticity parameters of wall and particle, and $\sigma_{p,w}$ is the specific adhesion energy at the interfacial contact area. Another interesting theory was presented by Derjaguin et al. [476], who studied the effect of contact deformations on the adhesion of particles and reported that the adhesion energy is equivalent to the first power of the particle diameter. The same dependency is predicted when using Eq. (105). Slightly different is Eq. (106), where the critical velocity varies with $d_p^{5/6}$. A comparison of different equations is shown in Fig. 70. It can be seen that both models predict

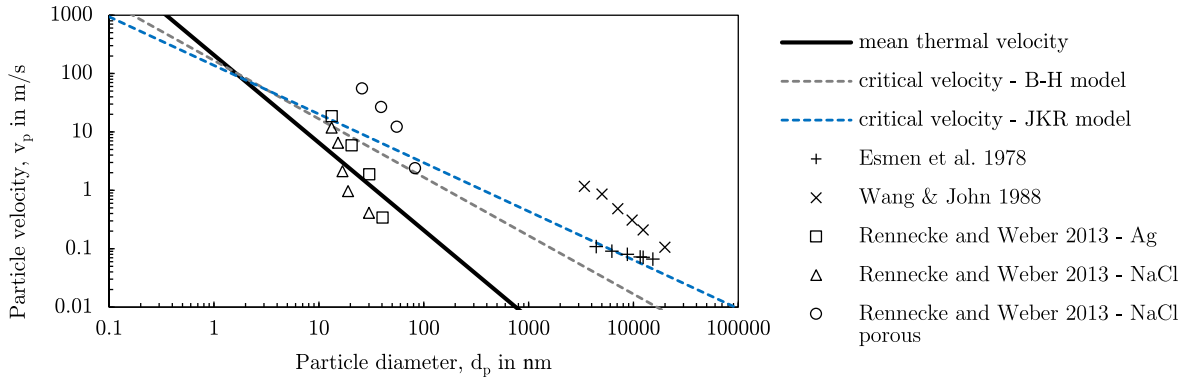

Fig. 70. Comparison of particle mean thermal velocity with critical velocity values predicted using different theories and measured critical velocities (adopted from Wang and Kasper [467], measurements from [415,419,468]). Parameters for the prediction of curves are: $A_H = 0.7 \cdot 10^{-20}$ J, $\Delta = 0.4$ nm, $\rho_p = 2$ g/cm^3, k_w+$k_p = 5 \cdot 10^{-11}$m^2/N, $\sigma_{pw} = 0.04$ J/m^2.

Table 20
Bulk material properties at room temperature for Ag, NaCl and Mica. Values taken from Rennecke and Weber [468]. Originally from [419,470–473,510].

Quantity	Symbol	Unit	Ag	NaCl	Mica
Hamaker constant	A_H	in 10^{-19} J	4.0	0.7	1.35
Surface energy	γ	J/m^2	1.25	0.25	0.149
Yield strength	Y	10^6 N/m^2	330	600	204
Density	ρ_p	kg/cm^3	10500	2170	2883

quite similar results: an increasing critical velocity with decreasing particle diameter. Interesting is the behavior of the mean thermal impact velocity v_{imp}, which increases strongly as the particle size becomes smaller. According to this theory, particles smaller than $d_p = 2$ nm will rebound. This controversy effect is known as thermal rebound [473]. However, for ash deposition it is most likely not relevant, since, even aerosols are significantly larger. As shown in Fig. 70, all larger particles will stick. Since typical combustion aerosols are much larger, with sizes around 100-300 nm, it is confirmed that these particle will stick no matter of bulk flow conditions or temperatures. However, a recent experimental study reported a different behavior for nanoparticles. Rennecke and Weber [468] used for the first time a low pressure impactor in order to determine the critical velocity of nanometer-sized NaCl and Ag particles on a mica substrate, avoiding contact charging. The authors used the JKR theory assuming full plastic failure of the particle during the approach regime, adhesion during particle rebound and constant hardness as well as constant surface energy during collision. With these assumptions Weir and McGavin [469] derived the following equation:

$$v_{cr,JKR} = \sqrt{\frac{16 \cdot \gamma^2}{3^{1/3} \cdot 5 \cdot \rho_p \cdot Y \cdot d_p^2}}, \tag{107}$$

where γ is the surface energy. Parameters for Eq. (107) can be found in Table 20. Rennecke and Weber [468] found a relatively steep curve for the particle critical velocity, which implies that particles around 50 nm rebound above velocities much smaller than predicted by the JKR and B-H model. They further showed a relatively high critical velocity for porous NaCl particles compared with dense NaCl particles. This is useful information for aerosols, which are typically agglomerates, and thus, also porous. Hence, it is assumed that agglomerates dissipate much kinetic energy during collision due to deformation and rearrangement and, thus, have a high sticking probability. It was further predicted that very small particles experience plastic deformation, which is in contradiction to previous studies assuming that aerosols impact perfectly elastic. There are many unknown phenomena and to date there are only few experiments in this area. Further studies should focus on a combination of experimental work and new modeling approaches, such as improved theories implementing a reduced particle stiffness [474]. The goal should be a comprehensive model being able to predict nanoparticle sticking and rebound.

Two important characteristics for aerosol deposition on heat exchanging surfaces are illustrated in Fig. 71. Fig. 71(a) shows the effect of a porous deposit layer collecting all incoming particles. If particles are small, inertia is low and the probability of shedding diminishes. All incoming particles are collected no matter if they are sticky or not. A second important parameter is the particle shape. As illustrated in Fig. 71(b) agglomerates impact on a wall, deform and rearrange their structure. It is assumed that a large fraction of the particle kinetic energy is dissipated during this process, leading to an increased sticking efficiency of agglomerates compared with perfectly spherical ash particles. However, further work in this field is needed.

Further frequently cited aerosol deposition models can be found in health studies dealing with particle deposition in the respiratory tract. Typical particle capture efficiencies as a function of particle size can be seen in Fig. 72. These models incorporate particle impaction and sticking efficiency in the form of the capture efficiency. It can be seen that very small and coarse particles are captured within the respiratory tract, whereas only 20–30% of particles with a size of around 400 nm reach the surface and stick. The capture efficiency depends on the breathing frequency and the tidal volume, and thus, the channel diameter. Various, mostly empirical models have been developed and used to validate experimental results. Predictions show that only smallest particles are able to travel down to the alveolar, whereas larger particles deposit much earlier in the bronchial and extrathoracic tract. In general, an increased capture efficiency is observed for a larger tidal volume, probably caused by lower velocities and increased residence times. The application of health models for ash deposition studies is questionable. Physics of both, particles and deposition surface are quite different. Furthermore, they are based on an internal flow problem, compared with an external flow around tubes and along walls within a power plant.

In general, aerosol deposition behavior is relatively unknown. Only few experimental studies can be found and their applicability to boilers is questionable. The role of higher temperatures and rough surfaces might change the deposition process significantly. Furthermore, strong temperature gradients lead to an increased deposition velocity, as shown and discussed in Section 2.5.2. More or less

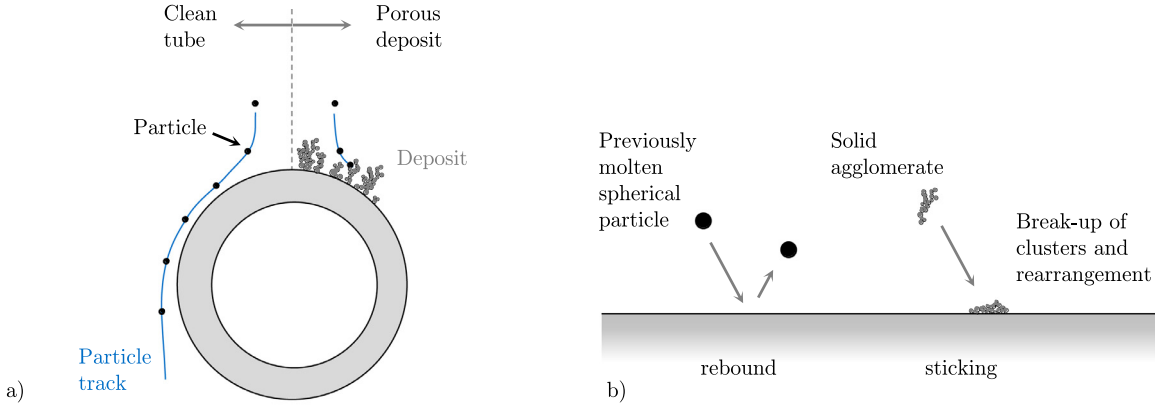

Fig. 71. Deposition of aerosols: (a) effect of existing deposit layers, and (b) deposition and sticking of agglomerates.

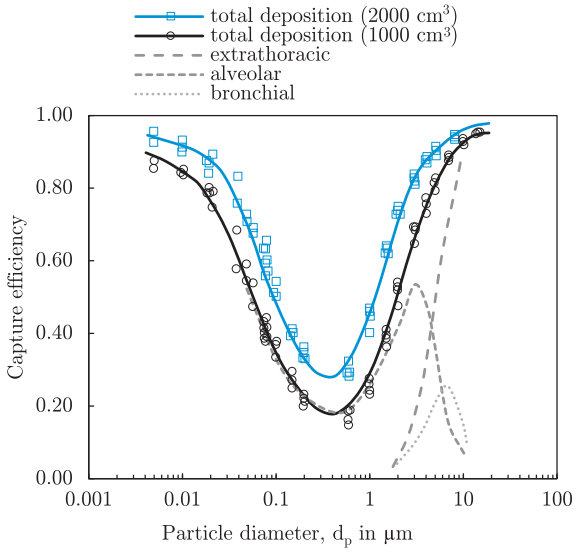

Fig. 72. Capture efficiency of aerosols in the respiratory tract as a function of particle size (unit density spheres), volume and breathing frequency in respiratory tract. Data points in figure: squares: tidal volume of 2000 cm^3 and breathing frequency of 3.75 min^{-1}; spheres: 1000 cm^3 and 7.5 min^{-1}. Data compiled from different studies [464–466].

unknown is the role and effect of electrostatic forces during impaction on heat exchangers in solid fuel fired boilers. Further work is needed in particular for aerosols and agglomerates at high temperatures. In addition, studies should focus on how aerosols affect the deposit formation and consolidation over time.

4.8. Overview on modeling studies

Modeling solid fuel combustion, ash formation and deposition started using one-dimensional stand-alone tools. There are various studies reporting good agreement of ash formation models with measurements, such as the work of Kang et al. [477,478], who calculated time-dependent char combustion and coalescence of ash grains with a cluster composed of char and ash sites. In this model, oxidation leads to particle shrinkage and partial coalescence of ash or char fragmentation. Monroe [23] studied ash formation at the MIT and developed a stand-alone tool based on Monte Carlo simulations of single coal particles for the prediction of ash formation. An interesting work was proposed by Charon et al. [85] and Barta et al. [72], the so-called "urn"-model, as mentioned earlier. This model enables the prediction of ash PSD and chemistry, simultaneously. A number of eleven mineral classes is used, which might be too low in order to predict the vast variance among fly ash particles, and their chemistry. Nevertheless, the approach is promising. Another highlight is the work of Wilemski and Srinivasachar [104], who used a scaled Monte Carlo simulation for mineral distribution. Char conversion includes a fragmentation model and considers different char structures. Good agreement for a bituminous coal is reported, whereas a second coal fails. The authors underline the importance of knowledge on the non-random mineral distribution and char structure. In general, most of the above mentioned stand-alone models report relatively good agreement with measured particle size distribution. These fundamental models are much more sophisticated compared with current CFD methods. Models predicting both, ash PSD and chemistry, are rare and require in-depth fuel characterization methods. Early deposition models used an Eulerian approach and go back to Friedlander and Johnstone [217]. In this model, there is no slip between the gas flow and the particle velocity. The concentration of particles in the flow parallel to the wall, is used to estimate a deposition rate. It is assumed that turbulent diffusion leads to particle transport towards the laminar sublayer. Only particles with high velocities are able to penetrate through this layer. However, this velocity has to be estimated and leads to high uncertainties. Baxter and DeSollar [13] developed the standalone code ADLVIC, which includes inertial impaction, thermophoresis, condensation, chemical reactions and uses bulk ash composition in order to predict the deposit chemistry. A good agreement with measurements is reported. Further standalone tools are included in the "Fuel Quality Advisor" developed at the Electric Power Reasearch Institute (EPRI). They include FOULER and SLAGGO, which have several submodels for ash formation, mineral transformation, and ash deposition. They predict the heat penalty caused by deposits. A similar code is developed at the University of North Dakota called LEADER predicting fouling propensities inside a boiler [57]. An inclusion of these or other sophisticated models in a CFD code enables the prediction of fuel conversion, slagging and fouling locations, their extent, and the optimization of operation or design. However, the incorporation of such standalone models into CFD codes is lacking behind [70]. Often too simple models are used, which may lead to wrong conclusions. A comprehensive overview of CFD studies on industrial boilers or pilot-scale test-rigs, is given in Table 21. Most studies on predicting ash deposition can be found for PF systems. There are some studies dealing with grate and FB combustion, however, modeling the combustion and ash formation process in fixed or moving beds is challenging. An overview on CFD studies dealing with FB can be found in the work of Singh et al. [479].

Among the pioneers in using CFD codes for the prediction of slagging and fouling are the studies of Boysan et al. [398], who calculated the rate of char impacting on walls, Richards et al. [408], and Wang and Harb [480]. Both of the latter two studies used the PCGC code, developed at the Brigham Young University. Richards et al. [408] applied two-dimensional simulations for a 1 MW_{th} test facility to calculate deposition rates. A first three-dimensional model was applied for a PF boiler, by Wang and Harb [480]. The PCGC code uses a different particle treatment compared with Lagrangian tracking, where particle clouds and their transport are calculated instead of individual tracks. Particle impaction and deposition rates are estimated based on particle concentrations near the walls. The authors use the viscosity concept of Walsh et al. [395] to calculate the deposition of a representative number of particles. The positions, at which slagging and fouling rates were predicted inside a boiler, were reduced to approximately 100–200 [480] and deposition rates were interpolated in between. Pseudo-transient calculations are used to account for deposit stickiness. A highlight is the use of CCSEM data, which enables the prediction of deposit chemistry. Many of today's CFD studies are still not able to predict chemistry and do not consider individual particle composition.

Lee and Lockwood [492] studied ash deposition of three British coals in a small combustion test rig using the CFD code CINAR. They use CCSEM data to predict fly ash composition in a pre-processor. A specified number of particle size classes and chemistry classes are used. This enables the prediction of deposit chemistry. Lee and Lockwood [492] used a critical velocity and viscosity approach. Particles with a velocity higher than the critical value are able to reach the wall. In the next step the viscosity decides whether a particle sticks or not. An increased iron deposition was found for early stages, whereas in later stages, the deposit composition was similar to the fly ash.

Božič [184] used the code FLOREAN of University of Braunschweig to predict mineral transformation and deposition. He used a post-processor and included 50 mineral matter transformation processes, in which chemical reactions and their kinetics, diffusion limitations, fusion, crystal and glass formation are incorporated. This process is highly complex, but enables studying the role of atmosphere and time on ash deposition. This model was further used and improved by Strelow [488]. Both report a relatively good agreement

Table 21
Overview of CFD studies predicting fly ash formation and deposition in GF, FB and PF combustion systems. Modified and extended from Weber et al. [384].

References	System[a]	Fuel	Code	Turbul. model	Radiation model[b]	Particle transp.[c]	Devol. model[d]	Char Comb.[d]	Ash formation	Ash chemistry	Sticking criteria	Deposition mechanisms[e]	Regions
Industrial boilers													
Wang and Harb 1997 [480]	PF: 85 MW_{el} tang.-fired boiler, Goudey USA	bit. coal	PCGC-3	$k-\varepsilon$	DO	LT	TR	own model	mineral distr. based on CCSEM, using full, partial & no coalescence model	individual particles	μ_{crit}	IN	boiler walls
Bernstein et al. 1999 [481]	PF: 800 MW_{el} boiler, Schwarze Pumpe Germany	brown coal	Fluent	n.i.	n.i.	n.i.	n.i.	n.i.	n.i.	n.i.	n.i.	n.i.	n.i.
Fan et al. 2001 [482]	PF: 300 MW_{el} tang.-fired boiler	hard coal	in-house	$k-\varepsilon$	Monte-Carlo	LT	SR	own model	n.s.	bulk ash	Walsh	IN	boiler walls
Eddings et al. 2001 [483]	PF: 900 MW_{el} tang.-fired boiler	bit. coal	GLACIER	$k-\varepsilon$	n.s.	n.s.	n.s.	n.s.	separate treatment for pyrite	n.s.	T_{crit}	IN, TP, EI	boiler walls
Richter 2002 [222]	PF: 450 MW_{el} wall-fired boiler, Schkopau Germany	brown coal	AIOLOS	$k-\varepsilon$	n.s.	LT	SR	KD	stand-alone tool, fly ash as separate injection	bulk ash	Walsh, Senior	IN, TP, EI	boiler walls
Müller et al. 2003 [484]	BFB: 35 MW_{el} CHP plant, Idbäcken Sweden	wood	Fluent	$k-\varepsilon$	DO	LT	own model		thermod. equilib. calculations		melting curve	IN	free-board, boiler walls
Božič 2003 [184]	PF: 600 MW_{el} tang.-fired boiler	lignite	FLOREAN	$k-\varepsilon$	flux model	LT	SR	KD	16 minerals for 4 size fractions	individual particles	n.s.	IN	furnace walls
Müller et al. 2005 [485]	BFB: 295 MW_{th} Rauhalahti plant, Jyväskylä Finland	peat/forest residue	Fluent	$k-\varepsilon$	DO	LT	SR	own model	ash particles released from the freeboard	n.s.	melting curve	IN	free-board, boiler walls
Kær et al. 2006 [360]	GF: 8.3 MW_{el} CHP plant, Masnedø Denmark	straw	Fluent	$k-\varepsilon$ RNG	DO	LT	grate model		based on measurements of fly and bottom ash	two particle types	melting curves	IN, TP, EI	platen superheater, tubes
Lundmark et al. 2010 [486]	BFB: 295 MW_{th} Rauhalahti plant, Jyväskylä Finland	peat/forest residue	Fluent	$k-\varepsilon$	DO	LT	SR	own model	ash particles released from the freeboard	n.s.	melting curve	IN	free-board, boiler walls
Vuthaluru et al. 2011 [487]	PF: 330 MW_{el} wall-fired boiler	sub-bit. coal	Fluent	$k-\varepsilon$	P1	LT	SR	KD	identification of regions based on particle tracks	bulk ash	none	n.s.	n.s.
Strelow 2013 [488]	PF: 944 MW_{el} tang.-fired boiler, Niederaußen Germany	lignite	FLOREAN	$k-\varepsilon$	flux model	LT	SR	KD	mineral distribution/ transf. based on oxide analysis	individual particles	melt fraction	IN	boiler walls
Taha et al. 2013 [489]	PF: 518 MW_{el} tang.-fired Maasvlakte boiler, Netherlands	coal-meat & bone meal	CFX	$k-\varepsilon$	DO[f]	LT	SR	KD	n.s.	bulk ash	crit. viscosity and Urbain	IN	location on boiler walls
Kreutzkam 2014 [490]	PF: 350 MW_{el} wall-fired boiler, Munich Germany	bit. coal	Fluent	$k-\varepsilon$ RNG	DO	LT	SR	KD	char fragmentation influences remaining PSD, full coalescence was assumed	bulk ash	FactSage melting curve	IN	boiler walls
Leppänen et al. 2014 [103]	Kraft recovery boiler	black liquor	Fluent	$k-\varepsilon$ real.	DO	LT & EF	droplet evap.		condensation and aerosol formation	alkali compounds	n.s.	TP, CO, DI	platen heat exchangers
Lab- or pilot-scale systems													
Richards et al. 1993 [408]	PF: 1 MW_{th} fireside performance test facility	bit. coal	PCGC-2	$k-\varepsilon$	DO	LT	TR	const. rate	fly ash is used as a separate cloud injection	bulk fly ash	Walsh / Urbain	IN	deposition panels
Huang et al. 1996 [491]	PF: 100 kW_{th} pulverized coal combustor	two US coals	Fluent	n.s.	n.s.	LT	none	none	fly ash is injected using RR PSD[g]	n.s.	Walsh	IN, TP	cooled tubes
Lee & Lockwood 1998 [492]	PF: 150 kW_{th} ash deposition test rig	bit. coals	CINAR	$k-\varepsilon$	DTM	LT	SR	KD	CCSEM of fly ash, is injected at specified locations	individual particles	viscosity, Urbain	IN	different positions

(*continued on next page*)

Table 21 (*Continued*)

References	System[a]	Fuel	Code	Turbul. model	Radiation model[b]	Particle transp.[c]	Devol. model[d]	Char Comb.[d]	Ash formation	Ash chemistry	Sticking criteria	Deposition mechanisms[e]	Regions
Pyykönen and Jokiniemi 2003 [99]	Kraft recovery boiler, isolated platen superheater	black liquor	Fluent 2D	$k-\varepsilon$ RNG	none	EF	none	none	fine dust is modeled	alkali comp.	n.s.	TP, EI, DI	platen superheater
Forstner et al. 2006 [493]	GF: 440 kW_{th} grate-–fired combustion unit		Fluent	$k-\varepsilon$ real.	DO	LT	emp. bed model		8 classes of ash released from bed		n.s.	IN, CO	boiler walls
Tomeczek and Wacławiak 2009 [253]	PF: isolated superheater tube	coal	Fluent 2D	$k-\varepsilon$	none	LT	none	none	different minerals are considered	n.s.	Walsh	IN, CO	superheater tube
Akbar et al. 2010 [258]	PF: 0.5 MW_{th} KSVA furnace, Stuttgart Germany	straw	AIOLOS	$k-\varepsilon$	n.s	LT	SR	KD	n.s.	KCl & Si-rich particles	melt fraction	IN, CO	on a probe and furnace walls
Schulze et al. 2010 [495]	GF: 70 kW_{th} pellet furnace	wood pellets	Fluent	$k-\varepsilon$ real.	DO	LT	bed model		bed model releases vapors and ash particles	Si- & salt-rich	viscosity/ melt fraction	IN, CO, TP	walls
Ai and Kuhlman 2011 [297]	Lab-scale deposition test rig	coal fly ash	Fluent 2D	$k-\varepsilon$	n.s	LT	none	none	ash particles are injected	bulk ash	Brach & Dunn	IN	cooled deposition probe
Degereji et al. 2012 [494]	PF: 0.2 MW_{th} furnace, Leeds UK	bit. coals	Fluent	$k-\varepsilon$ RNG	DO	LT	FG-DVC	intrinsic	n.s.	bulk ash	Energy balance	IN, TP	deposition panels
Losurdo et al. 2012 [342]	PF: lab-scale combustor, ECN Netherlands	bit. coals	Fluent	$k-\varepsilon$	n.s.	LT	n.s.	n.s.	n.s.	bulk ash	critical velocity	IN	cooled deposition probe
Venturini et al. 2012 [496]	PF: lab-scale combustor [391], isolated tube	straw	in-house	mod. $k-\varepsilon$	none	LT	none	none	ash particles are injected	bulk ash	Walsh, Urbain	IN	cooled deposition probe
Beckmann et al. 2016 [397]	PF: lab-scale plug-flow reactor, IEVB Germany	bit. coals	Fluent	$k-\varepsilon$	n.s.	LT	TR	intrinsic	none	bulk ash	various	IN, TP	cooled/uncooled dep. probe
Pérez et al. 2016 [301]	Kraft recovery boiler, isolated superheater tubes	black liquor	Fluent 2D unsteady	$k-\omega$ SST	none	LT	none	none	ash injected	bulk ash	Konstandopoulos	IN, TP	cooled tube
Yang et al. 2016 [303]	PF: EFR with co-firing	coal/palm kernel	Fluent 2D	$k-\omega$ SST	DO	LT	SR	intrinsic	diameter change	bulk ash	melt fr./ Mao et al.	IN	cooled dep. probe
Yang et al. 2017 [304]	PF: 300 kW_{th} pilot-scale furnace	Zhundong lignite	Fluent 2D	$k-\omega$ SST	DO	LT	none	none	ash injected	bulk ash	melt fraction	IN, TP, CO	cooled dep. probe
Wang et al. 2017 [455]	tube of MSW economizer	MSW ash	Fluent 3D	$k-\varepsilon$ RNG	none	LT	none	none	ash injected	bulk ash	Konstandopoulos	IN	H-type finned tube

n.s. - not specified or mentioned in the publication, n.i. - no information available

[a] System: PF - pulverized fuel, FB - fluidized bed, GF - grate firing, CHP - combined heat and power

[b] Radiation: DO - discrete ordinates, DTM - discrete transfer method

[c] Particle transport: LT - Lagrangian tracking, EF - Eulerian formulation

[d] Devolatilization: SR - single rate model, TR - two-competing rates model and char combustion: KD - kinetics, diffusion limited model

[e] Deposition mechanism: IN - inertial impaction, TP - thermophoresis, CO - condensation, EI - eddy impaction, DI - diffusional deposition, CR - chemical reactions

[f] not clearly stated

[g] RR – Rosin Rammler, PSD – Particle Size Distribution

with measurements in test facilities and conducted calculations for full-scale boilers. An interesting approach is presented by Bernstein et al. [481], in which they conducted coupled calculations between the fireside and the water-steam cycle. By using such a method, more appropriate boundary conditions, in particular temperatures, can be obtained for the fouling and slagging propensity. However, complexity increases strongly.

In the early 2000's, modeling studies for biomass combustion and ash deposition emerged; mainly in the Scandinavian region. Pyykönen and Jokiniemi [99], developed a condensation model for the formation of alkali chloride aerosols. The transport of aerosols is computed using a general dynamic equation in the Eulerian frame of reference. In this equation, additional velocity components on particles due to thermophoresis or Brownian diffusion are incorporated leading to aerosol deposition. Three deposition paths are identified, which are the formation of sub-micron fume particles in the flow and their deposition via thermophoresis, the direct condensation of vapors on heat exchangers, or the nucleation of finest particles in the boundary layer during cooling and their deposition. Kær [497] conducted CFD simulations on a straw-fired grate using ANSYS CFX. In a later study, Fluent was used instead [360]. The simulations include the release of combustible gases and fly ash particles from a grate model. The model considers both fine sub-micron particles similar to Pyykönen and Jokiniemi [99], and coarse fly ash particles. Melting curves were obtained using thermodynamic equilibrium calculations and used for an ash particle sticking criterion. Location, amount and chemistry of ash deposits were predicted and were in-line with observations during real operation. Leppänen et al. [103] developed a condensation model for the sub-micron particle formation in a Kraft recovery boiler burning black liquor, a residue of the paper industry. The modeling included particle dynamics and equilibrium chemistry for alkali compounds in a full, three-dimensional CFD model of the boiler. Fine particle transport is modeled using the Eulerian formulation and deposition is calculated based on a similar approach as used by Pyykönen and Jokiniemi [99], considering diffusion effects and thermophoresis. The model is partially validated with measurements from heat exchanging surfaces. The predicted chemistry of particles extracted from the flue gas agrees well with model results.

The majority of studies mentioned above estimate the amount of ash accumulation using the particle concentration near the wall and the concept of the deposition velocity, e.g. see [360]. The actual calculation would require a highly resolved boundary layer, and the exact geometry of thousands of convective heat exchanger tubes. Single tube studies were conducted by Tomeczek and Wacławiak [253], Haugen and Kragset [226], Venturini et al. [496], Weber et al. [206], Pérez et al. [300–302]. Typically, all these studies do not include combustion and ash formation processes. Ash particles are injected in a small domain, such as the flow around a superheater tube. Tomeczek and Wacławiak [253] were among the first to present an interesting deposit built-up model accounting for the forming layer. Later on, Weber et al. [206,384] identified an important and crucial aspect when predicting impaction rates of small particles. If the boundary layer is not resolved properly by a specified number of nodes in radial as well as circumferential direction, impaction rates for small Stokes numbers $St < 1$ are highly overestimated. This is crucial in particular for predicting the deposition of particles with small sizes and clean tubes. Furthermore, this effect can explain relatively high deposition rates predicted by early CFD studies as shown in Table 7. The group of Weber [206,384] recommends to place at least one node in radial direction within the displacement thickness and 384 nodes around the cylinder circumference in order to accurately predict particle tracks and deposition rates. Pérez et al. [301,302], who used a highly-resolved grid, studied the deposition of small ash particles on tubes using unsteady simulations. They developed a comprehensive energy-based sticking criterion, found time-dependent deposition around the full circumference of the tubes and vortexes between the tubes affecting ash deposition. A further model including a dynamic built-up by grid manipulation was presented [300]. By using this model, they found that tube arrangement affected vortexes and by this also deposition rates.

An important question is, how to use information from CFD simulations for practical aspects, such as boiler operation and optimization. First of all, if predictions are able to accurately predict locations of deposit formation, the position of soot-blowers as well as soot-blowing intervals can be optimized. Furthermore, this allows to design flow paths as well as the ideal location for the injection of additives. However, further work in this area is needed, in particular addressing the role of deposit structure and how to consider this in advanced CFD models.

4.9. Analogies to other research fields

There are many research areas dealing with similar problems of particle deposition and fouling. Often, literature from other fields is ignored and not used. Table 22 summarizes the main research areas, and highlights their parameters. Related fields of research are the icing of air crafts, ash deposition in aero-engines caused by volcanic ash particles, deposition of fine particles or vapors in gas turbines, spray deposition in internal combustion engines, spray coating, and aerosol deposition in the human body, such as the respiration tract. The major differences to other fields are relatively low particle velocities and high viscosity values of ash particles in combustion systems. Models from one field do not necessarily work in other fields, however, often they can be adjusted or extended. Further fields involve heat exchanger fouling in various industries such as crude oil, food, desalination, automotive or other processes. A good overview on heat exchanger fouling is given in the work of Müller-Steinhagen and Zettler [498].

5. Ash particle rebound behavior

Theories on the rebound behavior of solid particles on a substrate are often based on the pioneering work of Hertz [507] and Lord Rayleigh [508]. The majority of new models extend the basic theory for

Table 22
Particle deposition in other fields of research and their main characteristics (with the deposition mechanisms being IN - inertial impaction, TP - thermophoresis, CO - condensation, and DI - diffusional effects). Values are either taken from given references or estimated.

Research field	Deposition mechanism	Deposition velocity in m/s	Temperature range in °C	Particle type & composition	Particle size in μm	References
Icing on air crafts	IN, CO	70–250	−50–0	water droplets	10–50	[499,500]
Ash dep. in aero-engines	IN, TP	30–350[a]	0–1400[a]	volcanic ash particles	1–100	[501,502]
Dep. in gas turbines	TP, DI	30–350[a]	0–1400[a]	soot, aerosols	< 10	[502]
Respiratory tract	IN, DI	0–5	−20–40	aerosols or sprays	0.01–50	[465,503,504]
Spray coating	IN	0–150	−100 to 800[a]	droplets of paint	1–100	[505]
Diesel engines	IN	0–200	−20 to 1000[a]	diesel droplets	0.1–300	[506]

[a] partly estimated.

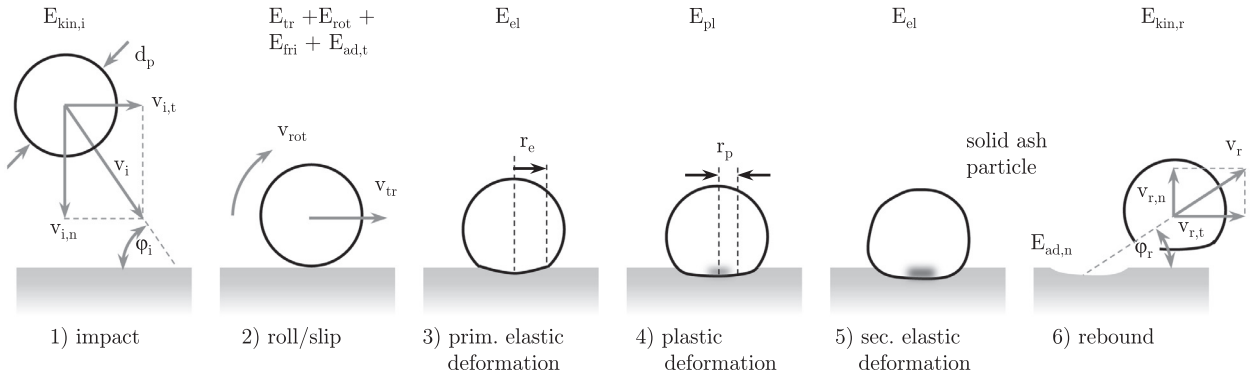

Fig. 73. Stages of a solid ash particle impaction on a surface (adopted and modified from Xu and Willeke [510] and Richter [222]).

phenomena such as plastic deformation and/or adhesion. Many studies can be found on the impact mechanics, however the phenomena of sticking and rebound is still poorly understood [414]. Most studies use idealized conditions, with the following assumptions [509]:

- There is no viscous drag due to a fluid phase between the particle and the surface,
- particles are smooth, non-rotating spheres,
- substrate is assumed to be smooth, flat and solid, and
- particles approach the surface with an initial kinetic energy much smaller than the thermal energy required to melt the particle.

Different stages of the impact of a solid particle with a solid substrate, and their respective energies, are shown in Fig. 73. A particle of mass m_p is colliding with the surface at an impact velocity v_i under an angle φ_i (velocity and energy components do not use the index "p" for particle in order to enhance readability). The tangential velocity component of an impacting particle $v_{i,t}$ can be responsible for rolling and sliding events upon impact (stage 2), where the friction coefficient f between the particle and the surface determines the behavior during stage 2 [222]. Losses occur during the transformation of the tangential kinetic particle energy $E_{kin,t}$ into translational E_{tr} and rotational E_{rot} energy. The losses are caused by friction E_{fri} or due to work of the rotating particle against the particle adhesion in tangential direction $E_{ad,t}$. The normal kinetic energy $E_{kin,n}$ is responsible for particle deformation. The deformation subdivides into elastic and plastic deformation stages. The energy involved during plastic deformation, E_{pl}, is lost in contrast to the energy stored during elastic deformation, E_{el}. This energy is left for particle rebound with a particle velocity v_r. Using the energy balance leads to the following expressions for the impact and rebound kinetic energy [222,510]:

$$E_{kin,i} = \underbrace{E_{el} + E_{tr} + E_{rot}}_{\text{useful energy}} + \underbrace{E_{pl} + E_{fri} + E_{ad,t}}_{\text{losses}} \tag{108}$$

$$E_{kin,r} = \underbrace{E_{el} + E_{tr} + E_{rot}}_{\text{useful energy}} + \underbrace{E_{ad,n}}_{\text{losses}}. \tag{109}$$

Eqs. (108) and (109) can be used to set up a sticking criteria when $E_{kin,r} > 0$. The kinetic energy during rebound is:

$$E_{kin,r} = E_{kin,i} - (E_{pl} + E_{fri} + E_{ad,n} + E_{ad,t}) \tag{110}$$

Using an expression for the kinetic energy $E_{kin,i} = 1/2 m_p v_i^2$ one can obtain the following relation for the absolute rebound velocity v_r:

$$v_r = \sqrt{v_i^2 - \frac{2(E_{pl} + E_{fri} + E_{ad,t} + E_{ad,n})}{m_p}} \tag{111}$$

The velocity component in normal direction $v_{r,n}$ depends on E_{pl} and $E_{ad,n}$, the components in tangential direction $v_{r,t}$ on the other hand depend on the $E_{ad,t}$ and E_{fri} [222]. Often, the so-called coefficient of restitution (COR or e) is used to predict rebound behavior. It is defined as the ratio of rebound to impact velocity according to the following expression:

$$e = \frac{v_r}{v_i} = \sqrt{1 - \frac{2(E_{pl} + E_{fri} + E_{ad,t} + E_{ad,n})}{m_p \cdot {v_i}^2}} \tag{112}$$

Eq. (111) can also be rearranged for a critical particle velocity $v_{p,crit}$ below which particles will stick. Therefore, the rebound velocity is set to zero $v_r = 0$, yielding the following expression:

$$v_{p,crit} = \sqrt{\frac{2(E_{pl} + E_{fri} + E_{ad,t} + E_{ad,n})}{m_p}} \tag{113}$$

The energies given in Eqs. (111) and (112) are all non-linear functions of the particle impact velocity v_i [510]. According to Xu and Willeke [510] these stages divide into primary and secondary elastic deformation stages. Kinetic energy of an impacting particle is partitioned into energy lost to plastic deformation and energy stored in primary elastic deformation (before plastic deformation begins) and secondary elastic deformation of the plastically deformed material. The individual components in Eq. (112) and their mathematical description can be found for instance in the work of Xu and Willeke [510]. The coefficient of restitution depends on the material properties and kinetic energy of both collision partners. It can be easily determined by measuring the height loss during a drop experiment (influence of aerodynamics are often mentioned to be below 5%). The following thresholds for e are defined:

e = 0: perfectly inelastic collision. Objects do not move after collision. Example: water droplet on large surface, where all kinetic energy is dissipated during deformation.

0 < e < 1: real solid body collision: Realistic collisions, where the exact value depends on the material properties, the flow conditions and the impact energy. Example: ping pong ball rebounds on a table with around $e \approx 0.7 - 0.85$ depending on the drop height, and table/ball properties.

e = 1: perfectly elastic collision: No losses occur during impact. This is a theoretical case, which does not occur in reality. Values greater than unity gain energy, e.g. due to detonations or chemical phenomena.

5.1. Normal impact and rebound on a solid, smooth surface

Most experimental studies are carried out for normal impact, when the impact angle equals $\varphi_i = 90°$. These experiments also yield the critical particle velocity, when sticking occurs $e = v_r/v_i = 0$. The

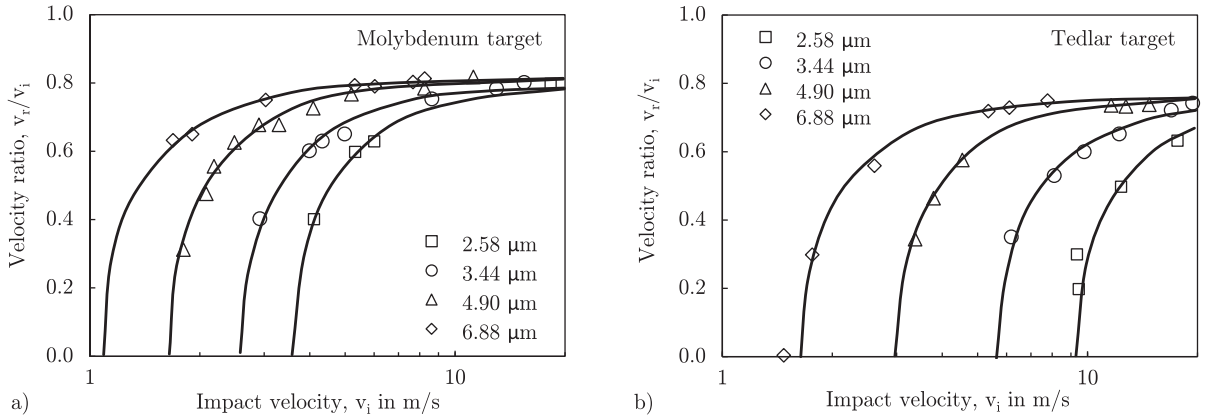

Fig. 74. Impact and rebound velocity ratio at low impact velocity for differently sized particles impacting on (a) molybdenum target and (b) fluorocarbon polymer target (tedlar). Continuous lines are fitted using the energy balance equation (figures reproduced from Wall et al. [414]).

critical particle velocity was found to depend on the impact angle [419] and on the particle size [414]. The study of Wang and John [419] showed that at constant impact velocity v_i and with decreasing impact angle φ_i, the critical velocity $v_{p,crit}$ decreased. Wall et al. [414] conducted a large number of experiments on the collision of different-sized particles with surfaces. Different material pairs were investigated by varying both, particle and substrate. The authors studied the collision over a broad spectrum of particle impact velocities (1 m/s $< v_i <$ 100 m/s). They found a critical particle velocity, which decreases with increasing particle size. Fig. 74 shows the restitution coefficient e, as a function of the impact velocity v_i, for a normal impact experiment. The results are obtained using ammonium (NH_4) fluorescein particles with varying size on molybdenum (Fig. 74(a)) and tedlar surfaces (Fig. 74(b)). It can be seen that the critical velocity depends on the particle size and the substrate when comparing both figures. The softer surface tedlar leads to a larger critical velocity and lower restitution coefficients. The particles of size $d_p = 2.58\,\mu m$ show a critical velocity of around 10 m/s, which decreases to around 3.8 m/s on a molybdenum substrate. The rebound velocity strongly increases with increasing impact velocity, reaching to a uniform value of $e \approx 0.8$, for all particle sizes. This behavior is explained by a strong decreasing ratio of E_{ad}/E_{kin}, i.e. the relevance of adhesive forces decreases with increasing impact velocities [222]. Wall et al. [414] furthermore observed a decreasing restitution coefficient at very high impact velocities ($v_i >$ 100 m/s). This is explained by plastic deformation caused when the stress inside the particle exceeds the material strength.

Often, the restitution coefficient e is measured as a function of the particle normal impact velocity $v_{i,n}$. Most studies use a setup with an impact angle of $\varphi_i = 90^\circ$ and a camera system, in order to measure particle velocity and height after rebound. Fig. 75(a) shows measurements on the restitution coefficient $e = v_{n,r}/v_{n,i}$ as a function of the normal impact velocity $v_{i,n}$. The data taken from Dunn et al. [424], was obtained using Ag-coated glass spheres on a stainless-steel surface. Given intervals show the scattering within which 95% of all data were found. It can be seen that the restitution coefficient increases with increasing impact velocity until a material-dependent, steady-state value of around $e \approx 0.8$ is reached. No decrease is observed indicating that no plastic deformation occurred. Dong et al. [420] studied the normal rebound behavior of fly ash particles, with a size of 75 $\pm$5 µm, which were mainly composed of quartz and mullite. A maximum value of $e \approx 0.43$ was observed followed by a decrease at higher impact velocity values. A similar behavior was found with the same device and material in an accompanying study as shown in Fig. 75(b). The role of particle size was studied and higher restitution coefficients were observed for larger particle sizes probably caused by higher kinetic energy. Interesting is the point where the restitution coefficient decreases, which is shifted to higher values when using larger particle sizes. They relate this phenomena to the work needed to break the connection between the two bodies. A possible explanation for the relatively low values of e is the particle shape, which was not perfectly spherical.

Thornton and Ning [290] developed a mathematical description of the restitution coefficient for adhesive elastic and adhesive elastic-

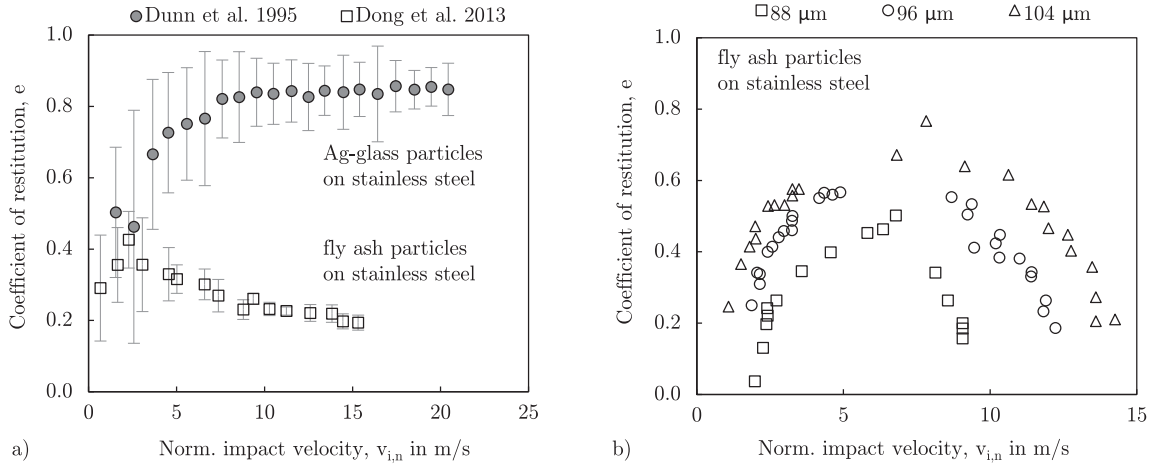

Fig. 75. Restitution coefficient e for normal impact ($\varphi_i = 90^\circ$) as a function of particle normal impact velocity $v_{i,n}$ at room temperature: (a) results from Dunn et al. [424] using Ag-coated glass spheres (1–30 µm) on a stainless-steel surface and Dong et al. [420] using fly ash particles (75 $\pm$5 µm, mainly composed of quartz and mullite) on stainless steel; (b) results from a different study of Dong et al. [421] using different-sized fly ash particles on stainless steel.

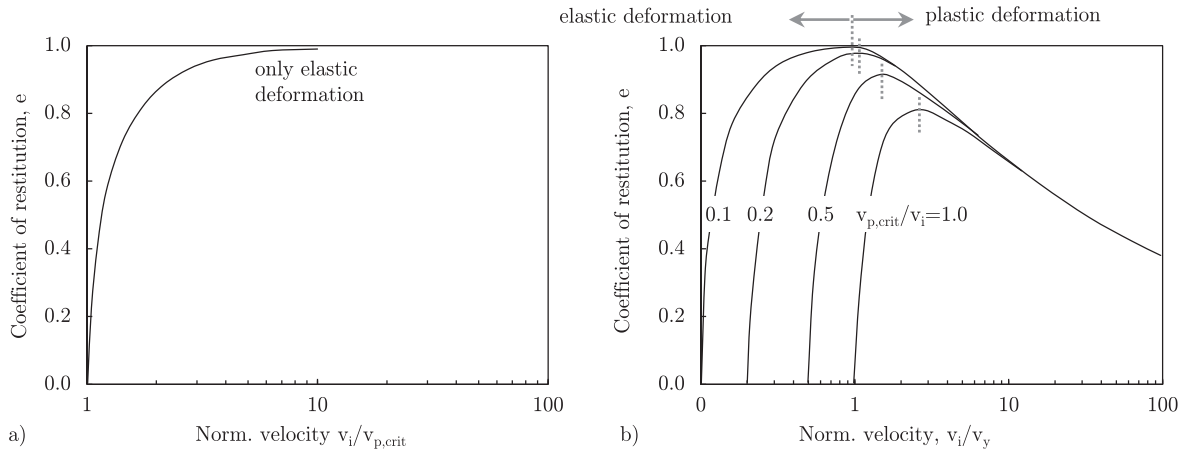

Fig. 76. Coefficient of restitution for (a) adhesive elastic spheres and (b) for perfectly plastic adhesive spheres [290].

plastic spheres. In the latter case, plastic deformation occurs after the particle deforms elastically, as shown in Fig. 73. The model for both scenarios is based on the theory of Johnson, Kendall and Roberts [431], commonly known as the JKR-theory. According to this theory, when two colliding surfaces come into contact, the normal force between the two bodies drops to a certain value (defined in [290]), due to van der Waals attractive forces. The velocity of the impacting sphere is then reduced gradually, accompanied with elastic wave propagation into the substrate. The incoming (loading) stage is completed as soon as the contact force reaches the maximum value, and the velocity reduces to zero. During the recovery stage, the stored elastic energy is then released and converted into kinetic energy moving the particle in the opposite direction. The work done during the loading stage is then recovered, but the particle still remains adhered to the surface caused by adhesive forces [290]. This idea is used in Eq. (76), in which Thronton and Ning [290] derive the critical velocity $v_{p,crit}$. They rewrite Eq. (76) for the case $v_i > v_{p,crit}$ to the following form,

$$1 - \left(\frac{v_r}{v_i}\right)^2 = \left(\frac{v_{p,crit}}{v_i}\right)^2, \tag{114}$$

where v_r/v_i is the definition for the restitution coefficient e:

$$e = \sqrt{1 - \left(\frac{v_{p,crit}}{v_i}\right)^2}. \tag{115}$$

The restitution coefficient for an elastic impact, as a function of the normalized impact velocity, can be seen in Fig. 76(a). Below $v_{p,crit}/v_i = 1$, a particle will stick. With increasing impact velocity v_i the restitution coefficient approaches a value of unity. In the case of elastic deformation, the maximum stress distributes as shown in Fig. 77(a) according to the Hertz theory [507] and Hertz pressure distribution. In case of plastic deformation, irreversible deformation occurs and the material strength is exceeded as shown in Fig. 77(b). Typically, the maximum contact pressure p_y is described as $p_y = \lambda \cdot Y$, where Y is the unaxial yield stress of the particle material (shown in Fig. 40), and λ is a parameter which can vary from $\lambda = 1.59$ to 3.20. According to van Beek [267], $\lambda = 1.59$ is the limiting case for elastic deformation, and $\lambda = 3.20$ occurs when the whole particle deforms plastically [267,301]. A case in between is shown in Fig. 77(b). The pressure reaches its maximum value in the region $r < r_p$, where r_p is the radius within which plastic deformation occurs. In the outer part ($r > r_p$ but $r < r_t$), elastic deformation is observed. The total contact radius r_t can be used to calculate the contact area between the substrate and the deformed particle. Pérez et al. [301] uses the following linear relation, in order to estimate the ratio of the area with plastic deformation, and the total contact area:

$$\lambda \approx 1.59 + \left(\frac{r_p}{r_t}\right)^2 \cdot (3.20 - 1.59) \tag{116}$$

Thornton and Ning [290] defined a yield velocity v_y, below which the impact is assumed to be perfectly elastic. Above this velocity, the impact leads to plastic deformation. The yield velocity for a particle impacting on a flat surface is obtained by:

$$v_y = 1.56\left(\frac{p_y^5}{E^{*4}\rho_p}\right)^{1/2} \quad \text{with} \quad p_y = \lambda \cdot Y \tag{117}$$

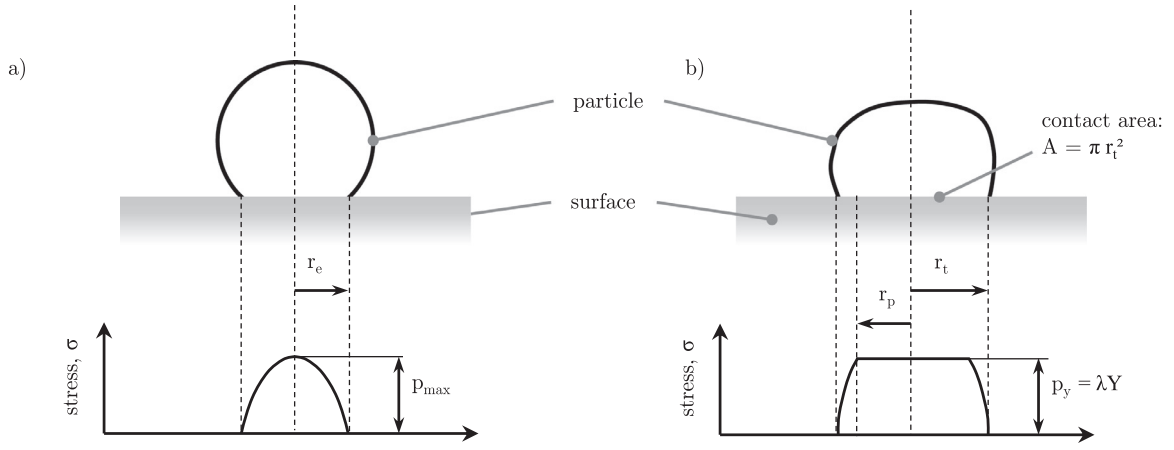

Fig. 77. Pressure distribution for an impacting particle: (a) for a pure elastic contact with Hertz distribution and (b) for an elastic-plastic contact (figure adopted and modified from [267,301,511]).

where p_y is the limiting contact pressure shown in Fig. 77(b), and Y is the yield stress. Thornton and Ning [290] used the JKR theory for adhesive elastic-plastic spheres, however, they did not solve equations analytically due to their complexity. Instead it was assumed that the work dissipated due to plastic deformation and the work dissipated due to adhesive rupture are additive. This simplified the problem and three regimes are derived to describe the coefficient of restitution: for $v_i \leq v_{p,crit}$

$$e = 0, \tag{118}$$

for $v_{p,crit} \leq v_i \leq v_y$

$$e = \sqrt{1 - \left(\frac{v_{p,crit}}{v_i}\right)^2} \tag{119}$$

and for $v_i \geq v_y$

$$e = \sqrt{\frac{6\sqrt{3}}{6}\left[1 - \frac{1}{6}\left(\frac{v_y}{v_i}\right)^2\right] \cdot \left[\frac{\left(\frac{v_y}{v_i}\right)}{\left(\frac{v_y}{v_i}\right) + 2\sqrt{\frac{6}{5} - \frac{1}{5}\left(\frac{v_y}{v_i}\right)^2}}\right]^{1/2} - \left(\frac{v_{p,crit}}{v_i}\right)^2}. \tag{120}$$

Eqs. (118)–(120) can be used to generate Fig. 76(b), by plotting the coefficient of restitution against the normalized velocity v_i/v_y, for different ratios of $v_{p,crit}/v_i$ [290]. At $v_i/v_y = 1$, plastic deformation begins and with increasing impact velocity a decrease in the coefficient of restitution is predicted, as observed in the experiments illustrated in Figs. 75(a) and (b), or as shown by the experiments of Wall et al. [414]. The model of Thornton and Ning [290] yields quite good results over a wide range, and is therefore often applied. Numerous models can be found in literature, and it is out of the scope of this review to discuss them all. Interesting might be for instance the work of Kim and Dunn [426], Krijt et al. [422], or Hærvig et al. [474].

5.2. Oblique impact and rebound on a solid, smooth surface

In the case of non-normal impact, which is typical for a PF power plant with superheater tubes, the determination of the restitution coefficient is more complicated. The rebound angle φ_r is not identical to the impact angle φ_i. There are some studies [512,514] reporting larger rebound angles than impact angles, which seems to be odd at the first glimpse. The particles seem to gain rebound velocity $v_{r,n} > v_{i,n}$ [301]. This behavior is explained by surface roughness effects and becomes important when a particle impacts a fouled layer. In this case, the angle of rebound can become unpredictable, showing a probability distribution. During oblique impact, frictional forces play an important role and have to be considered [512]. Fig. 78 shows definitions of angles, coordinates and the velocity components. The rebound angle and velocity of spherical particles depend on [513]:

- the impact angle φ_i,
- the initial impact speed v_i,
- the particle spin ω_i,
- the normal coefficient of restitution e_n,
- the surface roughness and surface energy of the particle and the substrate, and
- the impulse ratio of incoming and rebounding particle, which depends on the interface friction coefficient f).

The restitution coefficient, can be split into the normal and tangential component, according to the following definitions [513]:

$$e_n = -v_{r,n}/v_{i,n} \tag{121}$$

$$e_t = v_{r,t}/v_{i,t} = 1 - f \cdot (1 + e_n) tan(\varphi_i) \tag{122}$$

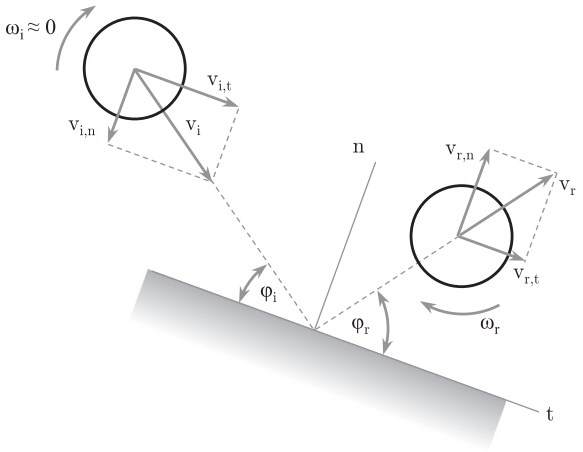

Fig. 78. Oblique impact and definition of angles, coordinates and velocity components [512,513].

Wu et al. [513], suggest the following equation for the calculation of the tangential restitution coefficient:

$$e_t = 1 - \frac{2}{5}\frac{d_p/2(\omega_r - \omega_i)}{f \cdot v_{n,i}}\frac{f}{cot(\varphi_i)} \tag{123}$$

The rebound angle can then be calculated using the following relation:

$$tan(\varphi_r) = \frac{v_{r,n}}{v_{r,t}} = -\frac{e_n}{e_t} tan(\varphi_i) \tag{124}$$

An analysis of the tangential coefficient of restitution e_t, was conducted in a previous study by Wu et al. [515]. They used FEM simulations to predict the tangential restitution coefficient e_t, as shown in Fig. 79(b). At low impact angles $\varphi < 30°$, sliding is frequently reported and dominates [512]. The friction coefficient f is too low to slow down the particle. At higher impact angles of $\varphi \geq 30°$ a value of $e_t \approx 5/7$ is reported to be a good approximation [515]. Pérez et al. [301] used an expression based on the experiments of Brach et al. [512]. The restitution coefficient is calculated according the following expression:

$$e_n = -v_{r,n}/v_{n,i} = \max\{0.75; 2.00 - 2.04 \cdot \varphi_i\}, \tag{125}$$

Stanton and Rutland [517] and O'Rourke and Amsden [518] studied droplet-wall interaction and suggested the following restitution coefficient:

$$e_n = 0.993 - 1.76 \cdot \varphi_i + 1.56 \cdot \varphi_i^2 - 0.49 \cdot \varphi_i^3, \tag{126}$$

where the angle has to be used in radians. Attention has to be paid for the definition of the impact angle φ_i with the substrate. Different definitions can be found in literature. A comparison of Eqs. (125) and (126) with experimental values of Li et al. [516] is shown in Fig. 79(a). The rebound angle can be calculated using the continuous line of Fig. 79(b), Eqs. (124) and (125). The result is illustrated in Fig. 80(a). At low impaction angles, higher rebound angles are predicted. However, the random distribution of rebound angles cannot be covered. The random rebound angle, often mentioned in experimental studies, can be explained by Fig. 80(b). The microscopic surface is rough and small particles barely hit the surface at the macroscopic angle. Therefore, following the suggestion of Pérez et al. [301] to use a probability function to calculate a random rebound angle, seems meaningful. However, the limit of these angles should be determined experimentally. Pérez et al. [301] suggested limits between $\varphi_r = \arcsin(-v_{r,n}/v_r)$ and $\varphi_r = \varphi_i$ (equations differ in original publication due to a different angle definition).

Tabakoff [519] studied the rebound characteristics of fly ash particles of 15 μm size on different metal surfaces and varying impact angles. Studied surface materials were stainless steel, aluminum, titanium and some others. Furthermore, equations predicting

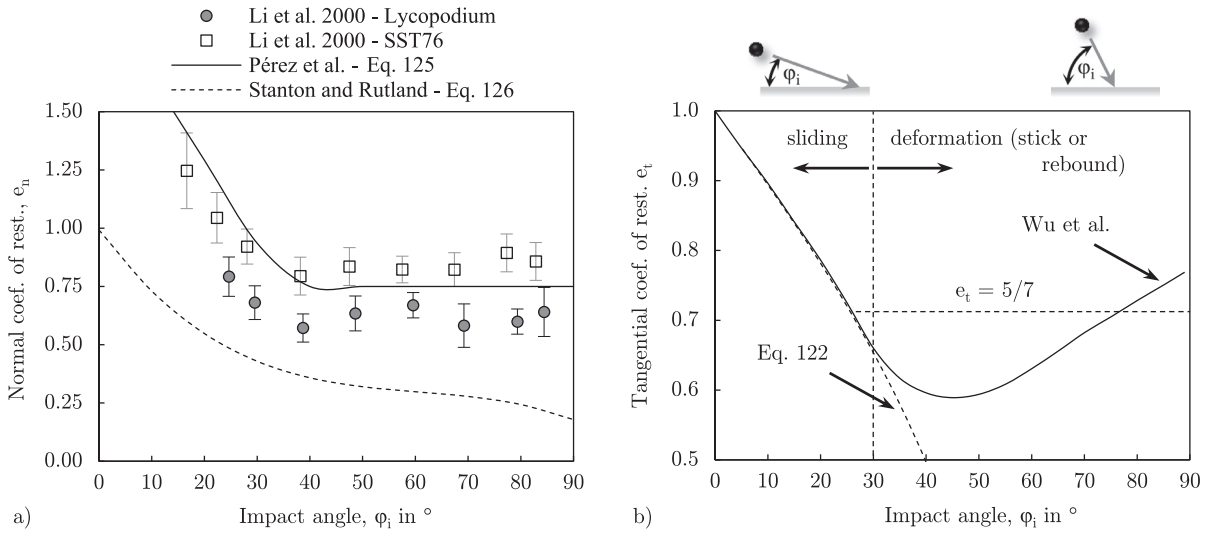

Fig. 79. Coefficient of restitution as a function of impact angle φ_i: (a) comparison of measured [516] and predicted normal coefficient of restitution e_n and (b) theoretical tangential coefficient of restitution e_t according to Wu et al. [515].

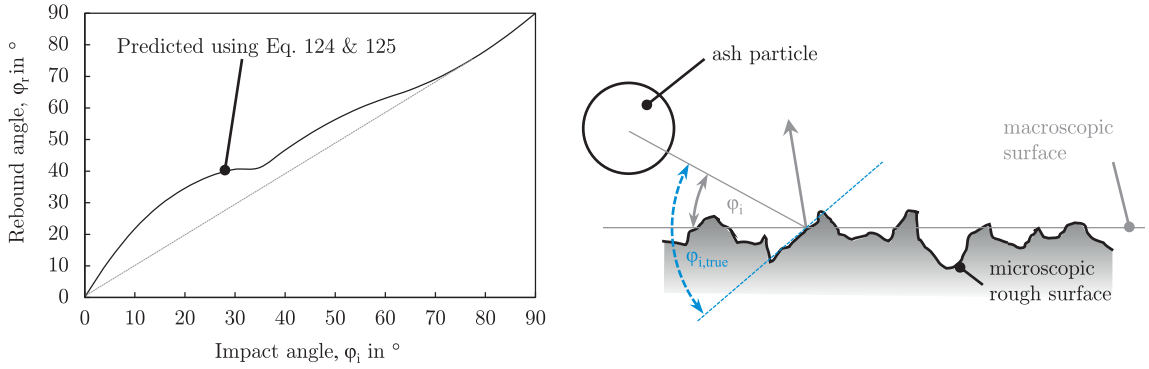

Fig. 80. Left: Predicted rebound angle as a function of impact angle and coefficient of restitution form Fig. 79. Right: Effect of surface roughness on particle rebound angle (similar to Mundo et al. [440]).

erosion behavior at high temperatures were presented. Findings of Tabakoff are presented in Figs. 81(a) and (b). Fig. 81(a) shows the velocity ratio of incoming and rebounding particles. With decreasing impact angle, the ratio approaches unity. The trend of mean measured points is well captured by Eq. (126), however with an offset. In addition, statistical distributions are shown within the figure for each measured point. Values are typically found within 20% showing a Gaussian distribution. Fig. 81(b) illustrates the so-called particle directional coefficient, which is obtained by dividing the rebound angle with the impact angle. The rebound angle seems to equal the impact angle at low impingement angles. However, with increasing impingement angles, the ratio drops to around 0.6 implying a reduced rebound angle compared with the impaction angle. A similar study was performed by Reagle et al. [520] using elevated temperatures (up to 800 °C) and high velocities (up to 102 m/s). The study uses road dust particles impacting stainless steel surfaces simulating the deposition of micro-particles under gas turbine conditions. Results indicate that temperature plays a minor role in energy transfer between particle and impact surface below a critical temperature. At 800 °C, the coefficient of restitution is reduced by an average of 16% compared with ambient temperature experiments. Their decrease is explained by an increase in velocity accompanied by the temperature rise. At higher temperatures reduced elastic modulus and yield strength are assumed to become relevant. A summary and overview on experiments aiming at particle deposition in gas turbines can be found in the work of Hamed and Tabakoff [502]. Particle velocities are considerably higher compared to power plants and therefore not included in this study. Values range from 65 up to 366 m/s [502]. A recent study dealing with ash and char particle rebound behavior was presented by Troiano et al. [456]. The authors studied particle-wall interaction phenomena for entrained flow gasifier using biomass ash and char particles from wood chips and corn stover. The impaction of particles on inclined hot and cold refractory material was recorded using a high speed camera. The authors found that even at ambient temperature, there are indications for plastic deformation. At high temperatures, there is a drop of the restitution coefficients in particular for low impact velocities. Typical restitution coefficients at room temperature were in the region of e = 0.2–0.6. At 1400 °C, values dropped to e = 0.05–0.4.

5.3. Impact and rebound on a powdery layer

Studies on particles impacting a powdery layer are rare in literature. However, these are the most realistic scenarios, in particular

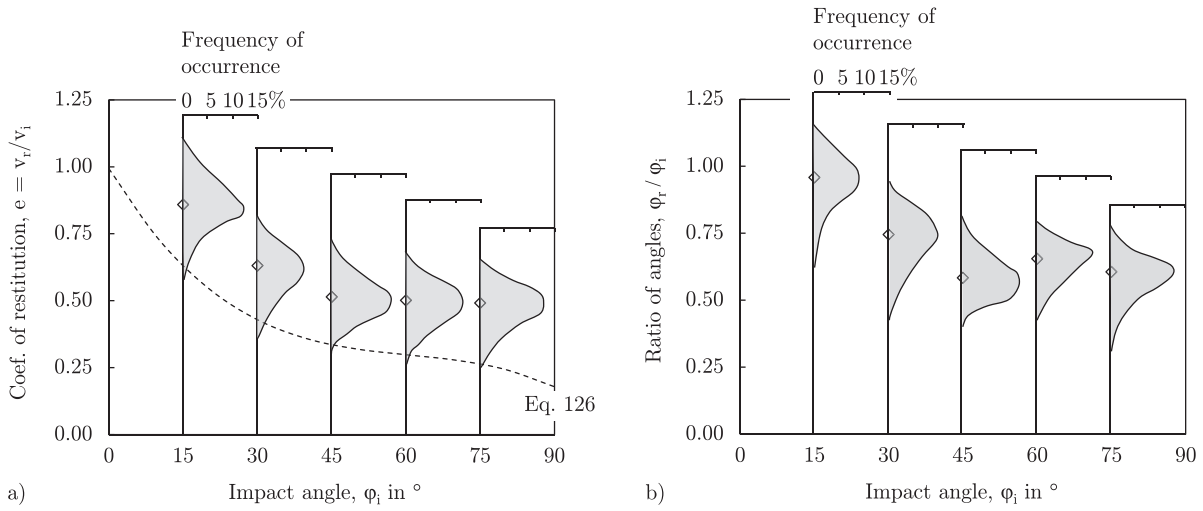

Fig. 81. Fly ash particle impaction on a stainless steel surface for different impaction angles: (a) coefficient of restitution and (b) ratio of rebound and impact angle. Both figures include the probability distribution for each measured point, data taken from Tabakoff [519].

within the convective section of a power station such as the economizer region. An interesting work was presented by van Beek et al. [268]. They studied the impaction of 50 μm glass particles on a thin layer of glass particles representing the fouling layer. Ash particles were simulated using glass spheres. Different scenarios were studied using a powdery (loose) or glued layer of glass, a varying impact angle in the range of $60 \le \varphi_i \le 90°$ and varying incident particle velocities in the range of 0.5 to 1 m/s. Experiments were recorded in a vacuumed column using a digital camera system [268]. Experimental results were modeled using a two-body collision model based on the rigid body theory (see Goldsmith [521]). This theory assumes that deformation during contact is negligible and the impact is described using linear and angular momentum conservation. In this theory, only two possible scenario can occur during rebound: sliding throughout the contact and rolling at exit [268]. Van Beek and co-workers [268] assumed that both the incident particle and the target particle are initially non-rotating and the target particle is resting with zero initial velocity. For the sliding-case, the normal and tangential rebound velocity components of the incident particle are calculated by [268,521]:

$$\vec{v}_{r,n} = \vec{v}_{i,n} - (1 + e_n) \cdot \frac{m_{p,2}}{m_{p,1} + m_{p,2}} \cdot \vec{v}_{i,n} \tag{127}$$

$$\vec{v}_{r,t} = \vec{v}_{i,t} - f \cdot (1 + e_n) \cdot \frac{m_{p,2}}{m_{p,1} + m_{p,2}} \cdot \frac{\left|\vec{v}_{i,n}\right|}{\left|\vec{v}_{i,t}\right|} \cdot \vec{v}_{i,n} \tag{128}$$

In above equations, $m_{p,1}$ and $m_{p,2}$ are the mass of the impacting and target particle, respectively, and the parameter f denotes again the Coulomb friction coefficient. The relation given in Eq. (128) is only valid in the case when the particles remain sliding over each other ($\varphi_i < 30°$). When rolling occurs (slip velocity is reduced to zero), the rebound velocity of the incident particle can be calculated by [268]:

$$\vec{v}_{r,t} = \vec{v}_{i,t} - \frac{2}{7} \cdot \frac{m_{p,2}}{m_{p,1} + m_{p,2}} \cdot \vec{v}_{i,t} \tag{129}$$

The minimum friction coefficient f_{min} required to bring the slip velocity to zero just at the end of the impact is given by [268]:

$$f_{min} = \frac{2/7 \cot(\varphi_i)}{1 + e_n} \tag{130}$$

The friction coefficient f and the normal restitution coefficient e_n were determined from experiments using a flat, solid glass target, where $m_{p,2} \gg m_{p,1}$. Using velocity components from the camera system, both parameters can be quantified using the following simplified equations:

$$v_{r,n} = -e_n \cdot v_{i,n} \tag{131}$$

$$v_{r,t} = v_{i,n} - f \cdot (1 + e_n) \cdot v_{i,n} \tag{132}$$

As already mentioned above, the normal restitution coefficient e_n accounts for the energy loss due to plastic deformation and adhesion. The measured normal restitution coefficient as a function of impact angle is shown in Fig. 82(a). It can be seen that with increasing angle, the coefficient of restitution increases, to $e_n \approx 0.8$ at normal impact. Van Beek et al. [268] conclude using the theory of Thornton and Ning [290], that the velocity is too low for plastic deformation and too high for adhesive forces to become important. Values agree with the study of Li et al. [516] at high impact angles. However, the relatively low value and the increase with increasing angle could not be explained. Results for the friction coefficient as a function of impact angle are shown in Fig. 82(b). Eq. (130) together with Eq. (125) are used to calculate f_{min}. At an impact angle of $\varphi_i = 33°$, the measured value is far below f_{min}, indicating that sliding occurs during the exit (rebound). A value of $f_{glass/glass} \approx 0.17$ is used for angles $\varphi_i < 45°$ [268]. A significant difference in studies using a powdery layer is that rebound velocities are typically lower, rebound angles show a broad scattering and particles from the substrate can be ejected. The lowered rebound velocity is mainly caused by the particulate layer absorbing kinetic energy of incoming particles. Particles inside the bed rearrange and typically a larger mass for the target particle is used for prediction as suggested by Werner [522] in the following form:

$$m_{p,2} = C_m \cdot m_{p,1}, \tag{133}$$

where C_m is a proportionality factor. The effective mass of the target particle is always larger than the mass of the target particle itself, considering the momentum transfer into the bed of particles around and beneath the target particle [268]. Van Beek et al. [268] found that the proportionality factor C_m is dependent on the bed porosity, the stickiness of bed particles, the layer thickness and the binding between target particles, and can be viewed as a system parameter. Is the binding perfect (e.g. for a molten layer or a solid, rough surface), the mass $m_{p,2}$ and C_m approach infinity. For a glass particle bed it was found to be in the range of $C_m = 2.6 - 3.5$ depending on the diameter ratio of incident to target particles. A smaller value of C_m is observed when the diameter of the incoming particle increases compared to the target particle diameter.

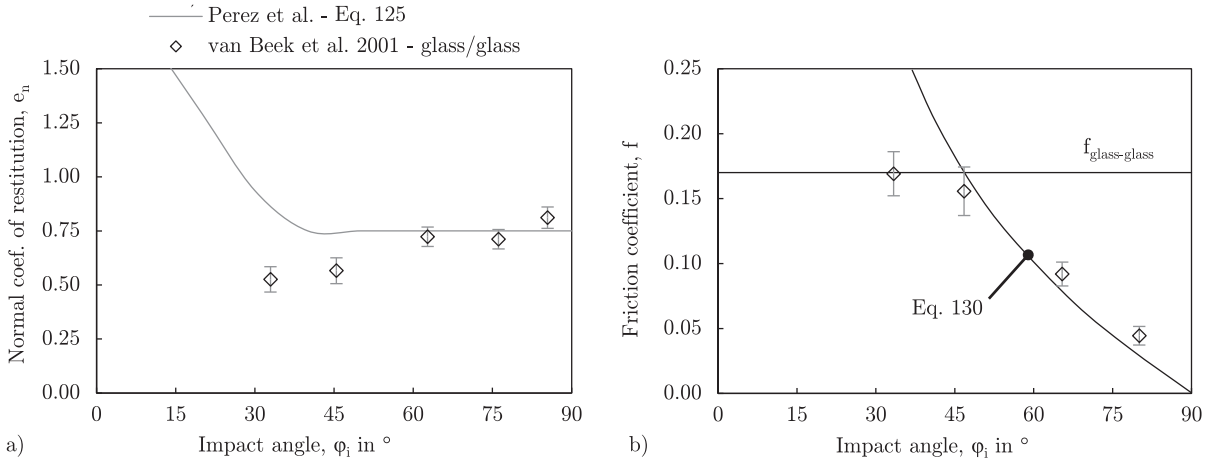

Fig. 82. Results from glass particle impaction on flat solid glass surface (taken from van Beek et al. [268]): (a) normal coefficient of restitution as a function of impact angle φ_i, and (b) friction coefficient f as a function of impact angle φ_i for a glass/glass material combination.

Fig. 83(a) shows a recorded image illustrating the impaction of a particle and the ejection of bed particles from a powdery surface. These images are used for the determination of rebound angles and velocity ratios. The measurements on the absolute rebound angle as a function of normal velocity ratio are shown in Fig. 83(b). The maximum rebound velocity ratio and thus the normal restitution coefficient is around $e_n = 0.58$. Most values are in the region $0.1 \leq e_n \leq 0.3$, indicating a high damping of a powdery glass layer. The absolute rebound angle shows a broad scattering with most particles rebounding at an angle of $\varphi_r \approx 40°$. A rebound in the negative tangential direction (left side) was nearly as common as a rebound to the positive tangential direction (right side). Therefore, when a particle impacts a rough surface a random distribution around $\psi_r \approx 50°$ to $\psi_r \approx -50°$ is observed. Van Beek et al. [268] used the two-body collision model described by Eqs. (127)–(130) together with Eq. (133) with $C_m = 3.5$ in order to predict rebound angles. Relatively good agreement with experiments is reported for the rebound angle and its distribution as well as the rebound velocity ratio. Thus, this kind of model can be applied.

It can be summarized that the normal coefficient of restitution and the friction coefficient are highly dependent on material properties of both collision partners - Young's modulus, yield stress - and process parameters - impaction velocity, impaction angle, particle sizes and surface roughness [268]. The tangential coefficient of restitution seems to be dependent on the friction coefficient of the material combination and can be approximated using the following equation:

$$f = \min\left\{f_{mat.1/mat.2}; \frac{2/7\,cot(\varphi_i)}{1+e_n}\right\}, \tag{134}$$

where $f_{mat.1/mat.2}$ is the friction coefficient of material 1 and 2. Using this equation and data from van Beek et al. [268], Fig. 84 can be calculated. It shows the tangential coefficient of restitution as a function of impact angle, analogously to Fig. 79(b). Predictions are compared to measurements of Müller et al. [523], who investigated the impaction of Al_2O_3 particles on steel at various impact angles. Relatively good agreement can be seen and a similar curve as predicted by Wu et al. [515], shown in Fig. 79(b), is obtained. However, a high sensitivity towards the friction coefficient f at high angles of impaction ($\varphi_i > 60°$) is observed.

Abd-Elhady et al. [524] used the same equipment as van Beek et al. [268] and studied the interaction and ejection of particles from a bed upon incoming particles. The two-body collision model was replaced by the so-called discrete element method (DEM), in which every particle contact including rearrangements in the bed, is described. Konstandopoulos [434] reports that the two-body collision model (with a higher effective mass for the target particle according to Eq. (133)) fails at higher kinetic energies of impacting particles, when they induce rearrangements or erosion of pre-deposited particles [434,524]. The DEM, developed by Cundall and Strack [525], treats every particle as a discrete entity, which interacts at its interface when in contact with other particles [524]. This method is

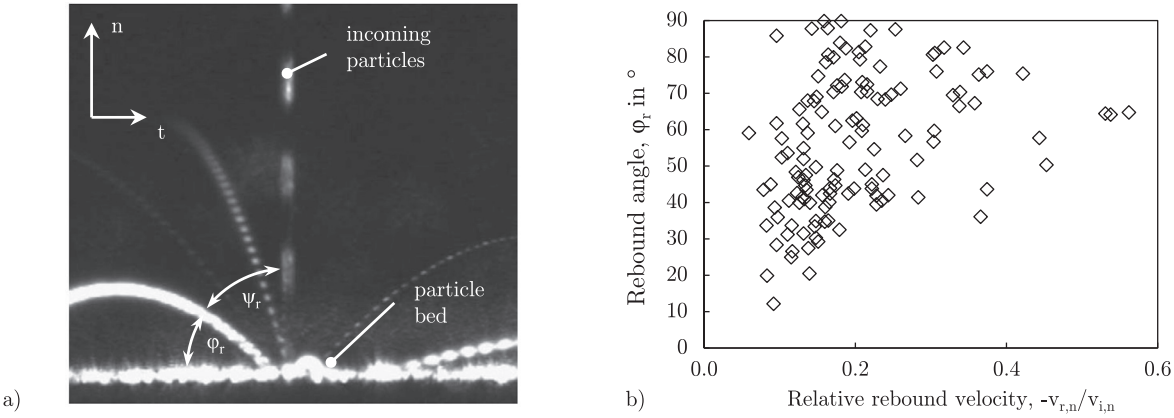

Fig. 83. Experimental results for glass particle impaction on a powdery glass particle layer (taken from van Beek et al. [268]): (a) characteristic image showing the ejection of bed particles form the surface and (b) rebound angle φ_r as a function of normal rebound velocity ratio $v_{r,n}/v_{i,n}$.

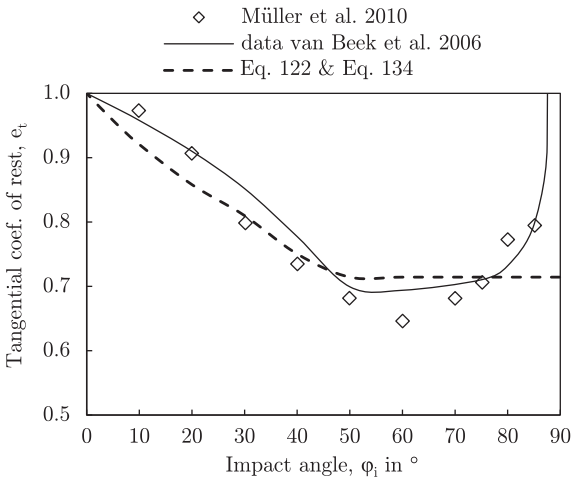

Fig. 84. Comparing measured and predicted tangential coefficient of restitution. Experimental points taken from a study of Müller et al. [523], who investigated Al_2O_3 particle impaction on steel at various impact angles.

often extended for plastic deformation upon contact using e.g. the model of Thornton and Ning [290] or the one proposed by Rogers and Reed [418]. An overview on the DEM and its capabilities can be found in the review of Li et al. [526]. Abd-Elhady et al. [524] conducted 490 experiments using spherical copper particles with a diameter of 54 μm and different impact speeds. The particles impact vertically on a bed which is composed of the same particles and had a porosity of 0.42. Experiments were conducted at room temperatures and the number of ejected particles were recorded. A regime map is derived from the experiment showing different zones - sticking, rebound and rebound with ejection of bed particles. The regime map is shown in Fig. 85. The particles will stick below a critical velocity of $v_{p,crit} \approx 0.3$ m/s. Rebound, is observed in the region of $0.18 \leq v_{p,n} < 1.1$ m/s. At higher values of $0.6 \leq v_{p,n} < 1.8$ m/s, the ejection of an additional particle, besides the incident particle, is observed. Two and more additional particles are ejected at $v_{p,n} \geq 1.5$ m/s. The overlap was explained by the impact angle. The incident particle can hit a bed particle at various microscopic angles, similar to Fig. 80. The DEM conducted by Abd-Elhady et al. [524] was able to predict the critical velocity and rebound velocity with a slight deviation. Furthermore, equations for energy loss due to plastic deformation, adhesion and stored elastic energy are

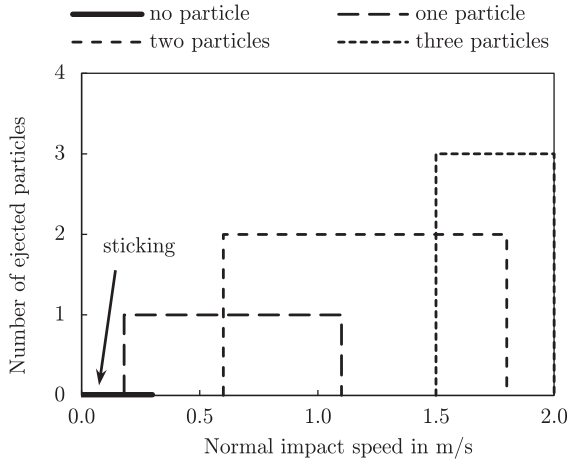

Fig. 85. Regime map showing the number of ejected particles from a bed as a function of incident particle vertical speed. Data and map from experiments of Abd-Elhady et al. [524] using uniform copper particles impacting a layer of copper particles at room temperature.

given. In addition, equations for the ejection time and the maximum deformation also referred to as the interpenetration distance of two equal sized particles as a function of material properties are presented and discussed. The maximum indentation of an incident particle hitting a bed of particles is shown to be directly proportional to the incident particle velocity and diameter if plastic deformation occurs [524].

An early study using DEM simulations in order to predict deposit growth for uniform particles was presented by Konstandopoulos [434]. Simulations were carried out in a three-dimensional domain using the FORTRAN code "FROZEN". The calculation is performed until a total number of 10^5 particles are deposited on 63x63 particle radii substrate with periodic boundaries [434]. The following parameters were chosen for the simulation: $e = 0.9$, $f = 0.2$, $E_\omega = 0$, 0.01, 0.1, and $\nu = 0.33$ [434,527], where E_ω is a dimensionless number relating kinetic energy to rotational energy. It relates the rotational energy barrier to the normal adhesion barrier [434]. Simulations are carried out using dimensionless parameters, where the velocity is normalized using the kinetic energy and particle mass. Model results are shown as two-dimensional cross-sections in Fig. 86 for different dimensionless impact velocities and impact angles. The author reports many common features compared with real particulate deposit pictures in literature. At low impact velocities, a "roughening" is observed which increases with decreasing impact angle. Orientated voids are caused by regions, where particle deposition is prevented and rebound will occur. These voids decrease with increasing particle velocity. At high impact velocities, the effect of impact angle diminishes and denser deposits are obtained. This is also reported by other studies such as the work of Ots [528]. Another finding shows that with increasing deposition velocity the number of rebounding particles increases. This is supported by experiments of Tsai and Cheng [529] using high loadings and an uncoated flat impaction surface. Furthermore, the number of impactions that a particle requires until it rests/sticks increases with increasing impact velocity. The results show that rebound velocity shows a multimodal nature and particles take up spin after collision. DEM simulations can be a useful, but computationally expensive, tool for the prediction of deposit structure, in particular at low temperatures such as the economizer region. At higher temperatures, sintering and melting occur leading to changes in structures and deposit growth. With this method, effects such as shedding and erosion can be predicted.

5.4. Impact and rebound on a liquid layer

Studies of particles impacting a solid substrate overlaid with a liquid layer are rare. These collision can be relevant for a variety of industries such as filtration or ash particle impaction on a slagged wall. Barnocky and Davis [530] conducted a series of experiments in which a solid ball drops on a quartz disk overlaid with a thin layer of Newtonian oil. Ball size and thus kinetic energy was varied from 1.6 to 6.4 mm, and material was either steel or polymer (lucite). Studied parameters comprise of the fluid layer thickness and viscosity, the ball size, density and elasticity. In their experiments, Barnocky and Davis [530] determined the critical drop height, and thus the critical velocity, that allowed the ball to rebound out of the fluid layer. The critical velocity, below which particles will stick, can be approximated by neglecting the air resistance $v_{p,crit} = \sqrt{2 \cdot g \cdot h_{crit}}$. According to the authors, this equation is valid within 5% accuracy for their experiments [530]. Results of their study can be seen in Figs. 87(a) and (b). In general, an increased critical drop height (height of falling, above which rebound begins) is observed with increasing fluid layer thickness. The particle is able to penetrate the fluid layer deeper and thus dissipation of the initial kinetic energy is increased. In the case of rebound, particles must deform elastically and thus be in close contact with the underlying solid surface. Fig. 87(a) shows the effect

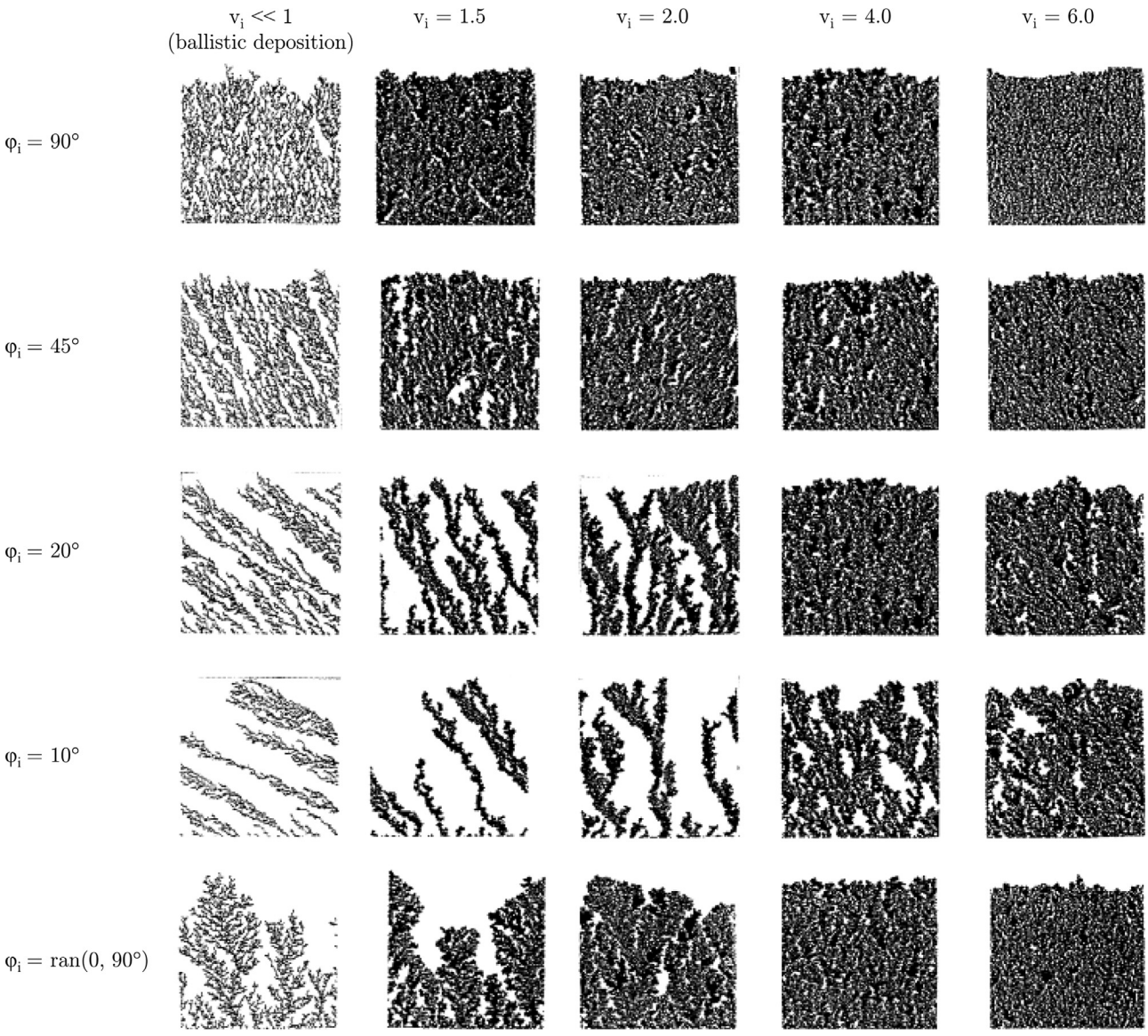

Fig. 86. Deposit morphologies predicted with DEM simulations using the FROZEN code at various normalized impact velocities v_i and angles of impact φ_i (taken from Konstandopoulos [434]).

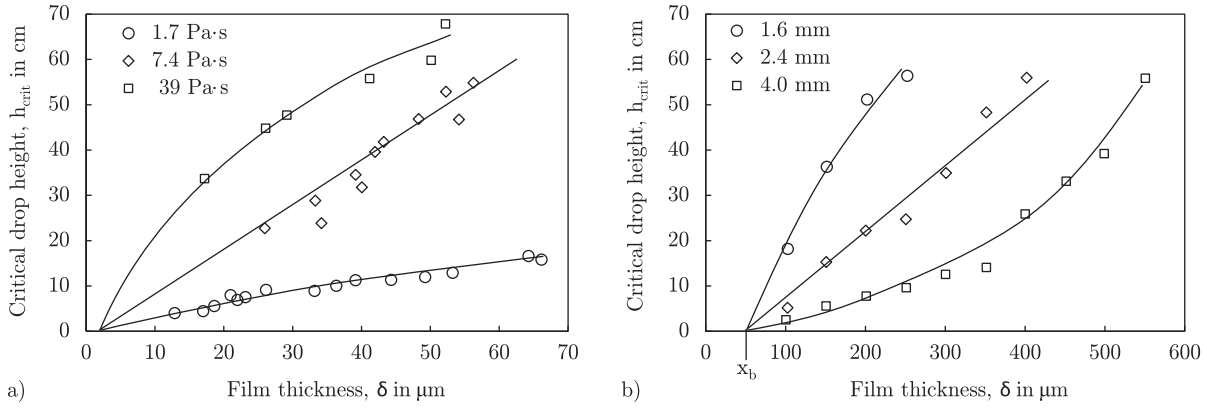

Fig. 87. Critical drop height versus film thickness : (a) for steel balls with d_p =3.2 mm colliding with a smooth quartz surface overlaid with fluids of various viscosities, and (b) for steel balls of various size colliding with a rough surface overlaid with a fluid of viscosity $\mu_{film} = 1.7$ Pa · s. Data taken from Barnocky and Davis [530].

of fluid viscosity on the rebound behavior of 3.2 mm steel balls. With increasing fluid viscosity, the drop height increases since a fluid with higher viscosity is able to dissipate more of the particle's kinetic energy. This energy misses for particle deformation and rebound. Fig. 87(b) illustrates the effect of surface roughness on the rebound behavior. Here, 75 μm glass beads (particles) were fixed to the landing surface using epoxy resin. The density was 17 beads/mm^2 [530]. The beads were half imbedded in the epoxy yielding a surface with 38 μm hemispherical bumps with a mean center to center distance of 150 μm. These bumps with a radius of $x_b = 38$ μm are overlaid with a film of viscous fluid. When comparing experimental results with a smooth surface, approximately one order of magnitude thicker fluid film is needed for the same critical height leading to particle rebound. Thus, the liquid film can be considerably thicker and the particle will still stick. A ball of the size 1.6 mm dropped from 0.6 m, rebounds at a film of approximately 60 μm for a smooth substrate compared to around 220 μm, for a rough surface. Barnocky and Davis [530] explain this drastic increase using a theory presented by Davis et al. [531], which is based on Hertz contact theory of solid elasticity together with viscous lubrication theory. Particles stick if:

$$p_{stick} = \begin{cases} 0 & \text{for } St > St_{crit} \\ 1 & \text{for } St \le St_{crit}, \end{cases} \tag{135}$$

where the Stokes number is calculated by $St = (2 \cdot m_p \cdot v_i) / \left(3 \cdot \pi \cdot \mu_{film} \cdot d_p^2\right)$ using the viscosity of the liquid film μ_{film} and the initial, relative particle velocity $v_{p,0}$ at an initial separation x_0 between the undeformed surfaces of both solid bodies (i.e. distance between surface and particle with a viscous fluid in between, e.g. oil in the study of Barnocky and Davis [530]). The initial velocity is estimated by $v_i = \sqrt{2 \cdot g \cdot h}$, again neglecting air resistance. The Stokes number calculation is based on the force that acts on the particle, and is caused by the surrounding fluid $F = 3/2 \cdot \pi \cdot \mu_{film} \cdot d_p^2 \cdot v_i / x$, assuming moderate fluid deformation, where x is the changing distance between the undeformed surfaces. Analysis by the authors showed that viscous forces dominate over any other force such as gravity or inter-particle van der Waals forces [530]. The critical Stokes number can be estimated using the following condition for a smooth surface underneath the liquid film:

$$St_{crit} = \ln(x_o / x_1) \qquad \text{for a smooth underlying surface,} \tag{136}$$

where x_0 is again the distance between the undeformed surfaces. This distance is not exactly equal to the film thickness δ since the nose of the particle must be wetted. The authors use the following expression for $x_0 = 2/3\delta$, where δ is the liquid film thickness. Here it is important that $x_0/d_p \ll 1$, which might be critical for ash particles known to be significantly smaller than the balls in the experiment of Barnocky and Davis [530]. The authors further argue, that for $St > 1$, the fluid velocity is only reduced by a few percent. Additionally, the authors use the capillary number defined as $Ca = \mu_{film} \cdot v_i / \gamma_{film}$, where γ_{film} is the air-liquid surface tension, in order to show that surface tension effects are negligible. For their experiments the Ca number is in the range of 10^3–10^5. On the contrary, in filter fibers with aerosol Ca numbers are in the region of 10^{-1}–10^2. Thus surface tension effects may sometimes be important, when Ca < 1 [530]. The parameter x_1 in Eq. (136) is the elasticity length scale. At this length scale, particles have enough inertia to penetrate to a distance, where deformation of the incoming particle can occur. It is defined as:

$$x_1 = \left[4 \cdot E^* \cdot \mu_{film} \cdot v_i \cdot (d_p/2)^{2/3}\right]^{2/5}, \tag{137}$$

where E^* is the elasticity parameter calculated with:

$$E^* = \frac{1 - \nu_1^2}{\pi \cdot E_1} + \frac{1 - \nu_2^2}{\pi \cdot E_2}. \tag{138}$$

The indices 1 and 2 in Eq. (138) stand for the particle and solid substrate, respectively. The elasticity length scale in the experiment of Barnocky and Davis [530] is in the range of $1 < x_0 < 10$ μm and thus small compared to surface roughness effects. In the case of a rough surface, the following relation is used to predict the critical Stokes number and thus the sticking and rebound threshold:

$$St_{crit} = (1 + 1/e)\ln(x_o/x_b) \qquad \text{for a rough underlying surface,} \tag{139}$$

where e is the restitution coefficient and x_b is the surface roughness. Both Eqs. (136) and (139) show relatively good agreement with experiments with $e = 1$. At higher Stokes numbers of $St > 4$ equations show some deviations, where particle deformation might become too large and the restitution coefficient is smaller than unity $e < 1$. It is shown that surface roughness has a strong effect on the rebound behavior when the roughness $x_b \gg x_1$.

The applicability of this theory for PF combustion, however, has still to be proven. The particle size is considerably smaller and thus less inertia (kinetic energy of particles) for penetrating the liquid film is available. Furthermore, the film layer viscosity is considerably higher with 10^1–10^3 Pa · s for molten slag compared to 1.7–39 Pa · s of oil in the study of Barnocky and Davis [530]. In addition, the film thickness can reach much higher values and rebound is unlikely. This confirms that if a particle impacts a liquid slag layer it will stick and rebound is very unlikely.

6. Comparison of different sticking criteria

Sticking criteria presented in Section 4 comprise of relatively simple models with just one parameter, up to complex models that require a number of temperature-dependent material properties for their mathematical description. These properties should ideally be known for all possible ash particle compositions. In addition, the majority of models does not account for a sticky surface or rebound behavior. Therefore, the goal of this section is a comparison and validation of different sticking criteria, the development of a mechanistic model considering all important parameters including the description of rebound behavior.

6.1. Experimental setup and results

In order to eliminate the influence of particle to particle variation in chemistry and size, soda-lime glass particles within a narrow size range are used. These particles have been applied in previous studies [1,201,222] and exhibit similar properties as ash particles. Glass particle deposition tests are conducted using an entrained flow reactor (EFR) for three size-graded particle classes (40–70, 150–210 and 500 μm) and three wall temperatures (800, 900 and 1000 °C). A detailed description of the test rig can be found elsewhere [185,188]. Tests are conducted for a short period, $t_{exp} \approx 10$ min, in order to eliminate sintering and erosion effects and reduce the influence of the deposit on capture efficiency. Experimental conditions and results are given in Table 23. Deposited mass is determined by weight difference. A previously described optical system is used to determine layer thickness and growth dynamics [188,312]. Deposition rates $\dot{m}_{dep}$, given in Table 23, show that at 800 °C only the smallest particle size leads to deposit formation. A minor amount is found for the intermediate particle size and no deposition occurs for large particles. The main reason for this is the lower temperature of large particles when impacting on the deposition probe. Residence times are too short and heating rates too low for larger particles to reach the wall temperature. At 900 °C, deposit formation is also observed for the intermediate particle size, 150–210 μm, whereas the largest

Table 23
Experimental conditions and results, as well as a comparison to CFD simulations with different sticking criteria C1 to C8.

Cases	T_{wall} in °C	$\dot{m}_{feed}$ g/h	$d_{p,50}$ in µm	$\overline{v}_p$ [a] in m/s	$\overline{T}_p$ [a] in °C	$\dot{m}_{dep}$ in g/h	C1	C2	C3	C4[c]	C5[c]	C6	C7	C8
							sticking criteria results for $\dot{m}_{dep}$ in g/h							
Exp. 1	800	179	63	1.4	679	2.93	–	–	2.71	4.87	1.38	0.05	0.64	0.75
Exp. 2	800	79	63	1.4	679	0.90	–	–	1.18	2.02	0.59	0.02	0.32	0.31
Exp. 3	800	327	171	1.9	631	0.08	–	–	0.03	2.44	0.22	–	0.12	–
Exp. 4	800	483	500	4.4	393	–	–	–	–	–	–	–	–	–
Exp. 5	900	500	63	1.4	763	19.80	6.50	1.49	17.2	18.4	16.9	0.08	1.52	2.20
Exp. 6	900	500	171	1.8	723	1.89	0.32	0.01	0.86	121	26.1	–	0.43	0.09
Exp. 7	900	500	500	4.5	456	–	0.02	–	–	5.96	0.44	–	–	–
Exp. 8	1000	450	63	1.5	852	15.52	10.0	2.45	9.59	10.0	10.0	0.07	0.71	2.18
Exp. 9	1000	518	171	2.0	807	10.57	31.6	1.68	6.32	123	123	–	0.19	0.02
Exp. 10	1000	500	500	4.5	523	–	–	–	–	2.68	1.93	–	–	–
Root mean square error (RMSE):							8.1	7.7	2.5	52	37	8.2	8.7	7.8
Correlation coefficient:							0.55	0.90	0.98	0.17	0.36	0.82	0.82	0.87

[a] Mean values for all particles at the position of the probe calculated with CFD.
[b] Initial problems led to non-constant feeding in particular for the finest fraction; given values are within ± 5%.
[c] C4 uses $\mu_{crit} = 10^{7.7}$ as proposed by Srinivasachar et al. [1], and C5 uses $\mu_{ref} = 10^{5.7}$ as estimated by Richter [222].

particles still rebound. Increasing the EFR wall temperature to 1000 °C revealed similar results with increased deposition rates. The deposit structure is mostly particulate and only experiment 8 showed a molten layer.

6.2. CFD model and comparison of results

Experimental results are used, and recalculated with a CFD model. The model predicts the flow field, temperatures as well as glass particle trajectories. The computational grid has a total number of 1.56 million nodes. Special attention is paid to an adequate resolution of the deposition probe, following suggestions established in the work of Weber et al. [206]. Two nodes are placed within the displacement thickness in radial direction in order to resolve the boundary layer and predict accurate particle tracks as well as impaction rates. A total number of 96 nodes around the circumference of the probe revealed independent deposition rates. The number is lower compared to the recommendation of Weber et al. [206], who suggested 384 nodes around the circumference. This could lead to an over prediction of the impaction efficiency at small Stokes numbers St < 1. However, since glass particles in the present work are relatively large, with smallest sizes in the range of 24.3 µm as given in Table 24, deposition rates are not over predicted and numerical accuracy is given. This grid revealed identical deposition rates compared to a mesh with four million nodes. More details on the computational mesh, the model selection and sensitivity studies can be found elsewhere [185,188]. In the CFD model, glass particles are injected as inert material, with a narrow-sized Rosin–Rammler distribution, fitted to measurements. Particle temperature is calculated using heat balance [534]. Particles close to the reactor wall almost reached the wall temperature, whereas particles in the center stayed below this value. Temperature-dependent properties of soda-lime glass are implemented in the CFD code, based on a literature review. Thermophysical properties of glass particles are calculated at each position using the local particle temperature, and thus consider a temperature change within the boundary layer of the probe. Hence, adhesion properties are calculated using local temperatures and not bulk values, which is a crucial aspect, in particular for small particles $d_p < 10 - 20$ µm, which cool down in the vicinity of a cold tube. Properties, PSD and glass composition are summarized in Appendix B. In addition, properties for the deposition probe, composed of Al_2O_3, are given. The only required quantity that is not found in the literature is a temperature-dependent contact angle of soda-lime glass on a ceramic substrate. In order to obtain values, the ash melting microscope EM 201 of the company "Hesse Instruments" is used [532]. A soda-lime glass sphere with a diameter of 1.5 mm is placed on a ceramic plate composed of the same material as the deposition probe. Three different heating rates are tested to ensure independent results. Fig. 88 shows shadow images recorded at different temperatures. The contact angle Θ_c is determined graphically from these images using the software ImageJ. The results are fitted with Eq. (54). The coefficients are determined as $A = 0, B = 180, C = 930$ and $D = 100$. The results are illustrated in the left part of Fig. 88. Deviations at lower temperatures are due to an insufficient resolution of the camera. The image at ambient temperature does not change up to 700 °C. Only values above that temperature can be determined properly, caused by a shade of the ceramic plate. The plate shadow makes it difficult to determine small changes in the contact angle at low temperatures. Nevertheless, values above $\Theta = 100^{\circ}$ can be calculated using Eq. (54). Once all required properties of soda-lime glass are known, sticking criteria can be investigated. A total of eight sticking criteria are implemented in the code and CFD results are compared with measurements. The sticking criteria are:

- C1: melt fraction, Eq. (69), proposed by Müller et al. [202].
- C2: melt fraction, Eq. (70), proposed by Zhou et al. [391].
- C3: critical viscosity as a function of particle kinetic energy, Eqs. (72) and Eqs. (73), [1,222].

Table 24
Soda-lime glass particle size distribution and characteristic temperatures (size fraction with uniform 500 µm particles could not be measured due to the large particle size).

Variable Unit	$d_{p,10}$ µm	$d_{p,50}$ µm	$d_{p,90}$ µm	IDT °C	ST °C	HT °C	FT °C
Glass 0-50	24.3	43.4	68.3	777	791	944	1175
Glass 40-70	48.3	62.7	79.1	790	790	961	1188
Glass 150-210	134.3	171.3	216.8	804	828	935	1161

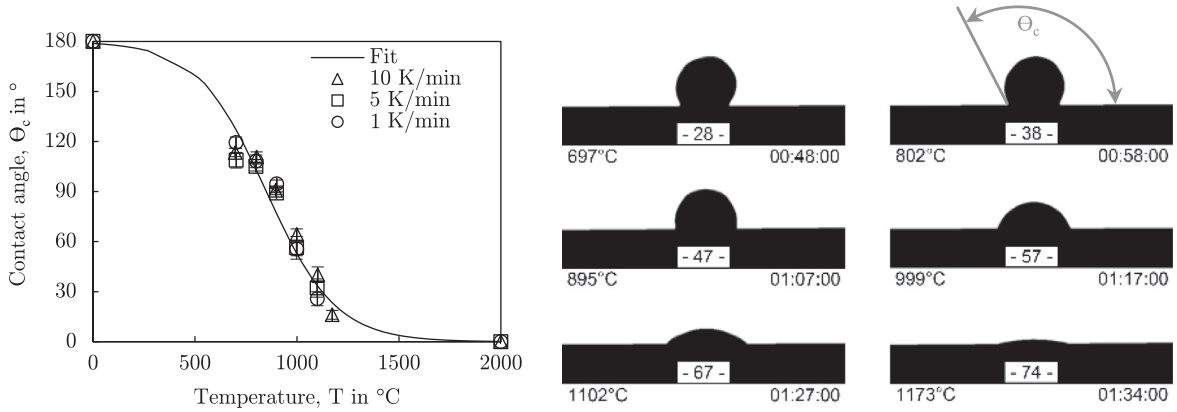

Fig. 88. Contact angle measurements of a 1.5 mm soda-lime glass particle on an Al_2O_3 ceramic substrate using an ash melting microscope and varying heating rates [532].

- C4: critical viscosity, Eq. (72), proposed by Srinivasachar et al. [1].
- C5: reference viscosity, Eq. (71), proposed by Walsh et al. [395].
- C6: critical velocity, Eqs. (75)–(80), proposed by Thornton and Ning [290].
- C7: critical velocity, Eqs. (75), (83) and (84), proposed by Brach and Dunn [428].
- C8: energy conservation and excess energy using Eqs. (91)–(95) proposed by Mao et al. [333,390,441].

Fig. 89(a) shows a graphical comparison of C2 (Zhou et al. [391]) and C5 (Walsh et al. [395]). The model of Zhou et al. [391] uses the melt fraction in order to calculate the sticking behavior. In the present case, thermodynamic equilibrium calculations using the software FactSage are applied to obtain the melt fraction as a function of temperature. However, it is questionable if it is meaningful to calculate the melt fraction for amorphous material, where there is no crystal formation. Nevertheless, this criterion is tested for completeness. Further details on FactSage can be found in the publication of Wieland et al. [312]. The model of Walsh [395] uses a reference viscosity of $\mu_{ref} = 100$ Pa · s, based on their experiments. The curve slope and the horizontal position can be adjusted by changing the reference viscosity. In addition Fig. 89(a) shows measured ash fusion temperatures for soda-lime glass are illustrated as vertical lines A, B, C and D. Softening (A) starts at around 790 °C and fluid temperature (D) is reached at 1170 °C. This range is used for glass particle sticking tests and simulations. Particle trajectories are calculated in ANSYS Fluent, exported and evaluated with sticking criteria C1 to C8 using a Matlab code. If a particle sticks to the reactor wall or the deposition probe, the calculation ends. If the particle rebounds, it will continue its track. Deposition rates are calculated for all ten experiments (Exp. 1 to Exp. 10) and compared with measurements. The root mean square error (RMSE) and the correlation coefficient are used as a quality indicator. It is calculated using all experiments and numerical simulation results. Simulation results and the coefficients are given in Table 23. The best correlation coefficient and RMSE are obtained for the model of Srinivasachar et al. [1] (C3) using Eq. (73), where critical viscosity is dependent on particle kinetic energy and thus its size, density and velocity. A parity plot comparing experiments and simulations is shown in Fig. 89(b). It can be seen that all three sticking criteria underpredict deposition rates, with the best agreement for Srinivasachar et al. [1] (C3). The higher deposition rates in the experiments are probably due to the stickiness of the deposit during build-up. The highest deposition rates are calculated for C4 and C5 as shown in Table 23. Both use a viscosity value at which sticking begins. They might yield better results by changing the critical or reference viscosity. However, Scholz [459] tested the sensitivity towards this threshold and results only improved slightly. Criteria based on energy or momentum conservation (C6, C7 or C8) yield acceptable results, when comparing the RMSE and correlation coefficient in Table 23. Here, the main difficulty is to find appropriate material properties, such as the Young's modulus as a function of

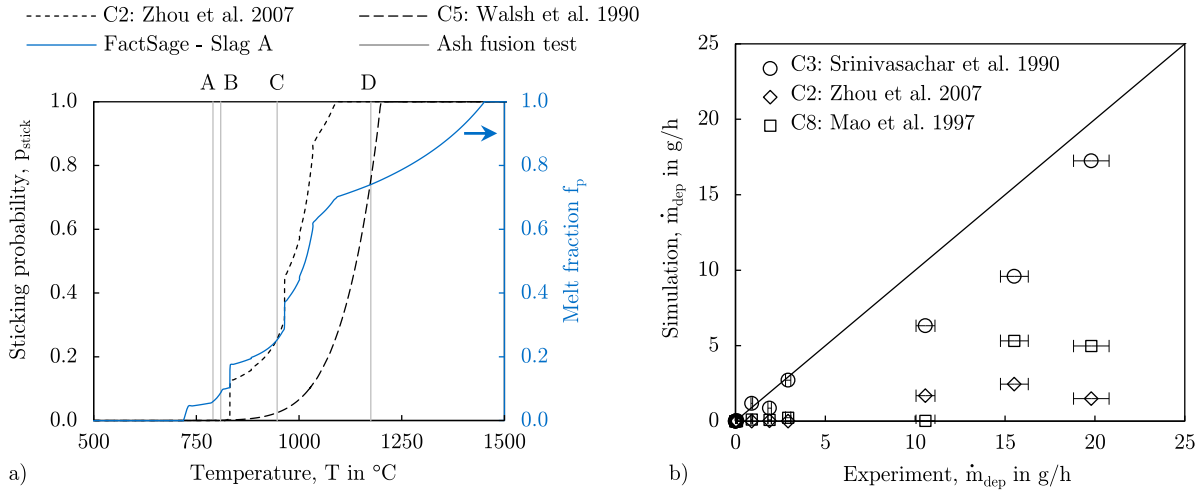

Fig. 89. Glass particle sticking probabilities: (a) comparison of sticking criteria and melt fraction as a function of temperature, and (b) comparison of experimental values with numerical results for three sticking criteria. Probe diameter and length inside the reactor are 15 mm and 120 mm, respectively.

temperature and for different ash particle chemistry. Relatively good results are achieved with criteria based on the melt fraction. A solution could be the coupling of thermodynamic equilibrium calculations with CFD. By far the best agreement is achieved by using criterion C3, which is simple, reliable and only requires one chemistry-dependent parameter: particle viscosity.

6.3. Mechanistic modeling approach

In the following part, the mechanistic model of Mao et al. [390] (criterion C8) is examined in detail in order to explain the dependence of the critical viscosity on the particle kinetic energy (shown by criterion C3). Part of this explanation was published previously [532] and is extended here. Mechanistic expressions for ash particle rebound or sticking behavior are rare in literature. The majority of studies with mechanistic models can be found in the field of liquid droplet impaction on a solid substrate. The deformation during impact is predicted and typically validated using photographs and images from experiments. However, there is very little work on ash particles and their rebound behavior. In this section, literature equations are investigated in terms of their suitability for a mechanistic ash particle sticking and rebound criterion. Mechanistic models are typically based on energy conservation, as already mentioned in Section 4.3. The impaction and deformation process is subdivided into five consecutive stages as shown in Fig. 90. The energy of a particle during impact at stage "0" is the sum of the kinetic E_0^{KE}, and the surface energy E_0^{SE}:

$$E_0 = E_0^{SE} + E_0^{KE} = \pi d_p^2 \gamma_p + \frac{1}{12}\pi d_p^3 \rho_p v_p^2, \tag{140}$$

where ρ_p is the particle density and γ_p the droplet surface tension. Often, potential energy is neglected due its small magnitude compared to kinetic and surface energy. At stage "2", when the particle deformation reaches its maximum, as shown in Fig. 90, the kinetic energy approaches zero $E_2^{KE} \approx 0$, yielding:

$$\begin{aligned} E_2 &= E_2^{SE} = E_{2,LV}^{SE} + E_{2,SL}^{SE} - E_{2,SV}^{SE} \\ &= \left(\frac{\pi}{4} d_{max}^2 + \frac{2}{3}\pi \frac{d_p^3}{d_{max}}\right)\gamma_{LV} - \frac{\pi}{4} d_{max}^2 (\gamma_{SV} - \gamma_{SL}), \end{aligned} \tag{141}$$

where surface energy at stage two E_2^{SE} can be expressed as the sum of liquid-vapor (LV) surface energy $E_{2,LV}^{SE}$, the energy of the new solid-liquid (SL) surface $E_{2,SL}^{SE}$ minus the solid–vapor (SV) surface energy $E_{2,SV}^{SE}$, lost in the process [390]. The indices "SL", "SV" and "LV" stand for the solid-liquid, solid-vapor and liquid-vapor surface tension. Young's equation is used to express the unknown $\gamma_{SV} - \gamma_{SL}$ by:

$$\gamma_{SV} - \gamma_{SL} = \gamma_{LV} \cdot cos\ \Theta_c, \tag{142}$$

where the liquid-vapor surface tension is approximated with the particle surface tension $\gamma_{LV} \approx \gamma_p$. Rewriting Eq. (141) and (142) yields then:

$$E_2 = E_2^{SE} = \left[\frac{\pi}{4} d_{max}^2 (1 - cos\ \Theta_c) + \frac{2}{3}\pi \frac{d_p^3}{d_{p,max}}\right]\gamma_p. \tag{143}$$

Eqs. (143) and (140) assume that the particle is shaped as a thin circular disk [390,441]. Major studies in this field [390,435,441] calculate the maximum spread factor, defined by $\xi = d_{p,max}/d_p$, in order to predict the impaction behavior of a liquid droplet: e.g. sticking, rebound or splashing. Energy conservation between stage "0" and "2" yields [390]:

$$E_0^{SE} + E_0^{KE} = E_2^{SE} + E_{0\to 2}^{DE}. \tag{144}$$

$E_{0\to 2}^{DE}$ stands for the energy losses due to viscous dissipation. This term is usually estimated from empirical correlations or theoretical considerations such as [390,441]:

$$E_{0\to 2}^{DE} = \int_0^{t_c}\int_V \phi dV dt \approx \phi V t_c, \tag{145}$$

where V stands for the volume of the viscous layer, t_c for the time from initial surface contact to the maximum spread, and ϕ for the viscous dissipation function given by:

$$\phi = \mu\left(\frac{\partial u}{\partial y} + \frac{\partial v}{\partial x}\right)\frac{\partial u}{\partial y} \approx \mu_p \left(\frac{du}{dy}\right)^2. \tag{146}$$

The definition of the spatial directions x, y and the velocity components u, v in Eq. (146) is shown in Fig. 63. The parameter μ_p is the particle dynamic viscosity, and du/dy is the normal velocity gradient in the boundary layer. Eq. (146) has been widely used, however, the determination of ϕ, V and t_c varies. Mao et al. [390] for instance distinguished between low and high viscosity droplets. High viscosity droplets are defined for cases in which the theoretical boundary layer thickness δ is larger than the droplet height. The following expression is presented for estimating the deformation energy between stage "0" and "2":

$$E_{0\to 2}^{DE} = 0.53 \frac{We_p}{Re_p} \xi^4 \pi d_p^2 \gamma_p \qquad for\ \delta > h_{p,min}, \tag{147}$$

where $Re_p = \rho_p \cdot v_p \cdot d_p/\mu_p$ is again the Reynolds and $We_p = \rho_p \cdot v_p^2 \cdot d_p/\gamma_p$ the Weber number. An analytical expression for ξ can be obtained by substituting Eqs. (147), (140) and (143) into Eq. (144):

$$\left(\frac{1}{4}\cdot(1 - cos\ \Theta_c) + 0.2 \cdot \frac{We_p^{0.83}}{Re_p^{0.33}}\right)\cdot\xi^3 - \left(\frac{We_p}{12} + 1\right)\cdot\xi + \frac{2}{3} = 0, \tag{148}$$

where the resulting cubic equation of type $x^3 + px + q = 0$ can be solved easily. As mentioned in numerous studies, the maximum spread factor ξ highly depends on the droplet viscosity and the ability to deform [532]. Eqs. presented above are developed for low

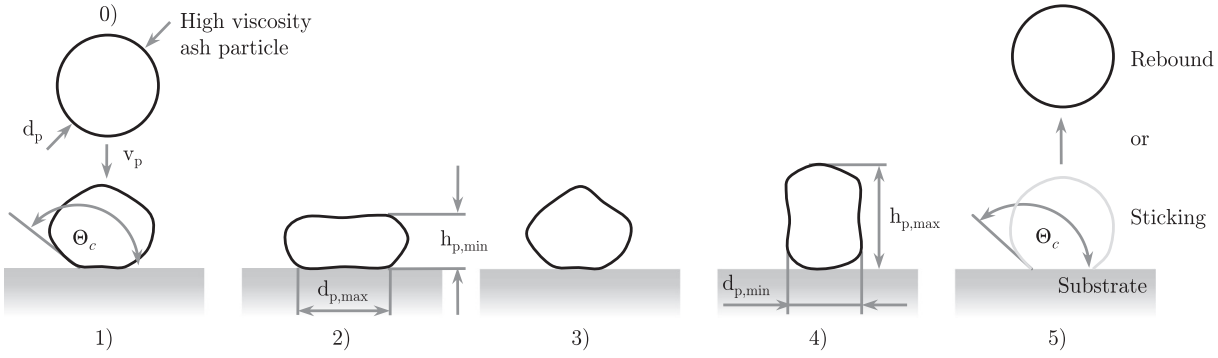

Fig. 90. Impaction stages for a high viscosity particle. Rebound probability strongly increases due to decreased deformation and energy dissipation [532].

viscosity droplets such as water or alcohol droplets. Ash particles on the contrary, can have a significantly higher viscosity values in the range of $0.001-10^9$ Pa · s. Fig. 90 illustrates the expected impaction stages for a high viscosity fluid, e.g. a molten ash particle [532]. Estimations based on Eq. (148) yield spread factors for ash particles in the range of $0 < \xi \leq 2.2$. A sticking or rebound criterion can only be derived if energy losses occurring during stage "3" and "4" are considered. A particle will stick if all energy from stage "0" is dissipated. If energy is left, the particle will rebound. Therefore, the energy dissipated during droplet deformation between stage "2" and "4" $E_{2\rightarrow 4}^{DE}$, and the surface energy at stage "4" E_4^{SE} have to be expressed. The droplet shape at different stages illustrated in Fig. 90 is more or less unknown for ash particles and should be studied in the near future in order to determine the exact deformation. In general, a droplet will rebound from its substrate if the following equation is satisfied:

$$E_4 = E_2 - E_{2\rightarrow 4}^{DE} - E_4^{SE} > 0. \tag{149}$$

The particle shape is needed in order to estimate the surface energy E_4^{SE} at stage "4". Mao et al. [390] assumed a spherical droplet, however, theoretical CFD simulations of Mahulkar et al. [450] predict an elliptical shape. In previous work [532], the particle shape was assumed to be a cylinder with $d_{p,\,min} \approx 0.4 \cdot d_p$ and two hemispheres at each end. This leads to:

$$E_4^{SE} = 43/25\pi d_p^2 \gamma_p. \tag{150}$$

The energy dissipated due to viscous deformation is calculated using the empirical correlation suggested by Mao et al. [390]:

$$E_{2\rightarrow 4}^{DE} = 0.12\xi^{2.3}\left(1 - cos\ \Theta_c\right)^{0.63}\pi d_p^2 \gamma_p. \tag{151}$$

Eqs. (150) and (151) can be substituted into Eq. (149) and divided by Eq. (150) yielding:

$$E_{ERE} = \frac{25}{172}\xi^2\left(1 - cos\ \Theta_c\right) + \frac{50}{129}\xi^{-1} - \frac{3}{43}\xi^{2.3}\left(1 - cos\ \Theta_c\right)^{0.63} - 1 > 0. \tag{152}$$

Eq. (152) calculates the excess rebound energy E_{ERE}, a parameter indicating whether there is energy left for rebound ($E_{ERE} > 0$) or all energy is dissipated during deformation ($E_{ERE} \leq 0$). Eq. (148) and (152) can be employed in order to predict glass particle deposition behavior as illustrated in Fig. 91. However, this requires temperature-dependent glass particle properties, which are again taken from the Appendix B. In total, ten equations are used to identify the critical temperature and thus, the critical viscosity, at which glass particles rebound and Eq. (152) fulfills the condition $E_{ERE} = 0$. These ten equations comprise of temperature-dependent properties that are viscosity, density, surface tension and contact angle, the Reynolds and Weber number, Eqs. (152) and (148), including equations for p and q of the cubic expression given by Eq. (148) [532]. The goal is to find the critical viscosity as a function of particle kinetic energy. Therefore, the particle kinetic energy is varied using a different particle velocities, whereas the particle diameter is kept constant at $d_p = 50$ μm. The same particle size was used in experiments shown in Fig. 91.

A comparison of the above-mentioned model, and equations originally proposed by Mao et al. [390] with glass particle measurements is presented in Fig. 91(a). It can be seen that the present model fits considerably better than the original equations of Mao et al. [390]. The difference between both approaches is the particle shape at stage 4 - given by Eq. (150). Equations of Mao et al. [390] under predict the critical viscosity by four to five orders of magnitude. Hence, resulting deposition rates are also expected to be under predicted. This is confirmed by simulations in Table 23 for criterion C8. Müller et al. [202] applied equations of Mao et al. [390], and found that the model does not work for particles smaller than $d_p < 75$ μm. Instead, they used the melt fraction criterion for small particles, where particles containing ≥ 15% molten phase are assumed to be sticky. Large particles with $d_p \geq 75$ μm rebounded, which was successfully predicted using the model of Mao et al. [390]. Some uncertainty concerning the grid resolution exists in this study. Weber et al. [206] found in a later study, that a relatively fine grid is needed for predicting accurate particle impaction rates. Nevertheless, it is concluded that this model might be suitable for larger particles and fails in the case of small ash particles [532].

An explanation, why the model of Mao et al. [390] works for larger particles, can be seen in Fig. 91(a). The critical viscosity increases at a particle kinetic energy of $E_{p,kin} = 10^{-9}$ J, which implies that high inertia particles are sticky even at lower temperatures. It can be explained by an increased particle deformation, and thus, less remaining energy for rebound. This behavior is more pronounced for particles impacting at high velocities or for large particles. However, experimental evidence is still due, and should be studied in future work. The presented equations can explain why particles with low

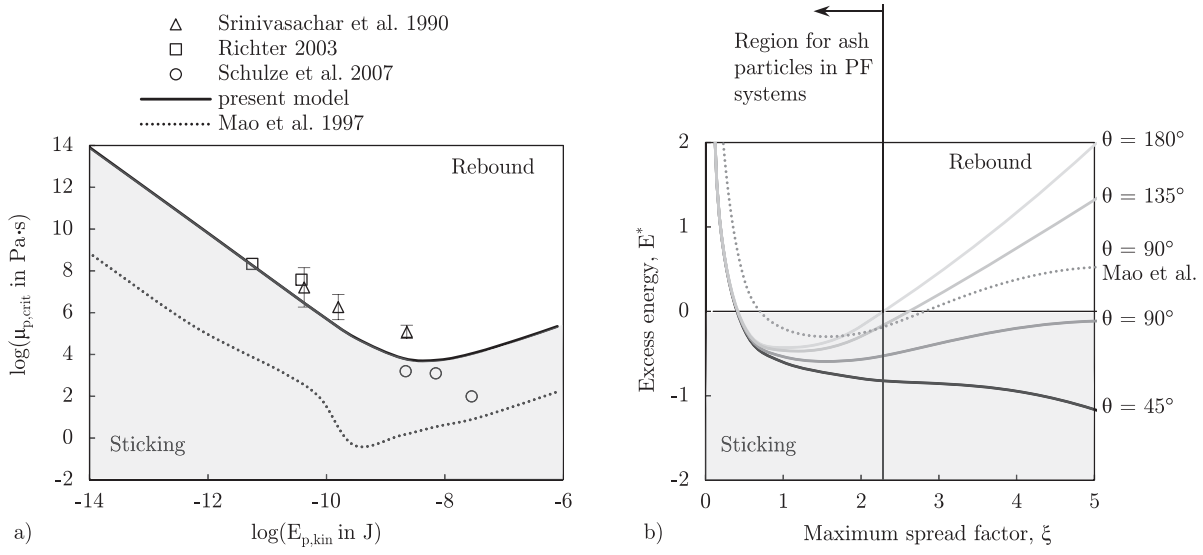

Fig. 91. Ash particle sticking and rebound behavior: (a) mechanistic model results compared with literature measurements [532], and (b) parameter variation of the contact angle.

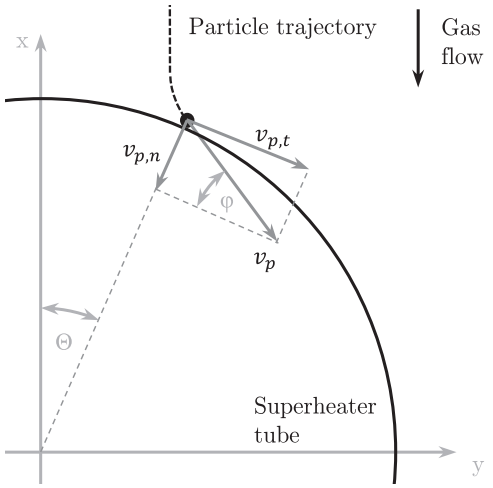

Fig. 92. Angle of impaction on a cylindrical obstacle. Normal and tangential impaction velocities are illustrated.

kinetic energy exhibit a higher sticking probability, as found in the glass particles tests of Srinivasachar et al. [1]. The developed model is therefore recommended for CFD implementation and detailed investigations. A parameter variation on the spread factor ξ and contact angle Θ_c is shown in Fig. 91(b). At low values of ξ, particles do not deform and rebound. At around $\xi \approx 0.5$ particles enter the sticking regime. The contact angle is only of relevance at higher deformations. Within the region of power plants $0 < \xi \leq 2.2$, the contact angle plays a minor role. Furthermore, a considerably lower sticking probability is again observed when using the equations of Mao et al. [390].

A crucial parameter is the angle of impaction φ since it influences the amount of kinetic energy, which can be dissipated during deformation and wetting. A graphical illustration is shown in Fig. 92. Particle velocity is split into a normal (index n) and tangential (t) component according to $tan\ \varphi = v_{p,n}/v_{p,t}$. The normal velocity is assumed to determine the impaction kinetic energy $E_{p,kin,n} = \pi/12 \cdot \rho_p \cdot d_p^3 \cdot v_{p,n}^2$ with $v_{p,n} = sin\ \varphi \cdot v_p$, which can be dissipated during impact. Solving Eq. (152) for a varying angle of impaction and determining the change in critical viscosity due to non-normal impact leads to Fig. 93(b). It can be seen that viscosity is strongly reduced, when the angle deviates slightly from $\varphi = 90^\circ$. Fig. 93(a) shows a calculated sticking regime map for different angles of impaction. This map can be explained using an example: A small glass particle, with a kinetic energy of 10^{-12} J, will stick upon normal impact ($\varphi = 90^\circ$) if its viscosity is below 10^{10} Pa · s. The same particle but with an impaction angle of $\varphi = 75^\circ$ will stick at a considerably lower viscosity of 10^5 Pa · s, as shown by the dashed line in Figs. 93(a) and (b). The corresponding threshold temperatures are 606 °C for normal and 816 °C for non-normal (75°) impact. Thus, a decrease in impaction angle reduces the sticking probability at a given temperature. The curve shown in Fig. 93(b) can be fitted using a tangent law, as given by the second term in Eq. (154).

The equations described above require temperature-dependent properties and involve complex expressions. Therefore, a simpler model is desired. Furthermore, they are obtained for a clean and solid substrate. However, clean heat exchanger surfaces can only be found during the commissioning of a power station. Therefore, there is a need to consider an existing deposit layer and its stickiness. Typically, deposits are classified into three categories: particulate, sintered or molten [266]. The impaction of solidified fly ash particles on a particulate deposit is highly complex, as shown and discussed in Section 5.3. These solid and maybe sharp particles can lead to erosion, shedding, or they can be captured in the porous structure. In case of a molten deposit layer, e.g. on a wall of a slagging gasifier, the problem simplifies [532]. If either the particle or the surface is sticky, the particle will adhere:

$$p_{stick} = \begin{cases} 0 & \text{for } \mu_p > \mu_{p,crit} \ \ \&\& \ \ \mu_{dep} > \mu_{p,crit} \\ 1 & \text{for } \mu_p \leq \mu_{p,crit} \ \ \| \ \ \mu_{dep} \leq \mu_{p,crit} \end{cases} \quad (153)$$

It is unclear if this equation is valid in case of particulate or sintered deposit. When sticking criteria are used, it is recommended to estimate the wall temperature and in case of a deposit layer its viscosity and the porosity. For CFD modeling, this can be done on a cell by cell basis as well as for wall faces. For highly porous layers, e.g. $p > 0.7$, an impacting particle can lead to shedding or more likely it is captured inside the structure, similar to a fabric filter. In all other cases, Eq. (153) can be used. Critical viscosity is then calculated using particle kinetic energy and an empirical equation fitted to measurements as shown in Fig. 91(a). It is recommended to only use the absolute particle velocity as suggested by Weber et al. [206]. The angle of impaction is introduced in a second term, using a tangent law, according to the following expression:

$$\mu_{p,crit} = A \cdot E_{p,kin}^B \cdot 10^{C/tan(\varphi)^D} = 5 \cdot 10^{-12} \cdot E_{p,kin}^{-1.78} \cdot 10^{-6.36/tan(\varphi)^{0.25}}. \quad (154)$$

The particle kinetic energy in Eq. (154) is caluclated with $E_{p,kin} = \pi/12 \cdot \rho_p \cdot d_p^3 \cdot v_p^2$. By using Eqs. (153) and (154) a sticking regime map, as shown in Fig. 94, can be calculated. The following steps are necessary: First, the deposit and particle viscosity have to be calculated temperature- and composition-dependent. Second,

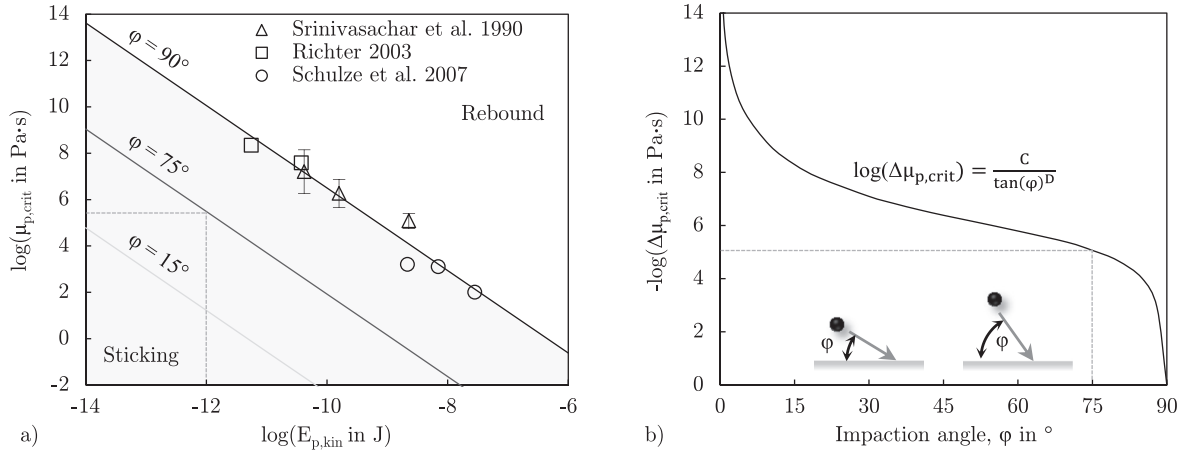

Fig. 93. Angle of impaction: (a) regime map for three impaction angles, and (b) influence on critical viscosity. The change in viscosity is calculated by the assumption that only the normal part of the particle kinetic energy leads to particle deformation. Thus, at small impaction angles, less kinetic energy is dissipated and rebound is more likely.

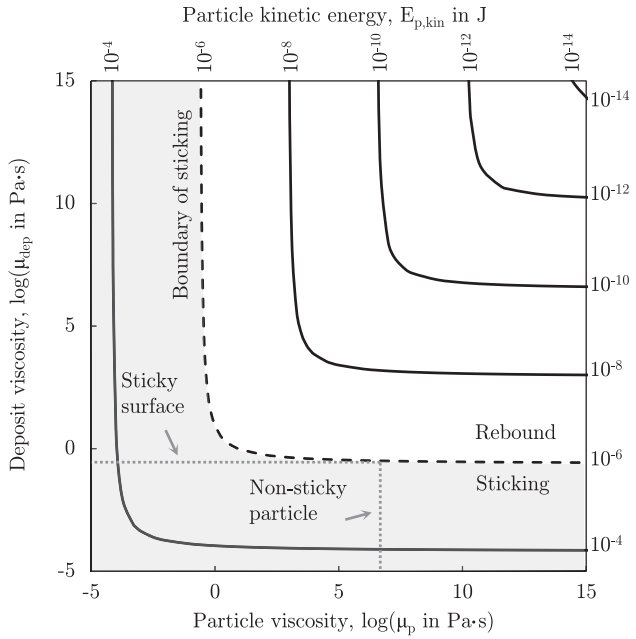

Fig. 94. Regime map for particle sticking or rebound behavior considering the deposit and particle viscosity in combination with the particle kinetic energy [532].

particle kinetic energy is calculated. And third, if the viscosity of either the deposit or the particle is below the line of constant kinetic energy it will stick and remain on the surface. In Fig. 94 the sticking area is plotted for a particle kinetic energy of $E_{p,kin} = 10^{-6}$ J. The isolines are derived using Eq. (154), $\varphi = 90^{\circ}$ and $\mu_{dep} = 1/\left(\mu_p - \mu_{p,crit}\right) + \mu_{dep,crit}$. This hyperbolic expression is an asymptotic approach towards the critical viscosity values as already presented elsewhere [532].

The rebound angle and velocity can be calculated using the remaining energy after the impaction. It is defined by

$$\Delta E = E_0 - E_4 \tag{155}$$

and the impaction angle φ. For an elastic collision on a smooth, clean surface with no particle deformation, friction or rolling, the rebound angle equals the impact angle. However, in real combustions systems, particles impact on a rough surface and deformation occurs.

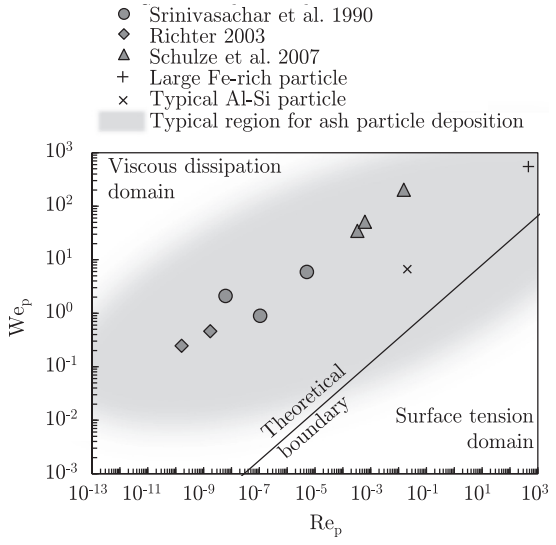

Fig. 95. Particle deposition regime map showing that energy losses due to viscous deformation are dominating ash deposition (see Table 19 for properties of the large Fe-rich and Al-Si particle).

Here, further work is needed to address this issue. A good assumption is to calculate the normal coefficient of restitution with

$$e_n^2 = \Delta E / E_{0,n}. \tag{156}$$

This equals the ratio of normal velocity components before $v_{p,n,0}$ and after $v_{p,n,5}$ impaction $e_n^2 = v_{p,n,5}^2 / v_{p,n,0}^2$.

6.4. Model sensitivity

A parameter study is conducted in order to evaluate model sensitivity towards process conditions and particle properties. Studied process conditions include particle diameter, velocity and temperature; thermo-physical properties are particle viscosity, surface tension, density and contact angle with the substrate. The latter are studied individually, even though they all change with a temperature increase. Fig. 96(a) and (b) show the effect of particle diameter and particle impact velocity on the excess rebound energy. Parameters used for the sensitivity study are summarized in Table 25. The base case uses soda-lime glass particles at 800 °C. As long as the particle velocity is below $v_p = 1$ m/s, particle remain in the sticking regime. For instance, a 100 μm particle will rebound in between $v_p = 1...30$ m/s. At higher values, plastic deformation cannot dissipate all kinetic energy, and particles will rebound. A much lower sensitivity is observed for the impaction angle φ. But still, decreasing the impact angle from $\varphi = 90^{\circ}$ to $\varphi = 30^{\circ}$ changes the deposition characteristics significantly. At $\varphi = 90^{\circ}$ all particles smaller than $d_p = 2$ μm stick, where this boundary moves to $d_p = 0.3$ μm at $\varphi = 30^{\circ}$. There is a non-linear behavior at small impaction angles. The highest sensitivity for particle properties is found for the particle viscosity. If the particle viscosity is below $\mu_p = 10^4$ Pa · s, all particles will stick, no matter which size. But a change to $\mu_p = 10^5$ Pa · s leads to rebound for all particles larger than $d_p = 2$ μm. This behavior underlines the existence for a critical value. Since viscosity is coupled exponentially to the particle temperature, an even higher sensitivity is found for particle temperature. The sensitivity towards particle properties, as shown in Fig. 97(a) and (b), follows the order from high to low: viscosity > surface tension > density > contact angle.

The sticking criterion given by Eqs. (153) and (154) can be implemented in CFD codes using subroutines with several sub-models for particle viscosity and density, which are all calculated composition- and temperature-dependent. A possible improvement can be achieved by incorporating van der Waals forces for small particles. However, additional parameters, in particular the distance between two surfaces in contact, are needed and unfortunately unknown. Often, it is discussed, whether surface tension effects and contact angle are important. Bennett and Poulikakos [533] compared different correlations predicting the spreading of droplets during impaction. They derived regimes in which viscous dissipation, or surface tension and wetting effects dominate. Their analysis showed that if

Table 25
Particle properties and process conditions used for sensitivity study. ••• high, •• medium, and • low sensitivity towards individual parameters.

Parameter	d_p	v_p	φ	T_p	μ_p[a]	γ_p[a]	ρ_p[a]	Θ[b,c]
Unit	μm	m/s	°	°C	Pa · s	N/m	g/cm³	°
Value	50	5	90[b]	800	$10^{5.2}$	0.42	2.47	141
Sensitivity parameter[d]	-	0.38	0.22	1.36	0.43	0.16	0.10	0.01
Sensitivity	•••	••	••	•••	•••	••	•	•

[a] at a temperature of T = 800 °C. Values taken from Fig. 98.
[b] at a temperature of T = 800 °C. Values taken from Fig. 88.
[c] normal impact.
[d] standard deviation of all values calculated for a particle size of $d_p = 10$ μm at T = 800 °C.

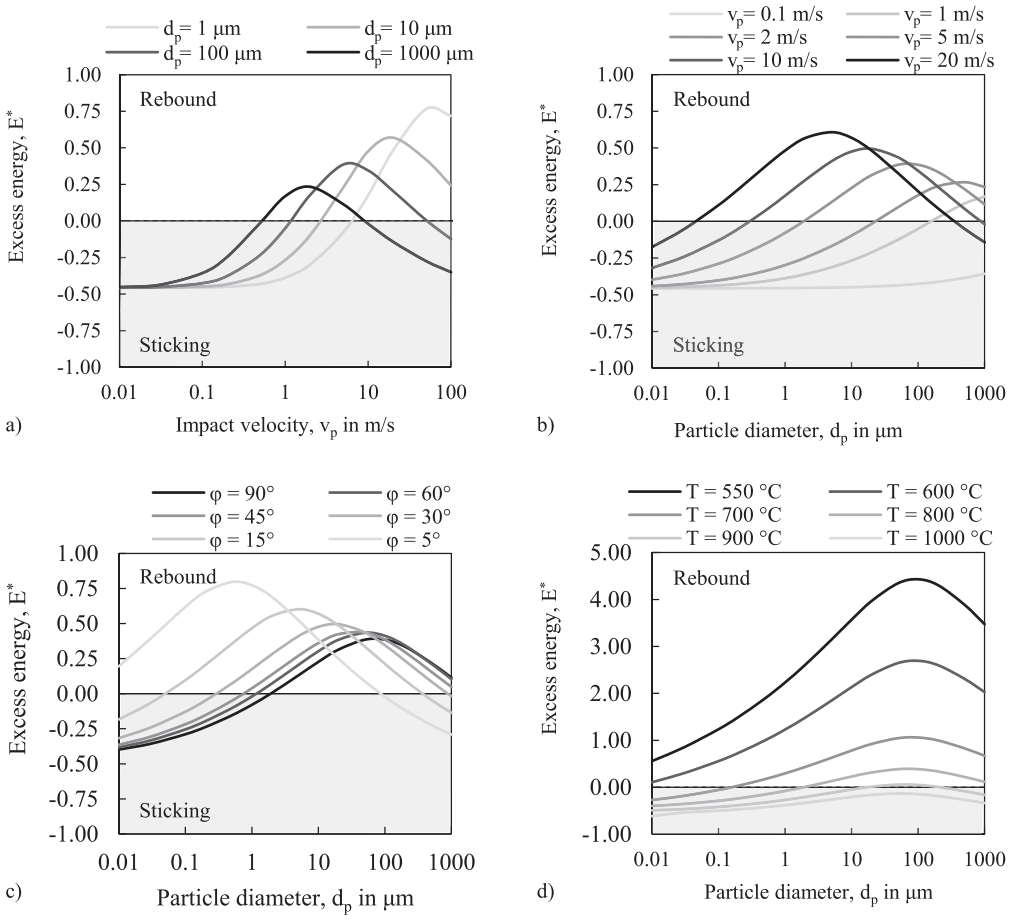

Fig. 96. Particle sticking behavior for soda-lime glass spheres as a function of process parameters: (a) and (b) effect of particle impact velocity and particle size, (c) role of impact angle and (d) role of the particle temperature accompanied by changing thermo-physical properties at a particle velocity of 5 m/s and a temperature of 800 °C (except figure d), where temperature is studied).

the following condition

$$We_p < 2.80 \cdot Re_p^{0.457} \tag{157}$$

is full-filled, surface tension and wetting become important. Above this criterion, spreading is dominated by the droplet viscosity and their ability to deform, as shown in Fig. 95. In this region, wetting and contact angle only marginally affect the deposition process. Fig. 95 shows a regime map including glass particle studies, a large Fe-rich particle at 1200 °C, and a typical Al–Si particle at 1100 °C. It can be seen that all particles are in the viscous dissipation domain, underlining the importance of viscosity. Deposition might be affected by surface tension and contact angle effects, however, controlling is the particle viscosity and the ability to deform due to low viscosity values. A further interesting topic is solidification of ash particles during the contact with the surface. Theoretical considerations and experiments of Aziz and Chandra [451] show that solidification does not change impaction as long as $Ste/\sqrt{Pe} \cdot \sqrt{\gamma_W/\gamma_p} < 1$. For the investigated glass particle experiments the term yields low values of 0.04. Nevertheless, it is assumed that solidification and thermal stresses induced by different thermal expansion of the steel tube and ash particles lead to rebound of a molten ash particle upon the contact. Shrinking during solidification might lead to detachment. Further research should also be directed towards this issue. The formation of a solid skin around a molten particle might also be of importance. The surface starts to cool inside the boundary layer through convection leading to a solid shell. Their role and effect on impact dynamics is, however, unknown.

7. Recommendations for modeling ash formation and deposition

Modeling ash formation, deposition and predicting the deposit chemistry, require simple and reliable models in particular when coupled with CFD in order to predict slagging and fouling propensities. There are excellent individual/standalone models available for predicting ash formation, rebound behavior or fuel conversion, however, if all models are combined and one model is inaccurate, others might suffer and the overall accuracy is not satisfying. The particle transport and the sticking criterion play a crucial role since they lead to selective deposition, where the sticking propensity mainly depends on the particle chemistry, size, velocity and temperature. Future studies predicting slagging and fouling should avoid using bulk ash chemistry. Instead detailed information on individual particle chemistry, e.g. provided by CCSEM, should be used instead. Otherwise, the prediction of the deposit chemistry, which is known to differ from the bulk ash, is not possible. Often, it is shown that ash deposits are enriched in iron [186] and/or alkali metals [535], depending on the fuel and location inside the boiler. Studies on co-combustion of wood and coal have shown that the deposit chemistry on the cylinder front face is similar to the fly ash fraction at around 2.5 µm, and the leeside deposit is similar to the sub-micron fraction at around 150 nm [66]. Hence,

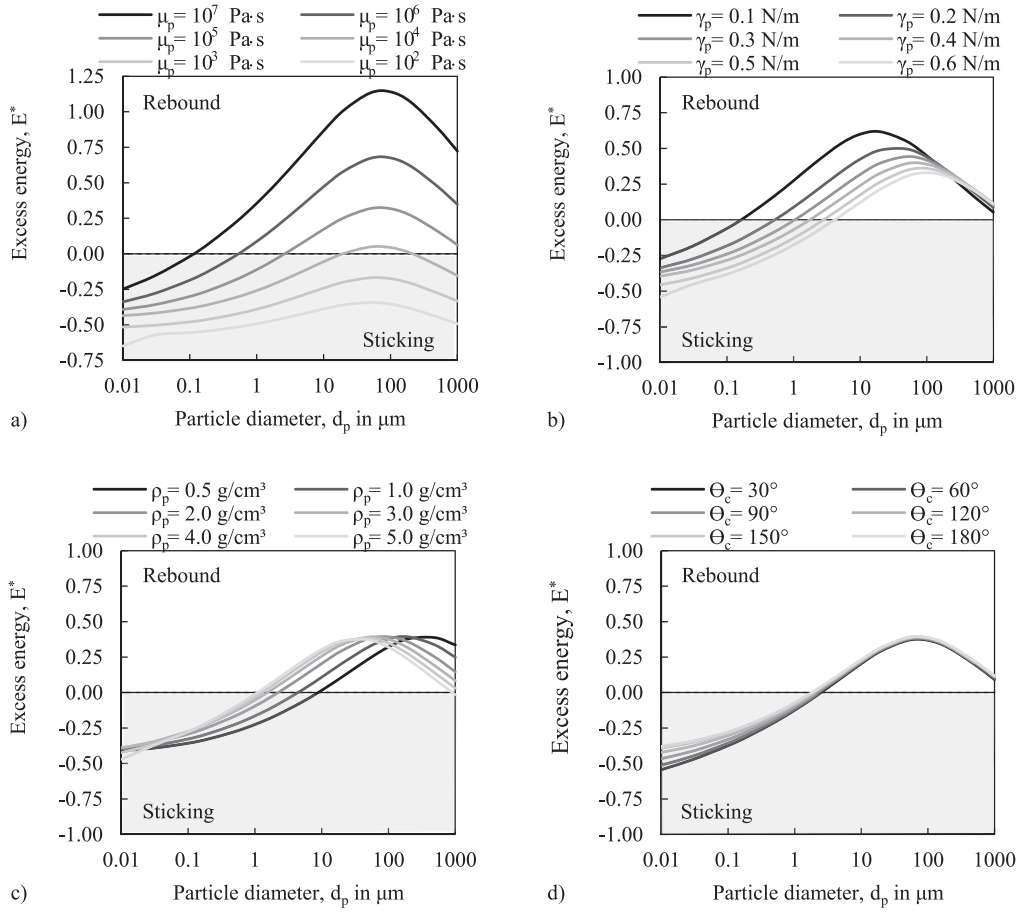

Fig. 97. Particle sticking behavior for soda-lime glass spheres as a function of particle thermo-physical properties during the impaction: (a) particle viscosity, (b) particle surface tension, (c) particle density and (d) contact angle with the substrate at a particle velocity of 5 m/s. If one parameter is varied, others are fixed to values at 800 °C.

models using bulk ash cannot predict ash deposit chemistry properly. A modeling approach should include solid fuel combustion, ash formation including the release of inorganics and aerosol formation, ash particle transport, ash deposition and deposit build-up. In order to describe the first three steps a number of fuel properties have to be measured or determined in advance. Fig. 97 shows the most important properties. They can be divided into fuel composition and fuel reaction kinetics. Fuel composition uses standard fuel characterization methods (ultimate, proximate and heating value analysis), particle size distribution, mineral analysis using CCSEM, as well as chemical fractionation. The first two are essential. CCSEM analysis are needed for individual particle inorganic chemistry, enabling the prediction of ash formation and deposit chemistry. X-ray powder diffraction analysis might also be a good alternative, in particular for biomass. For coal, the maceral-mineral association is important in order to model the distribution and number of mineral inclusions/grains per fuel particle. Chemical fractionation becomes more important for lower-grade fuels such as lignite or biomass with a high share of organically-bound inorganics. Components leachable in water and ammonium acetate are assumed to vaporize during devolatilization and char combustion, and thus, be responsible for chemical reactions and aerosol formation.

Reaction parameters include the kinetic parameters for devolatilization, and char combustion. The determination of these parameters requires high experimental efforts, and, carefully conducted experiments. Often, kinetic data is taken from literature using similar fuels. However, this can lead to high uncertainties. If fuel conversion and flame properties are of interest, the kinetic parameters have to be measured. With all fuel properties and kinetics being available, simulations on ash formation and deposition can be conducted. The ash formation model should be able to predict the vaporization of inorganic elements and the re-condensation of these inorganic vapors. Furthermore, coalescence, char and mineral fragmentation as well as shedding should be included - a challenging and difficult task. Here, a promising approach are percolation models such as the work of Kang et al. [477,478]. Devolatilization and char combustion are known to influence ash formation. Once ash formation can be predicted accurately in terms of chemistry and size distribution, ash deposition mechanisms are required. The most important ones are inertial impaction, thermophoresis and diffusion of aerosols. Eddy impaction can only be predicted when using unsteady simulations, ideally resolving small turbulent scales in space and time.

The ash particle sticking and rebound behavior can be described by a large number of models with varying level of detail. The following suggestions are based on the review in this work. Four different scenarios are discussed and recommendations are given:

Salt-rich ashes: typical for straw and herbaceous biomass

- Recommendation: Melt fraction as proposed by Isaak et al. [388,389] using Eq. (70). The melt fraction should be calculated as a function of temperature, ash particle chemistry, and gas composition surrounding the particle. Again, bulk ash should be avoided and particle to particle variation in chemistry should be considered. For the calculation of the melt fraction, commercially available tools can be used.

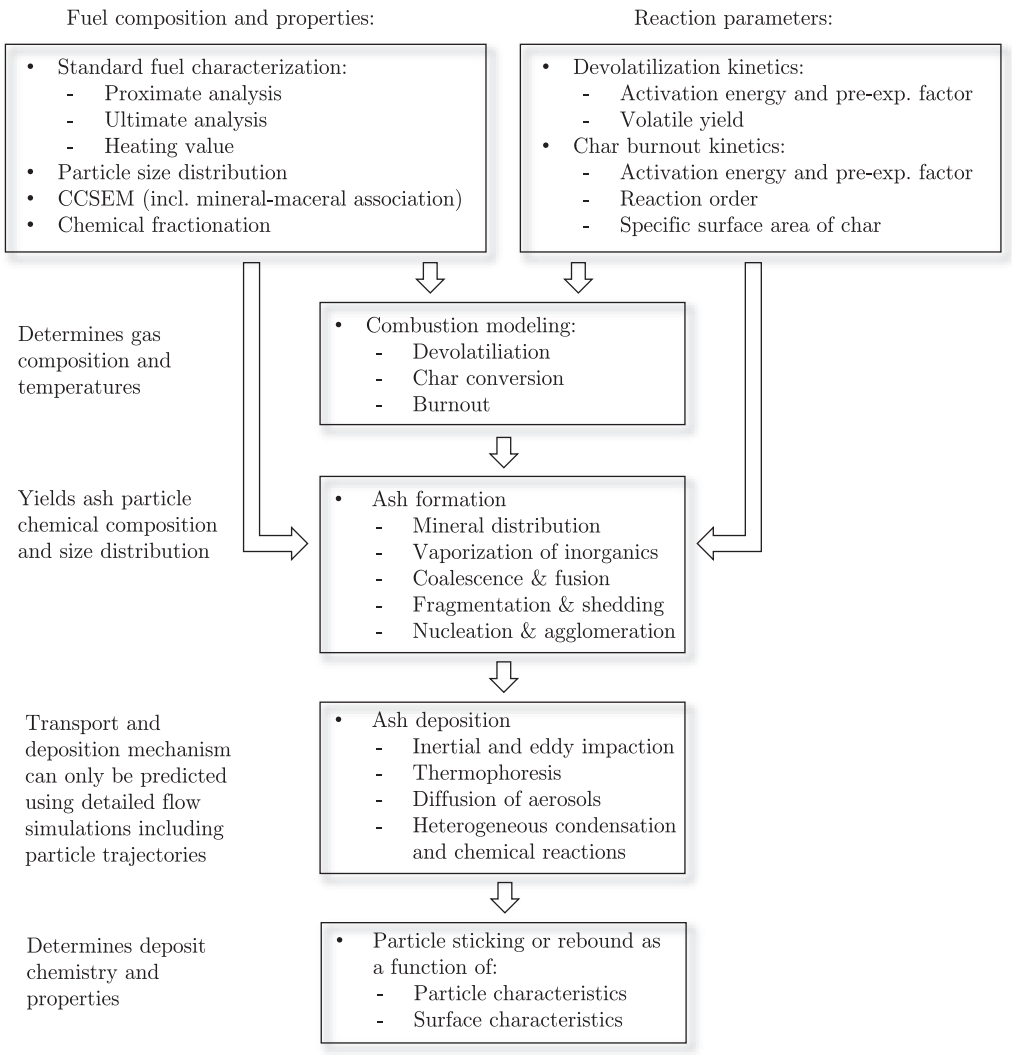

Fig. 98. Required measurements and input parameters for a comprehensive numerical simulation of ash formation and ash deposition.

- Strengths:
  - Gas atmosphere (reducing or oxidizing) can be considered
  - Relatively simple and straightforward
  - Can be used for a wide range of ash chemistry

- Problems:
  - Thermodynamic equilibrium calculations assume infinite time, which is not given in real combustion systems
  - Deposition of solid particles cannot be predicted (e.g. small solidified particles)
  - Inaccuracy for large molten particles, when rebound is likely (as shown by Müller et al. [202])
  - Deposit viscosity/stickiness is currently not incorporated
  - Impact angle is not considered
  - Difficult to implement in CFD codes and computationally expensive, when coupled with thermodynamic equilibrium calculations

Silicate-rich ashes: typical for coals in particular bituminous coals

- Recommendation: Critical viscosity as a function of particle kinetic energy using Eqs. (153) and (154) together with a suitable viscosity model. The choice of viscosity model is difficult. Typically, models are valid in the Newtonian range. The sharp viscosity increase at lower temperatures is normally not considered. The only model is the one proposed by Senior and Srinivasachar [316]. However, other models are more accurate in the Newtonian range. Another suggestion is to use the model of Browning et al. [314] together with a model considering the formation of crystals in the melt as presented by Eq. (49). In this case, the melt fraction is required and should be calculated using thermodynamic equilibrium calculations.

- Strengths:
  - Predicts sticking of small, unmolten particles
  - Considers the impact angle and the deposit/surface stickiness
  - Predicts rebound of large, molten particles with high kinetic energy
  - Very simple to implement in CFD codes

- Problems:
  - Relies on the accuracy of the viscosity model, which is only valid within a certain range
  - When combined with the solid fraction in the melt: difficult to implement in CFD codes

Particle properties:
$d_p = 20\ \mu m$
$v_p = 2.5\ m/s$

Substrate properties: inelastic wall with identical temperatures as particles
$\mu_{dep} = \mu_{wall} = \infty$

$T_p = 800\ °C$
$\rho_p = 2.42\ g/cm^3$
$\mu_p = 1.65 \cdot 10^5\ Pa \cdot s$
$\gamma_p = 0.42\ N/m$
$\Theta = 142\ °$

$T_p = 1200\ °C$
$\rho_p = 2.36\ g/cm^3$
$\mu_p = 1.00 \cdot 10^2\ Pa \cdot s$
$\gamma_p = 0.30\ N/m$
$\Theta = 11\ °$

Step	Symbol	Unit	Eq.								
	φ_i	°	-	90°	75°	60°	45°	30°	90°	60°	30°
1. Calculate particle kinetic energy	$E_{p,kin}$	J	-	$1.27 \cdot 10^{-11}$	$1.27 \cdot 10^{-11}$	$1.27 \cdot 10^{-11}$	$1.27 \cdot 10^{-11}$	$1.27 \cdot 10^{-11}$	$1.24 \cdot 10^{-11}$	$1.24 \cdot 10^{-11}$	$1.24 \cdot 10^{-11}$
	$E_{p,kin,n}$	J	-	$1.27 \cdot 10^{-11}$	$1.22 \cdot 10^{-11}$	$1.10 \cdot 10^{-11}$	$0.90 \cdot 10^{-11}$	$0.63 \cdot 10^{-11}$	$1.24 \cdot 10^{-11}$	$1.07 \cdot 10^{-11}$	$0.62 \cdot 10^{-11}$
2. Critical viscosity	$\mu_{p,crit}$	Pa·s	154	$1.25 \cdot 10^8$	$3.31 \cdot 10^3$	$3.56 \cdot 10^2$	$5.44 \cdot 10^1$	$6.31 \cdot 10^0$	$1.30 \cdot 10^8$	$3.72 \cdot 10^2$	$6.58 \cdot 10^0$
3. Sticking?	P_{stick}	-	153	1	0	0	0	0	1	1	0
4. Restitution coeff.	e_n	-	126	0.18	0.26	0.30	0.34	0.43	0.18	0.30	0.43
	e_n	-	125	0.75	0.75	0.75	0.75	0.93	0.75	0.75	0.93
	f	-	134	0.00	0.06	0.13	0.20	0.20	0.00	0.13	0.20
	e_t	-	122	0.71	0.71	0.71	0.73	0.84	0.71	0.73	0.84
5. Rebound angle and velocity	φ_r	°	124	90.0	54.0	35.8	24.6	16.5	90.0	35.8	16.5
	$v_{r,n}$	m/s	131	-0.45	-0.64	-0.65	-0.59	-0.54	-0.45	-0.65	-0.54
	v_r	m/s	-	-0.45	-0.79	-1.10	-1.42	-1.89	-0.45	-1.10	-1.89

Fig. 99. Example calculation for particle sticking and rebound using the critical viscosity criterion. Soda-lime glass particle behavior is predicted for different impact angles at an impact velocity of 2.5 m/s and a particle diameter of 20 μm. Grey values are either calculated using another equation or they give theoretical rebound behavior in case a particle sticks.

Economizer region: for solidified ash particles at low temperatures ($T < 500\ °C$)

- Recommendation: Critical velocity given by Eqs. (75) and (78) as suggested by Thornton and Ning [290]. An interesting model considering the impact angle is based on the work of Konstandopoulos [434]. Eqs. (85) and (86) as used by Pérez et al. [301] are recommended.

- Strengths:
  - Based on a mechanistic model and validated in depth
  - Very simple to implement in CFD codes

- Problems:
  - Elastic properties (E_i and ν_i) are required as a function of temperature and chemistry
  - Only valid for smooth surfaces and cannot consider an existing powdery deposit layer
  - Does not consider the impact angle in the standard version

Rebound behavior: for all non-sticking particles impacting a wall

- Recommendation: Calculate the tangential and normal coefficient of restitution according to Eqs. (122) and (125), respectively. The friction coefficient is estimated by Eq. (134). The rebound angle should be a random number distributed evenly around a mean value calculated using (124). The rebound angle should not be smaller than $\varphi_r < \varphi_i$ or greater than $\varphi_r > \pi - \varphi_i$. An improvement would be to calculate the normal restitution coefficient using Eqs. (118)–(120) or by using the energy conservation model of Section 6.3 with Eqs. (155) and (156). A promising approach might be the use of the discrete element method, which is able to describe the impact of particles on a powdery layer.

- Strengths:
  - This approach can predict a varying rebound angle
  - Relatively simple to implement in CFD codes

- Problems:
  - Empirical equations, which might not satisfy all situations
  - Particle rotation/spin is neglected
  - Particle kinetic energy does not change coefficient of restitution

The sticking behavior of wood ash is mostly unknown. Experimental data and detailed studies dealing with coarse wood ash particles are missing. This ash is rich in Ca and Mg with a relatively high melting point. Viscosity models fail in the case of Ca-rich ashes. Thermodynamic equilibrium calculations might be able to predict the melt fraction, however further studies and validations are needed in this field. A similar situation is found for ashes rich in P (found in manures) or S (for instance in lignites). In general, an energy conservation approach calculating a critical parameter is recommend. The viscosity might be a good parameter since it changes considerably with composition and temperature, and it is known to strongly affect the stickiness. The key is to find a correlation predicting the energy dissipated during particle deformation.

An exemplary calculation for silicate-rich ash particles is given in Fig. 99. Particle sticking or rebound behavior is predicted for different impact angles, an impact velocity of 2.5 m/s and a particle size of 20 μm at 800 and 1200 °C, respectively. It can be seen that a 800 °C particle only sticks at normal impact, whereas at 1200 °C particles stick at impact angles down to $\varphi_i = 60°$. The normal and tangential restitution coefficient increase with decreasing impact angle leading to a decrease in the rebound angle. The rebound velocity on the contrary increases with decreasing impact angle. Since both Eqs. (125) and (126) do not consider the energy loss during collision, the rebound velocity is identical for 800 and 1200 °C. Here an

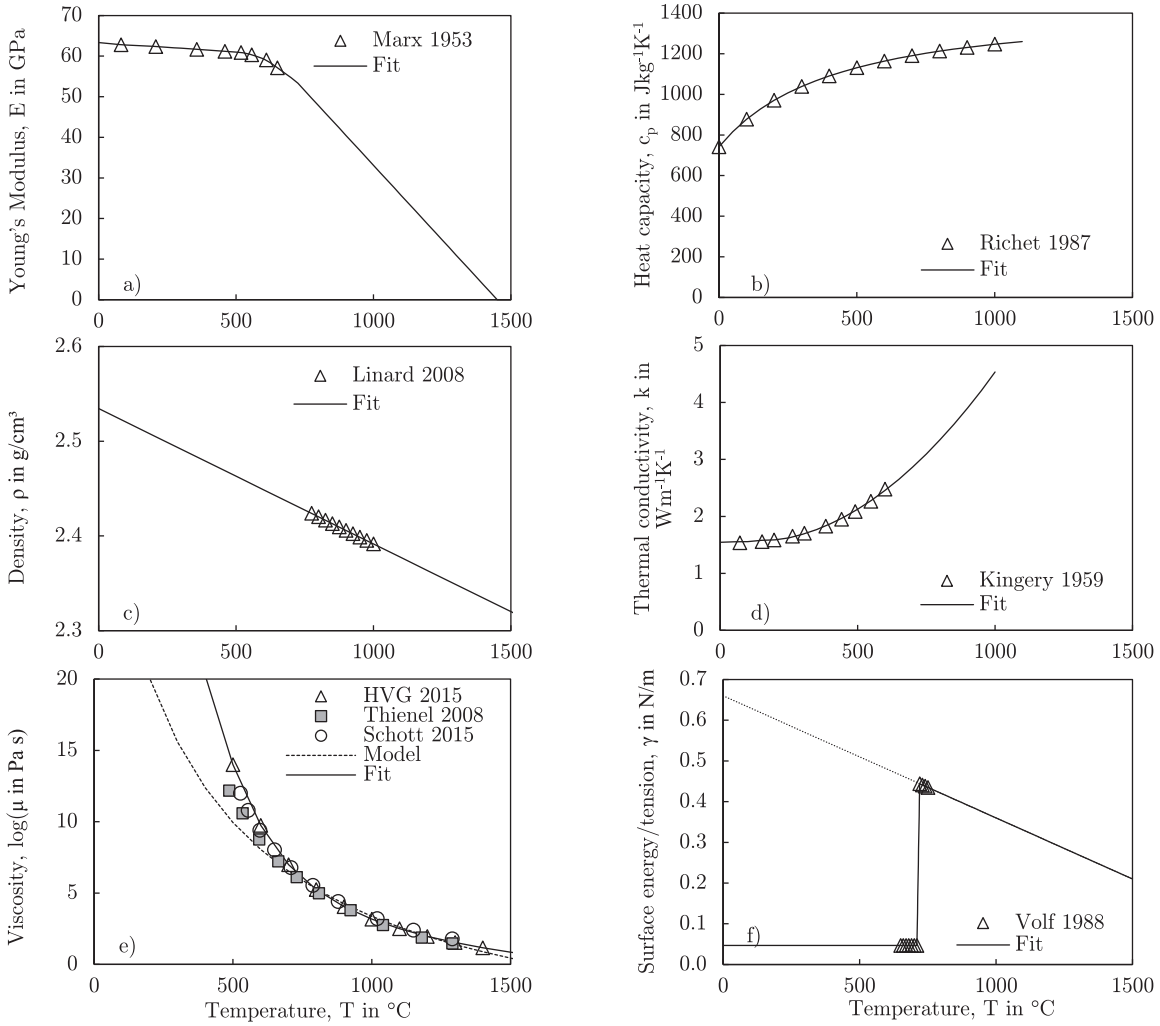

Fig. 100. Temperature-dependent soda-lime glass properties taken from literature: (a) Young's modulus, (b) heat capacity, (c) density, (d) thermal conductivity, (e) viscosity, and (f) surface tension. References can be found in the work of Scholz [459].

improvement is needed, e.g. as suggested by Eq. (156). However, the calculation of energy loss during collision is complex. There are many different equations for the calculation of the spread factor ξ and the energy dissipation of liquid droplets. Bennett and Poulikakos [533] compared different equations and give an overview on the calculation of the spread factor. In this area, more fundamental and experimental work is needed aiming at molten or partially molten ash particles.

8. Concluding remarks

The present work aims for a deeper understanding of ash deposition in particular the ash particle sticking and rebound behavior. The whole process of ash formation and ash deposition is discussed critically, and main findings and mechanisms are presented for a broad spectrum of solid fuels including coals, woody and herbaceous biomass.

Ash formation is a highly complex process, which can only be predicted when distribution, form and association of inorganic species in the fuel is known. Inorganics can be found as organically-bound inorganic elements, as dissolved salts, as mineral inclusions in the fuel matrix or as excluded mineral grains separated from the fuel. The chemical composition of individual mineral grains in a fuel sample differs significantly. This variation requires the use of sophisticated methods such as SEM/EDX or CCSEM characterizing the individual particle composition and revealing information on the amount and chemistry of inorganic species. A substantial number of particles has to be detected in order to obtain independent and statistically meaningful results. It is crucial to use SEM/EDX data instead of bulk ash chemistry when predicting ash formation and ash deposition. Otherwise, wrong conclusions concerning slagging and fouling behavior can be drawn. Often, single particle types with relatively low quantity in the fuel (individual minerals/inclusions or clusters of mineral grains) are causing ash related problems, whereas the majority of fly ash particles is unproblematic and harmless. For instance, when firing bituminous coal, pyrite in reducing conditions can be such a component leading to excessive slagging of heat exchangers. Another example are small, salt-rich particles in straw combustion systems. Therefore, bulk ash composition can be misleading and models should not be based on bulk ash analyses. Ash formation mechanisms are well understood for coal, however in the case of biomass further research is needed. The exact role of fusion, fragmentation and shedding during ash formation is more or less unknown. Relatively well understood is the vaporization and recondensation of inorganic elements for straw and wood combustion. A substantial quantity of the fuel, mainly elements such as Cl, P, Pb, S, Zn and to some extent Ca, K, Mg, Na, vaporizes, recondenses and forms aerosols during cooling.

Ash deposition mechanisms are inertial impaction including eddy impaction, thermophoresis, diffusion of aerosols, condensation and reactions between deposit and inorganic vapors.

Temperature-driven effects, such as condensation, chemical reactions and thermophoresis dominate during early stages and mainly depend on the quantity of particles and inorganic vapors in the vicinity of the heat exchanging surfaces. Thermophoresis is shown to be a function of the particle and gas thermal conductivity and models found in literature differ significantly from each other.

Ash particles can be classified based on chemistry, size and shape. The first two classifications are often found in literature, however shape is rarely discussed or reviewed. Frequently observed particle shapes are:

- molten, perfectly spherical particles,
- cenospherical particles with variable wall thickness (hollow spheres),
- plerospherical particles (hollow spheres filled with small ash particles),
- angular, sharp and unmolten particles,
- loose, irregular shaped and highly porous solids, and
- agglomerations of small particles.

Ash particle shape and morphology is often studied when exploring utilization options. For modeling purposes it is often assumed that ash particles are perfectly spherical. Particle trajectories and the sticking and rebound behavior are typically calculated for spheres and shape variants are ignored. This might be valid for coal ash, at least to some extent. However, biomass ash particles are found to differ significantly from spherical particles. In case of wood, loosely bound and irregularly shaped Ca-rich particles are frequently reported together with sub-micron salt particles. Straw particles are often spherical with sub-micron particles attached to their surfaces.

Ash particle properties and their mathematical description are essential when modeling ash particle sticking and rebound behavior. Properties are temperature- and composition-dependent and thus often difficult to predict. The following list summarizes findings from an extensive literature review:

- Elastic properties such as Young's modulus and the Poisson number are more or less unknown for ash particles. Some rare numbers can be found, however temperature-dependence and correlations considering composition are non existent.
- The melt or solid fraction in an ash system can be calculated as a function of particle temperature, particle and surrounding gas composition using thermodynamic equilibrium calculations. Often, good accuracy is reported when comparing results with ash fusion tests or measured melting behavior from differential scanning calorimetry analysis. Nevertheless, the method has uncertainties in particular for exotic ash compositions. In addition, calculations assume infinite time, whereas in combustion systems, time scales can be very short.
- The particle viscosity is known as an important parameter for the particle sticking probability [395]. The viscosity spreads over a wide range from 10^{-3} to 10^{9} Pa · s. The particle viscosity can be calculated using empirical correlations. A huge number of models has been developed. However, the accuracy is often not very good. Vargas et al. [323] reviewed viscosity measurements and model predictions and recommended the model of Bottinga and Weill [320] for silicate-rich ashes in the high-temperature regime, when the ash is perfectly molten and acts as a Newtonian fluid. A comparison in this work also revealed relatively good results for the model of Browning et al. [314]. When an ash particles cools down, crystals can form in the melt leading to a sharp increase in viscosity. There is only one model available incorporating this effect - the model of Senior and Srinivasachar [316]. This model is interesting and should be improved by correlating it to more measurements and a wider field of chemical compositions. Relatively good results are obtained when using a model accounting for the formation of crystals in the melt. The model of Roscoe [337], which goes back to Einstein [334] yields good results compared with measurements. The biggest concern with viscosity models is their limited range of applicability. Models easily under- or over-predict the actual viscosity by up to three orders of magnitude if used outside their validated range of composition or temperature. Models suitable for wood or herbaceous biomass are currently not available.
- Rheology of ash particles is an interesting field. But there are only few experimental studies indicating thixotropic flow behavior. Further work in this area is needed. The sintering and fusion behavior can be described using a modified equation of Mackenzie and Shuttleworth [354]. The particle density can be calculated using the method of partial molar densities as suggested for slags [345,353].
- The surface tension and contact angle of molten ash droplets can be estimated using a simple composition- and temperature-dependent approach. The surface tension varies within a narrow window (0.03 - 0.6 N/m) compared to the particle viscosity. The contact angle and thus the wetting behavior of ash particles with a solid surface is difficult to determine. Moza and Austin [349] developed a test procedure for measuring the contact angle with a supercooled substrate. Typical values are in the range of 50–150° strongly dependent on ash particle chemistry and the surface properties such as roughness, morphology and temperature.
- The thermal conductivity of ash particles and deposit strongly influences the surface temperature of a forming layer. The thermal conductivity of ash particles and/or deposits is dependent on the porosity, the temperature, the particle size, the chemical composition and radiative properties. Radiation is known to enhance thermal conductivity in porous media at high temperatures. The most important parameter is the porosity of the deposit or of particle agglomerates. Good agreement between predictions for the thermal conductivity of a porous layer with experimental data is observed when using the model of Brailsford and Major [381].

The **ash particle sticking behavior** is influenced by a number of parameters. The most important ones are: the particle properties (such as melt fraction, viscosity, surface tension/energy), the particle kinetic energy and the particle deformation upon impaction, the particle shape and surface roughness, the angle of impaction, the substrate roughness and geometry, the substrate properties, such as surface tension/energy, and forces between particles and the surface (e.g. adhesion or van der Waals forces). Different ash particle sticking criteria are used and described in literature. They are mostly empirical and based on simplified cases. The criteria can be categorized to the following groups and are based on the ash particle:

- melt fraction,
- viscosity, or
- energy conservation during impact.

The particle melt fraction is a popular approach for biomass in particular salt-rich particles. It has often been applied to predict the deposition and sticking tendency when firing biomass [202,258,391]. This approach can incorporate the effect of reducing conditions on the melting behavior of ash particles. Furthermore, modern tools can predict meaningful results for the melt fraction over a wide range of chemical compositions. Problems arise when describing the sticking tendency of solidified particles such as sub-

micron particles, which experience rapid cooling in the boundary layer or ash particles in the economizer region. Here, other approaches are required. A further missing effect is the angle of impact. It has been shown that particles impacting under a small angle of impact are very likely to rebound. Thus, a massive molten particle, which slightly touches a superheater tube at 90°, will not stick - it will rebound.

Another quite popular approach is to use the viscosity of an ash particle at contact with a surface. This approach, however, is often applied inaccurately. There are two concepts: the reference viscosity suggested by Walsh et al. [395] and the critical viscosity first proposed as a criterion by Srinivasachar et al. [1,407]. The reference viscosity is the value at which particles start to stick partially. The critical viscosity on the other hand is the value at which the whole particle will stick. The model of Walsh et al. [395] is often used as a theoretical case for bulk ash. An intermediate sticking probability, where only a small portion of the particle will stick might occur for liquids, however for high surface tension ash particles, it is unlikely. Frequently, the reference and critical viscosity are mixed up and bulk ash composition is used. Bulk ash composition will give an inaccurate and misleading deposition rate. Furthermore, the deposit composition will equal the bulk ash composition, which is known to be incorrect. Srinivasachar et al. [1] presented an interesting approach, where the critical viscosity for glass particles was measured to be a function of the particle kinetic energy. With this approach, small particles will still adhere even at lower temperatures. The problem with this approach is that a viscosity model is required. Models have been developed for silicate-rich ashes found in coal and to some extent in straw; however, not for wood ash or waste-based fuel ashes. Furthermore, these models do not consider the angle of impaction.

Energy conservation methods have been applied in two research fields: the impaction of liquid droplets and of solid, elastic spheres. In general, these methods use energy balances in order to calculate whether a particle sticks - kinetic energy of the incoming particle is completely dissipated - or a particle rebounds - particle kinetic energy is not completely dissipated. In the case of liquid droplets, the crucial parameters are the work of deformation (against the particle viscosity) and the adhesion to the substrate (surface tension, the wetted area and contact angle). Here, the theory of Mao et al. [390] proved to be a good approach. In the case of solid particles, a critical velocity is typically measured or predicted. Here it is commonly distinguished between elastic and elastic-plastic impaction processes. In the latter case, the particle is deformed permanently. A frequently used and accurate model is presented by Thornton and Ning [290], which requires Young's modulus and Poisson number of both collision partners.

A review on modeling studies reveals that most studies use the model of Walsh et al. [395] in combination with the bulk ash composition. Here, the latter is seen as problematic. In order to evaluate the accuracy, eight different sticking criteria based on all three methods and variants of these models are implemented in a CFD code and compared with measurements conducted in an entrained flow reactor. The mass deposited on probes is measured using three narrow size grades of soda-lime glass particles at three different temperatures mimicking coal ash particles. The best performance is found for the model of Srinivasachar et al. [1], where the critical viscosity, below which particle will stick, depends on the particle kinetic energy. A mechanistic explanation based on energy conservation and the work of Mao et al. [390] is extended in order to explain the dependence of the critical viscosity on the particle kinetic energy. Furthermore, the model now considers the impact angle and the stickiness of the substrate similar as it is proposed by Walsh et al. [395].

The **particle rebound behavior** is summarized for different scenarios: normal impact on a smooth surface including elastic and elastic-plastic deformation, oblique impact on a smooth surface, impact on a powdery layer, and impact on a liquid layer with an underlying solid substrate. Selected models from literature are discussed and equations are presented. These models are based on impact mechanics and require knowledge of material strength properties. Several experimental studies suggest that there is a distribution of rebound angles caused by the microscopic rough surface area. For small impact angles, rolling and sliding effects can become important depending on the friction coefficient. Interesting are the results of small spheres impacting a powdery layer. At high particle kinetic energy there is an increased chance, that particles are ejected from the bed depending on the connectivity between resting particles. A promising approach is the discrete element method for predicting the deposit formation at low temperatures, e.g. economizer region with solidified particles.

In the end, a holistic modeling approach including solid fuel combustion, ash formation and deposition is presented and recommendations for predicting particle sticking and rebound behavior are given. Currently, different approaches are recommended depending on the physical state of the particles, i.e. molten or solid, and, depending on the fuel ash chemistry. Research needs are identified and summarized in the following two sections.

8.1. Future experimental questions

Future experimental work should be directed towards a number of issues and research fields. The morphology, association and distribution of inorganic species within biomass fuels should be studied using advanced methods, such as SEM/EDX. Individual particle composition is essential for a relying ash formation model. This data should then be used as a model input. Sophisticated ash formation models, such as the percolation models developed for coal, should be applied for biomass and/or waste-based fuels. Mechanisms forming coarse fly ash particles are still not understood. Since biofuels are rich in volatile species, ash formation should be studied during devolatilization, and results should be compared to final ash composition. This helps in order to understand the interaction of Ca, Si and K species and the formation of coarse fly ash. Another crucial field of research are material properties. Viscosity measurements for typical biomass ashes, rich in Ca and/or salts are needed. Currently, viscosity measurements focus strongly on aluminosilicates. Material properties including Young's modulus, yield strength and Poisson number are more or less unknown for ash particles. These properties should be quantified for different chemical compositions and as a function of temperature focusing on higher temperatures in the range of 300–1000 °C. In order to find a generally valid sticking criteria, fundamental particle impaction studies are required. High speed cameras should record the impaction process. These fundamental studies should be carried out for other materials such as salt particles (pure salts or mixtures of two or more salts), Ca-rich or Fe-rich particles. It is crucial to use uniform particle size and chemistry. The particle sticking threshold should be determined for each size and chemical composition, and be related to particle properties such as viscosity, melt fraction and the particle kinetic energy. Furthermore, the role of cenospheres and non-spherical particles should be studied. A difficult field is the particle sticking behavior of sub-micron particles. Experimental studies are rare and should be carried out. In addition, studies on particles impacting on a powdery layer have to be extended. They are valuable since clean tubes never appear in a power plant. Another controversy parameter is the impact angle. Models and experimental results often disagree here and more fundamental work on the role of impact angle on the sticking tendency is needed, in particular at high temperatures. Most of the above mentioned fields cover fundamental research. Today, the majority of studies found in literature use fuels and/or bulk ash, and try to relate their findings to empirical correlations. However, computational

methods, such as CFD or DEM, require more fundamental data and no empirical equations or indices.

8.2. Challenges for future modeling studies

An urgent need is a more sophisticated ash formation model in CFD codes. This is particular challenging for lower-grade fuels such as biomass or when fuel mixtures are fired, e.g. co-firing of coal and biomass. Here, various chemical reactions and interactions are possible leading to further complexity. The are numerous studies using a constant mineral matter content per fuel particle. Furthermore, it is assumed that mineral matter equals ash content. Therefore, standalone tools should be developed and subsequently be included in the code. There is also a need for a more fundamental viscosity model considering the network former theory. The applicability of viscosity models should be widened for straw ashes (salt-rich and K-aluminosilicates), wood ashes (Ca-rich), and SRF ashes (various compositions). An interesting aspect, is the particle cooling and deceleration within boundary layers.

CFD methods should be used to accurately predict particle behavior in the vicinity of heat exchanging surfaces. Here, the criterion of Weber et al. [206] has to be considered when constructing computational grids. Furthermore, the cooling behavior and deformation of molten droplets upon impact could be studies using volume of fluid methods. Mechanistic models based on energy conservation should be investigated and improved. A general method valid for liquids and solids is desirable. This model could be implemented in DEM simulations predicting ash deposition with a high level of detail. More work is needed in order to predict the deposit structure, erosion and shedding, as well as the collection efficiency of a porous layer.

Acknowledgments

The authors would like to thank the support of “Energie Baden-Württemberg AG” (EnBW) for the cooperation in the frame of KW21. The research joint-venture has been funded by the “Bayerisches Staatsministerium für Wissenschaft, Forschung und Kunst”, the “Bayerisches Staatsministerium für Wirtschaft, Infrastruktur, Verkehr und Technologie”, the “Ministerium für Wissenschaft, Forschung und Kunst Baden Württemberg” and EnBW. The work has been carried out in the frame of the sub-project BY4DE. In addition, this project has received funding from the European Union's Horizon 2020 research and innovation programme under grant agreement No. 727616. Furthermore, we want to thank Professor T.F. Wall from Newcastle University, Australia, who recommended a review on ash particle sticking and rebound behavior during the Impact of Fuel Quality Conference in Puchberg, Austria in 2012, and encouraged us to start this work.

Appendix A

The following section summarizes different empirical viscosity models in a chronological order. Equations are empirical in nature and try to relate slag or ash composition to measured viscosity values. Values for the viscosity μ are given in Pa · s, and for the temperature T in K, if not stated otherwise.

Watt and Fereday model:. A simple correlation was proposed by Watt and Fereday in 1969 [319]. It was developed for British coal ash slags and uses an Arrhenius-type equation:

$$log\ \mu = \frac{10^7 \cdot \alpha}{(T - 423.15)^2} + \beta \tag{158}$$

The coefficients α and β are defined as:

$$\alpha = 0.00835 \cdot SiO_2 + 0.00601 \cdot Al_2O_3 - 0.109, \tag{159}$$

$$\beta = 0.0415 \cdot SiO_2 + 0.0192 \cdot Al_2O_3 + 0.0276(equiv.\ Fe_2O_3) + 0.0160 \cdot CaO - 3.92, \text{ and} \tag{160}$$

$$equiv.\ Fe_2O_3 = Fe_2O_3 + 1.11 \cdot FeO + 1.43 \cdot Fe, \tag{161}$$

where slag components are expressed as normalized weight percentages and sum up to 100% (SiO_2 + Al_2O_3 + equiv. Fe_2O_3 + CaO + MgO = 100). This correlation was suggested for high silica (> 80%) or high iron contents (> 15%) [314].

S² *Correlation:.* The so-called S^2 correlation was also developed for British coal ash slags with silica contents less than 55% and iron oxide contents below 5% [314]. The equation is given by:

$$log\ \mu = 4.468 \cdot \left(\frac{S_r}{100}\right)^2 + 1.265 \cdot \left(\frac{10^4}{T}\right) - 7.44. \tag{162}$$

The silica ratio is defined by $S_r = SiO_2/(SiO_2 + Fe_2O_3 + CaO + MgO)$. Ash oxides are in wt.% and sum up to 100%, and the Fe_2O_3 content is expressed by Eq. (161).

Bottinga and Weill:. Bottinga and Weill [320] use the abundance of viscosity data for the development of mathematical relation. The viscosity of anhydrous silicate liquids is calculated using tabulated constants D_i in the following form:

$$log\ \mu = \sum_i x_i \cdot D_i - 1 \tag{163}$$

where x_i is the molar fraction, and D_i a tabulated constant of species i. D_i values are typically given for different levels of SiO_2 and temperatures in the range of 1200–1800 °C. They can be found e.g. in the work of Vargas et al. [323].

Urbain Model:. Urbain [321] developed a frequently used equation. They fitted measurements of SiO_2-Al_2O_3-CaO-MgO systems to a Weymann-type equation [314]:

$$\mu = 0.1 \cdot \alpha \cdot T \cdot e^{\left(\frac{10^3 \cdot \beta}{T}\right)} \tag{164}$$

In Eq. (164) the viscosity is in Pa · s and the temperature in K. The coefficient α is a function of β in the form of:

$$\alpha = e^{(-0.2693 \cdot \beta - 11.6725)} \tag{165}$$

The coefficient β can be calculated according to the following equations:

$$\beta = \beta_0 + \beta_1 \cdot N + \beta_2 \cdot N^2 + \beta_3 \cdot N^3 \tag{166}$$

$$\beta_0 = 13.8 + 39.9355 \cdot \delta - 44.049 \cdot \delta^2 \tag{167}$$

$$\beta_1 = 30.481 - 117.1505 \cdot \delta + 129.9978 \cdot \delta^2 \tag{168}$$

$$\beta_2 = -40.9429 + 234.0486 \cdot \delta - 300.04 \cdot \delta^2 \tag{169}$$

$$\beta_3 = 60.7619 - 153.9276 \cdot \delta + 211.1616 \cdot \delta^2 \tag{170}$$

The parameter N in Eq. (166) stands for the mole fraction of SiO_2. The quantity δ is the ratio of the mole fractions of CaO and the sum of CaO and Al_2O_3:

$$\delta = \frac{CaO}{CaO + Al_2O_3} \tag{171}$$

Table 26
Low and high temperature coefficients for b_i.

	High temperature	Low temperature
b_0	−224.98	−7563.46
b_1	636.67	24431.69
b_2	−418.70	−17685.4
b_3	823.89	32644.26
b_4	−2398.32	−103681.0
b_5	1650.56	74541.33
b_6	−957.94	−46484.8
b_7	3366.61	146008.4
b_8	−2551.71	−104306.0
b_9	387.32	21904.63
b_{10}	−1722.24	−68194.8
b_{11}	1432.08	48429.31

Kalmanovitch model:. Kalmanovitch and Frank [322] modified Eqs. (165) and (171) and included oxides of iron, magnesium, sodium, potassium, and titanium (again as mole fractions) [314]:

$$\alpha = e^{(-0.2812 \cdot \beta - 11.8279)} \tag{172}$$

$$\delta = \frac{CaO + MgO + Na_2O + K_2O + FeO + TiO_2}{CaO + Al_2O_3 + MgO + Na_2O + K_2O + FeO + TiO_2} \tag{173}$$

Senior and Srinivasachar model:. The model proposed by Senior and Srinivasachar [316] aims at the prediction of ash particle viscosities in a broad temperature range. They therefore introduced a low and high temperature regime and use the same type of equation for the temperature-dependence as proposed by Urbain [321]:

$$\mu = 0.1 \cdot T \cdot 10^{\left(\alpha + \frac{10^3 \cdot \beta}{T}\right)} \tag{174}$$

The coefficient α is defined as:

$$\alpha = a_0 + a_1 \cdot \beta + a_2 \cdot \frac{NBO}{T}, \tag{175}$$

where NBO/T is the ratio of non-bridging oxygens to tetrahedral oxygens given by:

$$\frac{NBO}{T} = \frac{CaO + MgO + FeO + Na_2O + K_2O - Al_2O_3 - Fe_2O_3}{(SiO_2 + TiO_2)/2 + Al_2O_3 + Fe_2O_3}. \tag{176}$$

This parameter describes the behavior of glass melts and their network, explained in Section 3.3. A negative value of NBO/T indicates that there is an insufficient number of modifier ions to stabilize Al^{3+} and Fe^{3+}, which are known to act as amphoterics, i. e. they either act as glass formers or modifiers. Modifiers are known to disrupt the glass structure and thus tend to lower the viscosity [316]. Coefficients a_i in Eq. (175) are given in Table 28. Values depend on the regime (low or high temperature) and on the value of NBO/T. The coefficient β is derived by multiple regression analysis and can be calculated using the following equation [316]:

$$\beta = b_0 + b_1\delta + b_2\delta^2 + b_3 N + b_4 N\delta + b_5 N\delta^2 + b_6 N^2 + b_7 N^2\delta + b_8 N^2\delta^2 + b_9 N^3 + b_{10} N^3\delta + b_{11} N^3\delta^2, \tag{177}$$

where N is again the mole fraction of SiO_2, δ is computed as shown in Eq. (171), and the coefficients b_i can be taken from Table 26. The viscosity is calculated using Eqs. (174)–(177) for low and high temperature coefficients. The higher value of μ is then used as the viscosity at a given temperature.

Browning Model:. Browning et al. [314] recently published an interesting approach, in which they investigated 1715 data points for 117 slag compositions and came up with an empirical equation in the form of:

$$log\frac{\mu}{T - T_s} = \frac{14788}{T - T_s} - 10.931 \tag{178}$$

The temperature shift T_s in Eq. (178), is computed with

$$T_s = 306.63 \cdot ln(A) - 574.31, \tag{179}$$

where A is a molar ratio according to:

$$A = \frac{3.19Si^{4+} + 0.855Al^{3+} + 1.60K^{+}}{0.93Ca^{2+} + 1.50Fe^{n+} + 1.21Mg^{2+} + 0.69Na^{+} + 1.35Mn^{n+} + 1.47Ti^{4+} + 1.91S^{-2}} \tag{180}$$

The quantities of each component in Eq. (160) are mole fractions, where all components sum up to unity.

Appendix B

Soda-lime glass is used to simulate ash for the development of a particle sticking and rebound criterion. The chemical composition in terms of oxides from different studies is given in Table 25. Only minor differences are found and it can be assumed that glasses from different studies behave similarly. The particle size distribution for different size-fractions is given in Table 27. Particles are in a relatively narrow window with the d_{50} being 43, 63 and 171 μm. Ash fusion temperatures are determined for all three size-fractions. It can be seen that the fluid temperature is almost identical. Furthermore, it is observed that smaller particle sizes lead to lower IDT and ST. This is probably caused by a higher packing factor and thus an increased sintering rate at lower temperatures. The conditions and settings of different glass particle experiments from literature (shown in Fig. 60), are summarized in Table 28. Srinivasachar et al. [1] and Richter [222] used an uncooled probe composed of Al_2O_3. Schulze et al. [201] used a cooled steel probe. The particle diameters range from 40 up to 105 μm. Particle velocities range from relatively low values of 0.33 up to 4 m/s. The soda-lime glass particle properties as a function of temperature are shown in Figs. 100(a)–(f). Measurements are not found for all properties over a broad tempera-

Table 27
Soda-lime glass composition as oxides.

Sample	Unit	Al_2O_3	CaO	Fe_2O_3	K_2O	MgO	Na_2O	SiO_2	TiO_2
Srinivasachar et al. [1]	wt.%	0	8.0	0	0	5.0	15.0	72.0	0
Richter [222]	wt.%	0.8	9.3	0.2[a]	0.2	3.6	12.9	72.9	0.1
Schulze et al. [201]	wt.%	1.0	8.0	0	0.5	4.0	14.2	72.3	0
Present study[b]	wt.%	1.4	9.2	0.3	0.4	3.0	13.4	72.2	0.1

[a] FeO instead of Fe_2O_3.
[b] data from the glass manufacturer.

Table 28
Low and high temperature coefficients for a_i.

	High temperature	Low temperature			
		$\frac{NBO}{T} \geq 1.3$	$0.2 \leq \frac{NBO}{T} < 1.3$	$0.0 \leq \frac{NBO}{T} < 0.2$	$\frac{NBO}{T} < 0.0$
a_0	−2.81629	−0.982	2.478718	9.223	9.223
a_1	−0.46341	−0.902473	−0.902473	−0.902473	−0.902473
a_2	-0.35342	0	−2.662091	-37[a]	0

[a] suggested by Richter [222] to reproduce results of Senior and Srinivasachar.

Table 29
Chosen properties for the Al_2O_3 substrate at 1000 °C. Values are assumed to remain constant in the range of 800–1000 °C. Soda-lime glass properties at 1000 °C are given for comparison. References can be found in the work of Scholz [459].

Quantity Unit	E GPa	ν -	c_p J/(kg K)	ρ g/cm^3	k W/(m K)	μ Pa · s	γ[a] J/m^2 or N/m
Al_2O_3 (> 99.7% purity)	75	0.23	900	2.55	25	10^{20}[b]	1
Soda-lime glass	34	0.22	1220	2.39	4.5	$10^{3.5}$	0.35
Steel at 500 °C	145-165	0.4-0.5	~550	7.7-7.8	35-45	-	2.4[c]
K_2SO_4[d]	30	0.3	-	2.665	-	-	0.15

[a] surface energy for solid Al_2O_3 and steel.
[b] Al_2O_3 is solid at this temperature and therefore a very high value is chosen.
[c] pure iron at room temperature.
[d] values taken from Perez et al. [301].

ture range. In such cases, extrapolations are carried out, e.g. for the Young's modulus as shown in Fig. 100(f). Properties of the substrate Al_2O_3 are assumed to be constant due to missing literature data. A comparison of the chosen values with soda-lime glass is given in Table 29.

References

[1] Srinivasachar S, Helble JJ, Boni AA. An experimental study of the inertial deposition of ash under coal combustion conditions. Symposium (International) on Combustion 1991;23:1305–12.
[2] Vassilev SV, Kitano K, Takeda S, Tsurue T. Influence of mineral and chemical composition of coal ashes on their fusibility. Fuel Process Technol 1995;45(1):27–51.
[3] Huggins FE. Overview of analytical methods for inorganic constituents in coal. Int J Coal Geol 2002;50(1):169–214.
[4] Werkelin J, Skrifvars BJ, Zevenhoven M, Holmbom B, Hupa M. Chemical forms of ash-forming elements in woody biomass fuels. Fuel 2010;89(2):481–93.
[5] Vassilev SV, Baxter D, Andersen LK, Vassileva CG. An overview of the chemical composition of biomass. Fuel 2010;89(5):913–33.
[6] Zevenhoven M, Yrjas P, Skrifvars BJ, Hupa M. Characterization of ash-forming matter in various solid fuels by selective leaching and its implications for fluidized-bed combustion. Energy Fuels 2012;26(10):6366–86.
[7] Sami M, Annamalai K, Wooldridge M. Co-firing of coal and biomass fuel blends. Prog Energy Combust Sci 2001;27(2):171–214.
[8] McLennan AR, Bryant GW, Stanmore BR, Wall TF. Ash formation mechanisms during pf combustion in reducing conditions. Energy Fuels 2000;14(1):150–9.
[9] Yan L, Gupta RP, Wall TF. A mathematical model of ash formation during pulverized coal combustion. Fuel 2002;81(3):337–44.
[10] Doshi V, Vuthaluru HB, Korbee R, Kiel JHA. Development of a modeling approach to predict ash formation during co-firing of coal and biomass. Fuel Process Technol 2009;90(9):1148–56.
[11] Boström D, Skoglund N, Grimm A, Boman C, Öhman M, Boström M, Backman R. Ash transformation chemistry during combustion of biomass. Energy Fuels 2012;26(1):85–93.
[12] Raask E. Mineral impurities in coal combustion: behavior, problems, and remedial measures. Taylor & Francis; 1985. ISBN: 978-0891163626.
[13] Baxter LL, DeSollar RW. A mechanistic description of ash deposition during pulverized coal combustion: predictions compared with observations. Fuel 1993;72(10):1411–8.
[14] Benson SA, Jones ML, Harb JN. Ash formation and deposition. Coal Sci Technol 1993;20:299–373.
[15] Couch GR. Understanding slagging and fouling in pf combustion. London: IEA Coal Research; 1994. ISBN: 92-9029-240-7
[16] Bryers RW. Fireside slagging, fouling, and high-temperature corrosion of heat-transfer surface due to impurities in steam-raising fuels. Prog Energy Combust Sci 1996;22(1):29–120.
[17] Pronobis M. Evaluation of the influence of biomass co-combustion on boiler furnace slagging by means of fusibility correlations. Biomass Bioenergy 2005;28(4):375–83.
[18] Frandsen FJ. Utilizing biomass and waste for power production – a decade of contributing to the understanding, interpretation and analysis of deposits and corrosion products. Fuel 2005;84(10):1277–94.
[19] Frandsen FJ. Ash research from Palm Coast, Florida to Banff, Canada: entry of biomass in modern power boilers. Energy Fuels 2009;23(7):3347–78.
[20] Y. Niu H. Ash-related issues during biomass combustion: alkali-induced slagging, silicate melt-induced slagging (ash fusion), agglomeration, corrosion, ash utilization, and related countermeasures. Prog Energy Combust Sci 2016;52(1):1–61.
[21] Haynes BS, Neville M, Quann RJ, Sarofim AF. Factors governing the surface enrichment of fly ash in volatile trace species. J Colloid Interface Sci 1982;87(1):266–78.
[22] Helble JJ, Sarofim AF. Factors determining the primary particle size of flame-generated inorganic aerosols. J Colloid Interface Sci 1989;128(2):348–62.
[23] Monroe L. An experimental and modeling study of residual fly ash formation in combustion of a bituminous coal. Cambridge: MIT; 1989 PhD thesis.
[24] Seeker WR, Samuelsen GS, Heap MP, Trolinger JD. The thermal decomposition of pulverized coal particles. Symposium (International) on Combustion 1981;18:1213–26.
[25] Hansen LA, Frandsen FJ, Dam-Johansen K, Sørensen HS, Skrifvars BJ. Characterization of ashes and deposits from high-temperature coal–straw co-firing. Energy Fuels 1999;13(4):803–16.
[26] van Dyk JC, Benson SA, Laumb ML, Waanders B. Coal and coal ash characteristics to understand mineral transformations and slag formation. Fuel 2009;88(6):1057–63.
[27] Werther J, Ogada T. Sewage sludge combustion. Prog Energy Combust Sci 1999;25(1):55–116.
[28] Lopes MH, Abelha P, Lapa N, Oliveira JS, Cabrita I, Gulyurtlu I. The behaviour of ashes and heavy metals during the co-combustion of sewage slugeds in a fluidised bed. Waste Manage 2003;23(9):859–70.
[29] Fytili D, Zabaniotou A. Utilization of sewage sludge in EU application of old and new methods – a review. Renewable Sustainable Energy Rev 2008;12(1):116–40.
[30] Öhman M, Nordin A, Skrifvars BJ, Backman R, Hupa M. Bed agglomeration characteristics during fluidized bed combustion of biomass fuels. Energy Fuels 2000;14(1):169–78.
[31] Skrifvars BJ, Backman R, Hupa M. Characterization of the sintering tendency of ten biomass ashes in FBC conditions by a laboratory test and by phase equilibrium calculations. Fuel Process Technol 1998;56(1):55–67.
[32] Baxter LL, Miles TR, Miles TRJ, Jenkins BM, Milne T, Dayton D, Bryers RW, Oden LL. The behavior of inorganic material in biomass-fired power boilers: field and laboratory experiences. Fuel Process Technol 1998;54(1–3):47–78.
[33] EU-Project: Biofficiency, developing the next generation of CHP plants. Proposal for the project No. 727616. European Union: Horizon 2020; 2016.
[34] Montgomery M, Karlsson A, Larsen OH. Field test corrosion experiments in Denmark with biomass fuels. Part 1: straw–firing. Mater Corros 2002;53(2):121–31.
[35] Spliethoff H. Power generation from solid fuels. Heidelberg and New York: Springer; 2010. ISBN: 978-3642028557
[36] Dolezal R. Dampferzeugung: Verbrennung, Feuerung, Dampferzeuger. New York: Springer; 1985. ISBN: 978-3540137719

[37] Ward CR. Analysis and significance of mineral matter in coal seams. Int J Coal Geol 2002;50(1):135–68.
[38] Benson SA, Holm PL. Comparison of inorganics in three low-rank coals. Ind Eng Chem Prod Res Dev 1985;24(1):145–9.
[39] Marschner H. Marschner's mineral nutrition of higher plants. Academic Press; 2011. ISBN: 978-0123849052
[40] Jensen PA, Frandsen FJ, Dam-Johansen K, Sander B. Experimental investigation of the transformation and release to gas phase of potassium and chlorine during straw pyrolysis. Energy Fuels 2000;14(6):1280–5.
[41] Knudsen JN, Jensen PA, Dam-Johansen K. Transformation and release to the gas phase of Cl, K, and S during combustion of annual biomass. Energy Fuels 2004;18(5):1385–99.
[42] Tchoffor PA, Davidsson KO, Thunman H. Transformation and release of potassium, chlorine, and sulfur from wheat straw under conditions relevant to dual fluidized bed gasification. Energy Fuels 2013;27(12):7510–20.
[43] Steenari BM, Schelander S, Lindqvist O. Chemical and leaching characteristics of ash from combustion of coal, peat and wood in a 12MW CFB – a comparative study. Fuel 1999;78(2):249–58.
[44] van Lith SC, Alonso-Ramírez V, Jensen PA, Frandsen FJ, Glarborg P. Release to the gas phase of inorganic elements during wood combustion. Part 1: development and evaluation of quantification methods. Energy Fuels 2006;20(3):964–78.
[45] Pedersen AJ, van Lith SC, Frandsen FJ, Steinsen SD, Holgersen LB. Release to the gas phase of metals, S and Cl during combustion of dedicated waste fractions. Fuel Process Technol 2010;91(9):1062–72.
[46] Fagerström J, Nyström I, Boström D, Öhman M, Boman C. Reduction of fine particle- and deposit forming alkali by co-combustion of peat with wheat straw and forest residues. In: Proceedings of the Conference Impacts of Fuel Quality on Power Production and Environment, Lapland, Finland; 2010.
[47] Carroll JP, Finnan JM, Biedermann F, Brunner T, Obernberger I. Air staging to reduce emissions from energy crop combustion in small scale applications. Fuel 2015;155:37–43.
[48] Gallagher NB, Peterson TW, Wendt JOL. Sodium partitioning in a pulverized coal combustion environment. Symposium (International) on Combustion 1996;26:3197–204.
[49] Mwabe PO, Wendt JOL. Mechanisms governing trace sodium capture by kaolinite in a downflow combustor. Symposium (International) on Combustion 1996;26:2447–53.
[50] Dou B, Shen W, Gao J, Sha X. Adsorption of alkali metal vapor from high-temperature coal-derived gas by solid sorbents. Fuel Process Technol 2003;82:51–60.
[51] Waindich A, Müller M. Alkali removal at 1400°C under gasification conditions. Fuel 2014;116:889–93.
[52] Blasing M, Zini M, Muller M. Influence of feedstock on the release of potassium, sodium, chlorine, sulfur, and phosphorus species during gasification of wood and biomass shells. Energy Fuels 2013;27(3):1439–45.
[53] Skrifvars BJ, Yrjas P, Kinni J, Siefen P, Hupa M. The fouling behavior of rice husk ash in fluidized-bed combustion. 1. fuel characteristics. Energy Fuels 2005;19:1503–11.
[54] Benson SA, Fegley MM, Hurley JP, Jones ML, Kalmanovitch DP, Miller BG, Miller SF, Steadman EN, Schobert HH, Schobert BJ, Weber BJ, Weinmann JR, Zobeck BJ. Project sodium: a detailed evaluation of sodium effects in low rank coal combustion systems. Final technical report. North Dakota, United States: EERC; 1988.
[55] Hurley JP, Benson SA, Erickson TA, Allen SE, Bieber J. Project calcium, Final technical report. North Dakota, United States: EERC; 1992.
[56] Vassilev SV, Tascón JMD. Methods for characterization of inorganic and mineral matter in coal: a critical overview. Energy Fuels 2003;17(2):271–81.
[57] Benson SA, Hurley JP, Zygarlicke CJ, Steadman EN, Erickson TA. Predicting ash behavior in utility boilers. Energy Fuels 1993;7(6):746–54.
[58] Parr SW. The analysis of fuel, gas, water, and lubricants. McGraw-Hill Book Co; 1922. ISBN: 978-1330876428.
[59] Müller M, Wolf KJ, Smeda A, Hilpert K. Release of K, Cl, and S species during co-combustion of coal and straw. Energy Fuels 2006;20(4):1444–9.
[60] Porbatzki D, Stemmler M, Müller M. Release of inorganic trace elements during gasification of wood, straw, and miscanthus. Biomass Bioenergy 2011;35(4):79–86.
[61] Vassilev SV, Menendez R, Alvarez D, Diaz-Somoano M, Martinez-Tarazona MR. Phase-mineral and chemical composition of coal fly ashes as a basis for their multicomponent utilization. 1. Characterization of feed coals and fly ashes. Fuel 2003;82(14):1793–811.
[62] Dunnu G, Maier J, Scheffknecht G. Ash fusibility and compositional data of solid recovered fuels. Fuel 2010;89(7):1534–40.
[63] Weidong L, Ming L, Weifeng L, Haifeng L. Study on the ash fusion temperatures of coal and sewage sludge mixtures. Fuel 2010;89(7):1566–72.
[64] Koppejan J, van Loo S. The handbook of biomass combustion and co-firing. Routledge; 2012. ISBN: 978-1844072491.
[65] Zhang Q, Liu H, Qian Y, Xu M, Li W, Xu J. The influence of phosphorus on ash fusion temperature of sludge and coal. Fuel Process Technol 2013;110:218–26.
[66] EU-Project: Prediction of ash and deposit formation for biomass PF co-combustion. Final Report: project No. JOR3-CT98-0198. European Union; 1999.
[67] Lebiedzik J, Burke KG, Troutman S, Johnson Jr GG, White EW. New methods for quantitative characterization of multiphase particulate materials including thickness measurement, Scanning Microscopy, 1973, 122.
[68] Zygarlicke CJ, Ramanathan M, Erickson TA. Fly ash particle-size distribution and composition: experimental and phenomenological approach. Inorganic Transformations and Ash Deposition during Combustion 1992: 525–44.
[69] Gomez CO, Strickler DW, Austin LG. An iodized mounting medium for coal particles. J Electron Microsc Tech 1984;1(3):285–7.
[70] Sarofim A, Helble J. Mechanisms of ash deposit formation. Proceedings of the Engineering Foundation International Conference, Solihull, England 1993. ISBN: 978-1560322931.
[71] Wall TF, Bailey JG, Wibberley LJ. In: Proceedings of the Engineering Foundation Conference on Mineral Matter and Ash in Coal; 1990. p. 249.
[72] Barta LE, Horvath F, Beer JM, Sarofim AF. Variation of mineral matter distribution in indivudual pulverized coal particles: application of the "urn" model. Symposium (International) on Combustion 1991;23:1289–96.
[73] Helble JJ, Srinivasachar S, Boni AA. Factors influencing the transformation of minerals during pulverized coal combustion. Prog Energy Combust Sci 1990;16(4):267–79.
[74] Straszheim WE, Markuszewski R. SEM-AIA measurement of the association of mineral matter with the organic coal matrix for predicting fine coal cleanability. Coal Prep 1992;10(1-4):59–75.
[75] Wigley F, Williamson J, Gibb WH. The distribution of mineral matter in pulverised coal particles in relation to burnout behaviour. Fuel 1997;76(13):1283–8.
[76] Gottlieb P, Agron-Olshina N, Sutherland D. The characterisation of mineral matter in coal and fly ash. In: Proceedings of the Engineering Foundation International Conference, Palm Coast, USA; 1991.
[77] Creelman RA, Ward CR. A scanning electron microscope method for automated, quantitative analysis of mineral matter in coal. Int J Coal Geol 1996;30(3):249–69.
[78] Liu Y, Gupta R, Sharma A, Wall T, Butcher A, Miller G, Gottlieb P, French D. Mineral matter–organic matter association characterisation by QEMSCAN and applications in coal utilisation. Fuel 2005;84(10):1259–67.
[79] Liu Y, Gupta R, Wall T. Ash formation from excluded minerals including consideration of mineral–mineral associations. Energy Fuels 2007;21(2):461–7.
[80] Rayner JE, Marskell WG. The distribution of mineral matter in pulverized fuel and solid products of combustion. J Inst Fuel 1963: 113–25.
[81] Littlejohn R. Mineral matter and ash distribution in as-fired samples of pulverized fuels. J Inst Fuel 1966;39(301):59–67.
[82] Unsworth JF, Barratt DJ, Roberts PT. Coal quality and combustion performance: an international perspective. Coal Sci Technol 1991;19:1–609. ISBN: 978-0444887030.
[83] Cloke M, Lester E, Belghazi A. Characterisation of the properties of size fractions from ten world coals and their chars produced in a drop-tube furnace. Fuel 2002;81(5):699–708.
[84] Zhang H, Mo Y, Sun M, Wei X. Determination of the mineral distribution in pulverized coal using densitometry and laser particle sizing. Energy Fuels 2005;19(6):2261–7.
[85] Charon O, Kang SG, Graham K, Sarofim AF, Beer JM. Variation in coal composition. A computational approach to study the mineral composition of individual coal particles. Division of Fuel Chemistry, USA: American Chemical Society; 1989. Preprints of Papers (34), CONF-8904163.
[86] Barta LE, Toqan MA, Beér JM, Sarofim AF. Prediction of fly ash size and chemical composition distributions: the random coalescence model. Symposium (International) on Combustion 1992;24:1135–44.
[87] Hansen LA, Frandsen FJ, Dam-Johansen K, Sørensen HS. Quantification of fusion in ashes from solid fuel combustion. Thermochim Acta 1999;326(1):105–17.
[88] van Dyk JC, Waanders FB, Benson SA, Laumb ML, Hack K. Viscosity predictions of the slag composition of gasified coal, utilizing FactSage equilibrium modelling. Fuel 2009;88(1):67–74.
[89] Bryers R. Influence of segregated mineral matter in coal on slagging. Mineral matter and ash in coal 1986: 353–74. ISBN: 978-0841209596.
[90] Frandsen FJ, Moiraghi L, van Lith SC, Lin W, Skytte R, Zevenhoven M, Skrifvars BJ. Residual ash formation during oxidative thermal conversion of spruce and bark under lab-scale fixed-bed conditions. Impacts of Fuel Quality on Power Production Conference; 2006.
[91] Quann RJ, Sarofim AF. Vaporization of refractory oxides during pulverized coal combustion. Symposium (International) on Combustion 1982;19:1429–40.
[92] Quann RJ, Neville M, Janghorbani M, Mims CA, Sarofim AF. Mineral matter and trace-element vaporization in a laboratory-pulverized coal combustion system. Environ Sci Technol 1982;16(11):776–81.
[93] Helble JM, Neville M, Sarofim AF. Aggregate formation from vaporized ash during pulverized coal combustion. Symposium (International) on Combustion 1988;21:411–7.
[94] Mitchell RE, Akanetuk AE. The impact of fragmentation on char conversion during pulverized coal combustion. Symposium (International) on Combustion 1996;26:3137–44.
[95] Sarofim AF, Howard JB, Padia AS. The physical transformation of the mineral matter in pulverized coal under simulated combustion conditions. Combust Sci Technol 1977;16(3-6):187–204.
[96] Baxter LL. Char fragmentation and fly ash formation during pulverized-coal combustion. Combust Flame 1992;90(2):174–84.
[97] Goodarzi F, Sanei H. Plerosphere and its role in reduction of emitted fine fly ash particles from pulverized coal-fired power plants. Fuel 2009;88(2):382–6.
[98] Pyykönen J. Computational simulation of aerosol behaviour. VTT Technical Research Centre of Finland; 2002. PhD thesis, ISBN: 9513859789.

[99] Pyykönen J, Jokiniemi J. Modelling alkali chloride superheater deposition and its implications. Fuel Process Technol 2003;80(3):225–62.
[100] Jöller M, Brunner T, Obernberger I. Modeling of aerosol formation during biomass combustion in grate furnaces and comparison with measurements. Energy Fuels 2005;19(1):311–23.
[101] Brunner T. Aerosols and coarse fly ash in biomass fixed bed combustion. TU Eindhoven; 2006. PhD thesis, ISBN: 3-9501980-3-2.
[102] Jöller M, Brunner T, Obernberger I. Modeling of aerosol formation during biomass combustion for various furnace and boiler types. Fuel Process Technol 2007;88(11):1136–47.
[103] Leppänen A, Tran H, Taipale R, Välimäki E, Oksanen A. Numerical modeling of fine particle and deposit formation in a recovery boiler. Fuel 2014;129:45–53.
[104] Wilemski G, Srinivasachar S. Prediction of ash formation in pulverized coal combustion with mineral distribution and char fragmentation. In: Proceedings of the Engineering Foundation International Conference, Solihull, England; 1993. ISBN: 978-1560322931.
[105] Wu H, Wall TF, Liu G, Bryant G. Ash liberation from included minerals during combustion of pulverized coal: the relationship with char structure and burnout. Energy Fuels 1999;13(6):1197–202.
[106] Nowok JW, Hurley JP, Stanley DC. Local structure of lignitic coal ash slag and its effect on viscosity. Energy Fuels 1993;7(6):1135–40.
[107] Tu CM, Davis H, Hottel HC. Combustion rate of carbon-combustion of spheres in flowing gas streams. Ind Eng Chem 1934;26(7):749–57.
[108] Kerstein AR, Niksa S. Fragmentation during carbon conversion: predictions and measurements. Symposium (International) on Combustion 1985;20:941–9.
[109] Kerstein AR, Edwards BF. Percolation model for simulation of char oxidation and fragmentation time-histories. Chem Eng Sci 1987;42(7):1629–34.
[110] Baxter LL. Char fragmentation and fly ash formation during pulverized-coal combustion. Combust Flame 1992;90(2):174–84.
[111] Zhang X, Dukhan A, Kantorovich II, Bar-Ziv E. Fragmentation of highly porous char particles burning in regime I. Combust Flame 1996;106(1):203–6.
[112] Dacombe PJ, Hampartsoumian E, Pourkashanian M. Fragmentation of large coal particles in a drop-tube furnace. Fuel 1994;73(8):1365–7.
[113] Feng B, Bhatia SK. Percolative fragmentation of char particles during gasification. Energy Fuels 2000;14(2):297–307.
[114] Senneca O, Urciuolo M, Chirone R, Cumbo D. An experimental study of fragmentation of coals during fast pyrolysis at high temperature and pressure. Fuel 2011;90(9):2931–8.
[115] Kantorovich II, Bar-Ziv E. Role of the pore structure in the fragmentation of highly porous char particles. Combust Flame 1998;113(4):532–41.
[116] Srinivasachar S, Toqan MA, Beer JM, Ettouney HM. Percolation model for coal char particle combustion and fragmentation. Combust Sci Technol 1988;57(1-3):55–70.
[117] Kreutzkam B, Wieland C, Spliethoff H. Improved numerical prediction of ash formation and deposition using a novel developed char fragmentation model. Fuel 2012;98:103–10.
[118] Shah KV, Cieplik MK, Betrand CI, van de Kamp WL, Vuthaluru HB. A kinetic-empirical model for particle size distribution evolution during pulverised fuel combustion. Fuel 2010;89(9):2438–47.
[119] Lin L, Strand M. Investigation of the intrinsic CO2 gasification kinetics of biomass char at medium to high temperatures. Appl Energy 2013;109:220–8.
[120] Lin L, Morgella M, Strand M. Study on char fragmentation during biomass gasification in bubbling fluidized bed. 23rd European Biomass Conference and Exhibition 2015: 652–5.
[121] Syred N, Kurniawan K, Griffiths T, Gralton T, Ray R. Development of fragmentation models for solid fuel combustion and gasification as subroutines for inclusion in CFD codes. Fuel 2007;86(14):2221–31.
[122] Costa FF, Wang G, Costa M. Combustion kinetics and particle fragmentation of raw and torrified pine shells and olive stones in a drop tube furnace. Proc Combust Inst 2015;35(3):3591–9.
[123] Costa FF, Costa M. Evaluation of particle fragmentation of raw and torrified biomass in a drop tube furnace. Energy Procedia 2015;66:277–80.
[124] Sudhakar DR, Reddy KS, Kolar AK, Leckner B. Fragmentation of wood char in a laboratory scale fluidized bed combustor. Fuel Process Technol 2008;89(11):1121–34.
[125] Scala F, Chirone R. Combustion and attrition of biomass chars in a fluidized bed. Energy Fuels 2006;20(1):91–102.
[126] No SY, Syred N. Thermal stress and pressure effects on coal-particle fragmentation and burning behaviour in a cyclone combustor. J Inst Energy 1990;63:195–202.
[127] Gajewski W, Kosowska M, Otwinowski H. Fragmentation of coal particles - thermal fragmentation of coal particles. Powder Handling Process 2002;14(3):226–8.
[128] Dacombe P, Pourkashanian M, Williams A, Yap L. Combustion-induced fragmentation behavior of isolated coal particles. Fuel 1999;78(15):1847–57.
[129] Chirone R, Massimilla L. Primary fragmentation of a coal in fluidized bed combustion. Symposium (International) on Combustion 1989;22:267–77.
[130] Solomon PR, Beer JM. Fundamentals of coal conversion and relation to coal properties. Energy 1987;12(8-9):837–62.
[131] Salatino P, Miccio F, Massimilla L. Combustion and percolative fragmentation of carbons. Combust Flame 1993;95(4):342–50.
[132] Walsh PM, Li T. Fragmentation and attrition of coal char particles undergoing collisions during combustion at temperatures from 900 to 1100 K. Combust Flame 1994;99(3):749–57.
[133] Senneca O, Urciuolo M, Chirone R. A semidetailed model of primary fragmentation of coal. Fuel 2013;104:253–61.
[134] Sreekanth M, Prasad BVSSS, Kolar AK. Stresses in a cylindrical wood particle undergoing devolatilization in a hot bubbling fluidized bed. Energy Fuels 2008;22(3):1549–59.
[135] Werkelin J, Skrifvars BJ, Hupa M. Ash-forming elements in four Scandinavian wood species. Biomass Bioenergy 2005;29(6):451–66.
[136] Arvelakis S, Vourliotis P, Kakaras E, Koukios EG. Effect of leaching on the ash behavior of wheat straw and olive residue during fluidized bed combustion. Biomass Bioenergy 2001;20:459–70.
[137] Arvelakis S, Jensen PA, Dam-Johansen K. Simultaneous thermal analysis (STA) on ash from high-alkali biomass. Energy Fuels 2004;18:1066–76.
[138] Flagan RC, Friedlander SK. Particle formation in pulverized coal combustion - a review. Recent Developments in Aerosol Science. Wiley; 1978.
[139] Damle AS, Ensor DS, Ranade MB. Coal combustion aerosol formation mechanisms: a review. Aerosol Sci Technol 1981;1:119–33.
[140] McCain JD, Gooch JP, Smith WB. Results of field measurments of industrial particulate sources and electrostatic precipitator performance. J Air Pollut Control Assoc 1975;25:117–21.
[141] Schmidt EW, Gieseke JA, Allen JM. Size distribution of fine-particulate emissions from a coal-fired power plant. Atmos Environ 1976;10:1065–9.
[142] Ensor DS, Lawless PA, Damle AS, Sparks LE. Evaluation of the United McGill Electrostatic Precipitator. 3rd Symposium on Transfer and Utilization of Particulate Control Technology, Orlando, USA. EPA; 1981.
[143] Ensor DS, Cowen S, Shendrikar A, Woffinden G, Pearson R, Scheck R. Kramer station fabric filter evaluation. Report CS-1669. EPRI; 1981.
[144] Nussbaumer T, Hasler P. Bildung und Eigenschaften von Aerosolen aus Holzfeuerungen. Holz als Roh- und Werkstoff 1999;57:13–22.
[145] Hüglin C. New applications of aerosol photoemission: Characterisation of wood combustion particles and time resolved thermal desorption studies. ETH Zürich; 1996. PhD thesis Nr. 11975.
[146] Hüglin CH, Gaegauf CH, Künzel S, Burtscher H. Characterization of wood combustion particles: morphology, mobility, and photoelectric activity. Environ Sci Technol 1997;31(12):3439–47.
[147] Wiinikka H, Gebart R. The influence of fuel type on particle emissions in combustion of biomass pellets. Combust Sci Technol 2005;177(4):741–63.
[148] Mohr M, Schmatloch V. Charakterisierung der Partikelemission aus Stückholzfeuerungen mit modernen Messtechniken, 5. Holzenergie-Symposium. ETH Zürich; 1998. p. 75–84.
[149] Christensen KA, Stenholm M, Livbjerg H. The formation of submicron aerosol particles, HCl and SO2 in straw-fired boilers. J Aerosol Sci 1998;29(4):421–44.
[150] Nielsen LB. Combustion aerosols from potassium-containing fuels. Technical University of Denmark; 1998, PhD thesis.
[151] Pagels J, Strand M, Rissler J, Szpila A, Gudmundsson A, Bohgard M, Lillieblad L, Sanati M, Swietlicki E. Characteristics of aerosol particles formed during grate combustion of moist forest residue. J Aerosol Sci 2003;34:1043–59.
[152] Johansson LS, Tullin C, Leckner B, Sjövall P. Particle emissions from biomass combustion in small combustors. Biomass Bioenergy 2003;25:435–46.
[153] Lillieblad L, Szpila A, Strand M, Pagels J, Rupar-Gadd K, Gudmundsson A, Swietlicki E, Bohgard M, Sanati M. Boiler operation influence on the emissions of submicrometer-sized particles and polycyclic aromatic hydrocarbons from biomass-fired grate boilers. Energy Fuels 2004;18:410–7.
[154] Wiinikka H. High temperature aerosol formation and emission minimisation during combustion of wood pellets. Lulea University of Technology; 2005. Phd thesis, ISNN: 1402-1544.
[155] Kauppinen EI, Pakkenen TA. Coal combustion aerosols: a field study. Enviorn Sci Technol 1990;24:1811–8.
[156] Lind T, Valmari T, Kauppinen E, Nilsson K, Sfiris G, Maenhaut W. Ash formation mechanisms during combustion of wood in circulating fluidized beds. In: Proceedings of the Combustion Institute, 28; 2000. p. 2287–95.
[157] Jöller M, Brunner T, Obernberger I. Modeling of aerosol formation during biomass combustion for various furnace and boiler types. Fuel Process Technol 2007;88:1136–47.
[158] Hinds WC. Aerosol technology: properties, behavior, and measurement of airborne particles. John Wiley & Sons; 2012. ISBN: 0-471-19410-7.
[159] Hasler P, Nussbaumer T. Partikelgrößenverteilung bei der Verbrennung und Vergasung von Biomasse, Bundesamt für Energie, Bern, Switzerland. 1997.
[160] Brunner T, Fluch J, Obernberger I, Warnecke R. Investigations of aerosol formation pathways during MSW combustion based on high-temperature impactor measurements. Fuel Process Technol 2013;105:154–60.
[161] Mikkanen P. Fly ash particle formation in kraft recovery boilers; PhD Thesis, ISBN: 951-38-5584-8.
[162] Jokiniemi JK, Lazaridis M, Lehtinen KEJ, Kauppinen EI. Numerical simulation of vapour-aerosol dynamics in combustion processes. J Aerosol Sci 1994;25(3):429–46.
[163] Bailey JG, Tate A, Diessel CF, Wall TF. A char morphology system with applications to coal combustion. Fuel 1990;69(2):225–39.
[164] Benfell KE, Liu GS, Roberts DG, Harris DJ, Lucas JA, Bailey JG, Wall TF. Modeling char combustion: the influence of parent coal petrography and pyrolysis pressure on the structure and intrinsic reactivity of its char. Proc Combust Inst 2000;28(2):2233–41.
[165] Helble JJ. Mechanisms of ash particle formation and growth during pulverized coal combustion. MIT; 1987, PhD thesis.
[166] Linak WP, Miller CA, Wendt JOL. Comparison of particle size distributions and elemental partitioning from the combustion of pulverized coal and residual fuel oil. J Air Waste Manage Assoc 2000;50(8):1532–44.

[167] Seames WS. An initial study of the fine fragmentation fly ash particle mode generated during pulverized coal combustion. Fuel Process Technol 2003;81(2):109–25.
[168] Helble JJ, Sarofim AF. Influence of char fragmentation on ash particle size distributions. Combust Flame 1989;76(2):183–96.
[169] Liu G, Wu H, Gupta RP, Lucas JA, Tate AG, Wall TF. Modeling the fragmentation of non-uniform porous char particles during pulverized coal combustion. Fuel 2000;79(6):627–33.
[170] Sutugin AG, Fuchs NA. Formation of condensation aerosols under rapidly changing environmental conditions: theory and method of calculation. J Aerosol Sci 1970;1(4):287–93.
[171] Friedlander SK. Smoke, dust and haze: fundamentals of aerosol behavior. New York: Wiley-Interscience; 1977. ISBN: 978-0471014683
[172] McNallan MJ, Yurek GJ, Elliott JF. The formation of inorganic particulates by homogeneous nucleation in gases produced by the combustion of coal. Combust Flame 1981;42:45–60.
[173] Fuchs N. The mechanics of aerosols. Dover Publications; 1989. ISBN: 978-0486660554.
[174] Wieland C. Simulation der Feinstaubentstehung bei der Kohlenstaubverbrennung. TU München, Dr. Hut Verlag; 2015. PhD thesis, ISBN: 978-3843924016.
[175] Balan G. Untersuchungen des Partikelverhaltens und der Hochtemperatur-Chlorkorrosion bei der Flugstromverbrennung mit dotierten Brennstoffen. TU München, Dr. Hut Verlag; 2014. PhD thesis, ISBN: 978-3843920094.
[176] Jöller M. Modelling of aerosol formation and behaviour in fixed-bed biomass combustion systems. TU Graz; 2008, PhD thesis.
[177] Mitchell RS, Gluskoter HJ. Mineralogy of ash of some American coals: variations with temperature and source. Fuel 1976;55(2):90–6.
[178] Magda A. Modelling of mineral matter transformation and deposition in furnaces. TU Braunschweig, Shaker; 2012. PhD thesis, ISBN: 978-3844015447.
[179] Srinivasachar S, Helble JJ, Boni AA, Shah N, Huffman GP, Huggins FE. Mineral behavior during coal combustion 2. Illite transformations. Prog Energy Combust Sci 1990;16(4):293–302.
[180] Srinivasachar S, Helble JJ, Boni AA. Mineral behavior during coal combustion 1. Pyrite transformations. Prog Energy Combust Sci 1990;16(4):281–92.
[181] Ten Brink HM, Smart JP, Vleeskens JM, Williamson J. Flame transformations and burner slagging in a 2.5 MW furnace firing pulverized coal: 1. flame transformations. Fuel 1994;73(11):1706–11.
[182] Srinivasachar S, Boni AA. A kinetic model for pyrite transformations in a combustion environment. Fuel 1989;68(7):829–36.
[183] Yan L, Gupta R, Wall TF. Fragmentation behavior of pyrite and calcite during high-temperature processing and mathematical simulation. Energy Fuels 2001;15(2):389–94.
[184] Božić O. Numerische Simulation der Mineralumwandlung in Kohlenstaubfeuerungen. TU Braunschweig, Shaker; 2003. PhD thesis, ISBN: 978-3832214005.
[185] Kleinhans U, Halama S, Spliethoff H. Role of gasification reactions during pulverized solid fuel combustion: char structural and kinetic parameters for a detailed char combustion model for pre-treated biomass and coal. Combust Flame 2017;184:117–35.
[186] Babat S, Spörl R, Maier J, Scheffknecht G. Investigation of deposit formation and its characterization for a pulverized bituminous coal power plant. Fuel Process Technol 2016;141:225–34.
[187] Goodarzi F. Morphology and chemistry of fine particles emitted from a Canadian coal-fired power plant. Fuel 2006;85(3):273–80.
[188] Kleinhans U. Fly ash formation and deposition during pulverized fuel combustion: numerical and experimental investigations. TU München, Dr. Hut Verlag; 2017. PhD thesis, ISBN: 978-3843931205.
[189] Valmari T, Kauppinen EI, Kurkela J, Jokiniemi JK, Sfiris G, Revitzer H. Fly ash formation and deposition during fluidized bed combustion of willow. J Aerosol Sci 1998;29(4):445–59.
[190] Wang S, Baxter L, Fonseca F. Biomass fly ash in concrete: SEM, EDX and ESEM analysis. Fuel 2008;87(3):372–9.
[191] Wu H, Glarborg P, Frandsen FJ, Dam-Johansen K, Jensen PA. Dust-firing of straw and additives: ash chemistry and deposition behavior. Energy Fuels 2011;25(7):2862–73.
[192] Xu M, Yu D, Yao H, Liu X, Qiao Y. Coal combustion-generated aerosols: formation and properties. Proc Combust Inst 2011;33:1681–97.
[193] Külaots I, Hurt RH, Suuberg EM. Size distribution of unburned carbon in coal fly ash and its implications. Fuel 2004;83(2):223–30.
[194] Nussbaumer T, Czasch C, Klippel N, Johansson L, Tullin C. Particle emissions from biomass combustion in IEA countries. International Energy Agency (IEA) Bioenergy Task, 32; 2008. ISBN: 3-908705-18-5.
[195] Klippel N, Nussbaumer T. Einfluss der Betriebsweise auf die Partikelemissionen von Holzöfen, Bundesamt für Energie und Bundesamt für Umwelt, Schlussbericht, Zürich Switzerland, 2007, ISBN: 3-908705-12-6.
[196] Xu M, Yu D, Yao H, Liu X, Qiao Y. Coal combustion-generated aerosols: formation and properties. Proc Combust Inst 2011;33:1681–97.
[197] Chimenos JM, Segarra M, Fernández MA, Espiell F. Characterization of the bottom ash in municipal solid waste incinerator. J Hazard Mater 1999;64(3):211–22.
[198] Hasler P, Nussbaumer T. Particle size distribution of the fly ash from biomass combustion. Biomass for Energy and industry, 10th European Conference and Technology Exhibition. Würzburg Germany; 1998.
[199] Williams A, Jones JM, Ma L, Pourkashanian M. Pollutants from the combustion of solid biomass fuels. Prog Energy Combust Sci 2012;38:113–37.
[200] Raask E. Cenospheres in pulverized-fuel ash. J Inst Fuel 1968;41:339–44.
[201] Schulze K, Hofmeister G, Jöller M, Scharler R, Obernberger I, Korbee R, Cieplik M. Development and evaluation of a flexible model for CFD simulation of ash deposit formation in biomass fired boilers. In: Proceedings Impacts of Fuel Quality on Power Production Conf., Snowbird USA; 2007.
[202] Mueller C, Selenius M, Theis M, Skrifvars BJ, Backman R, Hupa M, Tran H. Deposition behaviour of molten alkali-rich fly ashes—development of a submodel for CFD applications. Proc Combust Inst 2005;30(2):2991–8.
[203] Lindberg D, Niemi J, Engblom M, Yrjas P, Laurén T, Hupa M. Effect of temperature gradient on composition and morphology of synthetic chlorine-containing biomass boiler deposits. Fuel Process Technol 2016;141:285–98.
[204] Lokare SS, Dunaway JD, Moulton D, Rogers D, Tree DR, Baxter LL. Investigation of ash deposition rates for a suite of biomass fuels and fuel blends. Energy Fuels 2006;20(3):1008–14.
[205] Barker B, Casaday B, Shankara P, Ameri A, Bons JP. Coal ash deposition on nozzle guide vanes—part II: computational modeling. J Turbomach 2013;135(1):011015.
[206] Weber R, Schaffel-Mancini N, Mancini M, Kupka T. Fly ash deposition modelling: requirements for accurate predictions of particle impaction on tubes using RANS-based computational fluid dynamics. Fuel 2013;108:586–96.
[207] Samms JA, Watt JD. Physical mechanisms in the formation of boiler deposits. Mon Bull Br Coal Utilisation Res Ass 1966;30:225–59.
[208] Saffman PG. The lift on a small sphere in a slow shear flow. J Fluid Mech 1965;22(02):385–400.
[209] Waldmann L, Schmitt KH. Thermophoresis and diffusiophoresis of aerosols. Aerosol Science & Technology. New York USA: Academic Press; 1966. p. 137–62.
[210] Caporaloni M, Tampieri F, Trombetti F, Vittori O. Transfer of particles in nonisotropic air turbulence. J Atmos Sci 1975;32(3):565–8.
[211] Baxter LL. Ash deposition during biomass and coal combustion: a mechanistic approach. Biomass Bioenergy 1993;4(2):85–102.
[212] Kleinhans U, Rück R, Schmid S, Haselsteiner T, Spliethoff H. Alkali vapor condensation on heat exchanging surfaces: laboratory-scale experiments and a mechanistic CFD modeling approach. Energy Fuels 2016;30(11):9793–800.
[213] Laursen K, Frandsen F, Larsen OH. Ash deposition trials at three power stations in Denmark. Energy Fuels 1998;12(2):429–42.
[214] Young J, Leeming A. A theory of particle deposition in turbulent pipe flow. J Fluid Mech 1997;340:129–59.
[215] Israel R, Rosner DE. Use of a generalized Stokes number to determine the aerodynamic capture efficiency of non-Stokesian particles from a compressible gas flow. Aerosol Sci Technol 1982;2(1):45–51.
[216] Guha A. Transport and deposition of particles in turbulent and laminar flow. Annu Rev Fluid Mech 2008;40:311–41.
[217] Friedlander SK, Johnstone HH. Deposition of suspended particles from turbulent gas streams. Industrial & Engineering Chemistry 1957;49(7):1151–6.
[218] Schwendiman LC, Postma AK. Turbulent deposition in sampling lines. Rep. Tech. Inf. Div. TID-7628, USAEC 118. 1962.
[219] Wells AC, Chamberlain AC. Transport of small particles to vertical surfaces. Br J Appl Phys 1967;18(12):1793.
[220] Sehmel GA. Aerosol deposition from turbulent airstreams in vertical conduits. Report BNWL-578, Richland, Washington, USA. Batelle Northwest Laboratory; 1968.
[221] Liu BYH, Agarwal JK. Experimental observation of aerosol deposition in turbulent flow. J Aerosol Sci 1974;5(2):145–55.
[222] Richter S. Numerische Simulation der Flugaschedeposition in kohlestaubgefeuerten Dampferzeugern. University of Stuttgart, VDI-Verlag; 2002. PhD thesis, ISBN: 978-3183501069.
[223] Brun RJ, Lewis WM, Perkins PJ, Serafini JS. Impingement of cloud droplets on a cylinder and procedure for measuring liquid-water content and droplet sizes in supercooled clouds by rotating multicylinder method. Report 1215. NACA; 1955.
[224] Wessel RA, Righi J. Generalized correlations for inertial impaction of particles on a circular cylinder. Aerosol Sci Technol 1988;9(1):29–60.
[225] VDI Heat Atlas, 2nd edition, Berlin and New York, USA: Springer; 2010. ISBN: 978-3540778769.
[226] Haugen NEL, Kragset S. Particle impaction on a cylinder in a crossflow as function of stokes and reynolds numbers. J Fluid Mech 2010;661:239–61.
[227] Young JB. Thermophoresis of a spherical particle: reassessment, clarification, and new analysis. Aerosol Sci Technol 2011;45(8):927–48.
[228] Tyndall J. On dust and disease. Proc R Inst 1890;6:1–14.
[229] Cawood W. The movement of dust or smoke particles in a temperature gradient. Trans Faraday Soc 1936;32:1068–73.
[230] Walker KL, Homsy GM, Geyling FT. Thermophoretic deposition of small particles in laminar tube flow. J Colloid Interface Sci 1979;69(1):138–47.
[231] Cameron JH, Goerg-Wood K. Role of thermophoresis in the deposition of fume particles resulting from the combustion of high inorganic containing fuels with reference to kraft black liquor. Fuel Process Technol 1999;60(1):49–68.
[232] GökoĞlu SA, Rosner DE. Correlation of thermophoretically-modified small particle diffusional deposition rates in forced convection systems with variable properties, transpiration cooling and/or viscous dissipation. Int J Heat Mass Transfer 1984;27(5):639–46.
[233] Healy DP, Young JB. An experimental and theoretical study of particle deposition due to thermophoresis and turbulence in an annular flow. Int J Multiphase Flow 2010;36(11):870–81.
[234] Epstein PS. Zur Theorie des Radiometers. Zeitschrift für Physik 1929;54(7-8):537–63.

[235] Maxwell JC. On stresses in rarified gases arising from inequalities of temperature. Philos Trans R Soc Lond 1879: 231–56.
[236] Waldmann L. Über die Kraft eines inhomogenen Gases auf kleine suspendierte Kugeln. Zeitschrift Naturforschung Teil A 1959;14:589–99.
[237] Talbot L, Cheng RK, Schefer RW, Willis DR. Thermophoresis of particles in a heated boundary layer. J Fluid Mech 1980;101(4):737–58.
[238] Brock JR. On the theory of thermal forces acting on aerosol particles. J Colloid Sci 1962;17:768–80.
[239] Beresnev S, Chernyak V. Thermophoresis of a spherical particle in a rarefied gas: numerical analysis based on the model kinetic equations. Phys Fluids 1995;7:1743–56.
[240] Yamamoto K, Ishihara Y. Thermophoresis of a spherical particle in a rarefied gas of a transition regime. Phys Fluids 1988;31:3618–24.
[241] Dwyer HA. Thirteen–moment theory of the thermal force on a spherical particle. Phys Fluids 1967;10(5):976–84.
[242] Zhan Z, Fry AR, Wendt JOL. Deposition of coal ash on a vertical surface in a 100 kW downflow laboratory combustor: a comparison of theory and experiment. In: Proceedings of the Combustion Institute, 36; 2017. p. 2091–101.
[243] Kleinhans U, Barnerßoi M, Babat S, Wieland C, Spliethoff H. The role of thermophoresis during deposit build-up on a superheater tube. Heat Exchanger Fouling and Cleaning Conference, Enfield, Ireland; 2015. p. 5–10.
[244] Sinquefield SA. Deposition of sub-micron and micron-sized particles from combustion of black liquor. Oregon State University; 1998, PhD thesis.
[245] Lutro HF. The effect of thermophoresis on the particle deposition on a cylinder. Norwegian University of Science and Technology; 2012 Master thesis.
[246] Rezaei HR, Gupta RP, Bryant GW, Hart JT, Liu GS, Bailey CW, Wall TF, Miyamae S, Makino K, Endo Y. Thermal conductivity of coal ash and slags and models used. Fuel 2000;79(13):1697–710.
[247] Derjaguin BV, Storozhilova AI, Rabinovich YI. Experimental verification of the theory of thermophoresis of aerosol particles. J Colloid Interface Sci 1966;21(1):35–58.
[248] Prodi F, Santachiara G, Prodi V. Measurements of thermophoretic velocities of aerosol particles in the transition region. J Aerosol Sci 1979;10(4):421–5.
[249] Li W, James DE. Measurement of the thermophoretic force by electrodynamic levitation: microspheres in air. J Aerosol Sci 1995;26(7):1063–83.
[250] Mims CA, Neville M, Quann RJ, House K, Sarofim AF. Laboratory studies of mineral matter vaporization during coal combustion, emission control from stationary power sources: technical, economic, and environmental assessments. AIChE Symp Ser 1980;201(76):188–94.
[251] Dayton DC, French RJ, Milne TA. Direct observation of alkali vapor release during biomass combustion and gasification. 1. Application of molecular beam/mass spectrometry to switchgrass combustion. Energy Fuels 1995;9(5):855–65.
[252] Wilke CR, Lee CY. Estimation of diffusion coefficients for gases and vapors. Ind Eng Chem 1955;47(6):1253–7.
[253] Tomeczek J, Wacławiak K. Two-dimensional modelling of deposits formation on platen superheaters in pulverized coal boilers. Fuel 2009;88(8):1466–71.
[254] Baehr HD, Stephan K. Wärme- und Stoffübertragung. Springer; 2004. ISBN: 9783642365584.
[255] Scandrett LA, Clift R. The thermodynamics of alkali removal from coal-derived gases. J Inst Energy 1984;57(433):391–7.
[256] Haselsteiner T. Abkühlverhalten von Alkalien bei der Kohlevergasung. TU München, Dr. Hut Verlag; 2012. PhD thesis, ISBN: 978-3843907521.
[257] Nielsen HP, Baxter LL, Sclippab G, Morey C, Frandsen FJ, Dam-Johansen K. Deposition of potassium salts on heat transfer surfaces in straw-fired boilers: a pilot-scale study. Fuel 2000;79(2):131–9.
[258] Akbar S, Schnell U, Scheffknecht G. Modelling potassium release and the effect of potassium chloride on deposition mechanisms for coal and biomass-fired boilers. Combust Theory Modell 2010;14(3):315–29.
[259] Skrifvars BJ, Hupa M, Backman R, Hiltunen M. Sintering mechanisms of FBC ashes. Fuel 1994;73(2):171–6.
[260] Glarborg P, Marshall P. Mechanism and modeling of the formation of gaseous alkali sulfates. Combust Flame 2005;141(1–2):22–39.
[261] Aho M, Silvennoinen J. Preventing chlorine deposition on heat transfer surfaces with aluminium-silicon rich biomass residue and additive. Fuel 2004;83(10):1299–305.
[262] Aho M, Ferrer E. Importance of coal ash composition in protecting the boiler against chlorine deposition during combustion of chlorine-rich biomass. Fuel 2005;84(2–3):201–12.
[263] Lindner ER, Wall TF. An experimental study of sodium-ash reaction during combustion of pulverized coal. In: Proceedings mineral matter and ash deposition from coal, Fourth Engineering Foundation Conference. New York, USA: Engineering Foundation; 1988. p. 321–30.
[264] Guha A. A unified Eulerian theory of turbulent deposition to smooth and rough surfaces. J Aerosol Sci 1997;28(8):1517–37.
[265] Zbogar A, Frandsen F, Jensen PA, Glarborg P. Shedding of ash deposits. Prog Energy Combust Sci 2009;35(1):31–56.
[266] Stitt S, Junker H, Baxter LL. Optimisation of deposit removal in biofueled boilers: review of control systems, technologies and mechanisms, Eltra: Haan Germany, 2002, Project 3144.
[267] van Beek MC. Gas-side fouling in heat-recovery boilers. TU Eindhoven; 2001. PhD thesis, ISBN: 90-386-2632-0.
[268] van Beek MC, Rindt CCM, Wijers JG, van Steenhoven AA. Rebound characteristics for 50-um particles impacting a powdery deposit. Powder Technol 2006;165(2):53–64.
[269] Steadman EN, Erickson TA, Folkedahl BC, Brekke DW. Coal and ash characterization: digital image analysis applications. Engineering Foundation Conference on Inorganic Transformations and Ash Deposition during Combustion, ASME; 1991. p. 147–64.
[270] Smouse SM, Wagoner CL. Deposit initiation via thermophoresis. Part 2-experimental verification of hypothesis using a simulated superheater tube. Engineering Foundation Conference on Inorganic Transformations and Ash Deposition during Combustion, Palm Beach USA; 1991.
[271] Effenberger H. Dampferzeugung. Springer-Verlag; 1999. ISBN: 978-3642571664.
[272] Wynnyckyj J, Marr R, Rhodes E. Integrated monitoring system for control of fouling in coal-fired boilers. Mineral Matter and Ash Deposition from Coal, Santa Barbara, USA; 1990. p. 401.
[273] Zbogar A, Frandsen FJ, Jensen PA, Glarborg P. Heat transfer in ash deposits: a modelling tool-box. Prog Energy Combust Sci 2005;31(5):371–421.
[274] Skorupska N. Coal specifications - impact on power station performance. London, UK: IEA Coal Research; 1993. PhD thesis, ISBN: 978-9290292104.
[275] Wibberley L. Effect of coal composition on deposit formation in PF fired boilers. Australia: Institute of Coal Research, University of Newcastle; 1985, PhD thesis.
[276] Jackson PJ. Mineral matter in pulverized coal combustion. Fundamentals of the physical-chemistry of pulverized coal combustion. Springer; 1987. p. 269–87. ISBN: 978-9024735730.
[277] Heap MP, Kramlich JC, Pershing DW, Pohl DW, Richter WF, Seeker WR. Effects of coal quality on power plant performance and costs. Electric Power Research Institute (EPRI); 1986. Project 2256-1
[278] Wagoner CL, Yan XX. Ash impaction changes the shape of a superheater deposit with time. The Impact of Ash Deposition on Coal-Fired Power Plants, Proc. United Engineering Foundation International Conference, Birmingham, UK; 1993.
[279] Sondreal EA, Tufte PH, Beckering W. Ash fouling in the combustion of low rank western U. S. coals. Combust Sci Technol 1977;16:95–110.
[280] Hansen LA, Nielsen HP, Frandsen FJ, Dam-Johansen K, Hørlyck S, Karlsson A. Influence of deposit formation on corrosion at a straw-fired boiler. Fuel Process Technol 2000;64:189–2009.
[281] Kaufmann H, Nussbaumer T, Baxter L, Yang N. Deposit formation on a single cylinder during combustion of herbaceous biomass. Fuel 2000;79:141–51.
[282] Theis M, Skrifvars BJ, Hupa M, Tran H. Fouling tendency of ash resulting from burning mixtures of biofuels. Part 1: deposition rates. Fuel 2006;85:1125–30.
[283] Tobiasen L, Skytte R, Pedersen LS, Pedersen ST, Lindberg MA. Deposit characteristic after injection of additives to a Danish straw-fired suspension boiler. Fuel Process Technol 2007;88:1108–17.
[284] Bashir MS, Jensen PA, Frandsen F, Wedel S, Dam-Johansen K, Wadenbäck J, Pedersen ST. Ash transformation and deposit build-up during biomass suspension and grate firing: Full-scale experimental studies. Fuel Process Technol 2012;97:93–106.
[285] Kupka T, Zając K, Weber R. Effect of fuel type and deposition surface temperature on the growth and structure of an ash deposit collected during co-firing of coal with sewage sludge and sawdust. Energy Fuels 2009;23(7):3429–36.
[286] Weber R, Kupka T, Zając K. Jet flames of a refuse derived fuel. Combust Flame 2009;156:922–7.
[287] Weber R, Poyraz Y, Beckmann AM, Brinker S. Combustion of biomass in jet flames. Proc Combust Inst 2015;35:2749–58.
[288] Schumacher G, Juniper L. Practical aspects of slagging in operating boilers. Impact of Fuel Quality on Power Production Conference, Snowbird USA; 2012.
[289] Jensen PA, Stenholm M, Hald P. Deposition investigation in straw-fired boilers. Energy Fuels 1997;11:1048–55.
[290] Thornton C, Ning Z. A theoretical model for the stick/bounce behaviour of adhesive, elastic-plastic spheres. Powder Technol 1998;99(2):154–62.
[291] Wain SE, Livingston WR, Sanyal A, Williamson J. Thermal and mechanical properties of boiler slags of relevance to sootblowing. Inorganic Transformations and Ash Deposition during Combustion, Palm Coast USA; 1991459–70.
[292] Marx JW, Sivertsen JM. Temperature dependence of the elastic moduli and internal friction of silica and glass. J Appl Phys 1953;24(1):81–7.
[293] Wachtman JB, Lam DG. Young's modulus of various refractory materials as a function of temperature. J Am Ceram Soc 1959;42(5):254–60.
[294] Spinner S, Cleek GW. Temperature dependence of Young's modulus of vitreous germania and silica. J Appl Phys 1960;31(8):1407–10.
[295] Frost HJ, Ashby MF. Deformation-mechanism maps: the plasticity and creep of metals and ceramics. Oxford: Pergamon Press; 1982. ISBN: 978-0080293387
[296] Matsunaga T, Kim JK, Hardcastle S, Rohatgi PK. Crystallinity and selected properties of fly ash particles. Mater Sci Eng A 2002;325(1):333–43.
[297] Ai W, Kuhlman JM. Simulation of coal ash particle deposition experiments. Energy Fuels 2011;25(2):708–18.
[298] Roberts AP, Garboczi EJ. Elastic properties of model porous ceramics. J Am Chem Soc 2000;83(12):3041–8.
[299] Vanorio T, Prasad M, Nur A. Elastic properties of dry clay mineral aggregates, suspensions and sandstones. Geophys J Int 2003;155(1):319–26.
[300] Pérez MG, Vakkilainen E, Hyppänen T. 2D dynamic mesh model for deposit shape prediction in boiler banks of recovery boilers with different tube spacing arrangements. Fuel 2015;158:139–51.
[301] Pérez MG, Vakkilainen E, Hyppänen T. Unsteady CFD analysis of kraft recovery boiler fly-ash trajectories, sticking efficiencies and deposition rates with a mechanistic particle rebound-stick model. Fuel 2016;181:408–20.
[302] Pérez MG, Vakkilainen E, Hyppänen T. Fouling growth modeling of kraft recovery boiler fume ash deposits with dynamic meshes and a mechanistic sticking approach. Fuel 2016;185:872–85.

[303] Yang X, Ingham D, Ma L, Williams A, Pourkashanian M. Predicting ash deposition behaviour for co-combustion of palm kernel with coal based on CFD modelling of particle impaction and sticking. Fuel 2016;165:41–9.
[304] Yang X, Ingham D, Ma L, Zhou H, Pourkashanian M. Understanding the ash deposition formation in Zhundong lignite combustion through dynamic CFD modelling analysis. Fuel 2017;194:533–43.
[305] Shackelford JF, Han YH, Kim S, Kwon SH. CRC materials science and engineering handbook. CRC Press; 1980. ISBN: 978-0849326967.
[306] Bale CW, Chartrand P, Degterov SA, Eriksson G, Hack K, Mahfoud RB, Melançon J, Pelton AD, Petersen S. FactSage thermochemical software and databases. Calphad 2002;26(2):189–228.
[307] Petersen S, Hack K. The thermochemistry library ChemApp and its applications. Int J Mater Res 2007;98(10):935–45.
[308] Teixeira P, Lopes H, Gulyurtlu I, Lapa N, Abelha P. Evaluation of slagging and fouling tendency during biomass co-firing with coal in a fluidized bed. Biomass Bioenergy 2012;39:192–203.
[309] Slag Atlas. 2nd edition, Stahleisen GmbH (1995), ISBN: 978-3514004573.
[310] Jak E. Prediction of coal ash fusion temperatures with the F*A*C*T thermodynamic computer package. Fuel 2002;81(13):1655–68.
[311] Masiá AAT, Buhre BJ, Gupta RP, Wall TF. Characterising ash of biomass and waste. Fuel Process Technol 2007;88(11):1071–81.
[312] Wieland C, Kreutzkam B, Balan G, Spliethoff H. Evaluation, comparison and validation of deposition criteria for numerical simulation of slagging. Appl Energy 2012;93:184–92.
[313] Hoy HR, Roberts AG, Wilkins DM. Behavior of mineral matter in slagging gasification processes. J Inst Gas Engrs 1964;5:444–69.
[314] Browning GJ, Bryant GW, Hurst HJ, Lucas JA, Wall TF. An empirical method for the prediction of coal ash slag viscosity. Energy Fuels 2003;17(3):731–7.
[315] Nicholls P, Reid WT. Viscosity of coal-ash slags. Trans ASME 1940;62:141–53.
[316] Senior CL, Srinivasachar S. Viscosity of ash particles in combustion systems for prediction of particle sticking. Energy Fuels 1995;9(2):277–83.
[317] Weymann HD. On the hole theory of viscosity, compressibility, and expansivity of liquids. Kolloid-Zeitschrift und Zeitschrift für Polymere 1962;181(2):131–7.
[318] Reid WT, Cohen P. The flow characteristics of coal-ash slags in the solidification range. Trans ASME 1944;66:83–97.
[319] Watt JD, Fereday F. Flow properties of slags formed from ashes of British coals. 1. Viscosity of homogeneous liquid slags in relation to slag composition. J Inst Fuel 1969;42(338):99–103.
[320] Bottinga Y, Weill DF. The viscosity of magmatic silicate liquids; a model calculation. Am J Sci 1972;272(5):438–75.
[321] Urbain G. Viscosity of silicate melts. Trans J Br Ceram Soc 1981;80(4):139–41.
[322] Kalmanovitch DP, Frank M. An effective model of viscosity for ash deposition phenomena. Mineral Matter and Ash Deposition from Coal, Engineering Foundation Conference; 1988. p. 89–101. ISBN: 978-0939204403.
[323] Vargas S, Frandsen FJ, Dam-Johansen K. Rheological properties of high-temperature melts of coal ashes and other silicates. Prog Energy Combust Sci 2001;27(3):237–429.
[324] Reid WT. External corrosion and deposits: boilers and gas turbines. Fuel and Energy Science Series. New York, USA: American Elsevier; 1971.
[325] Oh MS, Brooker DD, Paz EFd, Brady JJ, Decker TR. Effect of crystalline phase formation on coal slag viscosity. Fuel Process Technol 1995;44(1):191–9.
[326] Sage WL, McIlroy JB. Relationship of coal-ash viscosity to chemical composition. J Eng Power 1960;82:145–53.
[327] Song W, Dong Y, Wu Y, Zhu Z. Prediction of temperature of critical viscosity for coal ash slag. AIChE J 2011;57(10):2921–5.
[328] Janz GJ. Molten salts data as reference standards for density, surface tension, viscosity, and electrical conductance: KNO_3 and NaCl. J Phys Chem Ref Data 1980;9(4):791–830.
[329] Janz GJ, Tomkins RPT. Molten salts: Vol. 5, Part 1, additional single and multi−component salt systems. Electrical conductance, density, viscosity, and surface tension data. J Phys Chem Ref Data 1980;9(4):831–1022.
[330] Scarfe CM, Cronin DJ. Viscosity-temperature relationships of melts at 1 atm in the system diopside-albite. Am Mineral 1986;71(5-6):767–71.
[331] Dingwell DB. Shear viscosity of alkali and alkaline earth titanium silicate liquids. Am Mineral 1992;77(3-4):270–4.
[332] 2016. HVG-DGG - Hüttentechnische Vereinigung der Deutschen Glasindustrie (HVG), Deutsche Glastechnische Gesellschaft (DDG), http://www.hvg-dgg.de/fileadmin/dateien/verein/Standardglas_Ia.pdf Service and research in the field of glass.
[333] Ni J, Yu G, Guo Q, Zhou Z, Wang F. Submodel for predicting slag deposition formation in slagging gasification systems. Energy Fuels 2011;25(3):1004–9.
[334] Einstein A. Eine neue Bestimmung der Moleküldimensionen. Annalen der Physik 1906;324(2):289–306.
[335] Vand V. Viscosity of solutions and suspensions. I. Theory. J Phys Chem 1948;52(2):277–99.
[336] Sherman P. Emulsion science. London: Academic press; 1968. 217-351, ISBN: 978-0387396828.
[337] Roscoe R. The viscosity of suspensions of rigid spheres. Br J Appl Phys 1952;3(8):267–9.
[338] Quemada D. Stability of thermodynamic systems. Lecture Notes in Physics. Berlin: Springer; 1982. p. 210–47. ISBN: 978-3540115816.
[339] Annen K, Gruninger J, Stewart G. Method for extending viscosity predicted formulas. Proc Flames Res Found 1983: 1–3.
[340] Meyers MA, Chawla KK. Mechanical behavior of materials. Cambridge: Cambridge University Press; 2009. ISBN: 978-0521866750
[341] Dantzig JA, Tucker CL. Modeling in materials processing. Cambridge University Press; 2001. ISBN: 978-0521779234.
[342] Losurdo M, Spliethoff H, Kiel J. Ash deposition modeling using a visco-elastic approach. Fuel 2012;102:145–55.
[343] Song W, Tang L, Zhu X, Wu Y, Zhu Z, Koyama S. Flow properties and rheology of slag from coal gasification. 17th International Symposium on Alcohol Fuels, 89; 2010. p. 1709–15.
[344] Rezaei HR, Gupta RP, Wall TF, Miyamae S, Makino K. Modelling the initial structure of ash deposits and structure changes due to sintering. Impact of Mineral Impurities in Solid Fuel Combustion; 2002. p. 753–66. ISBN: 978-0306461262.
[345] Mills KC, Rhine JM. The measurement and estimation of the physical properties of slags formed during coal gasification: 1. Properties relevant to fluid flow. Fuel 1989;68(2):193–200.
[346] Ramé-Hart Instrument Co, 2016. Information on contact angle.
[347] Yuan Y, Lee TR. Contact angle and wetting properties. Surface science techniques. Springer; 2013. p. 3–34. ISBN: 978-3642342424.
[348] Young T. An essay on the cohesion of fluids. Philos Trans R SocLond 1805;95:65–87.
[349] Moza AK, Austin LG. Studies on slag deposit formation in pulverized coal combustors. 1. Results on the wetting and adherence of synthetic coal ash drops on steel. Fuel 1981;60(11):1057–64.
[350] Abbott MF, Austin LG. Studies on slag deposit formation in pulverized-coal combustors: 6. sticking behaviour of slag drops from three Pennsylvania steam coals. Fuel 1985;64(6):832–8.
[351] Abbott MF, Conn RE, Austin LG. Studies on slag deposit formation in pulverized-coal combustors: 5. effect of flame temperature, thermal cycling of the steel substrate and time on the adhesion of slag drops to oxidized boiler steels. Fuel 1985;64(6):827–31.
[352] Restagno F, Poulard C, Cohen C, Vagharchakian L, Léger L. Contact angle and contact angle hysteresis measurements using the capillary bridge technique. Langmuir 2009;25(18):11188–96.
[353] Bottinga Y, Weill DF. Densities of liquid silicate systems calculated from partial molar volumes of oxide components. Am J Sci 1970;269(2):169–82.
[354] Mackenzie JK, Shuttleworth R. A phenomenological theory of sintering. Proc Phys Soc Sect B 1949;62(12):833–52.
[355] Senior CL. Predicting removal of coal ash deposits in convective heat exchangers. Energy Fuels 1997;11(2):416–20.
[356] Meinel D. Vergleich und Simulation von Depositionsverhalten und Sinterprozessen bei Verschlackungen. TU München; 2012 Master thesis.
[357] Gupta RP, Wall TF, Baxter LL. Impact of mineral impurities in solid fuel combustion. Springer Science & Business Media; 1999. ISBN: 978-0306461262.
[358] Robinson AL, Buckley SG, Yang N, Baxter LL. Experimental measurements of the thermal conductivity of ash deposits: part 2. Effects of sintering and deposit microstructure. Energy Fuels 2001;15(1):75–84.
[359] Robinson AL, Buckley SG, Yang N, Baxter LL. Experimental measurements of the thermal conductivity of ash deposits: Part 1. Measurement technique. Energy Fuels 2001;15(1):66–74.
[360] Kær SK, Rosendahl LA, Baxter LL. Towards a CFD-based mechanistic deposit formation model for straw-fired boilers. Fuel 2006;85(5−6):833–48.
[361] Anderson DW, Viskanta R, Incropera FP. Effective thermal conductivity of coal ash deposits at moderate to high temperatures. J Eng Gas Turbines Power 1987;109(2):215–21.
[362] Wall TF, Bhattacharya SP, Zhang DK, Gupta RP, He X. The properties and thermal effects of ash deposits in coal-fired furnaces. Prog Energy Combust Sci 1993;19(6):487–504.
[363] Powell RW, Ho CY, Liley PE. Thermal conductivity of selected materials. Natl Stand Ref Data Ser NBS 1966;8(25).
[364] Kingery WD. Thermal conductivity: XIV, conductivity of multicomponent systems. J Am Ceram Soc 1959;42(12):617–27.
[365] Takeda M, Onishi T, Nakakubo S, Fujimoto S. Physical properties of iron-oxide scales on Si-containing steels at high temperature. Mater Trans 2009;50(9):2242–6.
[366] Ratcliffe EH. A survey of most probable values for the thermal conductivities of glasses between about −150 and 100 C, including new data on twenty two glasses and a working formula for the calculation of conductivity from composition. Glass Technol 1963;4(4):113–28.
[367] Wall TF, Lowe A, Wibberley LJ, Stewart IM. Mineral matter in coal and the thermal performance of large boilers. Prog Energy and Combust Sci 1979;5(1):1–29.
[368] Mills KC, Yuan L, Jones RT. Estimating the physical properties of slags. J South Afr Inst Min Metall 2011;111(10):649–58.
[369] Rego-Barcena S, Saari R, Mani R, El-Batroukh S, Thomson MJ. Real time, non-intrusive measurement of particle emissivity and gas temperature in coal-fired power plants. Meas Sci Technol 2007;18(11):3479–88.
[370] Boow J, Goard PR. Fireside deposits and their effect on heat transfer in a pulverized-fuel-fired boiler. III influence of physical characteristics of the deposit on its radiant emittance and effective thermal conductance. J Inst Fuel 1969;42(346):412–9.
[371] Mulcahy M, Boow J, Goard P. Fireside deposits and their effect on heat transfer in a pulverised fuel fired boiler. Part I. The radiant emittance and effective thermal conductance of the deposits. J Inst Fuel 1966;39:385–94.
[372] Huang Y, Risha GA, Yang V, Yetter RA. Effect of particle size on combustion of aluminium particle dust in air. Combust Flame 2009;159:5–13.
[373] Eckert J, Holzer JC, Ahn CC, Fu Z, Johnson WL. Melting behavior of nanocrystalline aluminum powders. Nanostruct Mater 1993;2(4):407–13.

[374] Alavi S, Thompson DL. Molecular dynamics simulations of the melting of aluminium nanoparticles. J Phys Chem A 2006;110(4):1518–23.
[375] Puri P, Yang V. Effect of particle size on melting of aluminum at nano scales. J Phys Chem C 2007;111(32):11776–83.
[376] Wronski CRM. The size dependence of the melting point of small particles of tin. Br J Appl Phys 1967;18(12):1731–7.
[377] Tolman RC. The effect of droplet size on surface tension. J Chem Phys 1949;17 (3):333–7.
[378] Wall TF, Bhattacharya SP, Baxter LL, Richards G, Harb JN. The character of ash deposits and the thermal performance of furnaces. Fuel Process Technol 1995;44(1):143–53.
[379] Nimick FB, Leith JR. A model for thermal conductivity of granular porous media. J Heat Transfer 1992;114(2):505–8.
[380] Hadley GR. Thermal conductivity of packed metal powders. Int J Heat Mass Transfer 1986;29(6):909–20.
[381] Brailsford AD, Major KG. The thermal conductivity of aggregates of several phases, including porous materials. Br J Appl Phys 1964;15(3):313.
[382] Yagi S, Kunii D. Studies on effective thermal conductivities in packed beds. AIChE J 1957;3(3):373–81.
[383] Godbee HW, Ziegler WT. Thermal conductivities of MgO, Al_2O_3, and ZrO_2 powders to 850 C. II. Theoretical. J Appl Phys 1966;37(1):56–65.
[384] Weber R, Mancini M, Schaffel-Mancini N, Kupka T. On predicting the ash behaviour using computational fluid dynamics. Fuel Process Technol 2013;105:113–28.
[385] Thornton C, Yin KK. Impact of elastic spheres with and without adhesion. Powder Technol 1991;65(1):153–66.
[386] Abd-Elhady MS, Malayeri MR. Asymptotic characteristics of particulate deposit formation in exhaust gas recirculation (EGR) coolers. Appl Therm Eng 2013;60 (1–2):96–104.
[387] Cabrejos FJ, Klinzing GE. Incipient motion of solid particles in horizontal pneumatic conveying. Powder Technol 1992;72(1):51–61.
[388] Isaak P, Tran HN, Barham D, Reeve DW. Stickiness of fireside deposits in kraft recovery units. J Pulp Pap Sci 1986;12(3):184–92.
[389] Isaak P, Tran HN, Barham D, Reeve DW. Stickiness of fireside deposits in kraft recovery units. II: the effects of potassium and surface treatment. J Pulp Pap Sci 1987;13(5):154–8.
[390] Mao T, Kuhn D, Tran H. Spread and rebound of liquid droplets upon impact on flat surfaces. AIChE J 1997;43(9):2169–79.
[391] Zhou H, Jensen PA, Frandsen FJ. Dynamic mechanistic model of superheater deposit growth and shedding in a biomass fired grate boiler. Fuel 2007;86 (10):1519–33.
[392] Hansen LA. Melting and sintering of ashes. Technical University of Denmark; 1998, PhD thesis.
[393] Kær SK. Numerical investigation of ash deposition in straw-fired boilers: Using CFD as the framework for slagging and fouling predictions. Aalborg University; 2001. PhD thesis, ISBN: 978-8789179391.
[394] Brink A, Lindberg D, Hupa M, Tejada ME, Paneru M, Maier J, Scheffknecht G, Pranzitelli A, Pourkashanian M. A temperature-history based model for the sticking probability of impacting pulverized coal ash particles. Fuel Process Technol 2016;141:210–5.
[395] Walsh PM, Sayre AN, Loehden DO, Monroe LS, Beér JM, Sarofim AF. Deposition of bituminous coal ash on an isolated heat exchanger tube: effects of coal properties on deposit growth. Prog Energy Combust Sci 1990;16(4):327–45.
[396] Liebetruth M, Görner K, Hildebrandt V. Laufzeitkopplung von CFD und thermodynamischer Realphasenmodellierung zur Darstellung der Verschlackungsneigung. VDI Berichte 2002;1664:41–52.
[397] Beckmann AM, Mancini M, Weber R, Seebold S, Müller M. Measurements and CFD modeling of a pulverized coal flame with emphasis on ash deposition. Fuel 2016;167:168–79.
[398] Boysan F, Weber R, Swithenbank J. Modeling coal-fired cyclone combustors. Combust Flame 1986;63:73–86.
[399] Boow J. Sodium/ash reactions in the formation of fireside deposits in pulverized-fuel-fired boilers. Fuel 1972;51(3):170–3.
[400] Gupta SK, Wall TF, Creelman RA, Gupta RP. Ash fusion temperatures and the transformations of coal ash particles to slag. Fuel Process Technol 1998;56:33–43.
[401] Wall TF, Creelman RA, Gupta RP, Gupta SK. Coal ash fusion temperatures – new characterization techniques, and implications for slagging and fouling. Prog Energy Combust Sci 1998;24(4):345–53.
[402] Ellis GC. The thermomechanical, electrical conductance and chemical characteristics of coal ash deposits. NERDDP project no. 1181, final report, Vol. 3. Australia: SECV R&D Department; 1989.
[403] Rushdi A, Sharma A, Gupta R. An experimental study of the effect of coal blending on ash deposition. Fuel 2004;83:495–506.
[404] Buhre BJP, Browning GJ, Gupta RJ, Wall TF. Measurement of the viscosity of coal-derived slag using thermomechanical analysis. Energy Fuels 2005;19:1078–83.
[405] Raask E. Sintering characteristics of coal ashes by simultaneous dilatometry-electrical conductance measurements. J Therm Anal Calorim 1979;16(1):91–102.
[406] Wibberley LJ, Wall TF. Alkali-ash reactions and deposit formation in pulverized-coal-fired boilers: experimental aspects of sodium silicate formation and the formation of deposits. Fuel 1982;61(1):93–9.
[407] Srinivasachar S, Senior CL, Helble JJ, Moore JW. A fundamental approach to the prediction of coal ash deposit formation in combustion systems. Symposium (International) on Combustion, 24; 1992. p. 1179–87.
[408] Richards GH, Slater PN, Harb JN. Simulation of ash deposit growth in a pulverized coal-fired pilot scale reactor. Energy Fuels 1993;7(6):774–81.
[409] Yilmaz S, Cliffe KR. Simulation of coal ash deposition on to a superheater tube. J Inst Energy 1997;70(482):17–23.
[410] Costen PG, Lockwood FC, Siddique MM. Mathematical modeling of ash deposition in pulverized fuel-fired combustors. Proc Combust Inst 2000;28(2):2243–50.
[411] Rushdi A, Gupta R, Sharma A, Holcombe D. Mechanistic prediction of ash deposition in a pilot-scale test facility. Fuel 2005;84(10):1246–58.
[412] Laycock RG, Fletcher TH. Time-dependent deposition characteristics of fine coal fly ash in a laboratory gas turbine environment. J Turbomach 2012;135 (2):021003.
[413] Laycock RG, Fletcher TH. Erratum: time-dependent deposition characteristics of fine coal fly ash in a laboratory gas turbine environment. J Turbomach 2017;139 (12):127001.
[414] Wall S, John W, Wang HC, Goren SL. Measurements of kinetic energy loss for particles impacting surfaces. Aerosol Sci Technol 1990;12(4):926–46.
[415] Esmen NA, Ziegler P, Whitfield R. The adhesion of particles upon impaction. J Aerosol Sci 1978;9(6):547–56.
[416] Cheng YS, Yeh HC. Particle bounce in cascade impactors. Environ Sci Technol 1979;13(11):1392–6.
[417] D'Ottavio T, Goren SL. Aerosol capture in granular beds in the impaction dominated regime. Aerosol Sci Technol 1982;2(2):91–108.
[418] Rogers LN, Reed J. The adhesion of particles undergoing an elastic-plastic impact with a surface. J Phys D 1984;17(4):677–89.
[419] Wang HC, John W. Dynamic adhesion of particles impacting a cylinder. Particles on surfaces 1. Springer; 1988. p. 211–24. ISBN: 978-1461595335.
[420] Dong M, Li S, Xie J, Han J. Experimental studies on the normal impact of fly ash particles with planar surfaces. Energies 2013;6(7):3245–62.
[421] Dong M, Han J, Li S, Pu H. A dynamic model for the normal impact of fly ash particle with a planar surface. Energies 2013;6(8):4288–307.
[422] Krijt S, Güttler C, Heißelmann D, Dominik C, Tielens A. Energy dissipation in head-on collisions of spheres. J Phys D 2013;46(43):435303.
[423] Dahneke B. Further measurements of the bouncing of small latex spheres. J Colloid Interface Sci 1975;51(1):58–65.
[424] Dunn PF, Brach RM, Caylor MJ. Experiments on the low-velocity impact of microspheres with planar surfaces. Aerosol Sci Technol 1995;23(1): 80–95.
[425] Li X, Dunn PF, Brach RM. Experimental and numerical studies on the normal impact of microspheres with surfaces. J Aerosol Sci 1999;30(4): 439–49.
[426] Kim OV, Dunn PF. A microsphere-surface impact model for implementation in computational fluid dynamics. J Aerosol Sci 2007;38(5):532–49.
[427] Sorace CM, Louge MY, Crozier MD, Law VH. High apparent adhesion energy in the breakdown of normal restitution for binary impacts of small spheres at low speed. Mech Res Commun 2009;36(3):364–8.
[428] Brach RM, Dunn PF. A mathematical model of the impact and adhesion of microsphers. Aerosol Sci Technol 1992;16(1):51–64.
[429] Konstandopoulos AG. Particle sticking/rebound criteria at oblique impact. J Aerosol Sci 2006;37(3):292–305.
[430] Thornton C. Interparticle sliding in the presence of adhesion. J Phys D 1991;24 (11). 1942
[431] Johnson KL, Kendall K, Roberts AD. Surface energy and the contact of elastic solids. Proc R Soc Lond A 1971;324(1558):301–13.
[432] Aylor DE, Ferrandino FJ. Rebound of pollen and spores during deposition on cylinders by inertial impaction. Atmos Environ 1985;19(5):803–6.
[433] Rosner DE, Tandon P. Rational prediction of inertially induced particle deposition rates for a cylindrical target in a dust-laden stream. Chem Eng Sci 1995;50 (21):3409–31.
[434] Konstandopoulos AG. Deposit growth dynamics: particle sticking and scattering phenomena. Powder Technol 2000;109(1):262–77.
[435] Chandra S, Avedisian CT. On the collision of a droplet with a solid surface. Proc R Soc Lond A 1991;432(1884):13–41.
[436] Vander Wal RL, Berger GM, Mozes SD. The splash/non-splash boundary upon a dry surface and thin fluid film. Exp fluids 2006;40(1):53–9.
[437] Šlančiauskas A, Kalpokaitė R. Behaviour of a heavy fuel oil droplet on a hot surface. Int J Heat Mass Transfer 2006;49(5):1050–7.
[438] Šikalo S, Tropea C, Ganić EN. Impact of droplets onto inclined surfaces. J Colloid Interface Sci 2005;286(2):661–9.
[439] Wachters LH, Westerling NA. The heat transfer from a hot wall to impinging water drops in the spheroidal state. Chem Eng Sci 1966;21(11):1047–56.
[440] Mundo CH, Sommerfeld M, Tropea C. Droplet-wall collisions: experimental studies of the deformation and breakup process. Int J Multiphase Flow 1995;21 (2):151–73.
[441] Pasandideh-Fard M, Qiao YM, Chandra S, Mostaghimi J. Capillary effects during droplet impact on a solid surface. Phys Fluids 1996;8(3):650–9. (1994-present)
[442] Bai CX, Rusche H, Gosman AD. Modeling of gasoline spray impingement. Atomization Sprays 2002;12(1-3).
[443] Shen J, Graber C, Liburdy J, Pence D, Narayanan V. Simultaneous droplet impingement dynamics and heat transfer on nano-structured surfaces. Exp Therm Fluid Sci 2010;34(4):496–503.
[444] Negeed ESR, Hidaka S, Kohno M, Takata Y. High speed camera investigation of the impingement of single water droplets on oxidized high temperature surfaces. Int J Therm Sci 2013;63:1–14.

[445] Werner SRL, Jones JR, Paterson AHJ, Archer RH, Pearce DL. Air-suspension coating in the food industry: part II—micro-level process approach. Powder Technol 2007;171(1):34–45.
[446] Grover RO, Assanis DN. A spray wall impingement model based upon conservation principles. Fifth International Symposium on Diagnostics and Modeling of Combustion in Internal Combustion Engines; 2001. p. 551–9.
[447] Bai C, Gosman AD. Development of methodology for spray impingement simulation. SAE Technical Paper No. 950283; 1995.
[448] Rein M. Phenomena of liquid drop impact on solid and liquid surfaces. Fluid Dyn Res 1993;12(2):61–93.
[449] Yarin AL. Drop impact dynamics: splashing, spreading, receding, bouncing…. Annu Rev Fluid Mech 2006;38:159–92.
[450] Mahulkar AV, Marin GB, Heynderickx GJ. Droplet–wall interaction upon impingement of heavy hydrocarbon droplets on a heated wall. Chem Eng Sci 2015;130:275–89.
[451] Aziz SD, Chandra S. Impact, recoil and splashing of molten metal droplets. Int J Heat Mass Transfer 2000;43(16):2841–57.
[452] Rioboo R, Marengo M, Tropea C. Time evolution of liquid drop impact onto solid, dry surfaces. Exp Fluids 2002;33(1):112–24.
[453] Hsiao WK, Chun JH, Saka N. The effects of wetting and surface roughness on liquid metal droplet bouncing. J Manuf Sci Eng 2009;131(2). 021010-1
[454] Zhou Z, Chen L, Wang Z, Guo L, Huang Z, Cen K. Experimental and modeling investigation of oxy-coal combustion based on Langmuir–Hinshelwood kinetics and direct calculation of char morphology. Fuel 2017;208:702–13.
[455] Wang FL, He YL, Tong ZX, Tang SZ. Real-time fouling characteristics of a typical heat exchanger used in the waste heat recovery systems. Int J Heat Mass Transfer 2017;104:774–86.
[456] Troiano M, Montagnaro F, Salatino P, Solimene R. Experimental characterization of particle-wall interaction relevant to entrained-flow gasification of biomass. Fuel 2017;209:674–84.
[457] Fujimoto H, Oku Y, Ogihara T, Takuda H. Hydrodynamics and boiling phenomena of water droplets impinging on hot solid. Int J Multiphase Flow 2010;36(8):620–42.
[458] Arcoumanis C, Whitelaw DS, Whitelaw JH. Gasoline injection against surfaces and films. Atomization Sprays 1997;7(4):437–56.
[459] Scholz P. Entwicklung eines Haftkriteriums zur Beschreibung der Partikelablagerung auf quer angeströmten Zylindern. TU München; 2015 Master thesis.
[460] Walsh PM, Sarofim AF, Beer JM. Fouling of convection heat exchangers by lignitic coal ash. Energy Fuels 1992;6(6):709–15.
[461] Hsu L, Kubarych K, Stetson A, Metcalfe A. Mechanisms of fouling, slagging and corrosion by pulverised coal combustion. Solar Turbines No. DOE/PC/40272-8, San Diego, USA; 1984.
[462] Hamaker HC. The London—van der Waals attraction between spherical particles. Physica 1937;4(10):1058–72.
[463] Israelachvili JN. Intermolecular and surface forces. revised third edition Academic Press; 2011. ISBN: 978-0123751829.
[464] Stahlhofen W, Rudolf G, James AC. Intercomparison of experimental regional aerosol deposition data. J Aerosol Med 1989;2(3):285–308.
[465] Heyder J, Gebhart J, Rudolf G, Schiller CF, Stahlhofen W. Deposition of particles in the human respiratory tract in the size range of 0.005–15 μm. J Aerosol Sci 1986;17(5):811–25.
[466] Schiller CF, Gebhart J, Heyder J, Rudolf G, Stahlhofen W. Deposition of monodisperse insoluble aerosol particles in the 0.005 to 0.2 μm range within the human respiratory tract. In: Proceedings of the 6th Symposium on Inhaled Particles, Annals of Occupational Hygiene, 32; 1988. p. 41–9.
[467] Wang HC, Kasper G. Filtration efficiency of nanometer-size aerosol particles. J Aerosol Sci 1991;22(1):31–41.
[468] Rennecke S, Weber AP. The critical velocity for nanoparticle rebound measured in a low pressure impactor. J Aerosol Sci 2013;58:135–47.
[469] Weir G, McGavion P. The coefficient of resitution for the idealized impact of a spherical, nano-scale particle on a rigid plane. Proc R Soc Lond A 2008;464(2093).
[470] Christenson HK. Adhesion and surface energy of mica in air and water. J Phys Chem 1993;97:12034–41.
[471] Mulheran PA. Surface free-energy calculations and the equilibrium shape of NaCl crystals. Modell Simul Mater SciEng 1994;2:1123–9.
[472] Sayan P, Ulrich J. Effect of various impurities on the hardness of NaCl crystals. Cryst Res Technol 2001;36:1253–62.
[473] Mouret G, Chazelet S, Thomas D, Bemer D. Discussion about the thermal rebound of nanoparticles. Sep Purif Technol 2011;78:125–31.
[474] Hærvig J, Kleinhans U, Wieland C, Spliethoff H, Jensen AL, Sørensen K, Condra TJ. On the adhesive JKR contact and rolling models for reduced particle stiffness discrete element simulation. Powder Technol 2017;319:472–82.
[475] Bradley RS. The cohesive force between solid surfaces and the surface energy of solids. London Edinburgh Dublin Philos Mag J Sci 1932;13(86):853–62.
[476] Derjaguin BV, Muller VM, Toporov YP. Effect of contact deformations on the adhesion of particles. J Colloid Interface Sci 1975;53(2):314–26.
[477] Kang SG, Helble JJ, Sarofim AF, Beér JM. Time-resolved evolution of fly ash during pulverized coal combustion. Symposium (International) on Combustion, 22; 1989. p. 231–8.
[478] Kang SG, Kerstein AR, Helble JJ, Sarofim AF. Simulation of residual ash formation during pulverized coal combustion: bimodal ash particle size distribution. Aerosol Sci Technol 1990;13(4):401–12.
[479] Singh RI, Brink A, Hupa M. CFD modeling to study fluidized bed combustion and gasification. Appl Therm Eng 2013;52:585–614.
[480] Wang H, Harb JN. Modeling of ash deposition in large-scale combustion facilities burning pulverized coal. Prog Energy Combust Sci 1997;23(3):267–82.
[481] Bernstein W, Hildebrand V, Holfeld T. Modellierung der Verbrennung und ihre Validierung am Originalbraunkohledampferzeuger eines 800 MW Blockes. Deutscher Flammentag 19, VDI-Berichte, 1999, 45–55, ISBN: 3-18-091492-0.
[482] Fan JR, Zha XD, Sun P, Cen KF. Simulation of ash deposit in a pulverized coal-fired boiler. Fuel 2001;80(5):645–54.
[483] Eddings EG, Davis KA, Heap MP, Valentine JR, Sarofim AF. Mineral matter transformation during pulverized coal combustion. Dev Chem Eng Mineral Process 2001;9(3–4):313–27.
[484] Müller C, Skrifvars BJ, Backman R, Hupa M. Ash deposition prediction in biomass fired fluidised bed boilers – combination of CFD and advanced fuel analysis. Prog Comput Fluid Dyn Int J 2003;3(2-4):112–20.
[485] Müller C, Brink A, Hupa M. Numerical simulation of the combustion behavior of different biomasses in a bubbling fluidized bed boiler. In: Proceedings of 18th International Conference on Fluidized Bed Combustion, Toronto Canada; 2005.
[486] Lundmark D, Müller C, Backman R, Zevenhoven M, Skrifvars BJ, Hupa M. CFD based ash deposition prediction in a BFBC firing mixtures of peat and forest residue. J Energy Resour Technol 2010;132(3):031003.
[487] Vuthaluru HB, Kotadiya N, Vuthaluru R, French D. CFD based identification of clinker formation regions in large scale utility boiler. Appl Therm Eng 2011;31(8):1368–80.
[488] Strelow M. Mineralumwandlung in Feuerungen. Shaker; 2013. PhD thesis, ISBN: 978-3844023619.
[489] Taha TJ, Stam AF, Stam K, Brem G. CFD modeling of ash deposition for co-combustion of MBM with coal in a tangentially fired utility boiler. Fuel Process Technol 2013;114:126–34.
[490] Kreutzkam B. Analyse des Depositionsverhaltens bei staubförmiger Kohleverbrennung unter Berücksichtigung der Partikelfragmentation. TU München, Dr. Hut Verlag; 2014. PhD thesis, ISBN: 978-3843918725.
[491] Huang LY, Norman JS, Pourkashanian M, Williams A. Prediction of ash deposition on superheater tubes from pulverized coal combustion. Fuel 1996;75(3):271–9.
[492] Lee FCC, Lockwood FC. Modelling ash deposition in pulverized coal-fired applications. Prog Energy Combust Sci 1998;25(2):117–32.
[493] Forstner M, Hofmeister G, Jöller M, Dahl J, Braun M, Kleditzsch S, Scharler R, Obernberger I. CFD simulation of ash deposit formation in fixed bed biomass furnaces and boilers. Prog Comput Fluid Dyn Int J 2006;6(4-5):248–61.
[494] Degereji MU, Ingham DB, Ma L, Pourkashanian M, Williams A. Numerical assessment of coals/blends slagging potential in pulverized coal boilers. Fuel 2012;102(0):345–53.
[495] Schulze K, Scharler R, Telian M, Obernberger I. Advanced modelling of deposit formation in biomass furnaces – investigation of mechanisms and comparison with deposit measurements in a small-scale pellet boiler. Impact of Fuel Quality on Power Production and Environment, Lapland Finland; 2010.
[496] Venturini P, Borello D, Hanjalić K, Rispoli F. Modelling of particles deposition in an environment relevant to solid fuel boilers. Appl Therm Eng 2012;49:131–8.
[497] Kær SK. Numerical modelling of a straw-fired grate boiler. Fuel 2004;83(9):1183–90.
[498] Mueller-Steinhagen H, Zettler U. Handbook of heat exchanger fouling: mitigation and cleaning technologies. PP Publico Publications; 2011. ISBN: 978-3934736009
[499] Gent RW, Dart NP, Cansdale JT. Aircraft icing, Philosophical Transactions of the Royal Society of London A: Mathematical. Phys Eng Sci 2000;358(1776):2873–911.
[500] Politovich MK. Aircraft icing caused by large supercooled droplets. J Appl Meteorol 1989;28(9):856–68.
[501] Kim J, Dunn MG, Baran AJ, Wade DP, Tremba EL. Deposition of volcanic materials in the hot sections of two gas turbine engines. J Eng Gas Turbines Power 1993;115(3):641–51.
[502] Hamed A, Tabakoff WC, Wenglarz RV. Erosion and deposition in turbomachinery. J Propul Power 2006;22(2):350–60.
[503] Asgharian B, Hofmann W, Bergmann R. Particle deposition in a multiple-path model of the human lung. Aerosol Sci Technol 2001;34(4):332–9.
[504] Jin HH, Fan JR, Zeng MJ, Cen KF. Large eddy simulation of inhaled particle deposition within the human upper respiratory tract. J Aerosol Sci 2007;38(3):257–68.
[505] Champagne VK. The cold spray materials deposition process: fundamentals and applications. Woodhead Publishing; 2007. ISBN: 978-1845691813
[506] Koo JY, Martin JK. Droplet sizes and velocities in a transient diesel fuel spray. In: SAE Paper No. 900397, 1990.
[507] Hertz H. Miscellaneous papers. London, UK: Macmillan; 1896. 146–162.
[508] XXII Lord Rayleigh. On the production of vibrations by forces of relatively long duration, with application to the theory of collisions. London Edinburgh Dublin PhilosMag J Sci 1906;11(62):283–91.
[509] Andres RP. Inelastic energy transfer in particle/surface collisions. Aerosol Sci Technol 1995;23(1):40–50.
[510] Xu M, Willeke K. Right-angle impaction and rebound of particles. J Aerosol Sci 1993;24(1):19–30.
[511] Bitter JG. A study of erosion phenomena part I. Wear 1963;6(1):5–21.
[512] Brach RM, Dunn PF, Li X. Experiments and engineering models of microparticle impact and deposition. J Adhes 2000;74(1-4):227–82.
[513] Wu CY, Thornton C, Li LY. A semi-analytical model for oblique impacts of elastoplastic spheres. Proc R Soc Lond A 2009;465:937–60.

[514] Li X, Dunn PF, Brach RM. Experimental and numerical studies of microsphere oblique impact with planar surfaces. J Aerosol Sci 2000;31(5):583–94.
[515] Wu CY, Thornton C, Li LY. Coefficients of restitution for elastoplastic oblique impacts. Adv Powder Technol 2003;14(4):435–48.
[516] Li X, Dunn PF, Brach RM. Lycopodium spore impacts onto surfaces. Atmos Environ 2000;34(10):1575–81.
[517] Stanton DW, Rutland CJ. Modeling fuel film formation and wall interaction in diesel engines, 1996, SAE Paper No. 960628.
[518] O'Rourke PJ, Amsden AA. A spray/wall interaction submodel for the KIVA-3 wall film model, 2000, SAE Paper No.2000-01-0271.
[519] Tabakoff W. Measurements of particles rebound characteristics on materials used in gas turbines. J Propul Power 1991;7(5):805–13.
[520] Reagle CJ, Delimont JM, Ng WF, Ekkad SV. Study of microparticle rebound characteristics under high temperature conditions. J Eng Gas Turbines Power 2014;136(1):011501.
[521] Goldsmith W. Impact, courier corporation, 2001, ISBN: 978-0486420042.
[522] Werner BT. A physical model of wind-blown sand transport. California Institute of Technology; 1987, PhD thesis.
[523] Müller P, Tomas J, Antonyuk S, Heinrich S. The restitution coefficient of three characteristic granules. Abstracts and Proceedings, WCPT6; 2010.
[524] Abd-Elhady MS, Rindt CCM, Wijers JG, van Steenhoven AA. Modelling the impaction of a micron particle with a powdery layer. Powder Technol 2006;168(3):111–24.
[525] Cundall PA, Strack ODL. A discrete numerical model for granular assemblies. Geotechnique 1979;29(1):47–65.
[526] Li S, Marshall JS, Liu G, Yao Q. Adhesive particulate flow: the discrete-element method and its application in energy and environmental engineering. Prog Energy Combust Sci 2011;37(6):633–68.
[527] Lorenz A, Tuozzolo C, Louge MY. Measurements of impact properties of small, nearly spherical particles. Exp Mech 1997;37(3):292–8.
[528] Ots A. Mechanism of ash deposit formation, corrosion and sulphur capture by burning calcium and chlorine containing fuels. VGB PowerTech 2001;81(10):114–20.
[529] Tsai CJ, Cheng YH. Solid particle collection characteristics on impaction surfaces of different designs. Aerosol Sci Technol 1995;23(1):96–106.
[530] Barnocky G, Davis RH. The effect of Maxwell slip on the aerodynamic collision and rebound of spherical particles. J Colloid Interface Sci 1988;121(1):226–39.
[531] Davis RH, Serayssol JM, Hinch EJ. The elastohydrodynamic collision of two spheres. J Fluid Mech 1986;163:479–97.
[532] Kleinhans U, Wieland C, Babat S, Scheffknecht G, Spliethoff H. Ash particle sticking and rebound behavior: a mechanistic explanation and modeling approach. Proc Combust Inst 2017;36(2):2341–50.
[533] Bennett T, Poulikakos D. Splat-quench solidification: estimating the maximum spreading of a droplet impacting a solid surface. J Mater Sci 1993;28(4.):963–70.
[534] ANSYS Fluent 16.0, theory guide, 2015.
[535] Michelsen HP, Frandsen F, Dam-Johansen K, Larsen OH. Deposition and high temperature corrosion in a 10 MW straw fired boiler. Fuel Process Technol 1998;54(1):95–108.
[536] Werkelin J. Ash-forming elements and their chemical forms in woody biomass fuels elements. Finland: Abo Akademi; 2008, PhD thesis.
[537] Vassilev SV, Baxter D, Andersen LK, Vassileva CG, Morgan TJ. An overview of the organic and inorganic phase composition of biomass. Fuel 2012;94:1–33.
[538] Tremel A. Reaction kinetics of solid fuels during entrained flow gasification. TU München, Dr. Hut Verlag; 2012. PhD thesis, ISBN: 978-3843908160.
[539] Warren PH. Extrapolated partial molar densities of SO_3, P_2O_5, and other oxides in silicate melts. Am Mineral 1995;80(9):1085–8.
[540] Baxter LL, Mitchell RE. The release of iron during the combustion of Illinois No. 6 coal. Comb. Flame 1992;88:1–14.
[541] Chen S, Li S, Yang M. Sticking/rebound criterion for collisions of small adhesive particles: Effects of impact parameter and particle size. Powder Technology 2015;274:431–40.
[542] Hickey AJ, Mansour HM, Telko MJ, Xu Z, Smyth HDC, Mulder T, McLean R, Langridge J, Papadopoulos D. Physical characterization of component particles included in dry powder inhalers. I. Strategy review and static characteristics. J. Pharm. Sci. 2007;96:1282–301.